An Integrated Framework for Finite Element Modelling of Ultrasonic Inspections of Carbon Fibre Reinforced Polymer Components

A Thesis submitted in fulfilment of the requirements for the degree of Doctor of Engineering

Jeff Mainland Dobson

Centre for Ultrasonic Engineering

Department of Electronic and Electrical Engineering

University of Strathclyde

2019

Declaration of Authorship

This Thesis is the result of the author's original research. It has been composed by the author and has not been previously submitted for examination which has led to the award of a degree.

Signed:

Date:

Abstract

Over the last decade there has been a vast increase in the use of composite materials in many engineering aspects. This increase is due to their ability to provide increased mechanical strength while also yielding weight savings in structures. Not only can composites be manufactured to create complex geometry components, their layup can be designed to provide optimum strength and stiffness. Carbon Fibre Reinforced Polymer (CFRP) composite materials pose a challenge for ultrasonic Non Destructive Evaluation (NDE) inspections due to their anisotropic material properties and often complex morphology.

This Thesis develops an integrated framework to allow for accurate Finite Element Analysis (FEA) simulations of CFRP components to be constructed. The developed framework can generate the CFRP model geometry from a range of different sources. This enables the ability to construct models based on the design specification of the component, through scripting or importing of component design information, as well as creating models based on their real structure, from images taken from micrographs or X-Ray CT data. This allows for ultrasonic NDE inspections to be simulated to develop a better understanding of inspection performance, as well as act as a tool to aid inspection design.

A parametric study for the inspection of a flat CFRP component is presented to demonstrate the benefit of simulation to aid the understanding of the ultrasonic response and ability to optimise the inspection setup. Further work focuses on the simulation of inspections of tapered geometry components. This adds an additional level of complexity to the inspection and FEA simulation is shown to be an effective technique to optimise specific inspection parameters. Importantly, inspection amplitude maps are used as a tool, both to understand the limitations of an inspection configuration, and to develop new inspection approaches.

Acknowledgements

Firstly, I would like to thank my supervisors, Prof. Anthony Gachagan and Dr Richard O'Leary, for all of their support and guidance during my EngD.

I am grateful to OnScale for being an industrial partner of this work and for their sponsorship. I would especially like to thank Dr Andrew Tweedie and Dr Gerald Harvey for their supervision and help throughout my EngD.

Thank you to all at the RCNDE for the opportunity and organising a very enjoyable and rewarding EngD program. Thanks also to other EngD students, particularly my fellow 2013 cohort, for all the enjoyable times on our courses and at conferences.

Thanks to all of the members of CUE at Strathclyde who have helped me over the years, along with Dr Paul Murray for his help with the image processing.

My thanks also goes to Prof. Robert Smith and his composite NDE team at the University of Bristol for their collaboration and supply of data. Particular thanks to Christina Fraij for conducting the X-Ray CT scans on the laminate sample and Dr Rostand Tayong for providing experimental data.

I would like to thank my family, and in particular my parents, for all of their support and encouragement over these years.

Finally, I am eternally grateful to Jacqueline, who throughout my EngD became my wife and has always been there for me. Thank you.

Contents

List of Figures

List of Tables

List of Abbreviations

CFRP	**C**arbon **F**ibre **R**einforced **P**olymer
NDE	**N**on **D**estructive **E**valuation
EngD	**Eng**ineering **D**octorate
RCNDE	**R**esearch **C**entre for **N**on **D**estructive **E**valuation
CAE	**C**omputer **A**ided **E**ngineering
CUE	**C**entre for **U**ltrasonic **E**ngineering
SaaS	**S**olver-**as**-**a**-**S**ervice
FEA	**F**inite **E**lement **A**nalysis
GFRP	**G**lass **F**ibre **R**einforced **P**olymer
TFM	**T**otal **F**ocusing **M**ethod
FMC	**F**ull **M**atrix **C**apture
FFT	**F**ast **F**ourier **T**ransform
BEM	**B**oundary **E**lement **M**ethod
FD	**F**inite **D**ifference
FEM	**F**inite **E**lement **M**ethod
FIT	**F**inite **I**ntegration **T**echnique
EFIT	**E**lastic **F**inite **I**ntegration **T**echnique
GPU	**G**raphical **P**rocessing **U**nit
CPU	**C**entral **P**rocessing **U**nit
FRP	**F**ibre **R**einforced **P**olymer
CT	**C**omputed **T**omography
FDTD	**F**inite **D**ifference **T**ime **D**omian
MPI	**M**essage **P**assing **I**nterface
QNDE	**Q**uantitative **N**on **D**estructive **E**valuation
CFL	**C**ourant **F**riedrichs **L**ewy

CAD	**C**omputer **A**ided **D**esign
cueART	**C**entre for **U**ltrasonic **E**ngineering **A**coustic **R**esearch **T**oolbox
GUI	**G**raphical **U**ser **I**nterface
CSV	**C**omma-**S**eparated **V**alue
CT	**C**omputed **T**omography
SCNR	**S**ignal to **C**oherent **N**oise **R**atio
RMS	**R**oot **M**ean **S**quare
HPC	**H**igh **P**erformance **C**omputing

Chapter 1

Introduction

The use of Carbon Fibre Reinforced Polymer (CFRP) materials has become more prominent in industry due to their high strength and light weight. These materials pose challenges to ultrasonic Non-Destructive Evaluation (NDE) techniques as their anisotropic microstructure and laminate construction cause scattering and refraction of the beam, both of which can detrimentally affect inspection coverage. With the use of composite materials ever expanding, the requirement for advanced research into composite inspections increases. Simulation is a vital tool in the design of ultrasonic inspections, improving setup and helping understand wave propagation in complex components. This chapter provides an introduction to the Thesis, covering background information and the industrial motivation for the work. Also presented in this Chapter are the overall objectives and an outline of the Thesis.

1.1 Background

The research presented in this Thesis was conducted as part of an Engineering Doctorate (EngD) through the UK Research Centre for Non-Destructive Evaluation (RCNDE). The RCNDE is a collaboration between industry and academia to coordinate research into NDE technologies, with the EngD program allowing for industry relevant research to be conducted and transferred into industry. The project was sponsored by industrial partner OnScale (formally PZFlex [1]), a commercial Computer Aided Engineering (CAE) package designed to efficiently simulate large acoustic wave propagation and piezoelectric problems. The research was undertaken in partnership with the Centre for Ultrasonic Engineering (CUE) at the University of Strathclyde as the academic partner.

NDE inspections are a safety critical measure to asses component structural integrity and to detect any discontinuity or defects. Therefore, it is essential that the NDE requirements can be met when conducted on high value components and structures. For NDE techniques, such as ultrasonic testing, modelling is a critical tool for designing and evaluating inspections and helps to optimise the inspection in a small time frame and removes the expense of fabricating test components. A wide variety of NDE modelling techniques exist to simulate ultrasonic inspections and includes various analytical and numerical methods. All the different methods have their own advantages and disadvantages and the optimal approach for a simulation scenario is dependent on the simulation requirements. As ultrasonic NDE inspections evolve with new materials and manufacturing techniques, the simulation demands to simulate these inspection scenarios increase.

OnScale is the world's first Solver-as-a-Service (SaaS) based model for CAE in the cloud [2] and was designed with custom Finite Element Analysis (FEA) solvers that allow for computationally large simulations to be solved quickly and efficiently. OnScale has been used in different application areas including NDE, where it's computational efficiency makes it ideal to simulate ultrasonic NDE inspections. As simulation demands evolve it is important that research is conducted to extend the modelling capabilities to ensure the simulation demands are met. Advancing a simulation tool capability can enable new and advanced inspections to be simulated to gain a deeper understanding of the experimental behaviour and allow inspections to be evaluated and optimised in a reduced time frame and with a lower cost.

1.2 Industrial Motivation

The increased presence of CFRP materials in many industrial applications has resulted in challenges for NDE inspections. In particular there has been major advances in the aerospace industry, where CFRP materials are fast becoming the preferred material for a number of aircraft components. These components are proving difficult to inspect with conventional inspection techniques such as ultrasonic inspection. It was highlighted by a RCNDE industry member that tapered CFRP components were particularly challenging to inspect using ultrasonic methods. Due to the complex geometry and anisotropic material properties, the incident wave is highly scattered and refracted. The behaviour of the wave propagation was poorly understood and there was a lack of modelling capability. Therefore, the advancement of modelling NDE inspections of tapered composites would offer a great ability to help cope with the current demand.

Tapered CFRP components contain ply drops which allows for a variation in the component thickness. This creates a structure that contains ply layers which are no longer parallel with each other. These angled ply layers have a big impact on the ultrasonic inspection capability. This is due to the sound travelling faster along the plies than through the thickness and being reflected and refracted after interaction with angled ply interfaces. Modelling of these situations will allow for a deeper understanding of the scenario and allow for inspections to be designed.

While the use of composites in aerospace is increasing, the current composite designs are not being fully optimised. There is a lack of confidence in what is manufactured and so composite materials are over-designed with additional ply layers to reduce deviations from design [3]. By making the composites thicker and heavier than necessary, the benefit of using composite materials for weight savings is reduced. To allow for more efficient designs to be utilised and get the maximum weight savings, it is essential that there is a high level of confidence in the manufactured composite materials. This can be achieved through NDE and modelling will play an important role in this process.

1.3 Objectives

The main objective of this research was to improve the capability of modelling ultrasonic NDE inspections of CFRP components. There is a particular focus to the simulation of inspections of tapered CFRP structures which were identified as a current industrial problem. This research would look to increase the modelling capability to allow for these inspection scenarios to be evaluated and optimised. The research considers unidirectional and 2D woven CFRP structures, but the developed framework could also be used to model 3D woven structures and consider Glass Fibre Reinforced Polymer (GFRP) components. To achieve the overall aim of the research, a number of sub-objectives were identified:

- Fundamental evaluation of OnScale as an NDE simulation tool
- Efficient and valid modelling approach for CFRP components
- Advanced representative generation of complete CFRP structure geometries:
    - from component design specifications
    - from real structure information
    - including interply resin layers
- Implementation of appropriate material properties that accounts for ply layer orientation variances
- Generation of tapered CFRP structures from a simple plybook
- Framework to evaluate and optimise inspection of tapered CFRP structures
- Demonstrate how the framework can be utilised for parametric studies to investigate the ultrasonic NDE inspection of CFRP components

1.4 Outline of Thesis

Chapter 2 provides a literature review covering the research topics that are relevant to this Thesis. An overview of ultrasonic NDE modelling and the methods available are firstly presented before justification for selecting FEA for this research is given. An overview of the OnScale FEA software is provided along with how a model is implemented and how it compares against other packages. The Chapter ends with an overview of ultrasonic NDE of composite materials that includes a review of research into modelling ultrasonic NDE of composites.

Chapter 3 demonstrates validation and optimisation of the modelling method used in the research. This involves the comparison of Total Focusing Method (TFM) images generated from both experimental and FEA derived Full Matrix Capture (FMC) data sets. Results indicate the FEA models are able to accurately predict the experimental performance, provided the models utilise acceptable approximations and provide an accurate representation of the practical inspection.

Chapter 4 introduces the approaches created to allow for the generation of FEA models of CFRP structures. A range of techniques are presented that can construct high fidelity model geometries and encompass variations in material properties. Each approach is introduced and its method is described with an example before the advantages and disadvantages of the approaches are discussed.

Chapter 5 demonstrates how simulation can be used to perform a parametric study to investigate the effect varying transducer frequency and focal length has on the ability to characterise a CFRP component. FEA derived results are compared for two different geometry generation approaches and also verified against experimentally collected data.

Chapter 6 presents how the research can be utilised to evaluate and optimise the ultrasonic inspection of tapered CFRP components. Initial simulations are performed to replicate an experimental inspection of a tapered component. Simulations are then performed to demonstrate how simulation can be utilised to investigate the inspection of three tapers with different severities of taper angle. The performance of the inspections are evaluated and further simulations are performed to demonstrate how simulations can be used to improve defect detection.

Chapter 7 concludes the Thesis and details the key contributions achieved from the research. The technology transfer of the research and its benefits for the sponsoring company are also given. Finally, suggestions for future work to compliment this research is presented.

Chapter 2

Literature Review

Modelling and simulation tools play an important role in the NDE industry. In the case of ultrasonic NDE inspections, it is possible to model the generation and reception of ultrasonic waves as well as the wave propagation and defect interaction. These models can be utilised in the development of new inspections as well as optimisation and analysis of current techniques. Accurate and reliable simulation methods are becoming more essential due to the creation of highly challenging inspection scenarios which are arising from advanced modern manufacturing techniques and materials.

This Chapter introduces the research topics which are relevant to this Thesis. The modelling of ultrasonic NDE is a wide research area and a fundamental description can be found in Schmerr [4]. A basic overview of the current common modelling methods is provided to allow for comparisons in their suitability for this Thesis to be evaluated and give the rationale for opting for a FEA method. The FEA package, OnScale, utilised throughout this Thesis is then introduced to provide details on how models are implemented and how the software compares with other FEA packages. Finally, the ultrasonic NDE of composite materials is introduced along with an overview of the current research in modelling ultrasonic NDE inspections of composite materials.

2.1 Ultrasonic NDE Modelling

2.1.1 Introduction

Modelling is an important tool in NDE, with successful models capable of demonstrating the fundamental science of the inspection technique. The use of modelling can produce notable benefits at several stages of the NDE development process which aids in the design, validation and implementation of the inspection techniques [5]. With such an important role, modelling has been a part of the

NDE process since its earliest applications [6].

It is possible to model the generation and reception of ultrasonic waves and the wave propagation, which can allow for entire inspections to be simulated. Different test parameters can be investigated to aid the design and analysis of the inspection [4]. Using a model-based approach generates numerous benefits which can save both time and money in the development and validation of new and current inspection techniques. Validated models also offer valuable safety aspects by providing evidence that inspections can perform as required.

A wide variety of techniques have been developed for ultrasonic NDE modelling, including various analytical and numerical methods. Each method has its own associated advantages and disadvantages. Typically analytical methods are well developed and can produce solutions faster than numerical methods. However, these methods are becoming inadequate for many modern, exotic materials or components due to no exact solution existing. Numerical methods offer a solution to simulating these complex scenarios. Typically numerical methods are seen as computationally expensive but with computing power ever increasing, these methods are becoming more viable.

2.1.2 Analytical Methods

Analytical modelling methods offer a very computationally efficient solution to model ultrasonic wave propagation problems. Before the introduction of readily available computing power, analytical models were the main source of NDE modelling approaches. These methods are mathematical models that have a closed solution to the elastodynamic equations which are used to describe the ultrasonic wave propagation and its interaction with defects.

Exact analytical solutions only exist for certain specific cases and so many analytical methods include approximations [7]. For complex 2D or 3D modelling scenarios, such as complex defects or materials, analytical models can become inadequate due to the level of approximation required.

In both 2D and 3D, exact solutions exist for analytical simulations of specific cases, including: fields from point, line or simple transducer shapes in infinite media; plane wave obliquely incident on interfaces; and scattering of incident plane waves from a simple defect.

A modular approach can be applied to analytical modelling of an ultrasonic system with each section modelled separately. This allows for the transducer beam profile and the interaction of plane waves with boundaries and defects to be modelled individually. This is an effective method as long as interactions, such as multiple scattering, between individual parts can be ignored.

2.1.2.1 Huygens' Principle

In 1678 Christiaan Huygens, a Dutch physicist, produced a technique to analyse wave propagation [8]. Huygens proposed that each point on an existing wave front can be represented as a point source of a spherical wave. The summation of all these individual point source wave fronts defines the subsequent overall wave front. This technique is illustrated in Figure 2.1.

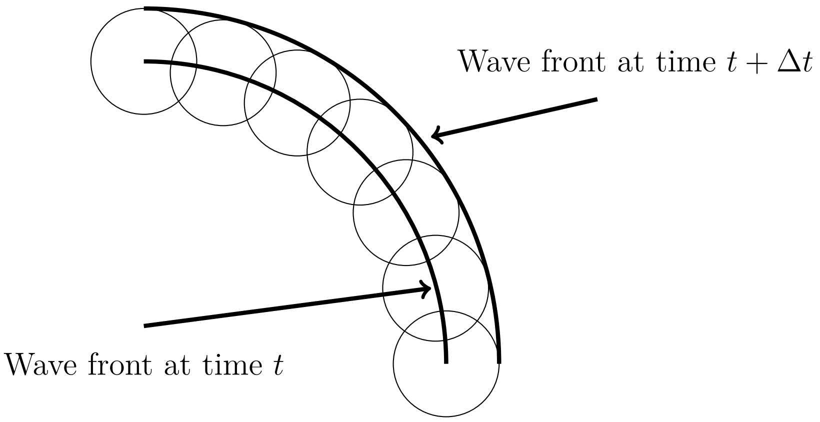

Figure 2.1: *Illustration of Huygens' Principle*

The practical application of Huygens' principle can predict the sound field from a point source or a series of point sources representing a surface or area. If we consider a 2D case, the field P, at a distance r, can be calculated for a single point source in an isotropic media using Equation 2.1.

$$P(r) = A\frac{1}{\sqrt{r}}e^{i(kr-wt)} \tag{2.1}$$

Where A is a complex number representing the source size and phase, k is the wave number, w is the angular frequency and t is time. This expression is an approximation which is not valid very close to the source. It can be seen that the $1/\sqrt{(r)}$ term represents the conservation of energy with the field decreasing when moving away from source. The expression can be extended to 3D as shown in Equation 2.2.

$$P(r) = A\frac{1}{r}e^{i(kr-wt)} \tag{2.2}$$

Huygens' Principle is commonly applied in ultrasonic transducer field modelling [9, 10]. This is done through the representation of the transducer surface as a number of point or line sources and then superposition of the fields from each source. This allows for the evaluation of the transducer beam spread, focusing capability and near field length. Jasiūnienė [11] demonstrated the capability of using Huygens to efficiently simulate the reflections from triangle reflectors in 3D.

2.1.2.2 Linear Systems

Sound wave packets contain a range of frequencies which often behave differently due to having different values of velocity or attenuation. In 1807 Joseph Fourier, a French mathematician and physicist, first demonstrated that for a linear system the frequency components can be analysed separately [12]. Time domain signals can be decomposed into a summation of sine waves and using the Fourier Transform can be converted between the time and frequency domains.

The Fourier Transform, or Fast Fourier Transform (FFT) in digital equivalence, converts signals between time and frequency domains using Equations 2.3 and 2.4, where $g(\omega)$ is the frequency domain and $F(t)$ is the time domain.

$$g(\omega) = F[f(t)] = \int_{-\infty}^{\infty} f(t)e^{-i\omega t}dt \tag{2.3}$$

$$f(t) = F^{-1}[g(\omega)] = \frac{1}{2\pi}\int_{-\infty}^{\infty} g(\omega)e^{-i\omega t}d\omega \tag{2.4}$$

The propagation of sound through any structure can be thought of as a transfer function, $H(\omega)$. An expression for a typical transfer function for an ultrasonic wave propagating from a transducer through a material to a receiver can be seen in Equation 2.5 [13].

$$H(\omega) = T_x(\omega)A(\omega)B_DX(\omega)\Delta(\omega)R_x(\omega) \tag{2.5}$$

In this expression, $Tx(\omega)$ represents the output of the source, $A(\omega)$ is the attenuation, B_D is the beam divergence, $X(\omega)$ is the reflection and transmission coefficients of features encountered in propagation, $\Delta(\omega)$ is the time delay between transmission and reception and $Rx(\omega)$ is the receiver characteristics. These individual components can be calculated for the specific case and the combination then allows for the ultrasonic wave received to be analytically modelled.

The linear systems technique has been used for effective modelling of piezoelectric transducers. Through equivalent circuits of transducers, including Mason [14] and KLM [15, 16], the transducer can be analysed using electrical network concepts. Hayward [17, 18] developed a new systems model for the thickness mode piezoelectric transducer which used physical properties as model inputs. This method used a system engineering approach to represent the transducer systems as a block diagram with feedback loops by deriving the relevant force-voltage and voltage-force equations. This method was essentially a frequency domain technique which relied on the linear systems theory. Through the use of the Z-transform, the systems model of a piezoelectric transducer can also be modelled in the time domain [19]. Hayward et al [20] then used linear systems theory to employ a three port model of the piezoelectric transducer using lattice techniques.

The use of conventional models such as Mason or KLM relies on the knowledge of the properties of the transducer. These properties are not always known and so a new method was established based on network theory by Lockwood et al [21]. This method offered the advantage of deriving the model from the transducers electrical ports, thus not requiring any knowledge of the often commercially sensitive transducer properties.

2.1.2.3 Ray Tracing

Ray tracing models can calculate the paths of plane waves propagating through a medium by considering its path as a straight line. Rays are propagated and when incident on an interface of two materials with different acoustic velocities, Snell's law can be used to calculate the transmitted and reflected ray paths. As well as refraction of the ray at the interface, mode conversion can occur with shear waves generated along with the reflected and refracted longitudinal wave. Snell's Law holds true for both longitudinal and shear waves and so all ray paths can be calculated. An illustration of the ray paths that occur when a wave is incident on a material interface between two solid media is shown in Figure 2.2.

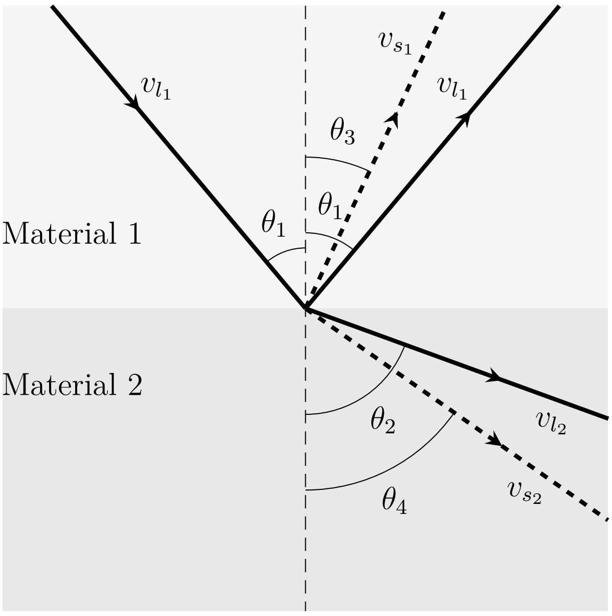

Figure 2.2: *Illustration of Snell's Law for longitudinal and shear waves for an incident wave at an interface between two solid media with* $v_{l_2} > v_{l_1}$ *and* $v_{s_2} > v_{s_1}$

In Figure 2.2, it is assumed that the longitudinal and shear wave velocities of Material 2 are greater than those of Material 1. The ray path angles can be calculated using Snell's Law, Equation 2.6, where θ_1 is the incident and reflected longitudinal angle, θ_2 is the refracted longitudinal angle, θ_3 is the reflected shear angle and θ_4 is the refracted shear angle. All angles are measured from the normal to the material interface. v_{l_1}, v_{s_1}, v_{l_2}, v_{s_2} are the longitudinal and shear velocities in materials 1 and 2 respectively.

$$\frac{\sin\theta_1}{v_{l_1}} = \frac{\sin\theta_2}{v_{l_2}} = \frac{\sin\theta_3}{v_{s_1}} = \frac{\sin\theta_4}{v_{s_2}} \tag{2.6}$$

Several programs based on ray tracing have been developed for the modelling of ultrasonic NDE. In 1991, Johnson et al [22] presented a computer program utilising the ray tracing approach to calculate ultrasonic fields in solids. This proved accurate in predicting fields in both solids and fluids. Ogilvy [23] also developed a ray tracing software package, Raytraim, which was capable of modelling ultrasonic wave propagation through austenitic steel [24] and welds [25]. A commercial software tool, CIVA [26, 27], has been developed and provides the capability to calculate ultrasonic beams in homogeneous and inhomogeneous materials. BeamTool [28] is another commercial software tool that allows for ultrasonic inspections to be easily and quickly visualised.

Ray tracing is an efficient analytical technique for modelling ultrasound propagation as calculations are only done at interfaces, reducing computation time. While being fast, ray tracing does not model various important features of ultrasonic wave propagation. For example, for a wave incident on a crack tip, a ray tracing model will only model the incident, reflected and transmitted rays in the field but in reality, there will be numerous diffracted waves propagating in multiple directions.

2.1.3 Numerical Methods

With advances in computing power, numerical methods for ultrasonic NDE modelling have become more common place in numerous applications. Analytical methods often cannot provide solutions for complex models and so approximate numerical methods are required. These methods are used to provide approximated solutions to a set of differential or integral equations and can handle complex geometries and materials. While being more computationally expensive, numerical techniques offer several advantages as they can offer an approach to model complex scenarios that cannot be accurately solved analytically. They can also provide a clearer understanding of the physical behaviour of a system when compared to an analytical equivalent [29].

2.1.3.1 Boundary Element Method

The Boundary Element Method (BEM) is a numerical method to simulate the ultrasonic wave propagation in materials by solving boundary integral equations. In this method, the boundaries of the materials are discretised into boundary elements, which are line elements for 2D models and surface elements for 3D models. This approach produces a numerical method with a reduced number of spatial dimensions. For models with a small surface to volume ratio, BEM is more computationally efficient in both solution time and memory requirements than other numerical approaches. However, the BEM is only applicable for functions where Green's functions can be calculated, which restricts the application of the method to linear homogeneous media.

Schafbuch et al [30] demonstrated the advantages of using the BEM for elastic wave scattering. This proves to be computationally efficient at modelling responses from scattering of various defects. Further work on wave scattering using BEM was conducted in [31] where defect quantification for Lamb and shear horizontal guided waves in a plate-like structure were carried out.

Despite the potential to provide a computationally efficient solution, BEM is less widely used in NDE modelling and, when compared to other methods, doesn't have any established commercially available software packages.

2.1.3.2 Finite Difference Method

The Finite Difference (FD) method reduces the model into a mesh of elements connected by nodes to calculate approximate solutions to differential equations, as first presented by Courant et al [32] in 1967. This approach replaces the partial derivatives at each grid point with approximations from neighbouring values obtained by Taylor expansions. The accuracy of the solution depends upon the number of expansion terms taken and the spacing between the mesh nodes. Reducing the element size will allow for the method to converge on the correct solution. However, for time dependant models, reducing the element size will require a smaller time step to maintain model stability which will result in a greater computation demand.

Bond [33, 34] illustrated that FD can be used to evaluate systems where there is no analytical solution available. The numerical models provided both visual and numerical results to illustrate ultrasonic wave propagation and scattering. Van Vossen et al [35] also demonstrated that FD can be applied in the modelling of ultrasonic wave propagation in fluid-solid configurations.

2.1.3.3 Finite Element Analysis

Finite Element Analysis (FEA) , also known as the Finite Element Method (FEM), is a numerical approach where, similarly to FD, the model geometry is discretised into a mesh of finite elements. These elements are sufficiently small in order to calculate their individual behaviour with reasonable accuracy. For each element, simple functions are used to describe the variations of the displacements, strain and stresses over its volume. Forces acting on the boundary of an element from neighbouring elements can lead to the calculation of displacement, strain and stress at any point in the element. Adjoining elements are connected together at points known as nodes. Using the relationship between the displacement of the elements nodes due to forces acting on the nodes, the element stiffness is calculated. The combination of each element stiffness matrix provides an overall matrix equation relating the forces and displacements of the entire structure. For a given load applied to the structure, the solution to the equation provides the displacement of each node. These displacements can then be used to calculate the stresses and strains anywhere in each element.

In ultrasound applications, FEA was originally used extensively for the simulation of piezoelectric transducers. In the late 1980's and early 1990's, Ostergaard and Pawlak [36] and Lerch [37, 38] utilised FEA for the analysis of piezoelectric structures in three-dimensions. This ability to analyse piezoelectric materials allows for ultrasonic transducers to be designed and optimised. Hossack and Hayward [39–41] utilised FEA for the investigation of 1-3 composite ultrasonic transducers. The design of piezoelectric transducers can be improved through the use of optimisation techniques and FEA models [42, 43]. There is also the ability to model a variety of transducer designs such as a deformable array [44] and capacitive micro-machined ultrasonic transducers (CMUTs) [45].

FEA has been frequently used in NDE and more specifically in ultrasonic inspection applications as it has been proven to be very effective at modelling ultrasonic wave propagation [46–49]. In 1996 Hladky-Hennion [50], developed a method of using FEA to analyse the propagation of acoustic waves in waveguides. This was then developed further to extend the method and analyse the wave propagation in an immersed waveguide [51]. FEA provides the capability to model different modes of ultrasonic wave propagation including guided waves [52] and Rayleigh waves [53].

2.1.3.4 Finite Integration Technique

Finite integration technique (FIT) is a discretisation scheme for solving electromagnetic field problems in the time and frequency domain. This technique applies Maxwell's equations in integral form to a set of staggered grids. Finite integration was introduced in 1977 by Weiland [54] to solve different electromagnetic wave problems. This idea was then adapted by Fellinger [55] to the elastodynamic case. There are numerous open source modelling codes available based on FIT including acoustic (AFIT), electromagnetic (EMFIT), elastic (EFIT), piezoelectric (PFIT) and electromagnetic-ultrasound (EMUSFIT) [56, 57].

The EFIT approach has been utilised in ultrasonic NDE modelling for wave propagation [58]. EFIT discretizes the governing equations of linear elastodynamics on a staggered voxel in grid space. This approach is easy to implement and capable of using various boundary conditions. However, in order to solve wave propagation problems, EFIT requires large computational power.

2.1.4 Hybrid Methods

Numerical methods are widely used in ultrasonic NDE to model complex systems where there is no exact analytical solution. However difficulties can arise when large models are required due to a large model geometry or a high wave propagation distance. A full 3D model can become very computationally intensive in both memory requirements and simulation time due to containing millions or even billions of elements. Moreover, when the wave propagation distance becomes in the order of hundreds of wavelengths, the effects of numerical dispersion become evident. Numerical dispersion is the deterioration of a propagating signals shape due to small errors of propagation velocities of different modal components of the signal. These small errors are common to all numerical models and accumulate as the wave propagates and lead to a mismatch between derived and exact solutions [59]. To overcome this problem, hybrid models have been developed to reduce the computation requirements with the combination of analytical and numerical methods. This incorporates the advantages of both methods for an optimised modelling suite [60–63].

Typically in ultrasonic modelling, a hybrid model utilises a numerical method to simulate the transduction and reception of the ultrasonic source as well as the interaction of the ultrasound waves with a target or defect. Analytical methods are then used to compute the wave propagation between the ultrasonic source and/or receiver and the target. A schematic diagram of the numerical and analytical sections of a hybrid model is shown in Figure 2.3. The numerical and analytical models are combined by extracting and inputting the calculated data along the boundary of the numerical models. This approach combines the accuracy of numerical models and their ability to model complex scenarios with the computational efficiency of analytical methods to calculating the wave propagation. An example of an effective use of this approach is to model the scattering of ultrasound when incident on a defect [64].

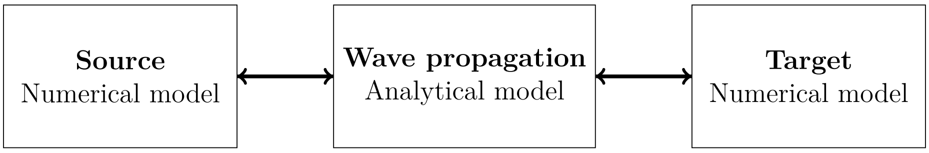

Figure 2.3: *Schematic diagram of a hybrid model configuration*

The advantage of a hybrid model is the model size remains constant for any source and scatterer, however a full numerical model size depends on the wave propagation path length [65]. A hybrid approach offers an efficient solution to a problem where there is a large propagation distance with no points of interest and the wave has no interactions. In cases where the distance between source and target is smaller, the hybrid model does not offer significant time savings compared to the fully numerical model due to the reduction in model size [62].

2.1.5 Selection of Modelling Method for this Research

This Thesis is focused on modelling ultrasonic inspections of composite materials. These composite materials are highly anisotropic and when combined with their often complex geometries, pose a difficult challenge to model wave propagation scenarios. A composite material contains multiple internal interfaces between individual ply layers, which will subject a wave propagating to reflect and/or refract at each interface. Analytical methods have been proven as a valuable tool to model wave propagation through composite structures, however, for this research a numerical approach is preferred. Selection of a numerical approach will allow for models of complex composite structures and account for the variation of elastic properties spatially and axially and all of the behaviour of incident ultrasonic waves.

Each numerical method has its own advantages and limitations and the selection of the most suitable approach is dependant upon the modelling requirements. A comparison of numerical methods for ultrasonic wave propagation problems is shown in Table 2.1, which is based on current literature and the authors perspective and experience [66, 67].

The computational demand of each method varies depending on the model requirements and set up. The BEM is often the most efficient approach, especially in cases there there is a low surface to volume ratio. However, composite materials contain multiple thin layers which will be very computationally demanding for a BEM approach, as the thin ply layers required to model contain a very high surface to volume ratio. For time dependent models, FD methods can employ a larger time step compared to FEA which results in a quicker time to obtain a solution. FEA has historically been seen as being the most computationally intense numerical method with high memory requirements and long solution times.

Table 2.1: *Comparison of numerical modelling methods for ultrasonic wave propagation problems*

Parameter	**BEM**	**FD**	**FEA**	**EFIT**
General computation efficiency	Very Good	Good	OK	Good
Complex geometry modelling	Poor	Good	Very Good	Good
Anisotropic materials	Yes	Yes	Yes	Yes
Commercially available software	No	No	Yes	No

Each method can simulate complex geometries and anisotropic material properties. However, for complex geometries, BEM is not very effective as it becomes difficult to implement and computationally expensive. FEA is a very flexible method and can implement complex geometries more easily than FD and EFIT. There are also several commercially available FEA software codes which can often be beneficial in offering a more practical and user friendly modelling suite.

FEA may be more computationally demanding than other methods, but it is also the most flexible and accurate method. It is well suited to model complex geometries and can easily handle the ultrasonic wave mode conversion at material interfaces, which can be difficult to implement in the other numerical methods. The availability of commercial software packages removes the requirement of developing software and offers the advantage of historical validation and technical support. With the increase in modern computing power and efficient FEA software, the drawback of demanding computational power is becoming less significant.

As a sponsor for this research, the commercially available FEA software package, OnScale, will be utilised throughout. An advantage of OnScale is its efficiency in modelling ultrasonic wave propagation while also offering the ability to handle complex material properties and import complex geometries. Details of the OnScale software and how it compares with other FEA packages will be given in the next Section.

2.2 OnScale FEA Software

2.2.1 Overview

Developing FEA code is complex and requires extensive time in order to produce memory efficient solvers which are robust. For this reason, commercial FEA software packages are often chosen in industry. These commercial packages are also well developed and supported. OnScale is a commercially available software package which was initially developed in the 1980s as PZFlex, where it was utilised to improve ultrasonic probe modelling. The software has developed over the years and it can now be used to solve very large wave propagation models in a very short run time. An explicit solver is designed and optimised specifically for wave propagation and when combined with a fully coupled Electro-Mechanical solver it is very well suited for modelling ultrasonic Non-Destructive Evaluation inspections.

This Section provides an insight into OnScale and how it utilises FEA to run simulations. With the ability to simulate large wave propagation problems with great efficiency, OnScale has been utilised in various different fields. As well as NDE [68], the software has been used in sonar [69], thermal [70], biomedical [71] and nonlinear [72] applications. OnScale can model piezoelectric, electrostrictive and magnetostrictive materials, as well as thermo-mechanical modelling.

2.2.2 Implementation of an OnScale Model

The process of performing FEA simulations can be simplified as breaking down a structure into elements to form a mesh, then applying boundary conditions and loads before solving for the stresses and strains on each element. This generalised process is the same for all FEA simulations. However, there are many different options available to change how the analysis is conducted. This includes the option of implementing different types of elements, meshes, boundary conditions and solvers. These different options will determine how the simulations perform and control how accurate and fast they can be solved. Therefore, it is important that the user of FEA software is aware of the options available and makes suitable considerations to ensure accurate results are achieved with efficient computation.

2.2.2.1 Element Options

In any FEA modelling, the model structure is divided into small sections called elements. These elements each encompass a single material and has its geometry defined by nodes at its corners and in some cases edges. Adjoining elements share nodes and the nodes form key reference points in the model. Various element types exist for 1D, 2D and 3D cases and are defined by its dimension, shape and formation of nodes. Elements are categorised into line, area and volume with reference to their shape.

OnScale mainly uses 2D, quadrilateral area, and 3D, hexahedral volume elements. These elements, illustrated in Figure 2.4, are quadrilateral or hexahedral and have four and eight nodes, respectively. The elements are linear elements and so utilise a linear shape function to determine variable values at points inside the element [73]. It is possible to use higher order elements which contain additional nodes on the mid-points of each of the element sides. Higher order elements provide a more accurate result for a given number of variables in a mesh as they utilise a quadratic shape function [73]. While higher order elements can reduce the number of elements required, this can exhibit a poorer model resolution as there are fewer nodes to define interfaces [74].

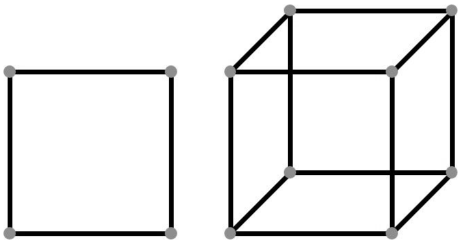

Figure 2.4: *OnScale (left) 2D quadrilateral and (right) 3D hexahedral elements with node indications at element corners*

As well as quadrilateral and hexahedral elements, other line and area elements can be used in OnScale. Line elements contain 2 or 3 nodes connected by a single line, while other area element options in OnScale include membrane and shell. Membrane and shell elements can be used in both 2D and 3D to model thin layer structures which are significantly smaller than the model element dimensions. The geometrical rectangular shape is identical for both, however they differ internally. Membrane elements model the in-plane stresses and strains only while shell elements can model membrane behaviour, bending stresses and strains, as well as through-thickness shear stresses and strains.

2.2.2.2 Meshing Approaches

Typically when creating the mesh, often referred to as the grid, OnScale operates with a structured rectilinear approach, also referred to as a Cartesian or ‘Standard Partition’. Element sides meet at right angles to each other and nodes are shared with neighbouring elements at uniform spacings. These structured rectilinear meshes, Figure 2.5, are extremely efficient for simulation due to low memory requirements and are ideal for wave-propagation models [75].

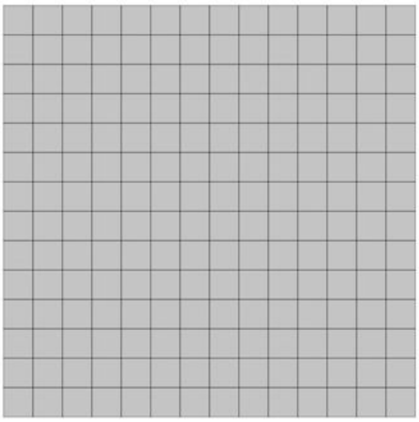

Figure 2.5: *OnScale 2D quadrilateral elements in a structured rectilinear mesh*

The density of the FEA model mesh has a major impact on its accuracy and stability. As the density increases, the solution will tend towards the exact solution but the computational costs will also increase. As the derived solution converges to the exact solution, the benefits of increasing the mesh density becomes limited and no accuracy gain is achieved but computation requirements are still increased. Convergence studies are often implemented to allow for a suitable mesh resolution to be determined that offers a derived solution within an acceptable error of the exact solution, while remaining computationally efficient.

The mesh density is determined by the dimensional size of the element implemented in the model. The element dimension is generally set to adequately mesh the smallest wavelength in the model to ensure result accuracy and stability. Typically, a minimum of 15 elements per wavelength is recommended, but additional elements may be used if increased precision is required, albeit at the expense of increased computation time and memory requirements. The calculation for the element dimension is shown in Equation 2.7, where v_{min} is the slowest velocity of sound in the model materials, f_{max} is the highest frequency of interest and $nelem$ is the number of elements per wavelength.

$$ElementDimension = \frac{v_{min}/f_{max}}{nelem} \tag{2.7}$$

In some cases, the element dimensions is not determined by the smallest wavelength but the model geometry. For example in cases where the geometrical detail is smaller than the smallest wavelength of interest, the element size may be reduced to better represent the geometry.

In OnScale it is possible to implement a curvilinear or 'skewed' mesh to accurately model a curved surface. Curvilinear meshes also utilise quadrilateral or hexahedral elements in the form of a structured mesh, but the element nodes are positioned in arbitrary locations, see Figure 2.6. This type of mesh can allow for greater accuracy through better representation of the model geometry. However, the arbitrary positioning of the element nodes requires an increase in memory requirements which leads to longer computation times [75]. The distorted element shapes can also reduce the minimum distance between a pair of nodes which can also impact the model performance due to the requirement for a smaller time step. In some modelling scenarios, a skewed grid can be more computationally efficient than a fine stair-stepped standard partition mesh [75] due to a reduction in the number of elements required.

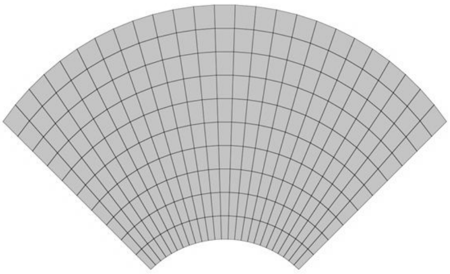

Figure 2.6: *OnScale 2D quadrilateral elements in a structured curvilinear mesh*

Lastly, it is also possible to use an unstructured general connectivity mesh in OnScale, Figure 2.7. However this meshing approach is very rarely used in OnScale as it is inefficient at solving large wave propagation problems and is very computationally demanding. As with a curvilinear grid, the memory requirements are increased as node locations need to be stored, as well as storing details of which nodes are connected.

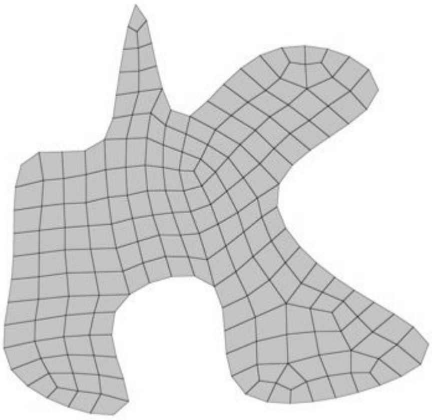

Figure 2.7: *OnScale 2D quadrilateral elements in an unstructured general connectivity mesh*

2.2.2.3 Boundary and Loading Conditions

In FEA, another important consideration is the proper application of boundary and loading conditions. The boundary conditions are set to determine how the modelled structure interacts with the surrounding environment, while loading conditions apply external forces to the modelled structure. The boundary and loading conditions in OnScale are applied to either a 2D or 3D plane of nodes, which typically define the boundary of the model or a material surface.

There are several different boundary conditions which can be applied in OnScale. The basic conditions which are most commonly used are free, fixed, symmetry and absorbing. A free boundary condition provides the nodes freedom to move and assumes a void boundary while a fixed boundary fixes the node positions and allows no motion. Symmetry boundary conditions applies symmetry along the nodes and absorbing boundary conditions absorbs incident waves.

An alternative to an absorbing boundary is the use of an impedance boundary which applies the mass and stiffness values of an infinite load of a given material on the stated boundary. This can offer benefits in certain cases by removing the requirement to model additional regions on the edge of models. There is also the option to apply a velocity boundary which can be used to load the model by applying a defined velocity profile to nodes on the model boundary.

It is preferable to simplify FEA models whenever possible to gain greater simulation efficiency. For models containing geometric and loading symmetry, it is possible to model half (or less) of the structure and apply symmetrical boundary conditions. This achieves the same results as a full model but due to the reduced model size, offers computation time and memory requirement savings. It is also possible to apply an axisymmetric boundary condition which allows for full 3D results to be generated from a 2D model. This is very efficient as it permits 3D performance to be evaluated with the use of a computationally efficient 2D model.

To apply loads in OnScale, users can either use the velocity boundary condition previously mentioned to directly load a boundary or loading can be applied to specific element nodes. Several loading types can be used but the common and most relevant to this research is a voltage load on piezoelectric materials or a pressure load. Piezoelectric loading can be performed with the implementation of applying an electrical driving function to electrode boundary conditions placed on a piezoelectric material. Alternatively, a pressure load can be applied to a single node or a specific selection of nodes, which offers the ability to apply the pressure load to a line, a surface or a volume. When a pressure load is implemented, the force applied to the node(s) is calculated in order to produce the specified input sound pressure. The voltage and pressure loads applied can be defined as a specific driving function using the provided functions in OnScale or as an arbitrary user defined function.

2.2.2.4 Solver Type

In FEA modelling there are two fundamental methods used to solve the differential equations - implicit and explicit. Implicit methods calculate the solution using the current system state and the system state at a later time, while explicit methods calculate the solution using only the state of the system at the current time. The main difference between the solvers is an implicit method considers the effect of each node on all others while in an explicit solver the nodes are effectively ‘de-coupled’ from each other. An implicit solver requires the generation and solution of a matrix for the entire structure which greatly increases the computation time.

OnScale uses an explicit solver for the majority of models but also has the capability to implement an implicit solver for sections of models. This capability to implement a hybrid solver is extremely useful as each type of solver has particular advantages. Explicit methods can solve larger mechanical wave propagation problems much faster and with less memory than implicit methods but is unsuitable for piezoelectric materials. This is due to the electrical wave propagation having a much faster speed and so will rapidly travel between nodes. Having the capability to implement both types of solvers is a great advantage and allows for piezoelectric materials to be solved in an small implicit solver model region, known as an electric window, while using the faster explicit solver for the rest of the simulation model.

2.2.3 Comparison with Other FEA Packages

In the NDE industry, OnScale is not the only FEA software package available for ultrasonic modelling wave propagation. A variety of other commercial codes are also available including Abaqus FEA (Dassault Systemes Simulia Corp., Providence, RI), COMSOL Multiphysics (Comsol Inc., Burlington, MA) and ANSYS (ANSYS Inc. Canonsburg, PA). There is also open source FEA packages available such as Pogo (Imperial College, London, UK).

In ultrasonic NDE modelling, Abaqus FEA, formerly ABAQUS, is a well recognised and widely used FEA modelling package. Abaqus FEA is well developed and supported and is used in many industries due to its level of performance [76]. COMSOL and ANSYS are less commonly used for ultrasonic NDE modelling but do offer the ability to simulate a wide range of engineering applications. Pogo has been recently developed at Imperial College, London, as an efficient solver for linear elastodynamic problems, making it attractive for ultrasonic NDE modelling [77].

The main differences between FEA software packages are in the element types used, meshing type and solver used. For most problems, OnScale uses low order quadrilateral or hexahedral elements in an orthogonal cartesian grid to achieve the highest computational performance [75].

Abaqus FEA software contains two different codes: Abaqus/Standard which is an implicit solver and Abaqus/Explicit which uses an explicit solver. The explicit solver code is more commonly used for ultrasonic NDE modelling due to its superior performance at solving wave propagation problems. Abaqus FEA also has an extensive library of elements and a variety of meshing techniques that can be used depending on the user's requirements. Like OnScale, quadrilateral or hexahedral elements are commonly used, however, while Abaqus FEA can produce a structured mesh, typically the mesh is not Cartesian.

COMSOL Multiphysics predominantly uses an implicit solver with triangular or tetrahedral elements. This makes the software less efficient for ultrasonic wave propagation problems. COMSOL and ANSYS are similar to Abaqus FEA in that it has a range of elements available and can mesh the model geometry in a number of ways. However, unlike OnScale, ANSYS typically does not use a structured Cartesian mesh.

Pogo is an explicit time domain solver like OnScale, making it efficient for solving wave propagation problems. Unlike OnScale, Pogo uses an unstructured mesh and primarily uses first order triangular elements. Another major difference is Pogo makes efficient use of Graphical Processing Units (GPUs), instead of the conventional Central Processing Units (CPUs). Using a GPU approach produces a run time 100-200 times faster than a CPU equivalent Abaqus model [77].

It can be seen that the main difference between OnScale and other FEA simulation codes is the meshing approach. While most other codes generate non-uniform meshes to accurately represent the model geometry, OnScale typically uses a Cartesian mesh. Using a uniform mesh with low order quadrilateral or hexahedral elements offers the most efficient performance [75]. The disadvantage of this approach is the representation of curved faces where stair stepping of the mesh occurs. Generally, this is not a major problem as the element size is much smaller than the wavelengths in the simulation and can accurately recreate experimental performance provided the mesh is fine enough to capture the required spatial changes in the model [75]. Since the element and mesh approach are very efficient, there is also the option to increase mesh density to more accurately model the geometry, while still not requiring intensive computation time or memory requirements.

OnScale is a cloud based software which offers a significant advantage over competitors with the ability to run hundreds of simulations in parallel. This can offer a huge reduction in computation time, when multiple simulations are required to be computed. Access to cloud High Performance Computing (HPC) clusters also allows for larger models to be simulated without the requirement to purchase large, and often expensive, computing hardware.

2.3 Ultrasonic NDE of Composite Materials

Over the last decade there has been a vast increase in the use of composite materials in many engineering aspects. The aerospace industry in particular, has seen major advances with composites fast becoming the preferred material for many aircraft components. This is epitomised by modern aircraft (2009), such as the Boeing 787 containing 50% composite material by weight [78]. The 787 utilises CFRP laminates in the wing, empennage and the fuselage as they are seen as the best choice due to their lightweight, durability, resistance to corrosion and fatigue, as well as allowing the opportunity for new designs [79]. Airbus have also moved towards increasing the use of composite materials with the launch of the A350XWB (2010) which contains over 50% composite material by weight and includes the use of carbon composite material for the wing and fuselage [80, 81].

NDE inspections are crucial to asses component structural integrity and to detect any material discontinuity or defects. Components are often inspected during and post manufacture to ensure they are acceptable for service. Once in service, routine inspections are then conducted to ensure the component remains fit for service. Therefore, it is essential that the NDE requirements can be met when conducted on high value components and structures. Composites pose a difficult challenge to inspect due to their anisotropy and often complex shape. As composites are utilised more widely, the need for advanced NDE inspections, which are reliable and robust, grows. The use of modelling also becomes a necessary tool to aid in the development and validation of these new inspection protocols.

2.3.1 Overview of Composite Materials

A composite material is the combination of two or more materials with different properties to create a new material with desired properties. The most common monolithic composites found in aerospace are fibre reinforced polymer (FRP) which consist of layers of fibres encapsulated in an epoxy resin matrix. There are several different fibres and polymers available but the most commonly used is CFRP, which consists of carbon filament within an epoxy resin matrix.

CFRP laminates can be constructed by layering sheets of carbon fibres on top of each other. The layers of carbon fibres can all be in the same direction to give a unidirectional laminate, Figure 2.8 (a) [82]. Unidirectional laminate are extremely strong and stiff in the fibre orientation direction. However, they are very weak in the perpendicular direction. The layers of carbon fibres can also be stacked at various angles, normally 0, 45, 90 or -45°, to produce a cross-ply, Figure 2.8 (b) or quasi-isotropic composite laminate, Figure 2.8 (c). By varying the fibre orientation, the strength of the resulting structure as a function of load direction, can be modified and so it is possible to design composite lay-ups to provide optimum strength and stiffness [82]. Laminates which have an equal number of plies in each of the four fibre orientation directions are called quasi-isotropic because they carry equal loads in all of the four directions.

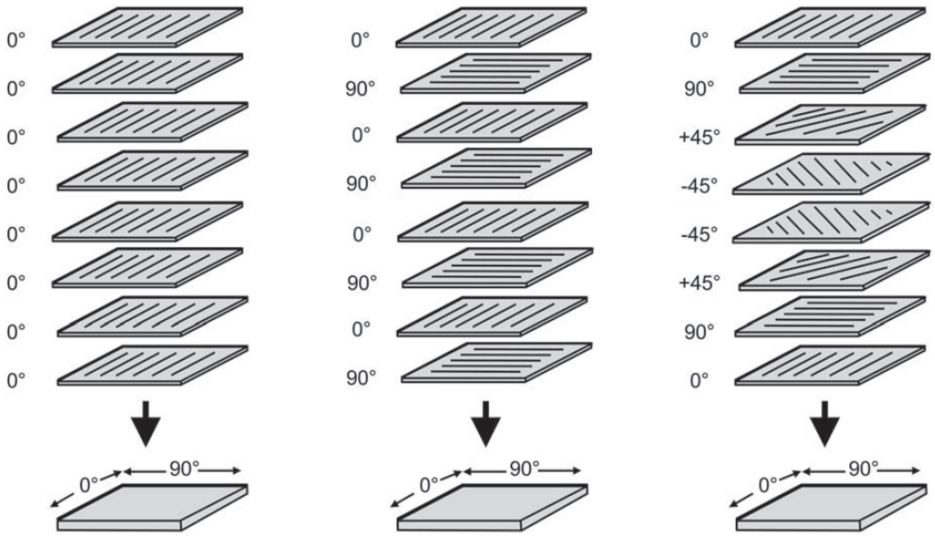

(a) (b) (c)

Figure 2.8: *Examples of CFRP Structures: (a) unidirectional, (b) cross-ply and (c) quasi-isotropic laminate lay-up. Modified from [82]*

When CFRP laminates are manufactured, they are often described by an orientation code that represents the orientation of the internal ply layers. Examples of common composite layup nomenclature are detailed in Table 2.2.

Table 2.2: *CFRP layup nomenclature examples*

Nomenclature	Full Layup	Details
[0/90]	0, 90	One layer of 0° and one layer of 90°
$[0/(90)_2]$	0, 90, 90	$(90)_2$ indicates two layers of 90°
[0/±45/90]	0, 45, -45, 90	±45 indicates one layer of 45° and one of -45°
$[0/90]_s$	0, 90, 90, 0	$_s$ indicates symmetric
$[0/\bar{90}]_s$	0, 90, 0	$\bar{90}$ indicates last ply is the midplane
$[0/90]_3$	0, 90, 0, 90, 0, 90	$_3$ indicates repeated 3 times
$[0/45/90/-45]_{2s}$	0, 45, 90, -45, -45, 90, 45, 0	repeated twice and symmetric

It is also possible to have layers of composite which involves the combination of two or more fibre orientations woven together. These woven fabrics are produced by interlacing warp (0°) and weft (90°) fibres in a regular weave or pattern. There are various weave patterns available including Plain, Twill and Satin as show in Figure 2.9 [83].

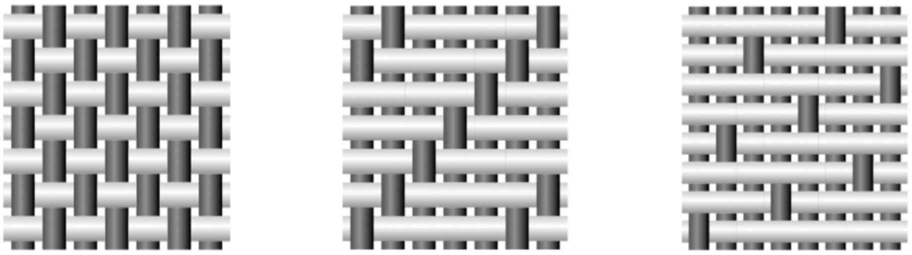

(a) **(b)** **(c)**

Figure 2.9: *Illustrations of different composite weave patterns, (a) Plain (b) Twill (c) Satin, where the light grey are warp fibres and the dark grey are weft fibres [83]*

Composites offer the ability to tailor the structure geometry and save weight, making them very suitable for the aerospace industry. Tapered composites are often utilised to provide a composite structure with a varying thickness. These structures are formed by terminating individual plies at discrete locations as illustrated in Figure 2.10 [84]. This allows for composites to be designed to have different thickness's in different regions of the structure depending on the required component strength in the area. While tapered composites have their benefits, they can also increase the possibility of failure in the component. Therefore there has been a lot of research to provide guidelines [84], considerations [85] and optimisation [86] for tapered composite design.

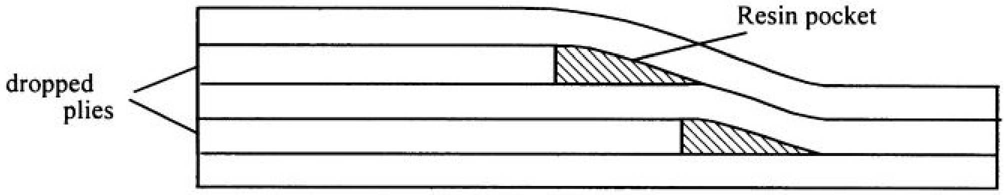

Figure 2.10: *Illustration of a ply drop in a composite*

2.3.2 Defects in Composite Materials

Composite materials can suffer various defects during the production stage or during their in service lifetime. The most significant defects in monolithic structures are porosity during manufacture and impact damage while in service [87]. These defects are generally internal and when composites suffer impact damage, unlike metallic materials, the composite can have little or no signs of damage on the surface, but an extended defect could be present in the internal structure.

The manufacturing process for composite materials can lead to the inclusion of many different types of defects. The most common of these is porosity but other potential defects include fibre waviness, misalignment of fibres or plies, inclusions and resin rich or resin starved areas [87, 88]. The introduction of these defects, can have a significant impact on the material properties and strength of the manufactured composite. The presence of voids have little effect on the longitudinal material properties which are fibre dominated, however they impact transverse tensile properties and interlaminar shear stress [89]. This affects the compression strength of the composite which is often the limiting factor.

During a composite component's service lifetime, the most common source of defect generation is impact damage. Impact on a composite structure can lead to matrix cracking and delamination of the internal ply layers [87, 88]. These defects can greatly reduce the material strength of the composite component. Delaminations are a critical failure mode in composites and can directly lead to through-thickness failure as well as in-plane failing [90].

2.3.3 NDE Techniques for Composite Material Inspection

The inspection of composites can be challenging due to their complex structure and anisotropic material properties. The vast majority of composite NDE inspections are performed using ultrasonics or low frequency techniques [87], however other techniques, such as visual inspection, radiography, thermography and shearography, are also used [91]. Each approach has its associated advantages and disadvantages, however ultrasonic techniques are the most commonly used NDE method for composite structures [87]. Along with defect detection and characterisation [92], ultrasonic NDE can be used for 3D characterisation of composite structure [3], determining ply layer orientations [93] and ply layer tracking [94].

Various different ultrasonic techniques exist including pulse echo, which only requires access to a single side of test component, and through transmission. These techniques all work well at detecting defects which are in the plane of the material but are less sensitive to out of plane defects. Ultrasonic techniques can detect defects that are equivalent in size to the wavelength, however for defects in composite structures the sensitivity is dependent upon the transmission and reflection of the ultrasound at each of the ply layer interfaces [95]. As the ultrasonic wavelength decreases, the sensitivity to defects increases but at a cost of higher scattering effects due to the composite structure.

Low frequency vibration methods, such as tap testing or mechanical impedance, are a very cost effective and fast inspection method that can detect planar defects across a large testing region. While this approach can readily detect defects such as delaminations and disbonds, it is difficult to identify the type of defect and detect subtle defects like porosity.

Radiography has been widely used for the inspection of composite materials. However in recent times, conventional radiography has become less utilised due to its health and safety dangers. Like ultrasound, radiographic techniques, using X-Rays or gamma radiation, are well suited at detecting the common defects in composite materials, particularly in plane defects such as delaminations. Conventional radiography not very sensitive to identifying porosity or changes in resin thickness and also requires access to both sides of the component.

X-Ray Computed Tomography (CT) is a very effective and growing NDE method for the inspection of composite materials as it is capable of providing full volumetric information of the component structure. This technique involves rotating the test component and taking multiple images during the rotation before using software reconstruction to allow 3D visualisation of the component. X-Ray CT can capture extremely high levels of detail and allow visualisation of individual fibres and porosity defects, but the size of the component that can be inspected is limited due to practical constraints.

Other NDE techniques for composite materials include thermography and shearography. These techniques are most efficient at detecting planar, in plane defects in flat samples but both can lose sensitivity for defects deeper in the test component.

2.3.4 Modelling Ultrasonic NDE of Composites

Modelling is a critical tool for designing and evaluating NDE inspections and helps to optimise the inspection in a small time frame. The advancement of modelling NDE inspections of composites would offer a great ability to help cope with the current demand. This view is shared by industry with Boeing including modelling of ultrasonic behaviour in composite structures as a NDE need and also state that as composite usage increases, there needs to also be an increase in modelling for technique development and verification [79].

In recent years there has been an increase in research into methods to model ultrasonic wave propagation in composite materials. Recent methods have tended to be heavily FEA based as this method has been proven to be capable of modelling the complex materials as well as the ultrasonic wave behaviour.

Historically, like many other NDE inspections, modelling of ultrasonic NDE of composites was done using analytical approaches. Many different matrix techniques exist for the modelling of ultrasonic waves through layered media [46]. These plane-wave techniques are very efficient but are often limited to normal incidence signals.

MLM-Propmat [96] is a multi-layer ultrasonic bulk wave propagation model based on transfer matrix formulations which has been applied to composites. This model was built on earlier work by Freemantle [97] and is capable of simulating the reflection and transmission responses of composite materials. Mienczakowski et al [98], demonstrated a model which can derive results that are close in form to experiments for the inspection of a CFRP panel with porous inclusions. In this work, it was also found that the initial modelling results had a more regular interply resonances than was observed in experiments, due to small but finite variations in the real component ply layers. To overcome this, the thickness of plies in the model was randomised about the mean thickness values of resin and fibre/resin mixture to derive results closer to experimental data.

Smith [99] produced a 1D analytical multi-layer model to aid the understanding of the ultrasonic response from composite materials. The model assumes normal incidence ultrasonic wave propagation through multi-layered composite materials which was validated against MLM-Propmat. Use of the model allows for the effects of ply and resin thicknesses and fibre volume fractions to be evaluated. Development of the model incorporated the ability to include porosity defects and frequency dependent attenuation.

Wang and Rokhlin [100–102] developed a technique for modelling wave propagation in layered anisotropic media which removed the numerical instability in the standard transfer matrix method. This approach introduced the layer stiffness matrix and used an efficient recursive algorithm to calculate the global stiffness matrix for the whole structure. Humeida et al [103], implemented a kernal plane wave model based on this technique and combined with an angular spectrum method to simulate ultrasonic FMC data of composite materials. The plane wave model was used to obtain the response for incident plane waves and was then combined with an angular spectrum method to simulate finite beams from transducer elements.

Gengembre et al [104], developed a ray theory based homogenization method to model the ultrasonic propagation in CFRP. This technique has been implemented in the CIVA software platform [105] and can be applied to non planar components, but due to the homogenization of the structure, does not model reflections from individual plies and the result accuracy is heavily dependant upon the validitiy of the homogenization process. More recently, to provide more accurate results, the ray theory based method has been combined with a Finite Difference Time Domain (FDTD) code to produce a hybrid model [106]. The ray model is used to compute the incident field in water and then the propagation in the composite material is conducted by the FDTD code. The use of FDTD allows for the individual plies of the composite structure to be taken into account and therefore simulate the structural noise.

Leckey et al [107, 108], have developed a custom 3D EFIT technique to simulate guided wave propagation in composites. The 3D EFIT code was implemented in parallel through the use of a Message Passing Interface (MPI) to allow for large simulations to improve computational efficiency. Despite parallelisation on 32 processors, simulations performed in [107] still required 44 hours to compute. This approach was used to produce a model incorporating realistic delamination data acquired from X-ray microfocus computed tomography.

Singh et al [109], used COMSOL to produce a 3D FEA model to simulate the scattering behaviour of guided waves with point impact damage in a composite plate. This model implemented homogenized material properties of CFRP throughout the plate thickness meaning that individual plies were not modelled.

Ng et al [110], produced a 3D FEA model to simulate the scattering of guided waves at a delamination in a composite laminate. The model was generated and meshed in ANSYS, but was solved using LS-DYNA (Livermore Software Technology Corporation), which is a general purpose FEA software that is predominantly used in the automotive industry for vehicle designs. An eight ply quasi-isotropic composite laminate containing unidirectional ply layers with different orientations was used. The individual plies are modelled using eight-noded 3D reduced integration solid brick elements. A single circular delamination was implemented in the centre between two layers using a volume split between nodes in the region of the delamination to produce a small distance between the delamination surfaces. Good agreement between the FEA derived and experimental measurements was shown to demonstrate the model's accuracy to predict the wave propagation in the laminate and the scattering at the delamination.

Pain [111] implemented a FEA model in Abaqus that simulated ultrasonic FMC data generation from a composite sample containing waviness. In this research, only 2D FEA models were conducted as the computational cost of a 3D model was prohibitive. The ply waviness was generated in the models by modifying the FEA mesh by adjusting the coordinates of the element nodes, however the model did not include any resin layers between adjacent ply layers. This assumes the resin layer thickness to be zero and while reflections from ply layer interfaces were observed, these were primarily due to changes in the different ply layer orientations changing the material properties. This research also included the modelling of a composite containing a woven finish layer on the outer face. This woven layer was approximated by modelling as a single layer with alternating sections of 0° and 90° fibre material along it's length. Each section length was equal to the tow length of the weave providing a very approximated representation of the woven structure.

A recent study by Leckey et al [112] provided a benchmark comparison of numerical codes for wave propagation of guided waves in a composite laminate. This experimentally validated study, considered both a defect-free sample and a sample containing a Teflon insert to represent a delamination and provided details on the accuracy and computation requirements for different simulation tools. The simulation tools considered were: EFIT, COMSOL, ABAQUS and ANSYS. For ABAQUS, simulations were done for both it's implicit and explicit solver. This research showed that with proper configuration, each simulation tool was capable of simulating the guided wave propagation in CFRP laminates with derived results providing correlation between with both theory and experiment. However, the computational demand of the simulation tools was very high. For example using 16 cores, COMSOL took 19.5 hours and 266GB of memory to compute, while ABAQUS explicit was even higher at 53 hours and 30GB of memory.

Veres et al [113] investigated modelling approaches for porosity within layered media. This study included the use of PZFlex to simulate the scattering of ultrasonic waves due to the presence of pores. The 3D model of a glass laminate aluminium reinforced epoxy composite included randomly distributed, spherical voids to represent porosity within a composite layer sandwiched between aluminium layers. The simulations conducted allowed for the attenuation to be evaluated for the scattering of the ultrasonic waves due to the presence of porosity.

Tayong et al [114] has studied the 3D characterisation of woven composites through 1D analytical and 3D FEA modelling. The 3D FEA modelling of the woven composites was conducted in PZFlex and utilised model generation approaches developed in this Thesis. Good agreement between experimental and model derived results was obtained and allowed for modelling to indicate the potential for detecting manufacturing errors or defects in woven composites.

The use of modelling techniques for composite NDE modelling is ever increasing, with FEA in particular becoming more prevalent. However, there is still a gap in the capability of FEA for modelling ultrasonic wave propagation in composite materials. Most previous research has omitted the resin layers between composite ply layers from the models. In certain cases, such as modelling guided waves along a composite, this is an acceptable approximation as the resin layers have only subtle effects on the wave propagation. Yet, for waves propagating through the thickness of a composite material, the resin layers have a more profound impact on the wave propagation and produce reflection of the wave at material interfaces. These resin layers are also not consistent in thickness across a sample due to the presence of fibre tows and manufacturing variability, which will again have different effects on the wave propagation. To accurately model these subtle variances in resin thickness, which is also present with ply layer waviness, it is essential that the FEA model geometry is accurately constructed.

2.4 Summary of Review

Modelling plays a very important role in ultrasonic NDE and when implemented correctly, offers a wide range of benefits. Composite materials pose a challenge to ultrasonic NDE due to their anisotropic material properties and complex geometries. There is a lack of efficient modelling for ultrasonic wave propagation in composites and this Thesis aims to offer a solution. Through the use of accurate model generation and efficient FEA implementation, an efficient approach to simulate ultrasonic NDE inspections of composite materials is proposed. The modelling approaches used in this Thesis are validated against experiments to ensure FEA derived results are accurate. The resulting models can then allow for the evaluation and optimisation of composite ultrasonic NDE inspections.

Chapter 3

Validation and Optimisation of the Modelling Method

An essential consideration for FEA models is the validity of the solution. Simulations can become extremely complex and in order to have confidence in the results, validation of the modelling approach must be conducted. Typically validation is achieved by comparing FEA derived system responses with an equivalent physical experiment. Good corroboration establishes confidence in the FEA derived data accuracy and reliability.

This Chapter presents validation of the FEA modelling method used in this research. A direct back to back corroboration between simulated and experimentally generated data for an ultrasonic phased array inspection of a homogeneous test block is conducted. In addition to providing suitable validation of the modelling methodology, methods to increase the computational efficiency of the simulation models are introduced. This is valuable for future models where the computation costs becomes more demanding as the size and complexity of models increases. This work was presented at the 42nd Annual Review of Progress in Quantitative Non Destructive Evaluation (QNDE), 2015 [115].

3.1 Introduction

3.1.1 Motivation

The manufacturing of test samples for designing and evaluating NDE inspections produces slow development phases and often high costs. An attractive alternative is the use of modelling, which can provide faster and more cost effective results compared to the ‘build and test’ approach by minimising the need for expensive test-piece fabrication. Modelling methods, such as FEA, also allow the flexibility of simulating multiple different test scenarios and can handle complex geometries and material structures or properties. However, it is critical that there is substantial confidence in the results obtained from the simulations performed.

When using a FEA software package, such as OnScale, it is important that the user has a good understanding of the problem and the capabilities of the model. FEA is a numerical technique and the level of accuracy in results is dependent on correct geometry, material property inputs, correct model set up and appropriate boundary conditions. There are many questions which need to be considered when trying to obtain confidence in simulation results. These include, but are not limited to:

- Has the right question been asked of the software?
- Has adequate and accurate information been provided?
- Is the software answering the question correctly?

These questions can all be answered by conducting validation of simulation models. By comparing simulation results with practical results to establish the accuracy of the simulation results can provide validation and confidence of the modelling approach. The validated modelling approach can then be extended to look at more complex simulation scenarios with enhanced confidence in the simulation results. Once the model has been validated, it can then be optimised to minimise the solution time and computational overhead.

3.1.2 Method of Investigation

In this research, initial validation was conducted for simulations of ultrasonic phased array inspections of a homogeneous test block. Simulations were conducted to replicate practical inspections as closely as possible, while also investigating techniques to ensure simulation efficiency. Corroboration of results and highlighting simulation result accuracy would give confidence in the modelling approach before extending to consider the more challenging simulation of composite materials.

The inspection scenario considered was an ultrasonic phased array Full Matrix Capture (FMC) [116] inspection of a stainless steel calibration block containing numerous side drilled holes. This technique generates the maximum amount of data from a standard phased array probe by storing a matrix containing an A-Scan signal for each transmit and receive element pair. A FMC scan is conducted by exciting on the first element of the array transducer while recording the received signal on all array elements. This is then repeated to excite each array element in turn. For an array transducer with N elements, the FMC data set will contain N^2 A-Scans.

Models were constructed and simulated in both 2D and 3D to produce FEA derived FMC data sets. The 2D models would approximate the experiment to only two dimensions which would provide solutions to the problem with a reduced computational overhead. While the 3D models would give a more accurate representation of the experiment but would be more computationally demanding. This would allow for an evaluation of the relative merits of 2D and full 3D models to be made in the current context.

The experimental and simulated FMC data sets would all be used to generate images using the Total Focusing Method (TFM) [116]. TFM is an imaging algorithm which has been established to generate enhanced images from FMC data sets. The generated image results were visually compared to determine simulation performance at predicting experimental performance. To enhance confidence in simulation results, additional quantitative comparison was conducted to look at the positional accuracy of the side drilled holes in the images.

The performance and model parameters of the simulations are also reviewed. The initial 2D simulation was optimised to produce a model with a minimal computation requirements before the model was expanded to the larger 3D model. Further optimisation was achieved by parallelisation of the model and tests are done to evaluate the performance in terms of simulation time.

3.2 FMC Data Generation

3.2.1 Experimental Data Acquisition

The test block used for the experimental scans was a Harfang Microtechniques Inc. (Quebec City, Canada), Type B stainless steel calibration block designed for phased array transducers [117]. Included in this test block are numerous side drilled holes and four angled holes at varying angles, as shown in Figure 3.1. The block is 150 mm wide, 100 mm high and 25 mm deep. This calibration block is common throughout industry and provides good baseline evaluation of phased array transducers capability and performance.

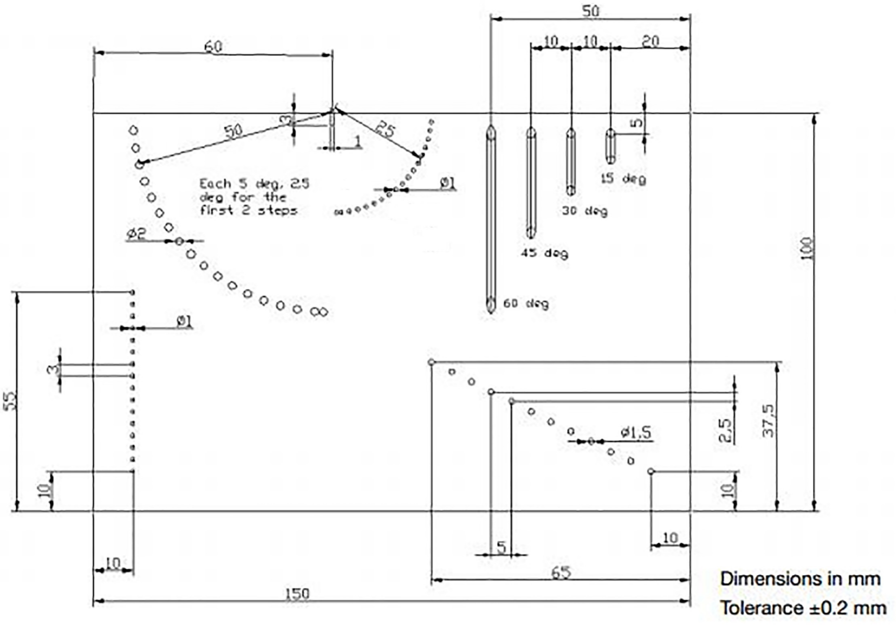

Figure 3.1: *Schematic of Harfang Type B calibration block [117]*

The ultrasonic scans were performed using a Vermon linear array transducer (Tours, France), with parameters as specified in Table 3.1. The transducer array excitation and data acquisition was through a Zetec-Dynaray phased array controller (Quebec, Canada). A Matlab (The MathWorks Inc., Natick, Massachusetts) interface was used to control the phased array controller and to store the acquired FMC data. The data acquisitions were conducted with the transducer positioned at four different locations on the calibration block, as outlined in Figure 3.2.

Table 3.1: *Phased array transducer specifications*

Array Parameter	**Value**
Number of elements	128
Element pitch (mm)	0.75
Element length (mm)	12
Centre frequency (MHz)	2.25

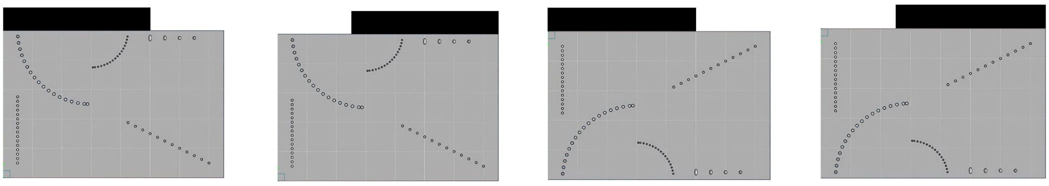

(a) *Location 1* **(b)** *Location 2* **(c)** *Location 3* **(d)** *Location 4*

Figure 3.2: *Diagram of test-piece with black rectangle indicating the four phased array transducer locations for the FMC data acquisitions*

In all locations, the edge of the transducer case was aligned to the edge of the calibration block. Photographs of the transducer placed at scan location 2 can be seen in Figure 3.3. These photographs demonstrate the alignment of the transducer and the calibration block. The knowledge of the transducer position is important to accurately recreate the experimental scans in the simulations.

The transducer was manually aligned at a scan location, with the use of an ultrasonic couplant gel, and a FMC data acquisition was conducted. The FMC data set was acquired and the process was then repeated at the remaining scan locations until each FMC dataset was collected.

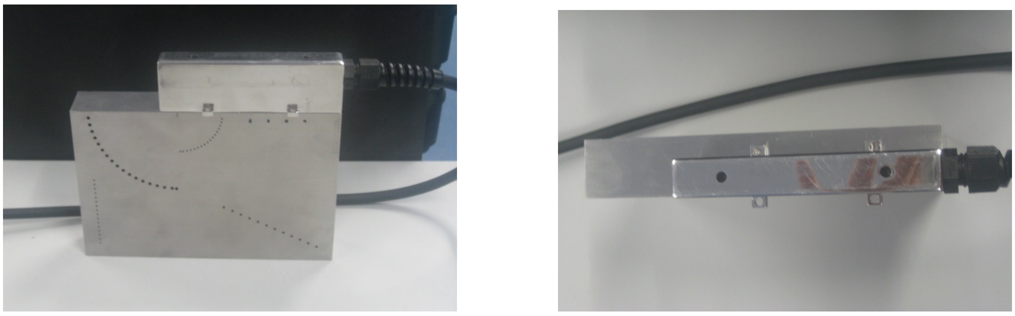

(a) *Side View* **(b)** *Top Down View*

Figure 3.3: *Photographs of experimental FMC data acquisition at transducer location 2 - showing alignment of transducer with calibration block*

3.2.2 2D Simulations

There are numerous points to consider when starting to construct a FEA model. The accuracy of the FEA derived results are dependent on the model set up and inputs. With advanced models, these become more complex and provide a greater potential for errors in the solutions. It can often be beneficial to begin with a simple model by using appropriate approximations and then gradually increasing the model complexity to reach the desired solution accuracy. Frequently, initial models are computed in 2D (or even 1D), as opposed to full 3D. These reduced models are less computationally intense and allows for model set up and debugging to be conducted in a reduced time frame. Once the model is correctly set up and produces the required output with the desired level of accuracy, extension to a 3D model can be readily converted with a degree of confidence.

A 2D model was constructed to replicate the experimental arrangement as accurately as possible while remaining computationally efficient. Care has to be taken with this reduction in dimension due to the presence of the four angled drilled holes, Figure 3.1, which would require a full 3D model. In this first phase of modelling, the angled holes were omitted from the simulations.

The calibration block FEA model, Figure 3.4, was generated using the schematic shown previously in Figure 3.1. The overall dimensions of the calibration block were used to create a region of stainless steel, with properties as shown in Table 3.2. The side drilled holes were then generated by creating void regions of the correct size and location in the stainless steel region. It would be possible to input the material properties of air for these regions, however the velocity of sound in air is far slower than in the steel and would require a much smaller model element size. This would greatly increase the computation of the models while not providing any substantial benefit. In the void region, elements are assigned zero density and zero stiffness. Since the acoustic impedance of air is several orders of magnitude lower than steel, this approximation is acceptable.

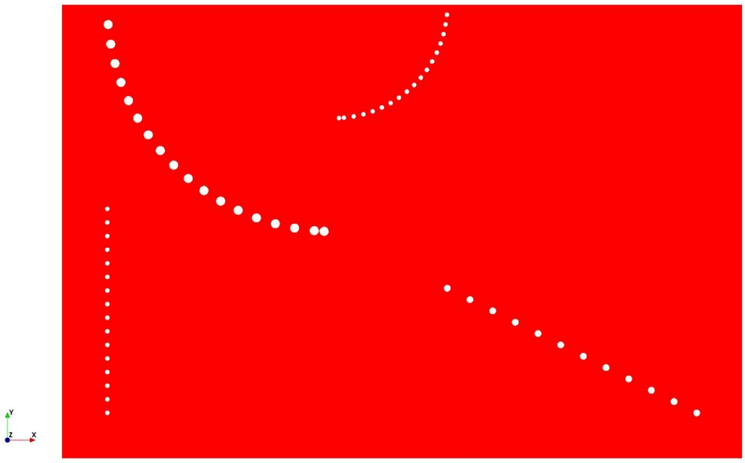

Figure 3.4: *2D FEA model geometry of Harfang Type B Calibration block*

Table 3.2: *Stainless steel material properties*

Stainless steel parameter	**Value**
Density (kg/m^3)	7890
Longitudinal velocity (m/s)	5620
Shear velocity (m/s)	3100
Longitudinal attenuation (dB/m)	0.3
Shear attenuation (dB/m)	1.2

The transducer used in the experiment was a commercial device and so full information on the device structure and material properties is unknown. As a result, accurately modelling the transducer structure is not possible with any confidence. A suitable solution is to represent the phased array transducer as a series of pressure loads. The pressure load can be applied to the model nodes located on the surface of the calibration block where the array elements are positioned. This removes the need to incorporate the transducer structure and piezoelectric materials in the model. This then produces a simplified yet representative, mechanical simulation.

To provide a more accurate simulation, a user defined time signal was used as the drive function of the pressure load. This time signal was generated by experimentally measuring an output signal from the array transducer itself. To acquire this signal, the transducer was coupled to a stainless steel block, containing no side drilled holes or any known defects, and a pulse echo signal was recorded from a single element to obtain a back wall reflection. The back wall reflection was truncated from the full signal and can be seen in Figure 3.5 along with it's spectrum. This recorded signal could then be used as the drive function to the mechanical pressure load in the FEA model. This pressure load would apply the signal as a pressure source on the models boundary elements that represent the transducer array element. In this scenario, it is assumed that each array element performs identically at all points across their surface. If further accuracy was required, the implementation of unique drive functions could be used for each array elements pressure load.

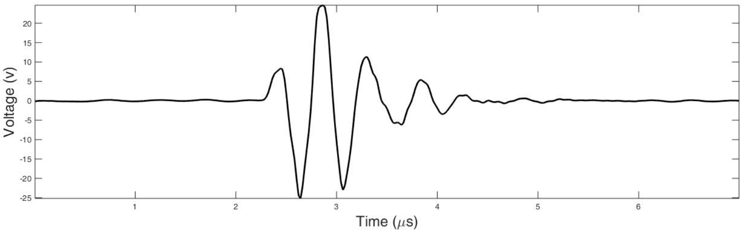

(a) *Time Domain Response*

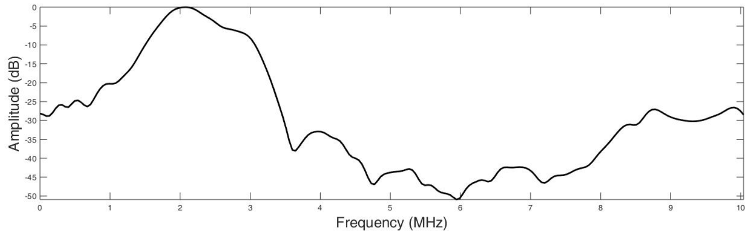

(b) *Frequency Domain Response*

Figure 3.5: *FEA model transducer input pulse*

To generate the simulated FMC data, A-scans for each transducer element must be recorded. The received echoes were recorded as the average time-variant, normal stress at each of the simulated array element locations. Each simulation generated 128 time traces to represent the A-scan signal received at each of the transducer elements, to allow for the FMC data set containing [128 x 128] time traces to be constructed.

The model was 2D plane strain and consisted of a structured Cartesian grid using quadrilateral elements. The model was meshed to give 15 elements per wavelength at 2 MHz for the shear acoustic velocity of the steel (3100 m/s). This frequency was selected as it was the peak of the measured input pulse that would be used as the input pulse, Figure 3.5. The shear wave velocity of the steel is selected to ensure the shear waves, which have a smaller wavelength than longitudinal, are adequately meshed. As discussed in Section 2.2.2, 15 is the minimum number of elements per wavelength to sufficiently discretize the wave. This produced a model containing a total of just over 1.3 million elements.

The Courant Friedrichs Lewy (CFL) condition [32] states that for a given space discretization, the time step must not be greater than a computable quantity. The time step for the model was increased, from the software default of 80%, to 95% of it's maximum allowable value by implementing a time stability factor of 0.95 to increase the time step value used in the simulation. This satisfies the CFL condition and the larger time step reduces the number of time steps required to solve the simulation. This then allows for a reduction in the computation time and inaccuracy caused by numerical dispersion [118].

An initial computational window was set up around the grid elements where the pressure load would be applied. This computational window then contains the only elements computed in the first time step and the window expands one grid element in all directions with each time step. This allows a faster computation in the initial time steps since only the region of interest in the model is solved. Provided the computational window includes every element that is subject to a load, this does not have any impact on derived results.

The simulations were run sequentially on a Dell workstation with 64 GB of RAM and 16 cores. The simulations were run using a single precision solver which is faster than using a double precision solver while still maintaining good result accuracy. Each individual simulation took approximately 17 seconds to compute and only required 80 MB of memory. This resulted in a total simulation time of 36 minutes to generate a full FMC data set. The simulations were repeated to recreate the experimental FMC data collections at all 4 locations as indicated in Figure 3.2.

3.2.3 3D Simulations

A 3D model was constructed to simulate the effects of inspecting the angled holes. This would give a better representation of the inspection but at the expense of a much larger and computationally demanding model. A Computer-Aided Design

(CAD) geometry of the calibration block was created in Midas NFX (Midas, Seoul, Korea) using the design specifications, as illustrated in Figure 3.6, and imported directly into a FEA model. The model geometry can be seen in Figure 3.7, where the four angled holes can be identified.

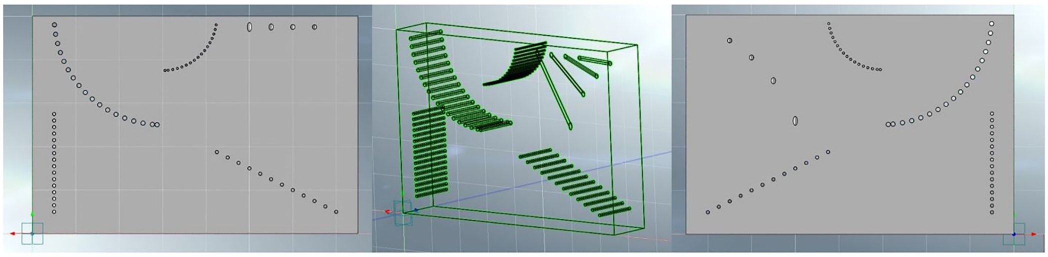

Figure 3.6: *Calibration block CAD file*

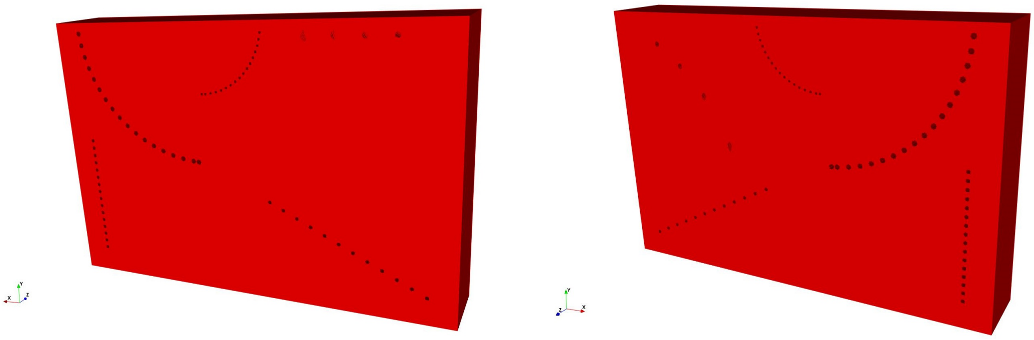

(a) *Front View* **(b)** *Back View*

Figure 3.7: *3D FEA model geometry*

The 3D model was set up using the same approach as the previous 2D models but utilised 3D hexahedral elements as opposed to the 2D quadrilateral elements. A structured Cartesian grid was again used with a mesh density capable to discretize the shear waves in steel at 2 MHz. This produced a model containing approximately 305 million elements which is approximately a factor of 234 increase when compared to the 2D model. This emphasises the benefit of approximating the problem to 2D and reducing the computational cost. The same input pulse signal was applied and echo signals recorded the same as before, but were now done over a 2D area representing each array element location on top of the calibration block as described in Table 3.1.

The 3D model was run on the same workstation as the 2D simulations and had a run time of approximately 5 hours for each simulation, requiring 53 GB of memory. Due to the model size increase, it was necessary to run the simulation in double precision due to single precision only having the ability to access approximately 8 GB of memory, due to the limited address space that can be defined. For a model of this size, this is a very efficient solution time and memory requirement. However, for this scenario where a FMC scan is being produced, the simulation needs to be run 128 times. This means it would take several days to generate the 3D FEA derived FMC dataset by running the simulations sequentially.

Solutions exist to reduce the computation of very large models by making use of modern computing power. One particular approach which has proven to be very beneficial is employing parallelisation through Message Passing Interface (MPI) [119]. This approach was seen to almost halve the time for a single run on the 16 core workstation. Further computation reductions were achieved by employing MPI on a 32 core Intel Xeon server. This 32 part MPI produced a single run time of only 87 minutes, with each thread only requiring 890 MB of memory. As each thread is only modelling a small section of the full model, the memory requirements are reduced and allow for a single precision solver to be utilised. More discussion on parallelisation and MPI will be given in Section 3.4.3.

3.2.4 Post Processing Imaging

Once FMC data has been generated, various post processing imaging algorithms can be applied to the data. One such method is TFM which processes the FMC data to focus the signals at every pixel in the image. TFM has been shown to produce higher resolution images, when compared to other imaging algorithms [116].

To focus at each individual pixel, the amplitude from each signal in the FMC data at the corresponding time location is summed. This requires the time of flight to be calculated for each sound path from the transmitter to the pixel and back to the receiver. These time of flights are then used to obtain the corresponding amplitude from each FMC signal. This is then repeated for every pixel to build up the resulting image. The TFM algorithm is presented in Equation 3.1, where A is the instantaneous amplitude value for pixel location (x, z), transmit element tx and receive element rx. A Hilbert transform (h) is used to convert the real time domain signal into its complex form and allow the signal magnitude to be determined. c_1 is the longitudinal velocity of sound in the imaging material.

$$A(x,z) = \left| \sum h_{tx,rx} \left(\frac{\sqrt{(x_{tx}-x)^2+z^2} + \sqrt{(x_{rx}-x)^2+z^2)}}{c_1} \right) \right| \tag{3.1}$$

The process times to generate TFM images can become very long. Large image sizes with high resolution will produce a greater number of pixels requiring more processing. The size of the FMC data set, which is determined by the number of array elements, will also have an effect on the processing time.

The desire to obtain real-time imaging has lead to the study of acceleration of the TFM process. Previous research conducted in CUE has developed a software package named cueART (Centre for Ultrasonic Engineering Acoustic Research Toolbox) [13, 120, 121]. This package is a LabVIEW-based program containing multiple advanced post-processing imaging algorithms. Included in cueART is an efficient implementation of TFM which uses GPUs to allow for parallel processing of the imaging process. The TFM algorithm can also efficiently account for refraction through an interface [122], allowing for the imaging of complex surface components to be conducted [123, 124].

The cueART TFM was used to process all of the FMC data sets and create an image in the area directly below the transducer with a depth of 120 mm to cover the full depth of the test block. A pixel size of 50 μm was used in both directions to give a good level of resolution, approximately 30 times smaller than the wavelength. A Hilbert transform was applied to each image and all images were then plotted on a dB scale and normalised to the maximum response amplitude of a central side drilled hole. Figure 3.8 illustrates the side drilled holes used in this process, with a different hole used depending on the array location on the calibration block. To ensure a fair comparison between experiment and simulation, the same side drill hole was used for both cases.

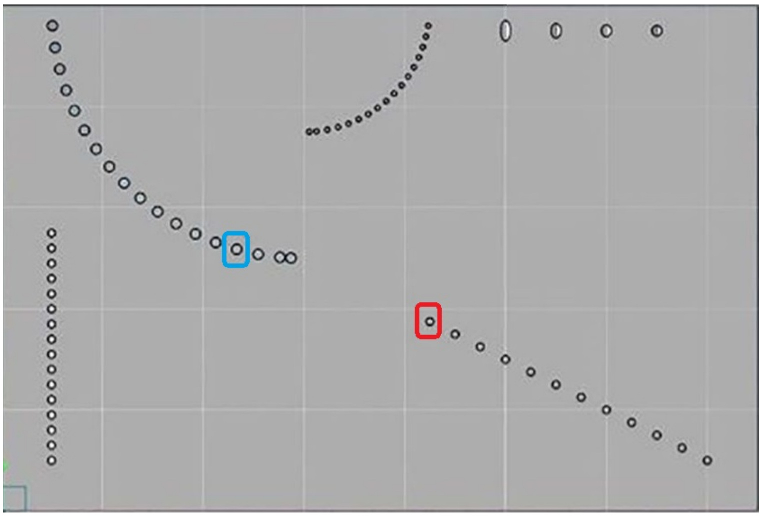

Figure 3.8: *Indication of SDH used for TFM image normalisation. Array locations 1 and 3 use the SDH contained in the blue box and locations 2 and 4 use the SDH in the red box*

3.3 TFM Images

3.3.1 Experiment and 2D Simulation

The resulting images for the experimental and 2D simulation data sets can be seen in Figures 3.9 - 3.12, for each array location illustrated in Figure 3.2. The images are set up to show the area of the calibration block directly below the transducer when the transducer is positioned at 0 mm on the x-axis. Each Figure contains the (a) experimental and (b) simulation data set at each array location.

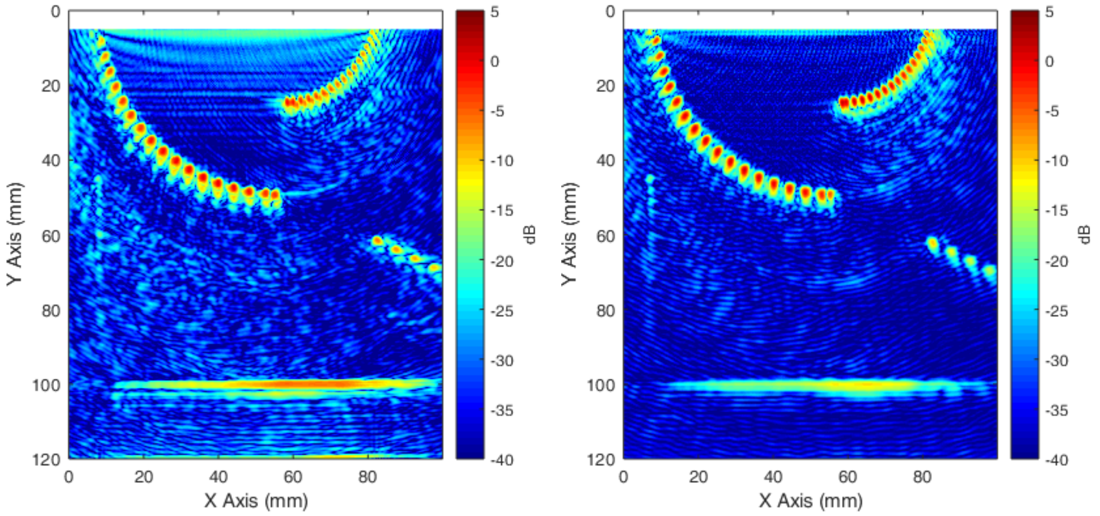

(a) **(b)**

Figure 3.9: *TFM images for (a) experiment and (b) 2D simulation FMC data sets at array location 1*

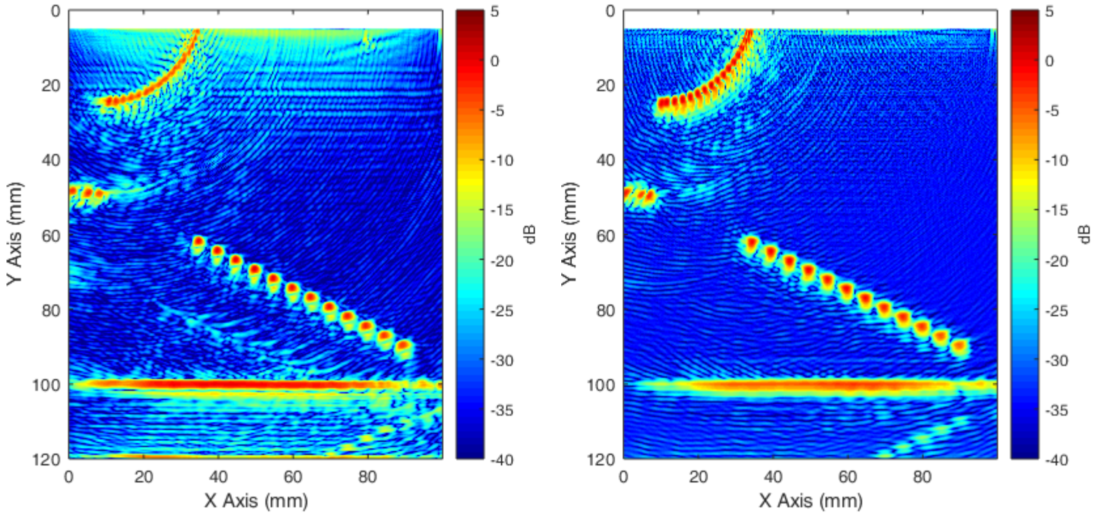

(a) **(b)**

Figure 3.10: *TFM images for (a) experiment and (b) 2D simulation FMC data sets at array location 2*

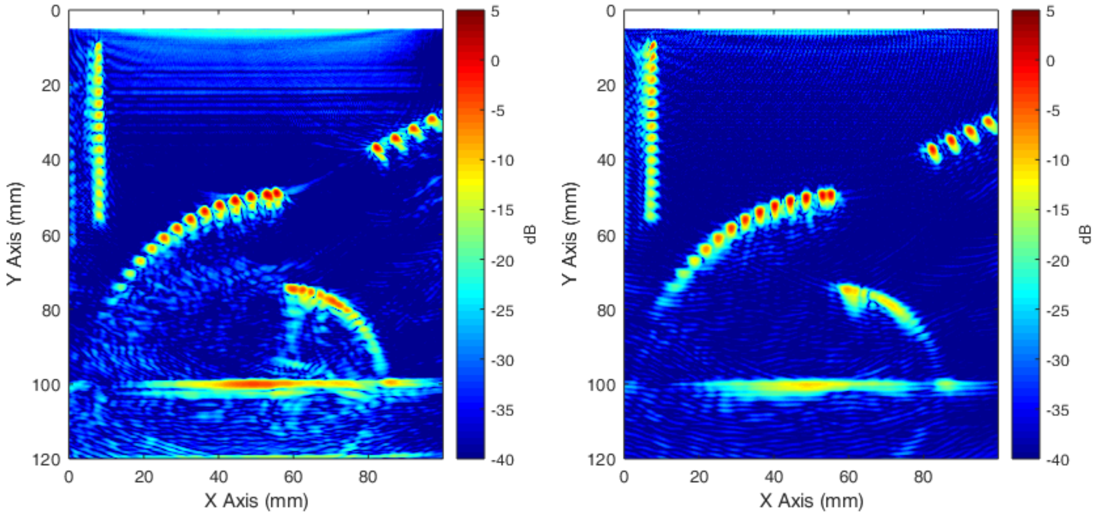

(a) (b)

Figure 3.11: *TFM images for (a) experiment and (b) 2D simulation FMC data sets at array location 3*

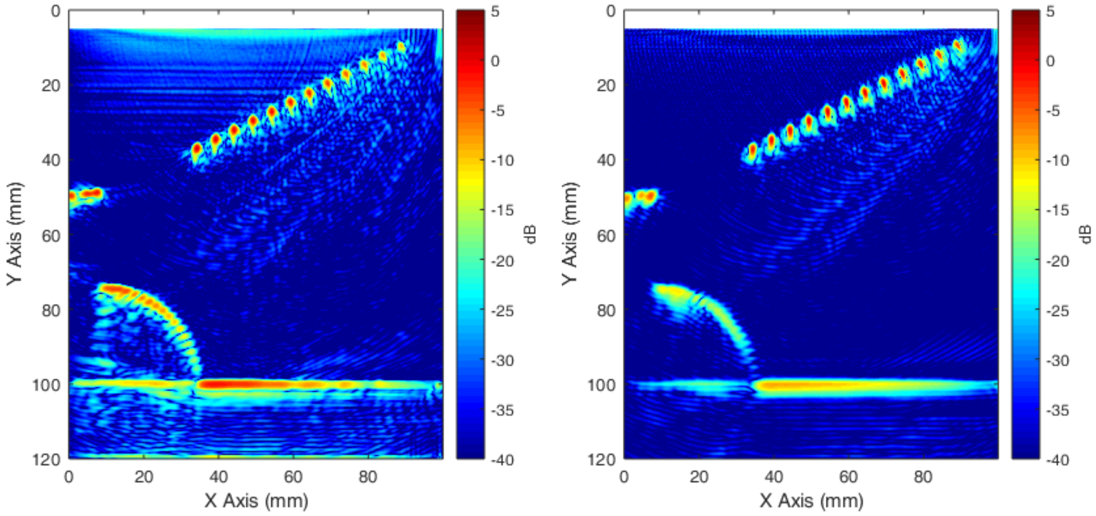

(a) (b)

Figure 3.12: *TFM images for (a) experiment and (b) 2D simulation FMC data sets at array location 4*

Initial comparison between experimental and FEA derived TFM images shows a clear visual correlation with the same side drilled holes can be seen in both images at each array location. The profile of the backwall is very similar in each position but the amplitude is lower in the simulation, which indicates the attenuation applied in the models is greater than the real attenuation in the test piece. The near surface of the images is also different with the experiment images displaying a higher amplitude region below the transducer known as the 'dead zone' which is caused by the ring down of the active element. As a mechanical pressure load is utilised in the simulations, this ring down effect is not replicated and so the dead zone is much smaller in the FEA derived TFM images.

3.3.2 Experiment and 3D Simulation

The experimental and 3D simulation TFM images can be seen in Figure 3.13. Again, the TFM images are set up to show the area of the calibration block directly below the transducer when the transducer is positioned at 0 mm on the x-axis.

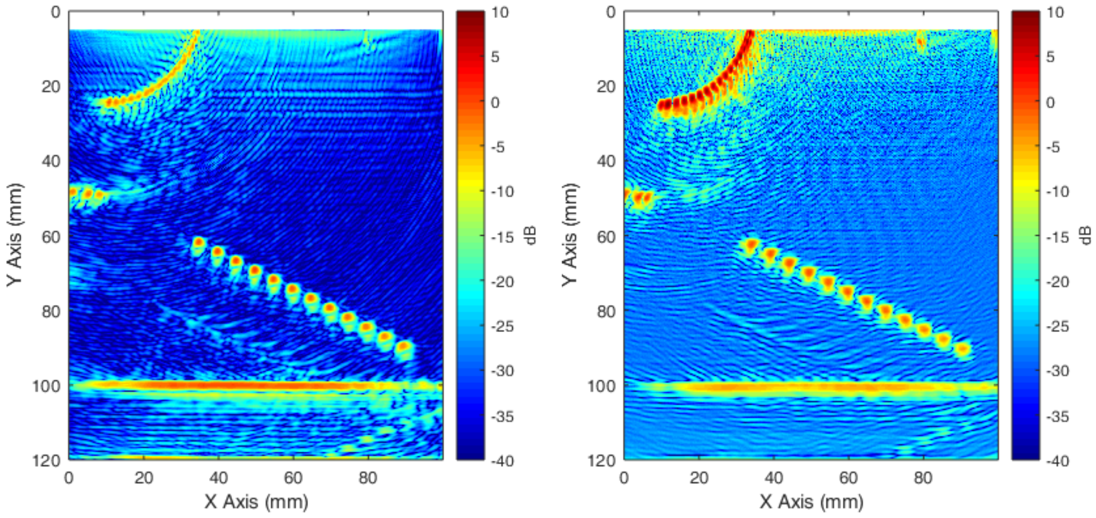

(a) **(b)**

Figure 3.13: *TFM images for (a) experiment and (b) 3D simulation FMC data sets at array location 2*

Once again, there is a good visual correlation between the experiment and FEA derived TFM images. The main difference from the 2D and 3D FEA models is the inclusion of the angled drilled holes and in the 3D FEA derived TFM images the presence of an angled hole at position (79 mm along X-axis and 8 mm in Y-axis) and be identified. This correlates well with the experiment image and will be discussed in more detail in the following Section.

3.3.3 Result Analysis

Evaluation of the TFM images shows excellent visual correlation between the simulated and experimentally generated data sets, with only slight differences in amplitude. In each of the images, back wall location is correctly positioned at 100mm. All of the defects present in the experimental images can be identified in the corresponding simulation data set.

The data set acquired with the array at location 2, shown in Figure 3.10, has the transducer placed over the angled holes in the calibration block. In the experimental image, Figure 3.10(a), one of these, at the shallowest angle, can be observed in the top right. This is not present in the corresponding simulation image as the defect was not present in the simulation. Additional artefacts can be seen in the experimental image below the set of holes near the back wall which are due to secondary effects from the scattering of the input wave with the angled holes.

The angled defects were incorporated into the 3D model and the presence of the shallowest angle can be identified in the TFM image (79 mm along X-axis and 8 mm in Y-axis), Figure 3.13(b). The artefacts below the set of holes near the back wall in the experimental image are also present in the 3D simulation image. This confirms that these artefacts are due to a 3D effect in the inspection, such as secondary scattering of the input wave with the angled holes or reflections from the component sides. These artefacts could also be indicative of the beam profile and spread, which in the 2D model is approximated as a plane wave. The inclusion of these subtle effects highlights the capability of 3D models to produce a complete representation of the practical inspection.

To provide a quantitative comparison, the 12 side drilled holes near the back wall, as indicated in Figure 3.14, were used to determine the positioning accuracy of the results. The centre of the holes was determined by taking the maximum amplitude of the TFM image for each hole. The resulting depths, Table 3.3, and horizontal positioning of the holes, Table 3.4, are presented along with the designed values from the schematic for reference. The holes are numbered with 1 being the top left and 12 the bottom right as seen in Figure 3.14. It should be noted that the design depth and horizontal position values and there tolerance have been produced from the schematic diagram of the calibration block, Figure 3.1, which may differ from the real position of the side drilled holes in the manufactured component. Also, the pixel size of all TFM images is 50 μm, which limits the precision of the measured positions from the images.

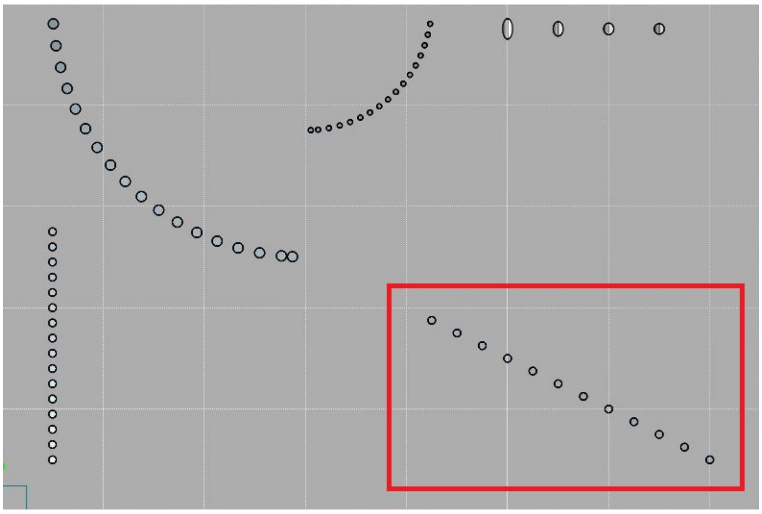

Figure 3.14: *Selected side drilled holes to determine positional accuracy, where the hole depth is measured in the vertical Y-axis and hole number 1 is the top left and hold number 12 is the bottom right*

Table 3.3: *Determined depth of side drilled holes from TFM Images*

Hole number	**Design depth (±0.2mm)**	**Experimental depth (±0.025mm)**	**2D simulation depth (±0.025mm)**
1	62.50	61.70	61.95
2	65.00	64.25	64.45
3	67.50	66.70	66.95
4	70.00	69.20	69.40
5	72.50	71.65	71.90
6	75.00	74.20	74.40
7	77.50	76.70	76.90
8	80.00	79.30	79.35
9	82.50	81.80	81.90
10	85.00	84.40	84.45
11	87.50	86.95	86.90
12	90.00	89.50	89.45

Table 3.4: *Determined horizontal position of side drilled holes from TFM Images*

Hole number	**Design horizontal position (±0.2mm)**	**Experimental horizontal position (±0.025mm)**	**2D simulation horizontal position (±0.025mm)**
1	34.375	34.70	34.40
2	39.375	39.70	39.45
3	44.375	44.65	44.45
4	49.375	49.65	49.45
5	54.375	54.65	54.50
6	59.375	59.65	59.60
7	64.375	64.60	64.65
8	69.375	69.60	69.70
9	74.375	74.50	74.75
10	79.375	79.35	79.80
11	84.375	84.30	84.70
12	89.375	89.25	89.80

The results from the depth and horizontal positioning provide good corroboration between experimental and FEA derived data sets, with a mean difference of 0.15 mm and 0.24 mm and maximum difference of 0.25 mm and 0.55 mm respectively. In terms of wavelength, the mean depth positioning difference is $\lambda/11$, with a maximum difference of $\lambda/7$. The mean horizontal positioning difference is $\lambda/7$, with a maximum difference of $\lambda/3$. This confirms that the simulations can accurately predict the experimental data.

As with the 2D model, the 3D model was successful in recreating all of the defects seen in the experimental results. The 3D FEA model was more than double in size than its 2D equivalent which results in a much greater computational overhead. The 3D model enabled the angled defects to be included in the simulation and could accurately predict the experimental performance and capture subtle effects, such as the artefacts below the angled set of side drilled holes. For the side drilled holes, the 2D and 3D FEA results are nearly identical, which indicates that the 2D approximation is sufficient to model the experimental response from these features. This demonstrates that when the modelling scenario permits, the approximation to a 2D model is a valid approach and will provide a much more computational efficient model.

3.4 Model Optimisation

One method of optimising FEA models by reducing the computation time is the implementation of parallelisation. This can be running multiple model instances in parallel or “breaking down” a large model into smaller sections which are then solved simultaneously. To provide information on the best approach for running multiple models to generate FMC data and how best to reduce large model computation costs various parallelisation methods were investigated.

3.4.1 OpenMP

The core of OnScale is written in the Fortran programming language and utilises OpenMP, which is an application programming interface that supports shared memory multiprocessing [125]. This allows for the parallelisation of simulations across users standard workstations, but can also be extended to supercomputers and clusters.

The use of Hyper-threading and OpenMP was investigated by running a single 2D simulation on the same workstation but limiting the number of cores used. To give a fair comparison, the time stability factor was set to the default 0.8 and the initial computational window was removed from all simulations run. Hyper-threading was turned off and simulations were performed using 1, 2, 4, 8 and 16 physical cores. The simulation times and the speed up versus the single core is shown in Table 3.5. A graph of the simulation time against number of cores can be seen in Figure 3.15 and a graph of the speed up versus one core can be seen in Figure 3.16.

Table 3.5: *2D simulations run using OpenMP parallelisation with different number of cores*

Number of cores	**Single run time (seconds)**	**Speed increase versus 1 core**
1	324	1
2	174	1.86
4	94	3.45
8	54	6.00
16	27	12.00

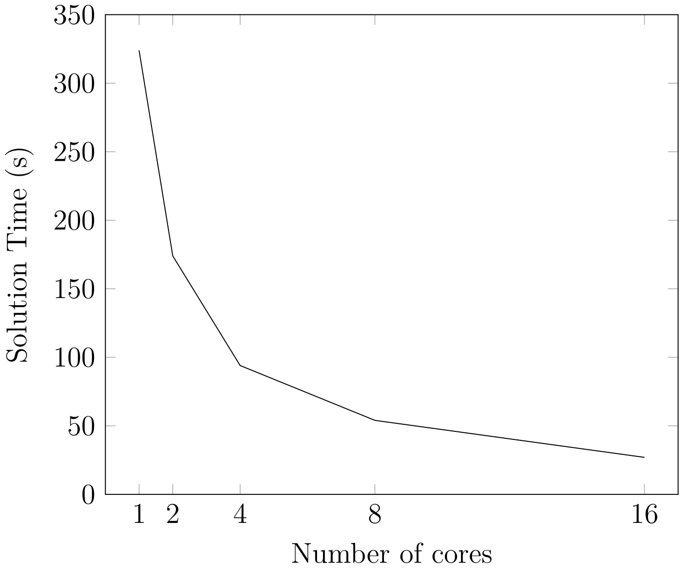

Figure 3.15: *Simulation time against number of cores*

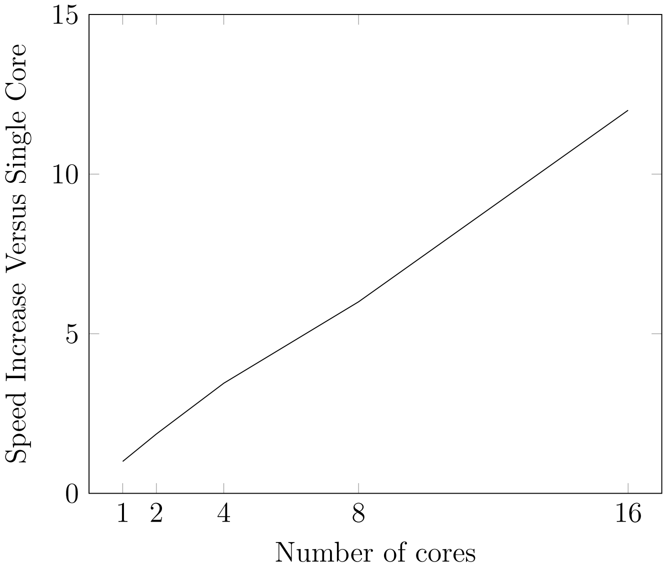

Figure 3.16: *Simulation time speed increase versus single core against number of cores*

It is shown that parallelising with OpenMP can offer improvements when the number of physical cores used is increased. Using 16 cores was 12 times faster than using only a single core and the speed increase is linear with core increase over the presented number of cores, Figure 3.16. Increasing the number of cores above 16 is likely to reduce computation time further, however it is expected that a point will be reached where the solution time will converge to the minimum possible time.

Hyper-threading was then turned on to give the workstation 32 virtual cores. The same simulation was run using OpenMP with 32 cores and produced a run time of 32.11 seconds. This is slower than the simulation using 16 physical cores without Hyper-threading enabled. Therefore, it can be concluded that physical cores are more important and hyper-threading decays performance efficiency.

3.4.2 Parallel Simulations

Further investigation into reducing the total simulation time to generate FMC data sets was done by running simulations in parallel. It has been previously shown that running PZFlex simulations in parallel can provide massive speed-up over sequential simulations [126]. The resulting simulation times were then used to calculate the time to generate the FMC data for the 128 element transducer. The optimised 2D model which had a time stability factor of 0.95 and an initial computational window was used as this would produce the shortest simulation time.

The first simulation run was a single simulation using OpenMP and all 16 cores. Then various number of simulations were run in parallel up to 16 simulations in parallel running on single cores. Details of the simulations and their run times can be seen in Table 3.6, which also includes the calculated time to generate the full FMC data set.

Table 3.6: *2D simulations run in parallel on same workstation*

Simulations run in parallel	Number of cores per simulation	Single run time (seconds)	FMC time (minutes)
1	16	16.99	36.25
2	8	33.87	36.13
4	4	64.16	34.22
8	2	126.27	33.67
16	1	237.65	31.69

Despite a single simulation having a much smaller simulation time when run across 16 cores opposed to a single core, it can be seen that running 16 simulations in parallel on individual cores produces the FMC data set faster than sequentially running all simulations across all 16 cores. The reasoning for this is that while the simulation time decreases with more cores, 16 cores does not provide an exact linear increase in simulation time, Figure 3.16. Instead, 16 cores provides an increase of approximately 12 over a single core simulation. Although the time to generate the FMC datasets are reasonably close, these results are based on a 2D model and hence, the reduced simulation time will have a significant impact on 3D model scenarios.

3.4.3 Message Passing Interface

MPI is a message passing technique that allows for a reduction of computation time of FEA models through parallelisation [119]. MPI is an efficient communication protocol which allows large problems to be divided into many partitions to take full advantage of modern computing hardware. Mechanical OnScale models using the explicit solver are ideally suited to MPI with significant reductions in memory requirements and run times.

The 3D FMC model was used to explore the advantages of employing MPI. A single run was simulated numerous times on a 32 core machine for different MPI part sectioning. The model would be partitioned in different ways to observe any improvements to the computation time.

Details of the simulations and their performance can be seen in Table 3.7. 1:32:1 MPI signifies the model has been partitioned for MPI with 1 section in the x direction, 32 sections in the y direction and 1 section in the z direction. This relates to partitions as slices of the calibration block and the same terminology is used for all entries presented.

Table 3.7: *3D MPI improvements*

OpenMP or MPI	**Single run time (minutes)**	**FMC time (hours)**	**Speed up versus 32 core OpenMP**
32 core OpenMP	227.41	485.15	1
1:32:1 MPI	99.33	211.91	2.29
2:16:1 MPI	93.08	198.57	2.44
4:8:1 MPI	89.33	190.57	2.55
4:4:2 MPI	86.88	185.35	2.62
8:4:1 MPI	84.59	180.46	2.69

Evaluating the results demonstrates the advantage of employing an MPI approach to large models. Each MPI partition run is over 2 times faster than the OpenMP equivalent. There is some variability in the simulation time for different MPI partitioning. The effectiveness of MPI is dependant on the number of elements that need to pass information to neighbouring partitions. The sliced MPI with a 1:32:1 partition, is a poor way to partition the model as each partition has lots of elements which need to pass information. The 8:4:1 partition produces the best speed up in simulation time as it is the closest to equally sized partitions.

3.5 Discussion

The comparison of FEA derived results with experimentally collected data is a common approach to provide confidence that the model set up is valid and capable of generating accurate and reliable results. The FEA model set up can have a big influence on the ability of the derived solution being a valid representation of experimental behaviour. There are multiple approaches to model generation and many parameters that have to be carefully considered to ensure model validity.

As detailed in Section 2.2.2, OnScale prominently implements a structured Cartesian mesh using low order quadrilateral and hexahedra elements. This approach was implemented in the simulation models with a mesh to give 15 elements per wavelength at a frequency of 2MHz using the shear wave velocity in steel. The 2MHz frequency was selected as it corresponds to the peak frequency in the drive input pulse, Figure 3.5 and the shear velocity is selected as the slowest velocity in the simulation. This ensures all the wave modes present in the model are meshed with at least 15 elements per wavelength to ensure they are sufficiently discretized. The structured Cartesian mesh implemented was chosen for it's efficiency but means the curved surfaces in the model are represented as jagged 'stair stepped' edges. However, since the element size is much smaller, $\frac{\lambda}{15}$, than the incident wavelength, the influence of the stair stepped mesh is lessened. As shown from the TFM results presented in Figures 3.9-3.12, the FEA derived results provide an excellent prediction of experimental performance which indicates that the model set up is acceptable.

As well as implementing efficient meshing, other settings used to optimise the run time were increasing time step used in the simulations and using an initial computational window. With a greater time step, less time steps were required to be computed to derive the FEA dataset. This reduces the computational time and also leads to more accurate results by reducing numerical dispersion. Numerical dispersion is common to all FEA codes and is the build up of small approximation errors [59]. Increasing the time step can, in certain cases, lead to instability of the model. However in these simulations performed, the model remained stable. The initial computational window, greatly reduces the time taken to solve the initial time steps. The initial window is set to a small region around the pressure load force and limits the region of the model that is initially solved to that region. The computation window is then extended after every time step, in all directions by one element until the computation window becomes the full model. When model size becomes large, this can produce a significant time saving for the initial simulation period.

With the FEA model confirmed as valid, optimisation of the model can be performed to minimise the computational time and memory requirements. As well as selecting efficient approaches in model set up, the computation time can be reduced through parallelisation of the simulation. It was demonstrated that the OpenMP parallelisation applied in OnScale can provide a linear speed increase for simulation solve time as the number of cores utilised is increased. This speed increase can be improved further through the use of MPI. It has also been shown that when multiple models are required to be simulated, it can be more efficient to run simulations in parallel on the same workstation using less cores per simulation.

3.6 Conclusion

This Chapter has outlined the work undertaken to validate and optimise the FEA modelling method used in this research. The developed models replicated experimental FMC data acquisitions of a stainless steel calibration block. Validation of the method was achieved through corroboration between the experimentally generated datasets on a standard phased array calibration block and the FEA derived datasets. The FEA models were optimised with efficient set up and parameter selection. Additionally, parallelisation methods were investigated to observe their benefits to computation time. The knowledge gained in this Chapter on how to set up FEA models to perform efficiently and accurately will be used in subsequent Chapters where more complex models will be computed.

Chapter 4

Generation of FEA models of CFRP structures

In order for FEA simulations to derive results that are representative of the real world situation, it is important that enough information is captured in the models. The FEA modelling of wave propagation through CFRP structures presents challenges due to the complex microstructure and the anisotropic material properties of CFRP. The modelled geometry and material properties will have a direct impact on the derived FEA results and so must be carefully defined to ensure derived results are representative of experimental performance. Various assumptions can be made as long as they are valid, such as approximating the modelling scenario to 2D for more computational efficiency. Therefore, it is important that, in this research, the generation of the model geometry and the material property definitions are investigated and implemented accurately.

This Chapter begins by describing the challenges of modelling wave propagation through CFRP materials. The approaches developed in this research to overcome these challenges and construct FEA models of CFRP structures include using a scripted input file, importing from a table file and through the use of a plybook. Each approach is described, with advantages and disadvantages discussed, and an example of implementation is presented. Although these examples only contain the CFRP laminate geometry for demonstration purposes, they could easily be extended to allow for a NDE inspection to be simulated.

4.1 Introduction

4.1.1 Motivation

The benefits of using modelling to design, evaluate or optimise ultrasonic inspections relies on the derived results being accurate and representative of experimental performance. Inaccurate results negate the benefit of modelling and could have severe consequences for safety critical engineering applications.

Inappropriately configured models could lead to incorrect manufacture of a device or an inadequate inspection set up, resulting in a loss of both time, expense and safety.

The aim of FEA models are to predict experimental performance. The ability for the simulations to match real world behaviour is dependent upon the FEA model set up. Often, the main source for differences between derived results and real performance is due to errors in material properties and model geometry. There are other sources of error that can arise due to approximations. However with good model set up these can be limited. Such approximations include: boundary conditions and loading and sampling in both time and space. The material properties and model geometry are typically the most challenging aspects as accurate knowledge of the model domain is required. If either of these are inaccurate, it is impossible for the derived results to match experimental performance.

CFRP materials contain a highly complex microstructure and have anisotropic and inhomogeneous material properties, which provides challenges for the FEA modelling of wave propagation. The anisotropic material properties of CFRP structures results in complex wave behaviour and the wave propagation through the structure can vary greatly depending on its direction relevant to fibre orientation. The CFRPs multilayered microstructure can also induce reflection of the propagating wave-front at each material interface. The anisotropic material properties of the CFRP plies can create a very large difference in acoustic velocity, as shown in Figures 4.1 and 4.2 for longitudinal and shear wave velocities in a unidirectional *IM7/8552* CFRP ply. These figures have been generated in Matlab using material properties taken from literature [127], which will be presented later in this Chapter. In the direction of the fibres, the material is very stiff and has a large sound velocity compared to the velocity perpendicular to the fibre direction where the material is less stiff. The acoustic velocity maps show the difference in sound velocity depending upon orientation, which means that waves propagating in the material will behave very differently depending on the angle of wave propagation relative to the fibre orientation.

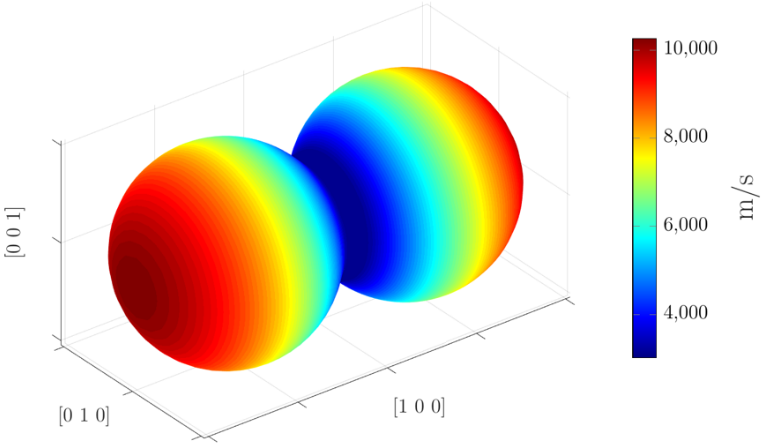

Figure 4.1: *Longitudinal velocity (m/s) map for a unidirectional IM7/8552 CFRP ply layer with fibres in the [1 0 0] direction*

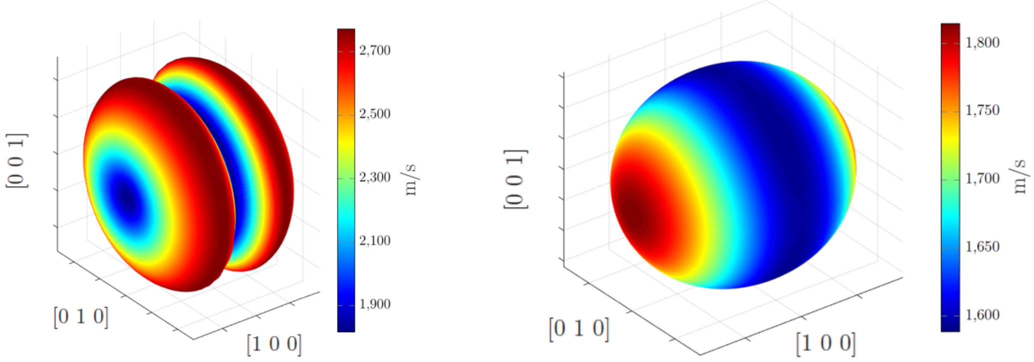

(a) *Shear vertical velocity (m/s)* **(b)** *Shear horizontal velocity (m/s)*

Figure 4.2: *Shear velocity maps for a unidirectional IM7/8552 CFRP ply layer with fibres in the [1 0 0] direction*

In order for this research to provide valid and tangible outcomes for the NDE community, it is essential that the generation of FEA models of CFRP structures for wave propagation simulations is investigated. This includes the accurate representation of material properties and the construction of the model geometry.

4.1.2 Investigation Method

4.1.2.1 Material Definition

As with other FEA packages, there are many options available in OnScale to define material properties and construct the model geometry. It is important that care is taken to ensure the material properties used are accurate and defined correctly. The same model geometry can be created in different ways with a varying level of complexity, so a good modelling knowledge is required to ensure the approach used is not overly complex and time consuming to set up but importantly, remains accurate.

Different OnScale commands exist for entering material properties for different material types. The most commonly used material types for NDE scenarios are linear elastic isotropic (type *elas* in OnScale) or linear elastic anisotropic (type *lean* in OnScale). Isotropic materials have consistent properties in all axis directions and the minimum requirements to define them are its density along with either its bulk and shear moduli or bulk and shear acoustic wave velocities. Anisotropic materials can have unique material properties in each axis direction and the material density, plus either its stiffness matrix or compliance matrix are required to define them.

CFRP materials will be defined as linear elastic anisotropic with their properties input as their mass density along with either a stiffness, or compliance matrix. Once the material properties have been defined, they can be transformed to a local coordinate system, relative to the local fibre orientation. Multiple local coordinate systems can be easily defined in the model through rotation of the origin axis. Rotation is applied using the right-handed rule and the rotations are performed in the order: θ_x, θ_y, θ_z, as illustrated in Figure 4.3. When the material definitions are assigned to the local coordinate system, their material properties are automatically transformed into the global coordinate system of the model.

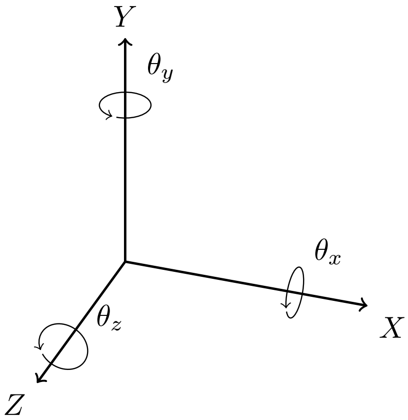

Figure 4.3: *Diagram of axis rotation to define local axis*

When a CFRP component is constructed, often the layers of carbon fibres are placed with different in-plane orientations. The variations in orientations are important to include in the FEA models to ensure the wave interactions at the ply interfaces are modelled. Therefore, the local axis for each in-plane orientation can be constructed to rotate the material properties to the required orientation.

Plies that vary in out-of-plane orientation, due to waviness or in a tapered sample containing ply drops, add an additional complexity to defining the material properties as their material properties will vary spatially. Figure 4.4 shows a simple CFRP taper diagram where the out of plane orientation variation of top ply layer is illustrated. These differences in orientation will require further rotation of the material properties throughout its geometry to fully represent the real structure condition. To overcome this, one solution is to segment the ply as multiple different materials related to the orientation of the fibres. Unique local coordinate systems can then be defined for each material segment to allow for the material properties to be firstly rotated for the in plane orientation, before a second rotation for out-of-plane orientation is performed.

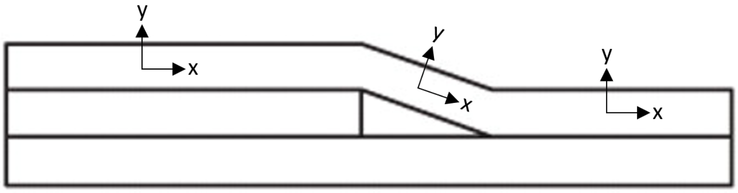

Figure 4.4: *Simple CFRP taper diagram showing the out-of-plane orientation variance of top ply layer*

4.1.2.2 Geometry Generation

Different methods exist to generate geometries in OnScale, including:

- Use of primitive shapes in an input script
- Importation of a CAD file
- Importation of an OnScale native table file

The use of primitive shapes, such as rectangles, blocks, cylinders, spheres etc, is the simplest approach to generate the model geometry. The primitive shapes can be rotated and used to add or remove materials to create desired geometries. This provides an easy method that can quickly generate full laminate structures with the use of “do loops” but can become insufficient as the model geometry becomes more complex.

CAD files are commonly used in industry to design components. The ability to import these files directly into a FEA model makes the generation of complex geometries straightforward. The limitation to the use of CAD file importation is the requirement for new CAD to be generated for any changes in component structure or dimensions.

OnScale table files are native files that contain geometric information that can be read into an input file to generate arbitrary geometries. Table files can be generated externally and contain a voxel grid of a defined size and resolution. Contained in the grid is numbers relating to the material name present at that location. As with importing CAD files into the model geometry, any modifications to component structure or dimensions requires a new table file to be generated. Further details on OnScale table files and their file structure is provided in Appendix A.

The microstructure of CFRP components contains a high level of detail as they are manufactured with multiple ply layers containing carbon fibres encapsulated in an epoxy resin matrix. For ultrasonic NDE modelling, the ply layers can be considered a single material, with effective material properties, as the individual fibres are several orders of magnitude smaller than the wavelength. However, it is important that the individual ply layers and the interply resin layers are incorporated into the FEA model for complete component representation and to simulate the complete wave behaviour within the component. As well as containing multiple ply and resin layers, the layers do not always maintain their pre-defined position, resulting in spatial variations.

Where components are planar and can be assumed uniform, primitive shapes can be utilised to easily generate the model geometry. However, for more complex components where the internal layers are no longer uniform, the use of primitive shapes is insufficient as they are extremely difficult and time consuming to implement. Similarly, the generation of a CAD file of a complex CFRP component would be unfavourable due to the level of detail required when modelling these structures.

Table files offer the optimum flexibility in terms of geometry definition for FEA modelling, due to the ability to generate them externally to include the individual ply and resin layers. The generation of the table file can be achieved manually through knowledge of the component structure or through the use of additional software. Specific textile modelling software programs exist that are capable of creating complex composite structures and generating both geometry and fibre orientation information. An example software capable of this is TexGen which is an open source code developed by the University of Nottingham [128]. TexGen is capable of generating 3D composite structures through its Graphical User Interface (GUI) or an input Python file. There is then the capability to export the structure as an Abaqus voxel file which saves both geometry and fibre orientation information. Using these outputs, it is then possible to manipulate the data into the native OnScale table format to allow for easy importation into the model environment.

4.2 Generating CFRP Structure Geometry in FEA Models

4.2.1 Material Definition

In each of the following examples of creating FEA models of CFRP structures, the CFRP material used will be *IM7/8552*. This material is commonly found in aerospace applications and comprises of *HexTow IM7* carbon fibres bound in *HexPly 8552* resin [108]. The fibres possess a high tensile strength and modulus [129], while the resin is a high performance tough epoxy matrix [130]. The elastic material properties for a single ply of unidirectional *IM7/8552* are detailed in Table 4.1, reproduced from [127]. The density of the single ply is also presented which has been taken from the manufacturers data sheet [130].

Table 4.1: *Hexel IM7/8552 elastic material properties with* E_{11} *in the fibre direction*

Property		Value
Density (kg/m^3))		1570
Elastic Modulus (GPa)	E_{11}	161
	E_{22}	11.38
	E_{33}	11.38
Shear Modulus (GPa)	G_{12}	5.17
	G_{23}	3.98
	G_{13}	5.17
Poisson's Ratio	ν_{12}	0.32
	ν_{23}	0.436
	ν_{13}	0.32

The elastic material properties figures have come from practical experimental tests, with variation in material properties expected in different manufactured components due to variability in the manufacturing process [112]. This effect is highlighted in Table 4.2 where measured material properties of *IM7/8552* are presented from different sources [127, 131–133]. This is important to consider when performing FEA simulations as the material properties will have a major impact on the derived results. One approach to ensure material properties used in simulations is to verify them against manufactured components using model-based inversion [134]. Material based damping is not included in the models as reliable data could not be found in the literature. However, should accurate data be available, material damping could be included in the models.

Table 4.2: *Comparison of measured elastic material properties of IM7/8552 within literature*

Property	Ref 1 [127]	Ref 2 [131]	Ref 3 [132]	Ref 4 [133]
E_{11} (GPa)	161	171.42	150	160.58
E_{22} (GPa)	11.38	9.08	11.0	11.5
G_{12} (GPa)	5.17	5.29	4.6	5.43
ν_{12}	0.32	0.32	0.30	0.31

The CFRP elastic material properties are used to calculate it's compliance matrix, S, Equation 4.1 [135]. The values from the compliance matrix can then be used to define the CFRP material as a linear elastic anisotropic material.

$$S = \begin{bmatrix} \frac{1}{E_{11}} & -\frac{\upsilon_{21}}{E_{22}} & -\frac{\nu_{31}}{E_{33}} & 0 & 0 & 0 \\ -\frac{\nu_{12}}{E_{11}} & \frac{1}{E_{22}} & -\frac{\nu_{32}}{E_{33}} & 0 & 0 & 0 \\ -\frac{\nu_{13}}{E_{11}} & -\frac{\nu_{23}}{E_{22}} & \frac{1}{E_{33}} & 0 & 0 & 0 \\ 0 & 0 & 0 & \frac{1}{G_{23}} & 0 & 0 \\ 0 & 0 & 0 & 0 & \frac{1}{G_{31}} & 0 \\ 0 & 0 & 0 & 0 & 0 & \frac{1}{G_{12}} \end{bmatrix} \tag{4.1}$$

Once the CFRP material has been generated, the anisotropic material properties can be transformed to a local coordinate system. The material properties are entered for the fibre direction in E_{11} which is in the X axis direction. This gives the out-of-plane direction in the Y axis and the in-plane direction in the Z axis, Figure 4.5. Unidirectional ply layers are typically characterised by their in-plane fibre orientation angle, for example 0° or 90° layers. This change of fibre orientation can be achieved through rotation of the material properties about the Y axis. It is then common for ply layers to contain out-of-plane orientation variances due to ply waviness [136]. To account for these out-of-plane orientations, the material properties need to be transformed by rotation of the Z axis.

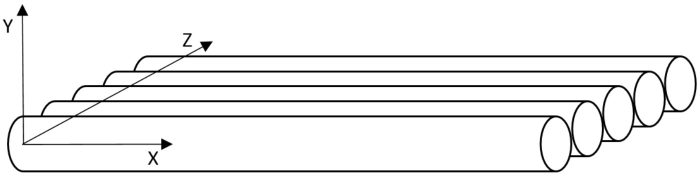

Figure 4.5: *Diagram of fibre orientation for material property definition*

The *HexPly 8552* resin material properties used for the 10 μm resin layers in between ply layers can be seen in Table 4.3 [127]. The Young's Modulus, E, and Poisson's ratio, v, are used to calculate the bulk, K, and shear, G, moduli using Equations 4.2 and 4.3 respectively. The resin material can then be defined as an isotropic linear elastic material using density, bulk modulus and shear modulus as inputs.

Table 4.3: *HexPly 8552 resin material properties*

Property	**Value**
Density (kg/m^3))	1301
Young's Modulus (GPa)	4.57
Poisson's Ratio	0.37

$$K = \frac{E}{3(1-2\nu)} \tag{4.2}$$

$$G = \frac{E}{2(1+\nu)} \tag{4.3}$$

4.2.2 FEA Mesh Setup

An important consideration when creating FEA models is the mesh set up and resolution. Mesh convergence studies can be utilised to aid the selection of element size. To perform a convergence study, simulations are run for a decreasing box size until there is no change in a measurable output in the derived result. At this point, it can be said that the model has adequately converged to the exact solution. However, as the element size decreases, the computation time and memory requirements increase due to the larger number of elements in the model. Therefore, a compromise is often required between result error and computation demands.

A simple CFRP laminate model, Figure 4.6, was constructed to allow a mesh convergence study to be performed. The model consisted of an 8 ply CFRP laminate, that contained alternate 0° and 90° ply layers, and would simulate a simple pulse-echo immersion inspection. Each ply layer had a thickness of 250 μm and the interply resin layers were 10 μm thick. A 5MHz wavelet signal was was applied through a pressure load across the full model width. Symmetry boundary conditions were applied to either side of the model to simulate an infinite plane wave. The average pressure at the pressure load source was calculated during the simulation to generate an A-scan output. Absorbing boundary conditions were applied to the top and bottom of the model.

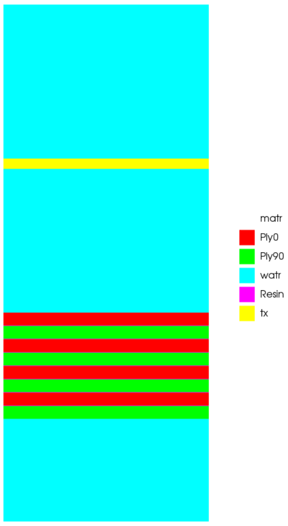

Figure 4.6: *Model used for mesh convergence study*

The FEA model was constructed with *keypoints* at the interface between each material which creates element nodes at this interface. This ensures the layers are positioned and sized correctly and can be utilised to ensure each layer is adequately meshed. However, their use is limited for non-uniform geometries and so would not be applicable for many CFRP component models. For this mesh convergence study, *keypoints* where utilised so that the level of meshing required for the resin layers could be determined.

Typically, the element size utilised in the FEA model is determined by the smallest wavelength in the simulation scenario. It was shown previously in Chapter 3 that 15 elements per wavelength was capable of reproducing experimental behaviour and performance. However, for CFRP components, there is the inclusion of thin interply layers that are often smaller than the element size. Since OnScale utilises low order elements, multiple elements through a layer thickness are often required to capture the stress gradients.

The minimum wavelength was calculated as 0.22 mm using the input drive frequency and the shear velocity of the resin. An input parameter was then used to represent the number of elements per wavelength used in the model. A second input parameter was utilised to set the minimum number of elements through a layer thickness. A mesh convergence study was then conducted with the number of elements per wavelength swept from 15 to 50 in steps of 5, giving an element size that varied between 14.67 μm to 4.4 μm. Another parameter sweep considered the minimum number of elements through every layer thickness, which was swept from 1 to 4 in steps of 1. Figure 4.7 provides images of selected mesh set ups generated in the convergence study.

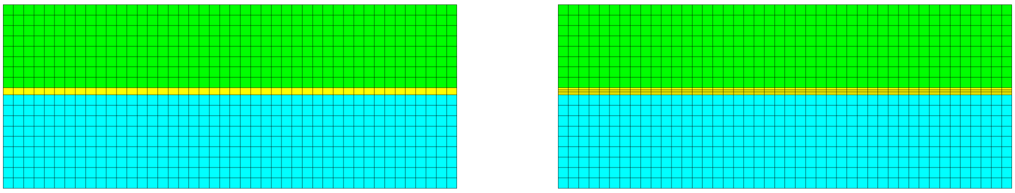

(a) *15 elements per wavelength and 1 minimum element per layer thickness*

(b) *15 elements per wavelength and 4 minimum elements per layer thickness*

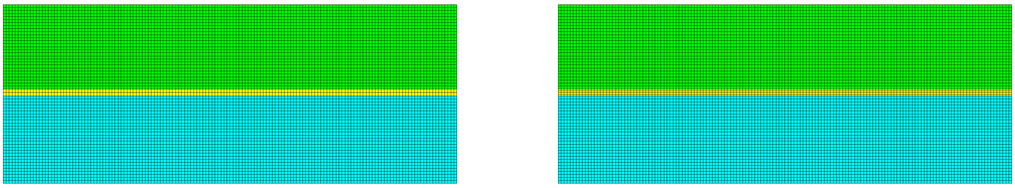

(c) *50 elements per wavelength and 1 minimum element per layer thickness*

(d) *50 elements per wavelength and 4 minimum elements per layer thickness*

Figure 4.7: *Images of various mesh settings for mesh convergency study showing interply resin layer between two ply layers*

To evaluate the mesh convergence, the back wall amplitude would be evaluated for each simulation. A Hilbert function was applied to each FEA derived A-scan before the peak amplitude of the backwall reflection was determined. The backwall amplitudes were normalised to the maximum backwall signal received and then the percentage difference was calculated. The result from this mesh convergence study can be seen in Figure 4.8.

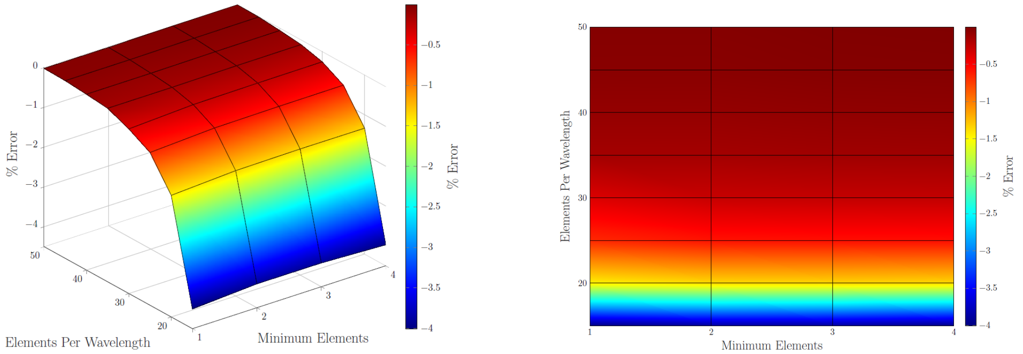

(a) *Parametric surface plot* **(b)** *Minimum elements against elements per wavelength*

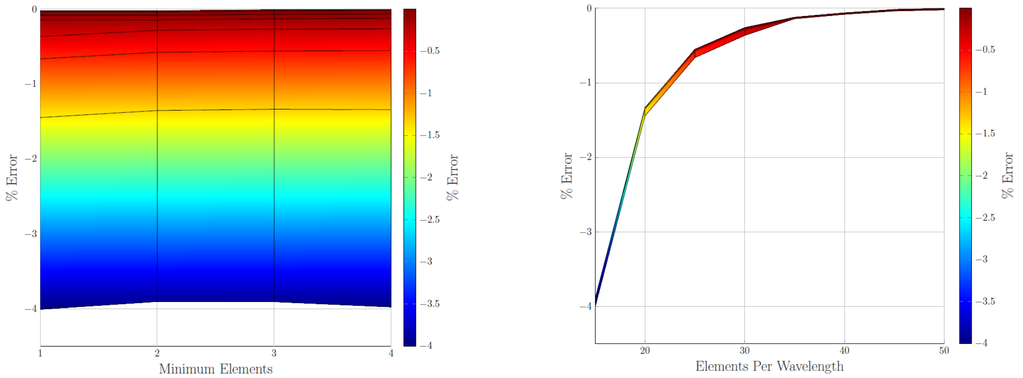

(c) *Minimum elements against percentage error* **(d)** *Elements per wavelength against percentage error*

Figure 4.8: *Mesh convergence study results*

It can be seen as the number of elements per wavelength increase, the result converges as expected. At 20 elements per wavelength, the amplitude of the backwall is within 1.5% of the converged result. The key finding from the mesh convergence study is that the minimum number of elements per layer thickness does not have a major impact on the derived result. This is of benefit as implementing a minimum of only 1 element per thickness is more computationally efficient.

When more than 1 element is required through the resin layer thickness, as well as increase the total number of elements in the model, it also reduces the model timestep.

4.2.3 Material Property Uncertainty

As detailed previously, there can often be an error in the measured material properties of CFRP components as presented in Table 4.2. This creates an uncertainty in the accuracy of the FEA model material properties implemented. To investigate the effect of material property errors, simulated parametric studies were performed where the material property values of the CFRP ply and resin layers were varied. The simulations used the the simple $IM7/8552$ CFRP laminate model from Section 4.2.2.

The first simulation sweep looked at varying the CFRP ply layer and resin layer densities by ±10%, using nominal values of 1570 kg/m^3 ply density, Table 4.1, and 1301 kg/m^3 resin density, Table 4.3. A total of 25 simulations were run to give a step size of 5% for each density. The A-scans generated in the simulations were used to calculate the time of flight by measuring the time between the frontwall and backwall reflections. The amplitude of the front and backwall reflections were also recorded for each simulation as well as the amplitude of the internal interply reflections. All of the generated A-scans can be seen in Figure 4.9.

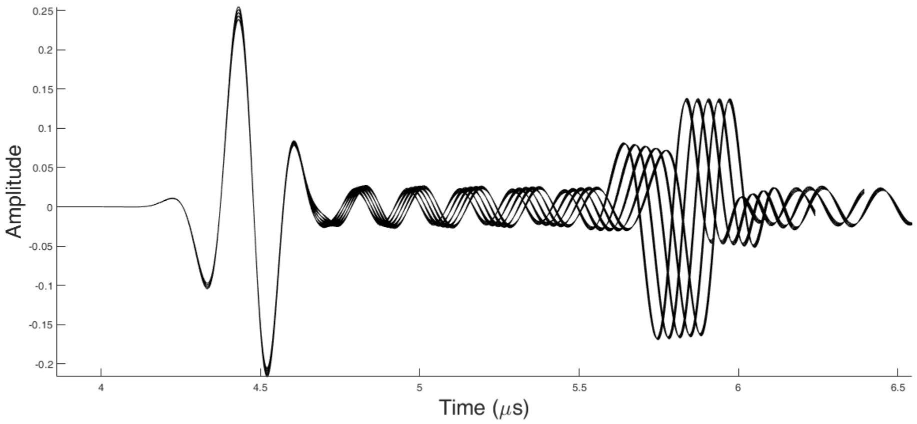

Figure 4.9: *All FEA derived A-scans for varying CFRP ply layer and resin layer densities*

It can be seen from the A-scans that the errors in the material properties have resulted in some differences in the generated A-scans. The frontwall reflections at 4.5 μs are very consistent, however some differences in both time and amplitude can be observed from internal reflections as the ultrasonic wave propagates through the structure. In particular, the backwall reflection is spread between 5.5 - 6 μs. The varying density of the materials results in a change in the acoustic velocity of the material, which explains the time shift in the backwall reflections. The inconsistency of backwall amplitude is a result of a change in the level of reflection at the ply and resin material interfaces. The change in material properties creates different transmission and reflection coefficients at each material interface and so affects the amplitude of the wave as it propagates through the component.

To better understand the effect of varying the density of the materials, Figure 4.10 was created to show the error of the calculated backwall time of flight as a function of the material densities. The error is calculated as the difference from the time of flight recorded using the nominal density values shown in Tables 4.1 and 4.3, and a positive error relates to an increase in calculated time of flight.

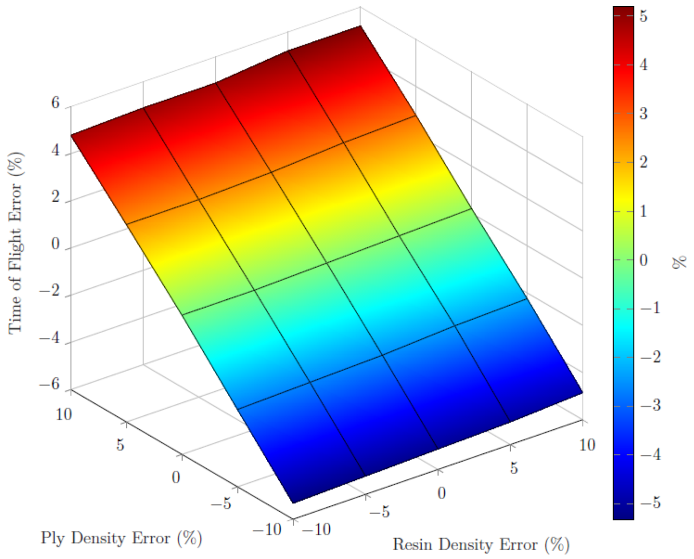

Figure 4.10: *Calculated time of flight error for varying ply and resin densities*

From Figure 4.10, it can be observed that the ply density dominates the time of flight, which is expected as the resin layers only comprise 3.5% of the sample. For both materials, ply and resin, there is a direct correlation between changes in density and resultant time of flight, due to the inverse relationship between material density and acoustic velocity.

The changes in density also affects the amplitude of the signal reflections from the material interfaces. The amplitude of the reflection from the frontwall, resin layers and backwall were extracted from each A-scan and used to calculate the amplitude error, Figure 4.11 The amplitude of the reflections were measured from the maximum instantaneous amplitude of the respected reflection and as previously, the error was calculated using the nominal density values, Tables 4.1 and 4.3.

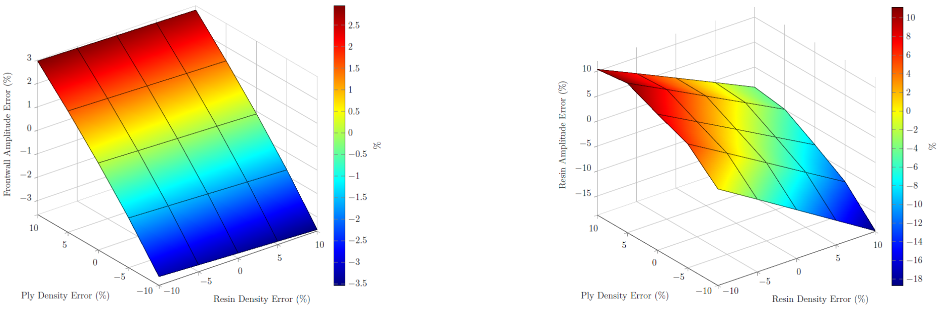

(a) *Frontwall amplitude* **(b)** *Resin layer amplitude*

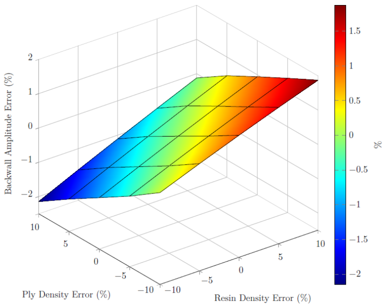

(c) *Backwall amplitude*

Figure 4.11: *Calculated signal reflection amplitude error for varying ply and resin densities*

It can be seen from these graphs that the errors of the CFRP ply and resin densities has resulted in changes in the amplitude of reflected signals. The change in density results in a change in the material impedance and therefore also modifies the reflection and transmission coefficients. The frontwall and backwall reflections have a maximum error between 2 and 3%, while the amplitude of the resin layer reflections can have an error greater than 15%. As expected, the frontwall amplitude is only affected by the CFRP ply layer density variation. The changing levels of reflection and transmission has an impact on the amplitude of the wave as it passes through the component. A larger reflection coefficient for the ply and resin layer interfaces will result in greater attenuation of the wave and reduce the amplitude of the wave encountering the backwall.

Further simulations were conducted to vary the CFRP ply layers out-of-plane elastic modulus, E_{22}, and the resin layers Young's Modulus, E, by ±10%. The out-of-plane elastic modulus of the CFRP ply layer was chosen as with the current simulation set up, it would have a larger impact than the in-plane modulus, E_{11}. Again, a step size of 5% was used for each property to give a total of 25 simulations and the same analysis was conducted on the received A-scans. The effect of material properties can be seen in Figure 4.12 where the error in the calculated time of flight and reflected signal amplitudes are plotted.

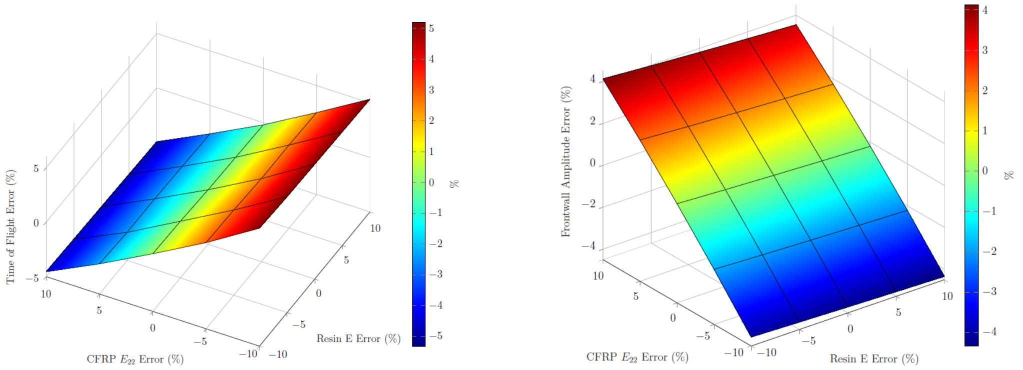

(a) *Time of flight* **(b)** *Frontwall amplitude*

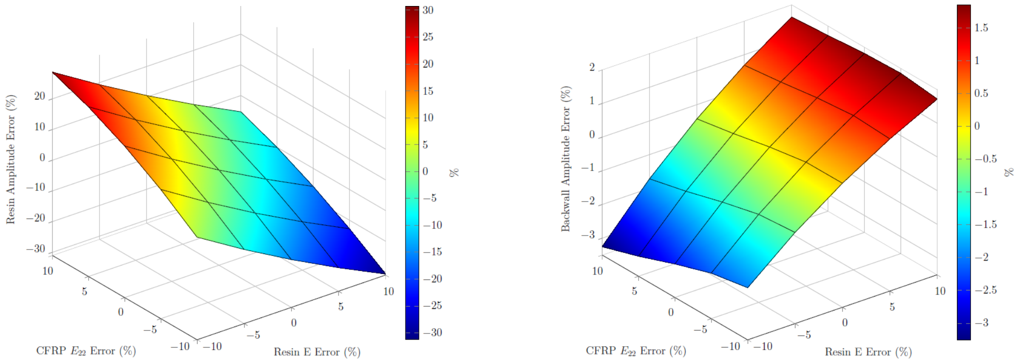

(c) *Resin layer amplitude* **(d)** *Backwall amplitude*

Figure 4.12: *Calculated time of flight and signal reflection amplitude error for varying CFRP ply out-of-plane elastic modulus and the resin layers Young's Modulus values*

Once again it can be seen that the changes in material properties has resulted in some error in the calculated time of flight and reflected signal amplitudes. The time of flight error is dominated by the ply E_{22} changes as the CFRP ply layers make up the majority of the sample thickness. As with the previous parametric study, the frontwall amplitude is only impacted by changes in the CFRP E_{22} changes. Also, a higher amplitude resin reflection leads to a greater attenuation through the sample and so results in a smaller amplitude backwall signal. It can be seen that with this parametric sweep of material properties, the amplitude of the resin layer reflections is the most sensitive to these changes in material elastic properties.

Overall, these simulations have demonstrated the ability of modelling to investigate the effect of material property variance and determine their impact on derived results. The material properties of manufactured composite components are affected by many factors including the age of the prepreg material, the curing conditions and the level of compaction [112]. This means the material properties acquired from a component by conducting experimental tests, will not be exactly the same as another as-manufactured component. The variation of ply and resin layer density had negligible effects on signal amplitude but due to the change of acoustic velocity, does impact the signals time of flight. In practice, error in time of flight can be accounted for through the use of appropriate scaling and so accuracy in ply and resin density is not significantly important. However, the variance in the ply's transverse stiffness, E_{22}, and resin Young's modulus has been shown to have a notable impact on the amplitude of reflected signals, where 10% error can lead to up to 30% error in resin layer amplitude. Therefore, these material properties are important to get correct in the FEA model as they directly impact the reflection coefficient of the resin layer and will develop the phononic band gap at a different rate, which will result in the first phase singularity occurring at a different depth.

4.2.4 Scripted FEA Input File

4.2.4.1 Overview of Approach

FEA models can be constructed in OnScale by using a coded script containing appropriate syntax. This approach is easy to use and is very flexible, allowing for greater control of simulation conditions and the ability to set up batch simulations to perform parametric studies. Using code also makes debugging simpler and can be readily edited and executed. However, using scripted code can be a limiting factor for complex geometries as the main method of constructing the model geometry is through the definition of a range of simple geometric shapes.

An example where using written code for CFRP wave propagation models is advantageous is a planar laminate geometry. The ply layers and inter ply resin layers for a planar laminate can easily be defined as rectangle or cuboid shapes. The code can incorporate a series of “do loops” in order to generate the geometry, into which the user can provide an input variable for the number of plies in the sample. The thickness of the ply layers and resin layers could also be variables, giving the user more inputs that could be varied in a batch simulation to test laminate designs or different inspection scenarios.

4.2.4.2 Method Development

The first step when creating a script input file is to define all the variables in the model. These can include details on the component geometry, such as the number of plies and their dimensions. It is also important to define the set up of the model mesh. This is typically determined by the smallest wavelength of interest in the model, however for these thin layered components it is often beneficial to set the mesh size as a factor of layer thickness. In scripting, this can be easily done and the element size can be set as a factor of either the ply or resin layer thickness.

The material properties for the CFRP are defined as described in the previous Section and then local coordinate systems are generated for the ply layer orientations. The local coordinate rotations can be manually defined or acquired from an external file containing the ply orientations. The CFRP material definition can be copied to a new material name, such as *CFRP0* for 0° orientated plies, and then assigned to the relevant local coordinate system to correctly transform the material properties for that ply layer.

The CFRP ply layers and the interply resin layers can be generated by creating rectangle or cuboid shapes. The full laminate structure can be produced by using a loop to generate all the layers. In the loop, the position and size of each layer can be determined from the thickness of the ply layers and the location of the previous layer. When generating the primitive shapes, the material name is assigned to the shape and can allow for different laminate layups to be constructed.

4.2.4.3 CFRP Laminate Geometry Example

To illustrate the scripting approach of generating FEA models of CFRP models, a simple planar laminate example is used. The CFRP laminate consisted of 8 ply layers with a lay up of $[0/\pm45/90]_s$ and a layer of resin between each ply. The laminate was 10 mm square with 125 μm ply layers and 10 μm interply resin layers generating an overall sample thickness of 1.07 mm. A 2D FEA model was initially generated using the scripting method described in Section 4.2.4. The mesh of the model was constructed using *keypoints* as discussed in Section 4.2.2 to allow the element size to be defined by the minimum wavelength in the simulation and ensure a minimum of 1 element through a layer thickness.

Four local axes were created to represent the $0°$, $45°$, $-45°$ and $90°$ in-plane rotations of the ply layers. This was achieved by defining the local axes as a rotation of the global axes around its y axis. The CFRP material defined was then copied four times to give material names *CFRP0*, *CFRP45*, *CFRP45n* and *CFRP90* which represent the four in-plane ply orientations. The ply layer material definitions were then oriented to its local axis to transform its material properties. The 2D model generated geometry can be seen in Figure 4.13 which includes an expanded view to show the thin interply layers.

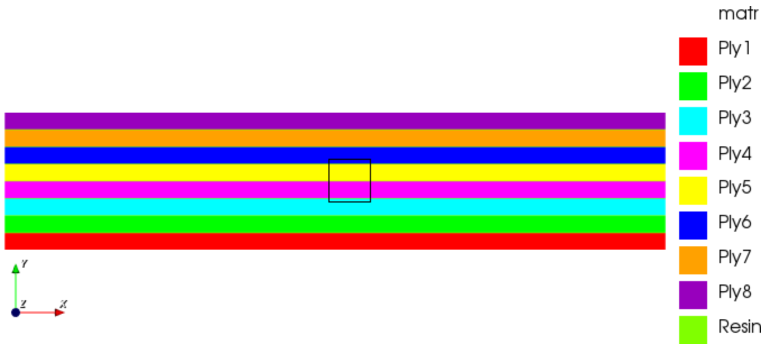

(a) *2D FEA model geometry with indication of close up region*

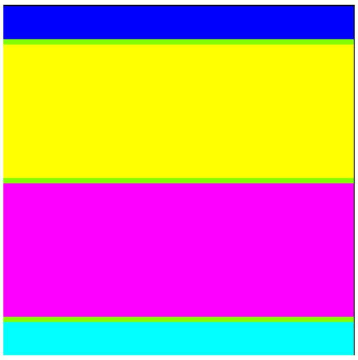

(b) *Close up image to view thin interply resin layers*

Figure 4.13: *2D FEA model geometry of planar laminate generated with a script*

The model was then extended to 3D, as in Figure 4.14, by including in the Z dimensions in the model set up. Since the component geometry is consistent in the Z dimension, the change from 2D to 3D (and vice versa) requires only a few modifications to the script. This allows for model set up, validation and optimisation to be done in 2D before extending to the more computationally intensive 3D models.

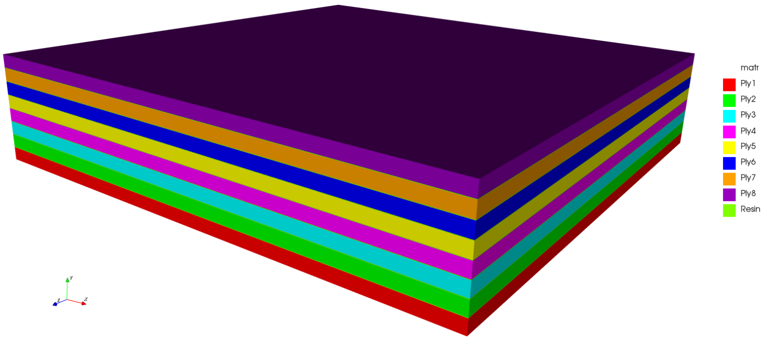

Figure 4.14: *3D FEA model geometry of planar laminate generated with a script*

4.2.5 Importing from Table File

4.2.5.1 Overview of Approach

Advances in FEA modelling led to the development of the ability to generate complex model geometries through the importation of component specifications that have been created using CAD. The output from the CAD software in the form of a STEP file can be readily employed to interface between CAD and the FEA modelling suite. However, for this research the generation of CAD files is not suitable due to the requirement to include the individual ply and resin layers of the CFRP structures, as well as any waviness or woven layers. A similar method available in OnScale facilitates importing table files.

A table file allows for externally created geometries to be read into the FEA model to allow for complex geometries to be created. The table file contains three vectors which represent the x, y and z node locations, which create grid coordinates, and material properties are assigned to each element in the grid. The material names in the table file are defined in the FEA model file and when the table file is read into the model, the materials contained in the table grid are interpreted onto the model grid. The table file is 3D but can be used for 2D models by selecting a slice of the table file grid to be used in the model. More details on the structure of OnScale table files can be seen in Appendix A.

Table files can be manually constructed through knowledge of the structure geometry or with the aid of specific composite material software packages capable of constructing textile structures. This research will use TexGen [128], which offers the ability to export voxel files containing information on the textile geometry and fibre orientation. This information can be manipulated to a table file and imported into a FEA model to recreate the component geometry and fibre orientations.

4.2.5.2 Method Development

Textiles can be created in TexGen in different ways. The GUI allows for blank textiles to be created and individual yarns to be added and manipulated to correct size and position. Wizards exist to allow for both 2D and 3D weaves to be readily created. These wizards are very easy to use and can be used to create different woven textile geometries. A more advanced method of creating textiles is through the use of python scripts. Python is an open source programming language which has been embedded into TexGen allowing for the scripts to be run from the GUI. These scripts can be used to easily access the entire functionality of TexGen.

Once a textile has been constructed in TexGen, there is the option to export to an Abaqus voxel file. This has been specifically designed to allow for the constructed textiles to be simulated in the Abaqus FEA software package. This output process generates three different files:

- '.inp' file containing the nodal locations, element types and associated nodes, boundary conditions, load cases and material definitions
- '.eld' file containing the element data including: yarn index, location, volume fraction and distance from the surface of yarn
- '.ori' file containing the yarn orientation vectors

The format of the voxel file is similar to what is required to include in a native OnScale table file which can be used to define a component geometry in the first stage of modelling in the OnScale FEA suite. A Matlab script was developed to read in the TexGen output voxel file data and translate it into a table file format. The orientation data output can also be utilised to allow for the table file to recreate the textile geometry and fibre orientations. To achieve this, multiple material names are created to represent different orientations of each yarn or ply layer. Once a table file has been generated, it can be read into the FEA input file to generate the geometry.

4.2.5.3 CFRP Laminate Containing Waviness Example

The benefits of using TexGen is the ability to easily include more complex CFRP geometries which would be difficult to generate through scripting. An example of this is a planar CFRP laminate containing waviness, which can occur during the manufacturing process and can reduce the strength of the laminate. The laminate dimensions and layup, Section 4.2.4.3 , were used to create a textile in TexGen. Using the GUI, the ply layers of the laminate were manually modified to incorporate ply waviness, as shown in Figure 4.15. The TexGen textile was then exported as an Abaqus voxel file, which was then converted into a table file.

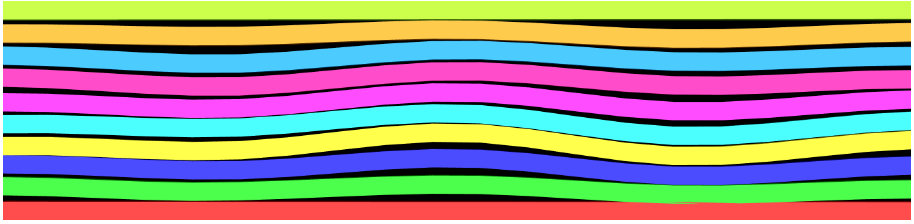

Figure 4.15: *Planar laminate containing out-of-plane ply waviness generated in TexGen*

The FEA input model was generated to create a 2D mesh with overall dimensions equal to that of the laminate height and width. For this example, the mesh is created without *keypoints*, Section 4.2.2, as the layers are not uniform and the geometry is read in from a table file. Instead, a structured rectilinear mesh is generated with an element size equal to one third of the resin thickness of 10 μm. This reduced element size is required to accommodate the spatial variance of the interply resin layers and ensure they are appropriately meshed at each point in the model.

The material properties for both the ply and resin layers were input in a similar method to the scripting method, however additional materials were defined. These additional materials were used to represent the different out-of-plane orientations of the ply layers. The material names were 'Ply' followed by a number representing the ply layer number and a second number representing the out-of-plane orientation. For example: Ply1.0 represents the first ply layer with an out-of-plane angle of 0°; Ply1.1 represents the first ply layer with an out-of-plane angle of 1°; Ply1.-1 represents the first ply layer with an out-of-plane angle of $-1°$. This is continued for subsequent out-of-plane angles and repeated for all remaining ply layers.

The table file containing the CFRP laminate with ply waviness was then read into the input file and positioned at the origin, resulting in the model geometry as shown in Figure 4.16 (a). In this model plot, each unique material is shown in a different colour to illustrate that the out-of-plane orientation of the ply layers is accounted for. It is also possible to plot the model geometry with the materials for each ply layer combined together, Figure 4.16 (b).

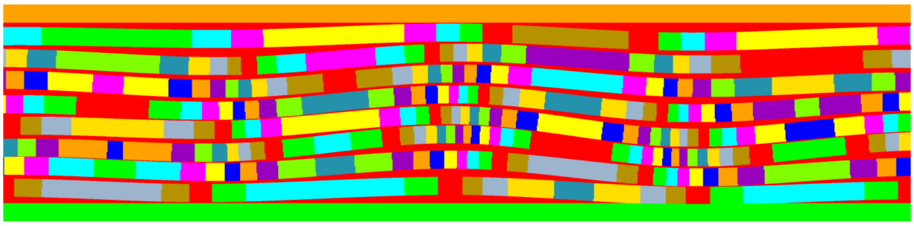

(a) *Plot of all unique materials*

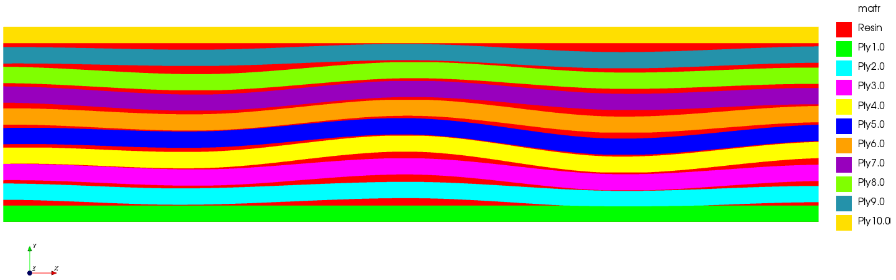

(b) *Plot with individual ply materials combined*

Figure 4.16: *2D FEA model geometry of planar laminate containing out-of-plane waviness generated from TexGen output*

4.2.5.4 2D Woven CFRP Structure example

The wizards in TexGen provide the capability for the creation of complex 2D and 3D woven textiles. The process of generating FEA models from TexGen allows for these complex woven textiles to be imported into the model. The generated model will not only have the complex geometry but will also account for the different material properties of each yarn due to the variances in orientation.

The process of creating the FEA model is the same as the previous example - the input file is set up with the required dimensions, the mesh resolution is set and materials are generated, including the different orientations of CFRP yarns or ply layers. The mesh of the FEA model was set to the same dimensions as the output voxel file from TexGen. It is important that this mesh resolution is set to an appropriate size to capture the required geometrical information. The table file generated from the exported TexGen file can then be imported into the FEA model and positioned and scaled accordingly. For structures that have repetition, a single table file of the repeating section can be generated and read in multiple times or copied in the FEA model.

An example 2D woven structure was created in TexGen, as shown in Figure 4.17, to import into a FEA model. The resultant model geometry is shown in Figure 4.18(a) where the geometry has been plotted to show all the materials that represent the warp and the weft yarns of the woven material. In addition, Figure 4.18(b) depicts the FEA model of the woven fabric with the materials that comprise each section of warp and weft unified to a single colour to aid identification.

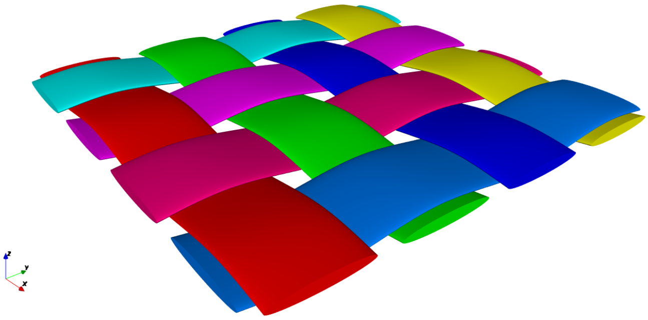

Figure 4.17: *2D woven structure generated in TexGen*

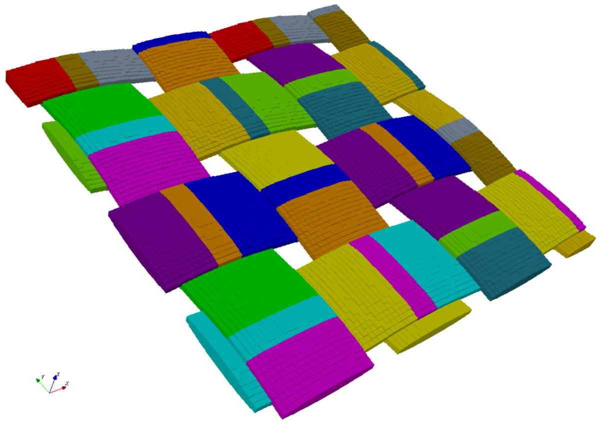

(a) *Plot of all unique materials*

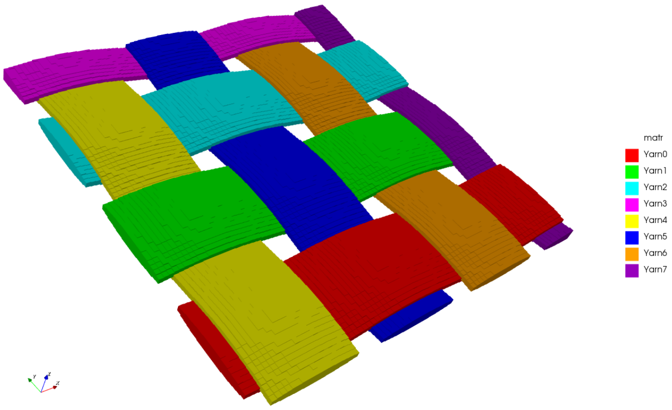

(b) *Plot with individual yarn materials combined*

Figure 4.18: *3D FEA model geometry of woven structure generated in TexGen*

4.2.6 Generation from Plybook

4.2.6.1 Overview of Approach

Tapered CFRP components are typically described using what is known as a ‘plybook’. The plybook contains an ordered list of the plies contained in the component, along with information on each ply including its length and orientation. The ability to generate FEA models from a plybook, to allow for wave propagation simulations to be performed, would allow for inspection scenarios for different taper geometries to be assessed and evaluated in software without the need for expensive and time consuming fabrication. This would identify specimens that would suffer from poor coverage in particular locations and allow engineers to consider component inspectability as part of the design process. This can be achieved through importing a table file generated from the plybook information, containing information on both the geometry and the fibre orientation of each ply layer. This becomes essential in tapered components where ply layers can have significant changes in their out-of-plane orientation which will have an effect on their material properties, the associated wave propagation and the interply transmission and reflection coefficients, potentially highlighting cases where mode conversion could arise.

4.2.6.2 Method Development

The generation of tapered CFRP components in FEA models is more suited to a CAD or table file import due to the variation of the individual ply layers. For wave propagation FEA models, the out-of-plane orientation of the ply layers is important to include, as the variation of fibre angles will change the material properties which in turn will effect how waves interact with the ply layers. As with the previous Section, a CAD file would be difficult and time consuming to generate due to the internal ply layer structure. However, importing of a table file can be adopted as a suitable solution to generate a FEA model of the tapered CFRP geometry and include variations of material properties due to fibre orientation.

The table file can be generated manually in Matlab or Python but for this work, TexGen would again be used as an intermediate stage. In order to generate a python script to generate a TexGen structure of a taper, the coordinates of each of the ply layers are required. This can be achieved through the use of a Matlab script which imports the data from the taper plybook. The plybook contains the location of where each ply terminates along the overall sample length, which gives the horizontal position of a ply drop. The vertical position of a ply drop will be dependant on the thickness of the sample at that location, which is determined by how many plies above or below, depending on whether the planar surface of the taper is the top or bottom, have been terminated. If an ideal tapered CFRP component geometry is considered, where the ply layers are uniform and perfectly planar (except at ply drop locations), the location of vertical location of each ply layer can be determined across the taper length. This is done by assuming when a ply is terminated, the ply above or below moves to the vertical position of the terminated ply. Using this assumption, the coordinates of the centreline of each ply layer can be determined and input into a TexGen python script.

Once a TexGen python script has been created to generate the tapered structure, the process of generating an FEA model becomes the same as previous examples. The python script can be run in TexGen to generate the structure before exporting as an Abaqus voxel file. The generated files can be converted to a table file and imported into the FEA input file which can be set up to incorporate the changes in material properties due to fibre orientation.

4.2.6.3 Tapered CFRP Component Example

A simple example plybook was created at a comma-separated value (CSV) file containing the information in Table 4.4. In this plybook the first column is the ply number starting with the top horizontal ply layer, the second column is the ply length in *mm* and the third column is the ply layer orientation in degrees. In this scenario, the ply length corresponds to the horizontal distance of the ply layer measured from a common location. The plybook was imported into Matlab and a TexGen python script was generated. The TexGen script generated a textile of the Taper, Figure 4.19, which could be exported and converted into a table file.

Table 4.4: *Plybook CSV File Containing Ply Names, Ply Lengths and Ply Orientation Angle*

Ply Name	**Ply Length (mm)**	**Ply Orientation (°)**
Ply1	50	0
Ply2	22	45
Ply3	50	90
Ply4	26	-45
Ply5	50	0
Ply6	28	-45
Ply7	50	90
Ply8	24	45
Ply9	50	0

Figure 4.19: *TexGen taper structure generated from plybook details contained in Table 4.4, where the top red ply is Ply1*

The FEA model was set up to the required dimensions of the table file and the element size was set to the same size as the table file resolution. The materials required to represent each ply layer and its orientations were generated. The table file was then imported and positioned in the FEA model and produced the geometry as illustrated in Figure 4.20. The FEA model geometry is shown with all unique materials plotted as well as individual ply layers combined.

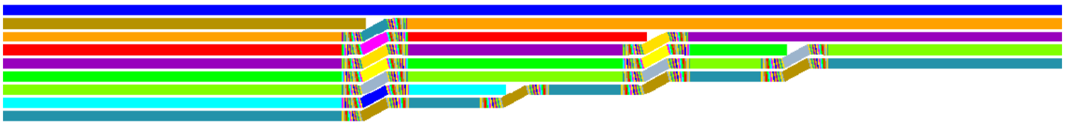

(a) *Plot of all unique materials*

(b) *Plot with individual ply layer materials combined*

Figure 4.20: *2D FEA model geometry of taper structure generated from plybook*

4.3 Discussion

Commonly the main challenge for FEA wave propagation problems is computational demand in terms of simulation time and memory requirements. For simulating wave propagation in CFRP structures there is an increased computation demand created due to the small element size required for adequately meshing the thin resin layers. However with computing power increasing and solutions available to run larger models in a reduced time frame, such as MPI and cloud computing, the computational demand is not the most significant challenge. Instead, the bigger challenge for CFRP modelling is the generation of the geometry and correctly assigning material properties. It is important this challenge is addressed due to the geometry representation and material properties being two of the biggest influences on the accuracy of FEA derived results.

Provided the FEA software used and its implementation is valid, discrepancies between FEA derived results and experiments are most likely due to differences in material properties and/or approximations in the geometry. CFRP materials contain complex geometry structures and material properties, which makes them challenging for FEA wave propagation problems. The flexibility of FEA modelling means there are several methods available to create the model geometry. This includes scripting and the importation of CAD or table files. Each technique can provide an advantage over others for certain scenarios or model requirements.

Scripting models in OnScale allows for models to be set up and easily modified to test different structures or geometries. User defined inputs can be established to modify the model geometry, such as the number of plies in the CFRP component, and this allows for quick and easy comparisons to be made. Variable inputs can also be used to set up batch simulations, which allows for a series of models for various scenarios to be run sequentially.

Typically for ultrasonic wave propagation FEA simulations, the element size is determined by the wavelength of interest, however for CFRP simulations, the element size is often determined by the thin ply and resin layers in the component. Depending on the modelling scenario, the element size implemented in the FEA model will be the smallest of the element size determined by the wavelength of interest and the element size required to model the thin geometry layers. If the component contains features such as ply waviness that creates changes in the resin layers, an element size smaller than the resin layer thickness may be required to capture the subtle variation in component geometry. The requirement to capture these small variations is dependent on the acoustic wavelength in the model, as if the variations is sub-wavelength, they may not impact the wave behaviour. Reducing the element size can greatly increase the computation requirement, therefore, it is often good practice to perform a mesh convergence study, such as that in Section 4.2.2, where simulations are performed to determine an element size that provides sufficient accuracy but is not too computationally demanding. The meshing of scripted OnScale models can be easily defined and ensures the level of meshing is adequate.

While the benefits of being easy to set up a scripted model for a planar laminate CFRP is attractive, the ideal geometry created is not very representative of practical configurations. The approach assumes each ply layer is planar and there are no variations in material properties spatially. Due to the variability in the manufacturing process, it is highly unlikely that planar CFRP components will be perfectly planar and have uniform ply and resin layer thickness. Meinzakowski et al [98] illustrated that analytically modelling through thickness inspections of uniformly planer laminates with regular ply layer thickness's, produces more regular interply resonances than in practice. In order to compensate, the authors added a randomness to the ply layers and found this improved performance. This solution could be adapted and easily utilised in OnScale scripted models to improve the representation of experimental behaviour.

Scripting CFRP components is also limited to planar and uniform CFRP components due to the difficulty to construct complex geometries. Geometry is constructed using primitive shapes and so the generation of highly detailed CFRP components to include waviness or woven structures becomes extremely complex and difficult.

Generating models in OnScale from table files is an effective method for creating complex geometry CFRP structures. Once the table file is generated, it can be imported ino the FEA model to the desired location. The table file can be generated manually or from an external data source to contain details of the complex geometry and fibre orientation. This allows for the complex structure and material properties of CFRP structures to be fully represented in a FEA model. TexGen has been specifically developed for the generation of textile structures and allows for various 2D and 3D structures to be generated. Converting the exported data into a table file suitable to be read into a FEA model gives an excellent method of creating complex CFRP structures in an FEA model. Another advantage of utilising the exported TexGen data is the ability to include the fibre orientation changes and adjust the material properties in the FEA model accordingly.

The TexGen software is easy to use and offers the ability to create and modify a CFRP structure using its GUI or through a selection of wizards available for generating woven structures. This allows for complex geometries to be created but a possible drawback is that the created structures are not representative of real structures. However, with the ability to create TexGen structures with a python script, it is possible to create structures based on real components. For CFRP laminates, if the individual ply layers locations can be determined from a cross section image of the component, a python script could be constructed to create a 2D TexGen structure based on the real component. This could be extended to 3D if the ply layer locations are known in the third dimension but this would require volumetric information of the real component.

The generation of a table file could also be done without the requirement of a software package like TexGen. Provided details on the CFRP component is known, such as location of ply layers, or can be determined from a photomicrograph or X-Ray CT data, a table file could manually be generated in a software package like Matlab or Python. This would remove the intermediate step and reduce the time to set up the FEA model as less time will be spent producing data from TexGen, which can become time consuming for large parts or when a high resolution is required.

The drawback of using a table file to generate the FEA model geometry is the increased complexity to produce and the requirement to generate a new file for any geometry changes. To investigate the performance of different component geometries, multiple unique table files need to be generated, which makes it more time consuming.

Generating FEA models of tapered CFRP components is challenging due to the anisotropic material properties and complex geometry. The approach described in Section 4.2.6 to overcome this challenge was based on creating the FEA model geometry from a plybook. This allowed for the complex model geometry to be created from a simple and easy to create plybook. The use of TexGen as an intermediate stage in the approach allowed for the fibre orientations to be considered when generating the FEA model materials to ensure the correct material properties are used, which is essential when considering tapered structures.

The approach presented is beneficial as it only requires a very simple CSV file containing the individual ply layers length and orientation. This input can easily be created to allow for different CFRP taper designs to be used in FEA models. However, the resulting geometry contains perfectly planar and uniform ply and resin layers which is not fully representative of real manufactured components. This is a similar drawback to creating FEA models of planar laminates with a scripting approach, which could be improved with varying each ply layer thickness.

Each of the approaches presented can generate FEA models of CFRP components from their design specifications. This leads to the modelled geometry being idealised, often with perfectly planar and uniform ply and resin layers. While this is not perfectly representative of the real component configuration, in many cases it will still provide a usable prediction of experimental performance. For more representative models, it is possible to generate FEA model geometries based on real components. A cross-sectional image from a photomicrograph or X-Ray CT data could be utilised to determine ply layers locations and generate a table file based on this information. This table file can then be imported and the generated FEA model geometry will be more representative of the real component. Both of these approaches will be performed later in this Thesis.

The selection of which approach to implement is dependent upon the required modelling scenario and the information available on the sample. For unidirectional laminates, the FEA geometry can be created 'as designed', from either design specifications, or 'as built', using an image of the samples cross-section. While the 'as built' provides an accurate representation, it is based on a single cross-section of the component and is unsuitable to model alternative component designs. The 'as designed' geometry can be constructed to include ply wrinkles or ply drops and can provide a method to create models of various component designs for testing. For woven components, the generation of the more complex geometry from images becomes more challenging and so the use of textile modelling software is the most suitable approach.

4.4 Conclusion

This Chapter has outlined the challenges of creating FEA wave propagation models of CFRP structures and proposed suitable solutions to achieve accurate models. The requirement of accurately representing the model geometry and correctly applying the correct material properties is important to ensure derived FEA results are accurate. This becomes challenging for CFRP structures due to their complex micro-structure and varying material properties. All of the developed methods in this Chapter will be utilised in the subsequent Chapters where NDE inspections of CFRP structures are simulated.

Chapter 5

FEA Simulations to Optimise Characterisation of a CFRP Laminate

In this Chapter, simulations are conducted to investigate the immersion pulse-echo B-scan inspection of a planar CFRP laminate plate consisting of unidirectional layers sandwiched between 2/2 twill layers on the top and bottom. A parametric study is utilised to investigate the effect of transducer frequency and focal length on the inspection's ability to characterise the CFRP component and demonstrate the benefit of modelling for optimisation of the experimental parameters.. Both 2D and 3D FEA models are used along with different approaches for constructing the model geometry. The FEA derived B-scans and their instantaneous parameters are analysed to determine inspection performance and results are compared with experimentally collected data.

5.1 Introduction

5.1.1 Motivation

A benefit of simulation is the ability to quickly evaluate and optimise inspection performance. Through the use of valid FEA models, parametric studies can be conducted to investigate optimum inspection parameters for a particular component or inspection scenario. This model driven approach offers both time and cost savings when compared to practically manufacturing components for testing or experimentally testing multiple inspection scenarios.

Chapter 3 has validated the general modelling approach utilised in this Thesis and methods of generating FEA models of CFRP components have also been outlined in Chapter 4. In this Chapter, a parametric study will be conducted to investigate the effect of transducer frequency and focal length when inspecting a CFRP laminate containing a woven top and bottom layer. Models are generated in both 2D and 3D to replicate an experimental configuration and will use different approaches to create the model geometry.

It is important that new modelling approaches are validated against experimental data to ensure the derived results from simulations are justified. Correct FEA set up is essential as any inaccuracies will result in imprecise derived simulation results. As discussed in Chapter 4, CFRP materials pose challenges in both geometry, due to its complex internal microstructure, and the inherent and varying, anisotropy of the ply layers within the component. Experimental data is collected to allow for the models to be validated through comparison of experimental and FEA derived results.

5.1.2 Method of Investigation

For this inspection scenario, the test component is a planar CFRP laminate consisting of unidirectional layers sandwiched between 2/2 twill top and bottom layers. A B-scan immersion inspection, with a linear step size of 0.2 mm, was performed using a focused single element transducer. The transducer was focused at the mid-plane of the CFRP sample and simulations were utilised to investigate the effect of transducer frequency and focal length on the ability to inspect and characterise the sample. The derived FEA model results are then validated through corroboration with experimentally collected data sets.

Initial 2D models were utilised for their computational efficiency to perform a parametric study to look at the effect changing the focused transducer frequency and focal length has on the inspection performance. The different frequencies selected for the parametric studies were selected to match the resonance frequency of the component and transducers available to collect experimental data for comparison. These initial models utilised the scripting approach described in Section 4.2.3 to generate the geometry of the unidirectional layers, while importing a table file for the top and bottom twill layers. This generates a FEA model based on the component design information and is straightforward to set up and can allow for different component designs to be quickly evaluated.

The FEA models generate A-scan signals for each transducer location which can then be combined to generate a B-scan image for each inspection. To further investigate the inspection performance at characterising the component structure, the instantaneous parameters of the signal (amplitude, phase and frequency) were analysed. These parameters can be calculated from the analytical signal and offer improved analysis of the structure and can be utilised to track ply layers and identify ply layer orientation [93, 94, 114, 137]. The analytical signal, $x_a(t)$, can be represented as the complex expression presented in Equation 5.1 [137].

$$x_a(t) = A(t)e^{i\phi(t)} \tag{5.1}$$

Where $A(t)$ is the instantaneous amplitude, which is calculated from the magnitude of the measured signal and $\phi(t)$ is the instantaneous phase which is calculated from the imaginary part of the signal after applying a Hilbert transform to the real part. The instantaneous frequency can then be calculated as the rate of change of phase with respect to time, Equation 5.2 [137].

$$f(t) = \frac{1}{2\pi}\frac{\partial\phi}{\partial t} \tag{5.2}$$

After the parametric study had investigated the effect of transducer frequency and focal length, further simulations were performed using a 3D model geometry. The extension to a 3D model makes the simulations more computationally demanding but provides a more accurate representation of the woven structure in the model geometry.

Finally, simulations were performed using an alternative approach for creating the model geometry. This second approach replaces the scripting for the unidirectional layers with a more representative table file generated from a photomicrograph of the laminate cross-section. This is a more time-consuming approach with additional resource required to capture and implement the information from the sample cross-section, but does offer a more representative model geometry based on the built component structure. However, this is limited to the imaged section of the component which may not be representative of the complete structure or component built with the same specifications.

5.2 FEA Model Development

5.2.1 Sample Overview

The test sample used in this Section of work was a flat CFRP laminate as shown in Figure 5.1. This laminate comprised of a woven 2/2 twill top and bottom layer, with 23 unidirectional layers in between. The sample material system was a *HTS40/977-2* carbon fibre epoxy pre-impregnated (prepreg) tape. The prepreg is comprised of *Tenax HTS40* fibres impregnated with *Cycom 977-2* epoxy resin. The carbon fibres are unidirectional with high tensile strength and are standard modulus aerospace grade [138]. The epoxy resin system is a typical high temperature curing aerospace grade system [139] which is used in modern aircraft construction such as Boeing 787 and Airbus A380 [140].

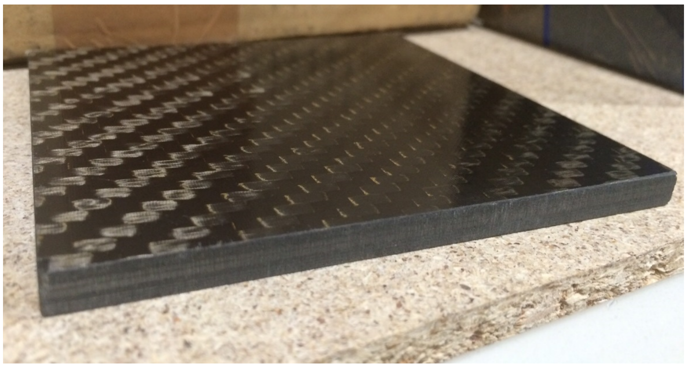

Figure 5.1: *Photograph of flat CFRP sample*

The laminate sample was 100 mm square and it had an average measured thickness of 6.2 ± 0.1 mm. The thickness of the twill layers, unidirectional layers and resin layers would be measured from the photomicrograph, as will be described in Section 5.2.2.1. To determine the orientation of the unidirectional plies, an X-Ray Computed Tomography (CT) scan was performed on the sample. More information of the X-Ray CT scans will be given in Section 5.2.2.2.

5.2.2 Sample Imaging

In order to generate a more representative FEA model that is based on the actual component geometry, detailed information of the sample structure is required. In order to obtain this information, detailed micrograph images or X-Ray CT scan data of the sample are required to view the component microstructure.

Micrograph or photomicrograph images of the sample cross-section is an effective approach to view each individual layer of the composite sample and how it varies across the sample cross-section. High resolution micrographs are capable of resolving individual fibres in the ply layers, which can allow for the fibre volume fraction to be evaluated [141]. Microscopic analysis is also an effective method of investigating the level of porosity and void content in a CFRP sample [142]. However, this approach can only provide details on the cross-section of the sample and not provide volumetric information. It is possible to generate volumetric information from micrographs by repeated imaging and polishing but this is a destructive and time consuming approach.

A more suitable approach to obtaining volumetric information of composite materials is the use of X-Ray CT scans. These scans are capable of providing 3D characterisation of composite structures and can also be utilised to generate FEA models [143]. However, X-Ray CT is often limited to small components, or sections due to the high resolution required to resolve the fibre layers [3]. Another challenge for imaging the component structure is the similarity in the atomic number of the composite fibres and the resin, which makes distinguishing between each material difficult [93].

In this work, both micrograph imaging and X-Ray CT scans were performed on the test sample to gain a deeper understanding of the component and evaluate each imaging technique. Photomicrograph images were taken of the sample cross-section which could then be used to build a more representative 2D FEA model geometry based on the components actual geometry. X-Ray CT scans were also conducted on a small section of the sample to provide volumetric information and view the ply layer orientations.

5.2.2.1 Microscopy

In order to facilitate microscopy, a sample was cut from the CFRP laminate. An exposed edge of the sample was then manually prepared using 1 μm lapping powder to produce a polished finish to the cross-section of the laminate. This would allow for the fine detail of the sample structure to be observed in microscopic images.

The polished edge of the sample was placed under a microscope with a camera operated using ToupView Software (ToupTek). This allowed for the microstructure of the sample to be viewed and for images to be saved. Figure 5.2 is an example image of the detail that can be seen from the microscope. As well as seeing the different ply layers, it is also possible to view individual fibres. From this image, it is not possible to differentiate between 45° and $-45°$ orientations as their fibre cross sections and colour shade are identical.

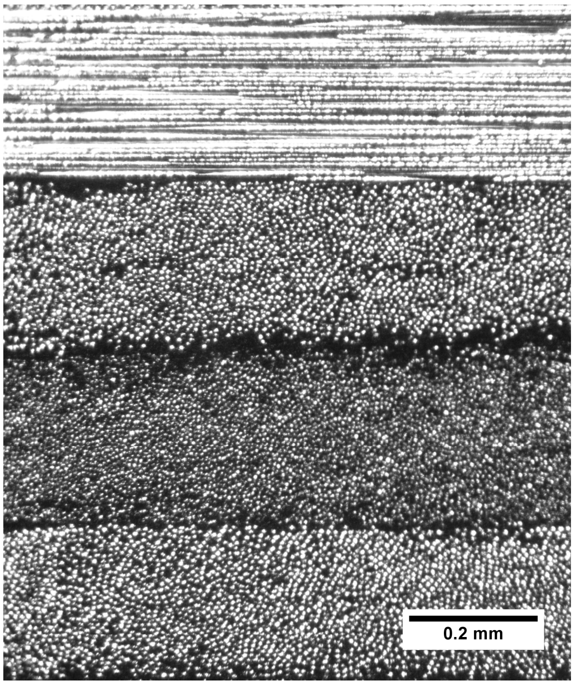

Figure 5.2: *Section of an individual microscopic image of composite sample showing (top to bottom)* 0°, (±)45°, 90° *and* (±)45° *ply layer orientations*

It is clear from Figure 5.2 that a single microscope image of the fibre orientations of the layers can be used to identify the individual layers and orientations. However, such single images only represent a snap shot of the sample, with the maximum imaged area from the microscopic images only approximately 2 mm x 3 mm. In order for optical microscopy to offer more utility in the current context, an image-stitching algorithm was employed in order to generate larger images of the sample cross-section. An example of this is shown in Figure 5.3 where several microscopic images have been stitched together. This gives an entire image through the thickness of a cross-section of the sample with a high level of detail.

Using the microscopic images, the thickness of the individual plies of the composite could be measured. The thickness of the top and bottom 2/2 Twill layers was measured to be 360 μm. The unidirectional plies in between had a thickness of 230 μm with approximately 10 μm thick resin layers in between. These measurements would be used when generating the sample geometry in the FEA model based on the sample design specification.

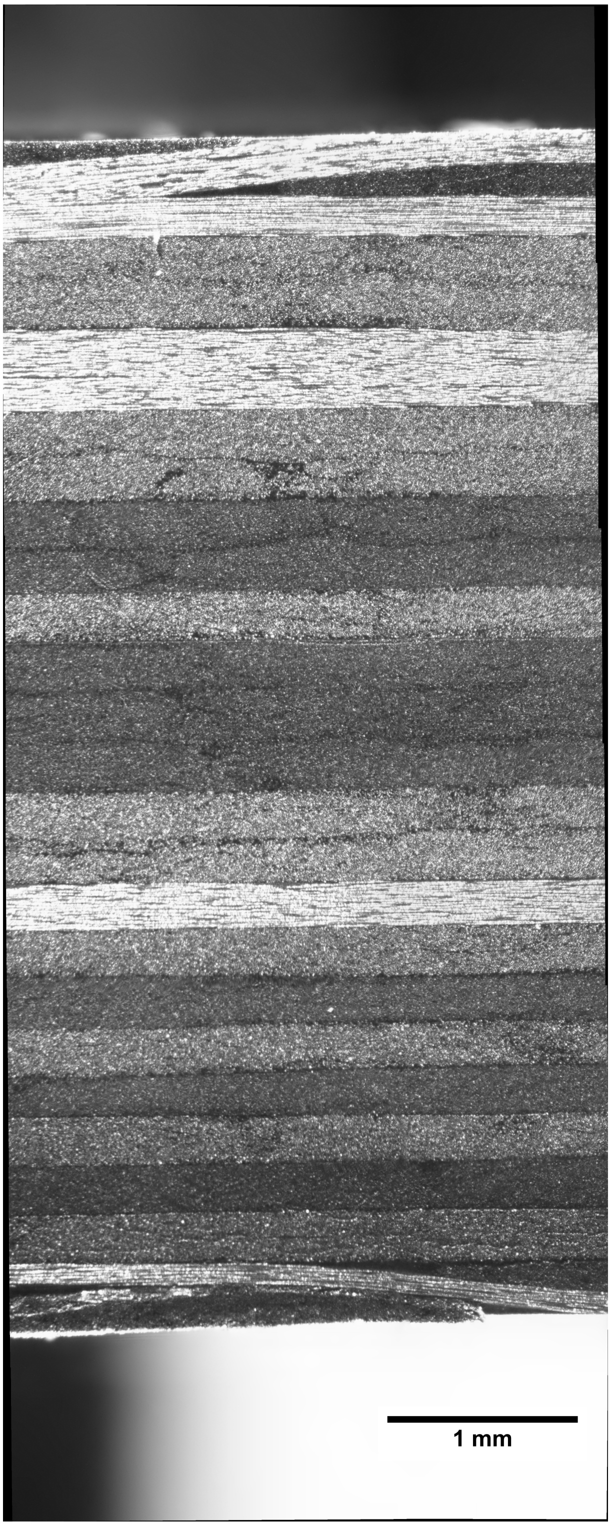

Figure 5.3: *Microscopic image of full composite sample layers, generated by stitching smaller individual images*

While the microscopy set up generated highly detailed microscopic images which enabled the component's ply layers to be identified and their fibre orientations determined, they only image a small area of the sample. It is possible to stitch the images together to produce an image of a larger area, but this was time consuming and challenging due to the high level of detail in the composite structure. In order to generate an image of the complete thickness cross-section, 4 or 5 images were required to generate sufficient overlap between images for the stitching algorithm. The width of the resulting image was approximately 2 mm but the FEA models required a sample width of at least 20 mm to cover the diameter of the ultrasonic probe. This would then require over 10 complete thickness images to generate an image that covers enough of the sample. This becomes impractical due to the difficulty and time consuming nature of the image stitching for the complex CFRP structure.

An alternative set up was implemented which used a smaller lens magnification with a camera to take photomicrograph images. This allowed for a larger area of the sample to be captured in each image but did result in a loss of detail. The loss of detail is acceptable, since the FEA model considers the ply layer as a homogeneous material, not individual fibres. An example of a captured image can be seen in Figure 5.4, where an area of approximately 11 mm x 7 mm has been captured. It can be seen that individual ply layers can still be seen, but with the lower magnification resulting in a loss of detail.

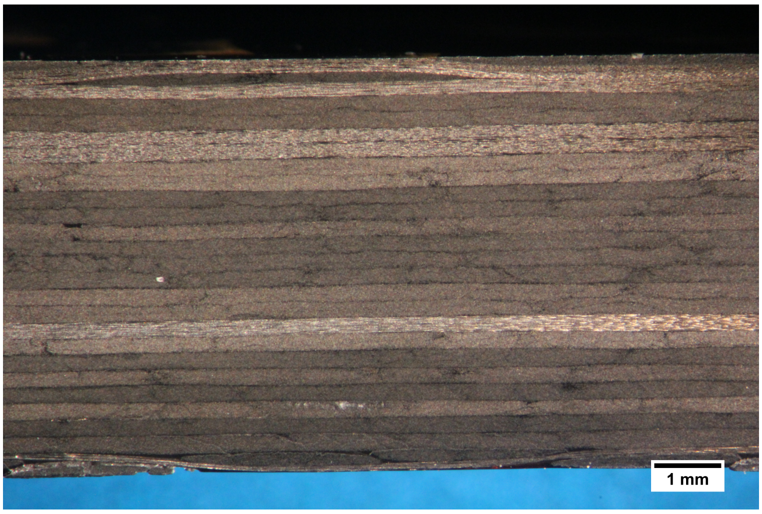

Figure 5.4: *Individual photomicrograph image of composite sample layers*

Individual photomicrographs could then be stitched together to provide an image showing a large section of the sample cross-section, as illustrated in Figure 5.5. This image covers approximately 35 mm x 7 mm of the samples cross-section and can be used to generate a FEA model including the individual ply layer variations across the sample. It can be seen in the photomicrograph that the sample ply layers are not planar but contain some out-of-plane waviness. This waviness is important to consider in FEA models as it will impact how ultrasonic waves propagate through the component. It can also be seen that there is a variation in the inter ply resin layer thickness, which will also affect the wave propagation through the sample by causing different levels of reflection at the ply layer interfaces.

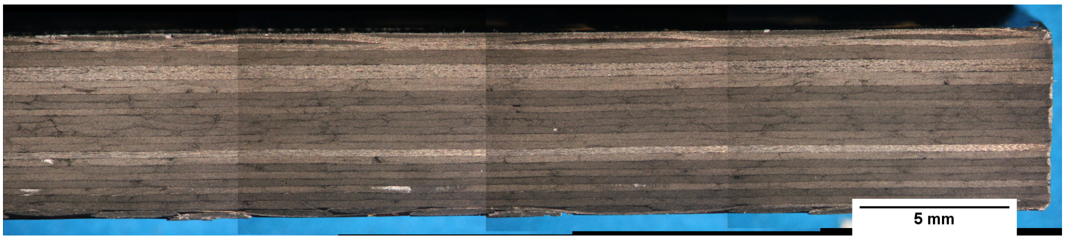

Figure 5.5: *Photomicrograph image of all composite sample layers, generated by stitching smaller individual images*

5.2.2.2 X-Ray CT

X-Ray CT scans were kindly conducted on the sample by Miss Christina Fraij from the Ultrasonics and Non-destructive Testing research group at the University of Bristol.

The X-Ray CT scans were performed on the small sample section of the CFRP and allow for volumetric information on the material to be obtained. This allows the fibre orientation in each layer to be viewed as well as providing multiple cross sectional images showing the ply layers. Two scans were performed with different levels of resolution, details of the scan set ups can be seen in Table 5.1.

Table 5.1: *X-Ray CT scan parameters*

Parameter	**Scan 1**	**Scan 2**
Resolution (μm)	30	15
Voltage (kV)	28	30
Current (μA)	536	933
Number of projections	2400	2400
Exposure time (ms)	2829	2000

Example images from the two scans can be seen in Figures 5.6 and 5.7.

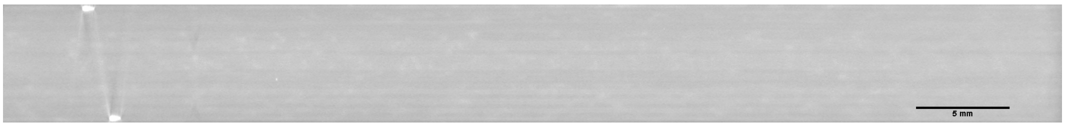

(a) *Side view showing sample cross section*

(b) *Top view showing* 0° *orientated fibres*

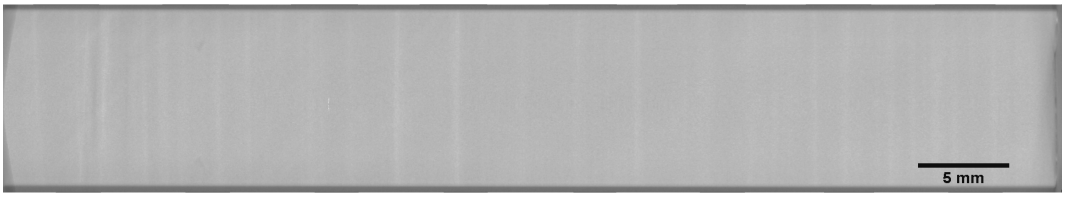

(c) *Top view showing* 90° *orientated fibres*

(d) *Top view showing* 45° *orientated fibres*

(e) *Top view showing* −45° *orientated fibres*

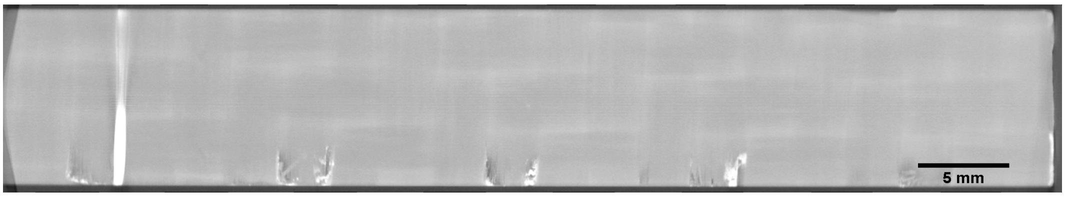

(f) *Top view showing 2-2 Twill ply layer*

Figure 5.6: *Images from X-Ray CT scan 1 (Low resolution)*

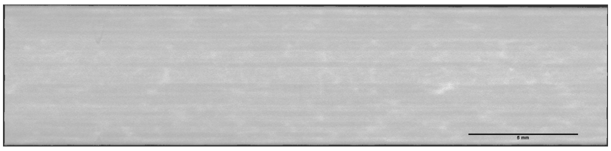

(a) *Side view showing sample cross section*

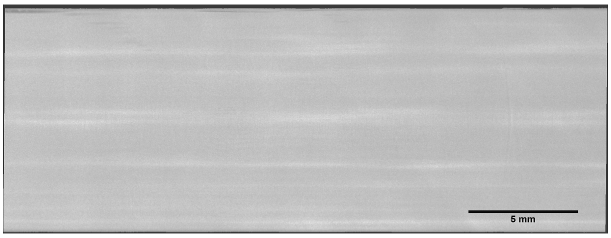

(b) *Top view showing* 0° *orientated fibres*

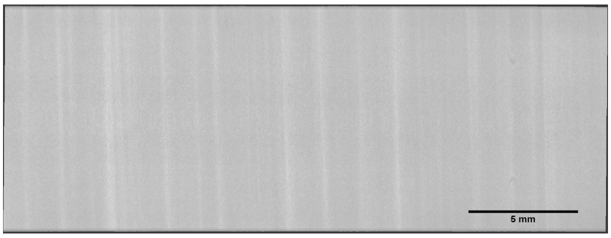

(c) *Top view showing* 90° *orientated fibres*

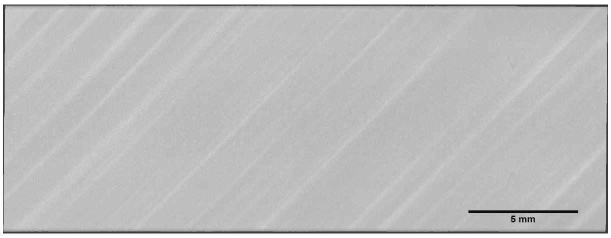

(d) *Top view showing* 45° *orientated fibres*

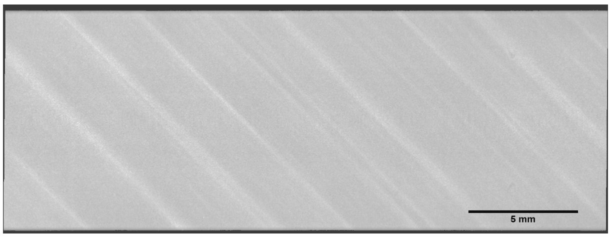

(e) *Top view showing* $-45°$ *orientated fibres*

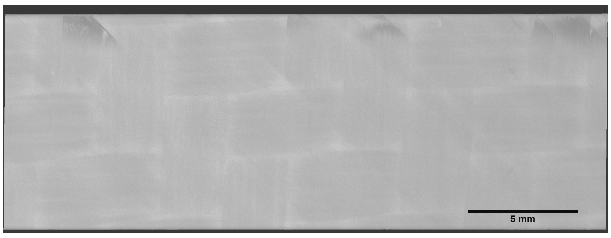

(f) *Top view showing 2-2 Twill ply layer*

Figure 5.7: *Images from X-Ray CT scan 2 (High resolution)*

Using the images that show the in-plane orientation for the ply layers, the fibre orientation of each ply layer can be determined to produce the sample ply lay up. The fibre orientation for the sample's unidirectional ply layers was determined as: [0/45/45/0/0/-45/-45/90/90/45/90/90/90/45/45/0/-45/90/45/90/-45/90/45].

5.2.3 Model Configuration

The FEA model geometry can be generated using approaches described in Chapter 4. The first approach aims to construct the ideal geometry through use of the design specifications, while the second approach uses the photomicrographs to build a more representative model.

The anisotropic material properties of the CFRP sample HTS40/977-2 plies are detailed in Table 5.2 [144, 145]. The CFRP material properties are transformed to a local coordinate system which relates to the fibre orientation. Accurate material damping data was not available, hence no material damping was applied. However, the main cause of attenuation in wave propagation through composite materials is due to reflection at ply interfaces, which will be accounted for. If specific material damping values are known or are experimentally measured, it would be possible to incorporate these into the models.

Table 5.2: *Flat laminate CFRP sample HTS40/977-2 material properties with* E_{11} *in the fibre direction*

Property		Value
Density (kg/m^3)		1620
Elastic Modulus (GPa)	E_{11}	153
	E_{22}	10.3
	E_{33}	10.3
Shear Modulus (GPa)	G_{12}	5.2
	G_{23}	3.43
	G_{13}	5.2
Poisson's Ratio	ν_{12}	0.3
	ν_{23}	0.5
	ν_{13}	0.3

The material properties of the Cycom 977-2 resin system used in the FEA models are detailed in Table 5.3 [144]. As with the CFRP fibres, no reliable acoustic attenuation data was available, hence no acoustic damping was applied. The water material properties used can be seen in Table 5.4 [146].

Table 5.3: *Cycom 977-2 resin material properties*

Property	Value
Density (kg/m^3)	1310
Young's Modulus (GPa)	3.32
Poisson's Ratio	0.35

Table 5.4: *Water material properties [146]*

Property	Value
Density (kg/m^3)	1000
Longitudinal Velocity (m/s)	1496
Shear Velocity (m/s)	0
Longitudinal Attenuation (dB/m)	0.002
Shear Attenuation (dB/m)	0

5.2.3.1 Focused Beam Approximation

The ultrasonic probe was represented as a pressure load in the FEA models to remove the requirement for knowledge of the internal transducer structure and remove the need for electro-mechanical calculations in the FEA simulations. This makes the simulations more efficient and, as shown in Chapter 3, is an acceptable approximation. The practical probe is spherically focused which to fully represent would require either an axisymmetric model or a full 3D model. Due to the CFRP test component, it is not possible to use an axisymmetric model. A 2D model is the more attractive option, as it has a lower computation demand due to containing a smaller number of elements, However, a 2D model will result in a cylindrical focused probe as the FEA elements are infinite in the non-modelled direction.

In the experimental set up, the probe is often up to 40 mm from the top surface of the CFRP component, resulting in a long propagation path through the water in terms of number of wavelengths. The total propagation path will be in the order of hundreds of wavelengths which becomes challenging to model using FEA due to numerical dispersion creating a mismatch between derived and exact solutions [59]. Reduction of the number of wavelengths of propagation through the water would reduce the influence of numerical dispersion and also reduce computation costs - resulting in a faster and more accurate model assuming valid approximations are made. One solution to reducing the water path length would be to implement a hybrid model approach where the wave propagation is solved analytically. Another possible solution is to approximate the transducer by reducing the water path length and transducer size while maintaining the same focusing angles or F-number (ratio of focal length and probe width).

For this work, the reduction of transducer focal length and size was chosen due to its ease of set up and, unlike the hybrid solution, only requiring a single FEA model. However, for this approximation there is a limit for the reduction in focal length that can be used. In order for a true focusing effect, the intended focal distance of the probe must be less than the natural focus or near field length [147]. If we assume the focused probe to be a flat square transducer, the natural focus, N, is given by Equation 5.3, where D is the transducer width and λ is the wavelength in the test medium.

$$N = 1.37\frac{D^2}{4\lambda} \tag{5.3}$$

Using this equation, the natural focus can be calculated for different transducer widths. For each width, the transducer focal length can also be calculated to maintain the same transducer F-number. Figure 5.8, plots the calculated natural focus, N, and focal length, s, for a range of element widths against the effective water distance from the element to the focal spot of a transducer with the same focal gain or F-number. These values have been calculated to match the focal gain of a transducer with diameter 0.5" and focal length 1.5" (constant F-number of 3) at a frequency of 7.5 MHz and in a water medium. The point at which these graphs cross, 5.4 mm water distance, is the point the focal distance of the probe is equal to the natural focus and will match the beam geometry of the experimental probe.

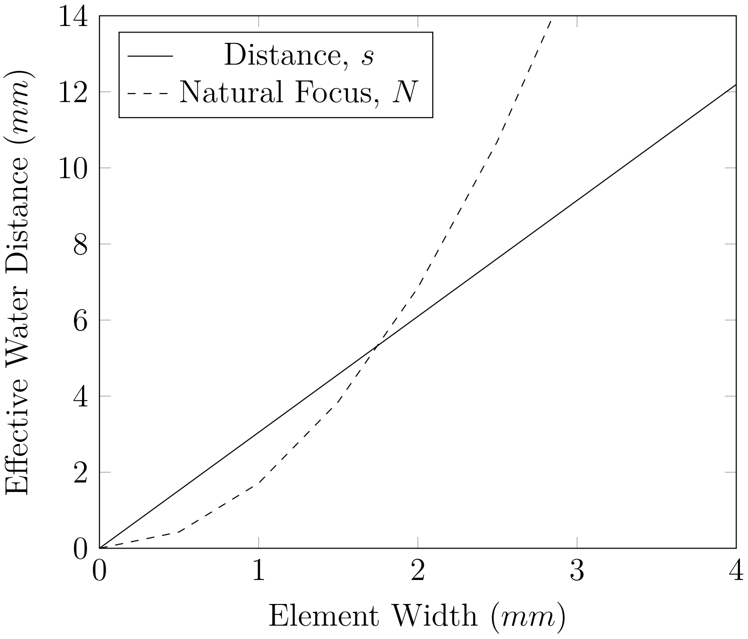

Figure 5.8: *Focal length and natural focus for different transducer widths operating at 7.5 MHz in a water load with a fixed F-number of 3*

The above process would be repeated for the different probe frequency and focal parameters simulated and the calculated transducer width and stand-off distance would be implemented in the FEA models. These parameters would be used for the input pressure load and the average acoustic pressure of this region would be calculated to generate the received A-scan signal.

5.2.3.2 Design Specification Geometry

The first FEA model geometry was constructed by considering the design specifications of the sample. The thickness of the sample ply layers, twill and resin were measured from the micrographs taken of the sample and used to build the FEA model. This would generate an ‘as designed’ geometry structure that is representative of an ideal ply layer structure.

The model geometry was constructed through the use of a scripted input file with the addition of importing a table file containing details of the twill layers. Using the measured twill dimensions, a table file was constructed using the approach described in Section 4.2.4. The generated TexGen textile can be seen in Figure 5.9. This textile was then reduced to a 2D cross section, exported as a voxel file, and then converted into a table file to allow for easy importation into the modelling suite.

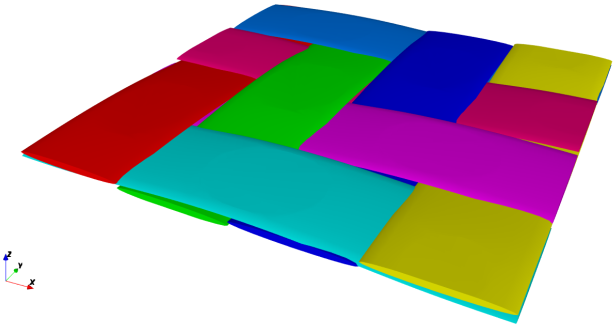

Figure 5.9: *2/2 twill weave textile created in TexGen software*

The FEA model was constructed to read in the twill table file twice for the top and bottom layers, while the unidirectional layers and resin layers were created through code scripting. The orientations of the unidirectional layers were determined from the X-Ray CT data. The resultant CFRP laminate geometry created can be seen in Figure 5.10, where each colour represents a different ply orientation.

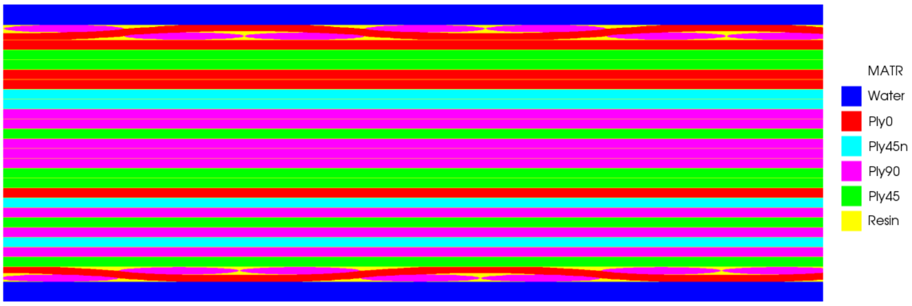

Figure 5.10: *FEA model for 'as designed' geometry*

The 2/2 twill weave layers had a thickness of 360 μm, unidirectional ply layers had a thickness of 230 μm and the intermediate resin layers were 10 μm. Note, the resin layers between plies are present in the FEA model shown in Figure 5.10, but are not visible due to their small thickness. This gave an overall sample thickness of 6.25 mm. The FEA model element size is determined by either the shortest wavelength of interest or model geometry dimensions. In this modelling scenario, the maximum frequency simulated is 7.5 MHz and the minimum wavelength of interest is the longitudinal wave in the water. This gives means the shortest wavelength of interest is 0.2 mm and to accurately mesh for this wavelength a minimum element size of 13.3 μm is required to generate 15 elements per wavelength. However, the thin resin layers are 10 μm and so this value is implemented for the element size for all frequencies to ensure a single element through the resin thickness, which was shown in Section 4.2.2 to be a valid approach.

5.2.3.3 Micrograph Image Processing Geometry

To increase the accuracy of the FEA model of the CFRP sample, the photomicrograph shown in Figure 5.5 was used to generate an additional table file to contain details of the 23 unidirectional layers. This approach would then account for the ply waviness observed in the ‘as built’ composite structure but will be limited to a 2D model as volumetric information cannot be obtained from a single micrograph image. This more representative model will capture the true ultrasonic wave propagation through the sample and fully capture the wave refraction and scattering caused by the non-planar ply layer structure.

The FEA input script generated the CFRP geometry through importation of the table files for the twill on the top and bottom as well as a table file for the unidirectional layers. This produced an overall thickness of 6.22 mm for the CFRP sample. Figure 5.11, shows the resulting FEA model geometry generated from the micrograph image processing. It can be seen that the model geometry is more representative of the actual component with the out of plane variance of the unidirectional ply layers.

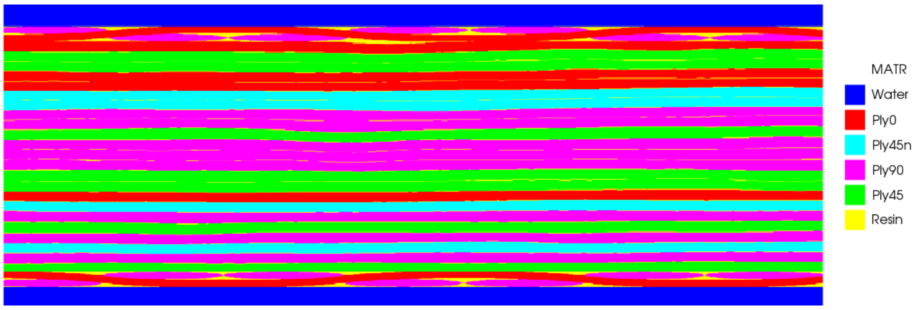

Figure 5.11: *FEA model for micrograph image processed generated geometry*

The inter ply resin layers of the unidirectional layers were constrained to 10 μm to ensure the ultrasonic wave was reflected at each ply layer interface. As with the previous Design Specification geometry, the minimum element size to accurately mesh the wavelengths of interest and the resin layer thickness is 10 μm. However, in this scenario the resin layer has spatial variation in the out-of-plane and so is no longer perfectly flat, which has the potential to require a smaller element size to accurately represent. Reducing the element size by half to 5 μm would result in a FEA model that is four times larger in a 2D scenario and 8 times larger in 3D. This leads to much more computationally demanding simulations and so the benefit of reducing the model size needs to be evaluated to determine if there is a substantial increase in derived result accuracy from using a more refined mesh. Figure 5.12 shows FEA derived A-scan results at three different locations of the as built model geometry for 5 μm and 10 μm element size.

It can be seen that the results are very similar and there is no significant justification to implement an element size smaller than 10 μm. The resin layers are 10 μm thick and it has been demonstrated previously, Section 4.2.2, that a single element through the resin thickness is sufficient to accurately model the wave interaction at the material interfaces. The larger element size is also adequate to resolve the wavelengths of interest in this simulation scenario and these A-scans demonstrate this element size also sufficiently captures the spatial variation of the ply and resin layer interface's.

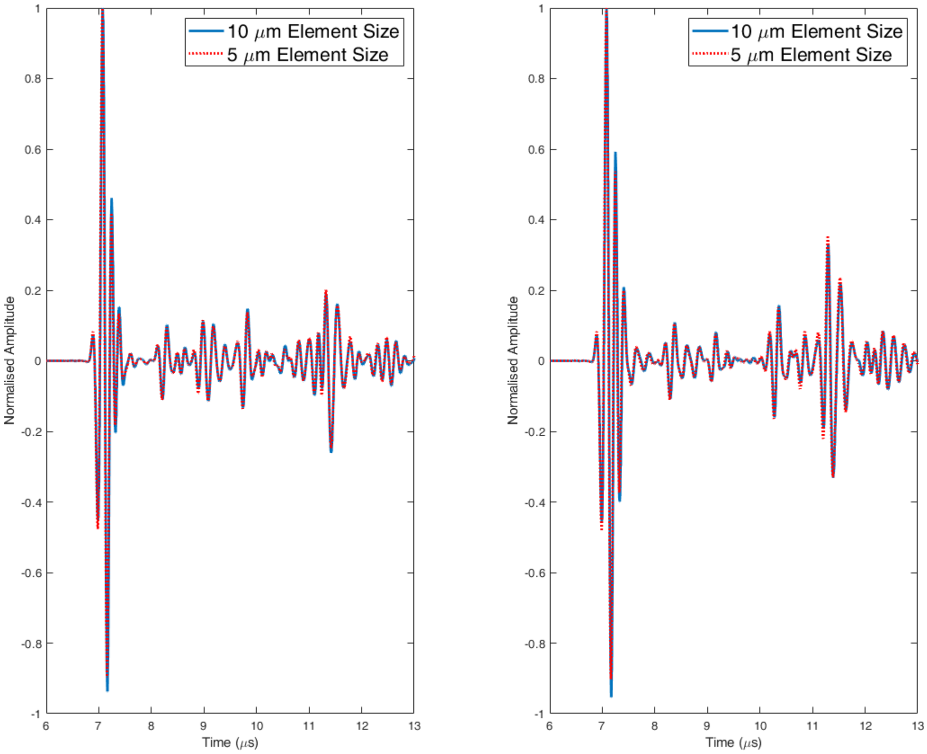

(a) *Transducer at 5 mm* **(b)** *Transducer at 10 mm*

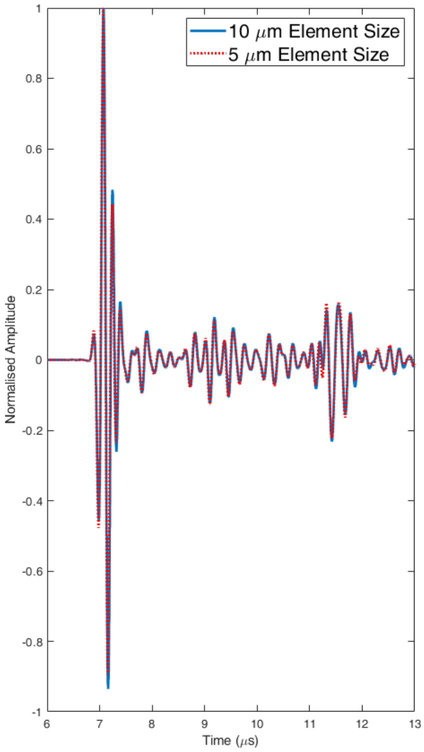

(c) *Transducer at 15 mm*

Figure 5.12: *Comparison of A-scan data for 5 μm and 10 μm element size at three different horizontal transducer locations*

5.2.3.4 Parametric Study Inputs

The parameters selected for the simulation study were the transducer frequency and focal length. The selected frequencies were 5 MHz, 6.5 MHz and 7.5 MHz. These frequencies correspond to the approximate resonance frequency of the unidirectional ply layers, 6.5 MHz, and transducers available to collect experimental data that could be used to compare FEA derived results with. The experimental probes had a focal length of 1.5” (38.1 mm) and a diameter of 0.5” (12.7 mm). The same transducer dimensions would be implemented for the 6.5 MHz inspection to maintain consistency. The second parameter investigated was the focal length of the probe. For these simulations, the frequency was constant at 6.5 MHz and the transducer dimensions were varied to give different F-numbers. All of the transducer inputs used in the parametric studies can be seen in Tables 5.5 and 5.6.

Table 5.5: *Parametric Study 1 Transducer Inputs*

Frequency (MHz)	**Focal Length (inches)**	**Diameter (inches)**	**F-number**
5	1.5	0.5	3
6.5	1.5	0.5	3
7.5	1.5	0.5	3

Table 5.6: *Parametric Study 2 Transducer Inputs*

Frequency (MHz)	**Focal Length (inches)**	**Diameter (inches)**	**F-number**
6.5	1.25	0.5	2.5
6.5	1.5	0.5	3
6.5	1.75	0.5	3.5
6.5	2	0.5	4
6.5	2.25	0.5	4.5
6.5	2.5	0.5	5

5.3 FEA Derived B-scan Results

The 2/2 twill layer is created by interlacing warp and weft fibres as illustrated previously in Figure 5.9. The woven Twill layer has a uniform repeating structure, known as a unit cell [148], and so the number of simulations performed can be reduced by copying the results from this repeating section to generate a B-scan image of a larger area. The B-scan imaging area of the composite contained four repetitions of the unit cell and is presented in Figure 5.13 using the ‘as designed FEA geometry.

Figure 5.13: *B-scan Imaging Area of Component*

5.3.1 Varying Transducer Frequency

The FEA derived B-scan images and plots of their instantaneous parameters for varying the transducer frequency can be seen in Figures 5.14 - 5.17. The instantaneous phase plots are presented with a different aspect ratio to better show their capability of identifying the interface between layers.

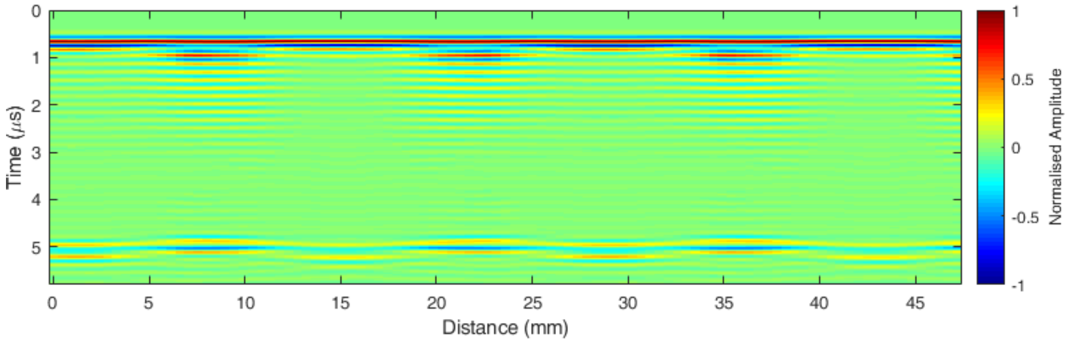

(a) *5 MHz*

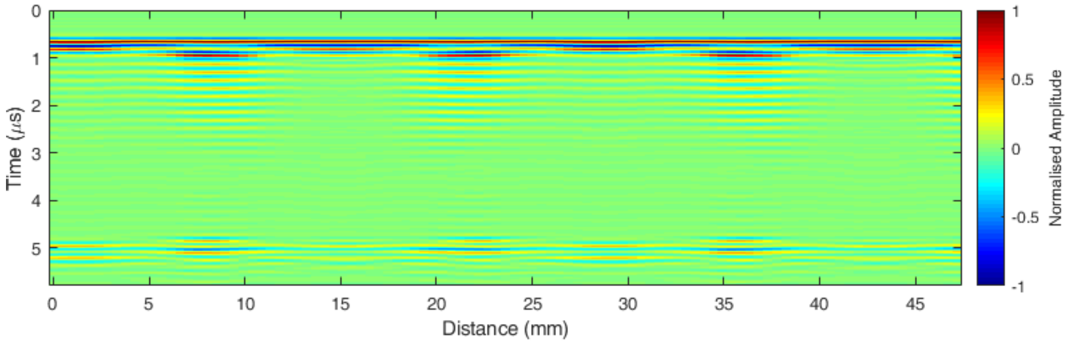

(b) *6.5 MHz*

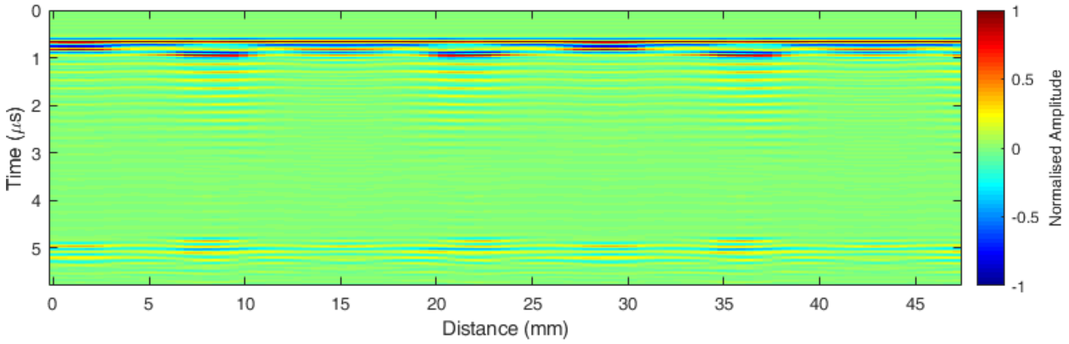

(c) *7.5 MHz*

Figure 5.14: *B-scan images of 'as designed' FEA geometry for varying transducer frequency*

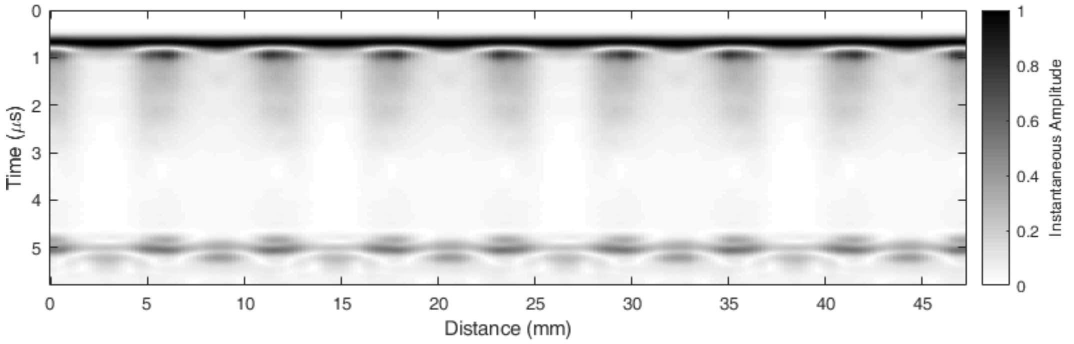

(a) *5 MHz*

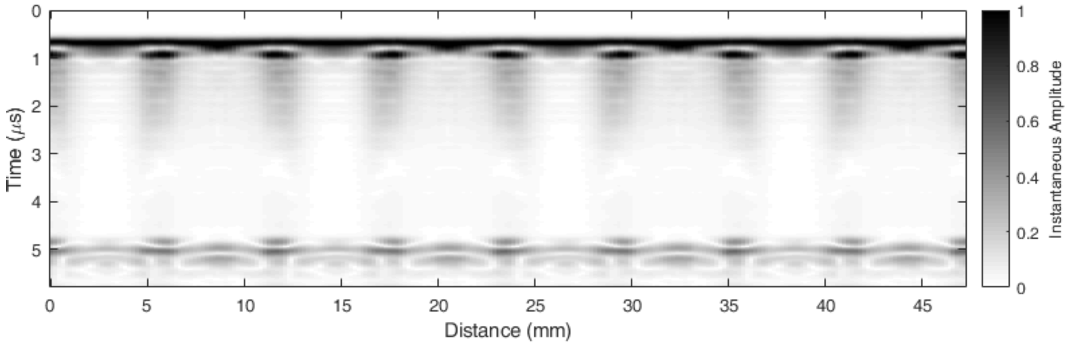

(b) *6.5 MHz*

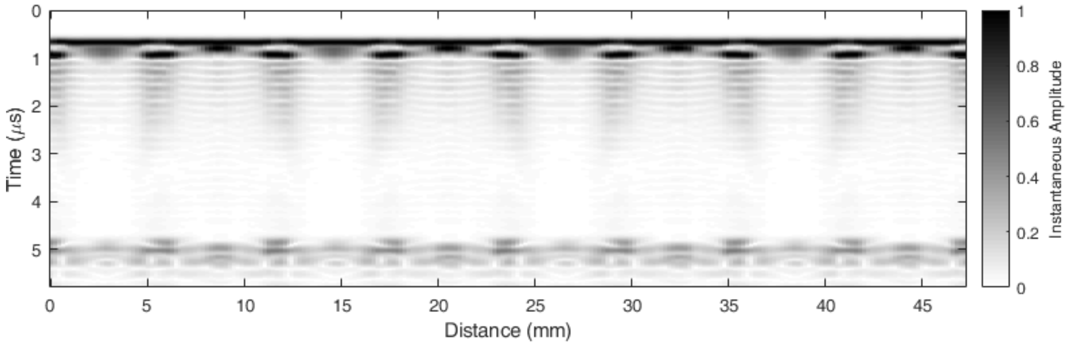

(c) *7.5 MHz*

Figure 5.15: *Instantaneous amplitude images of 'as designed' FEA geometry for varying transducer frequency*

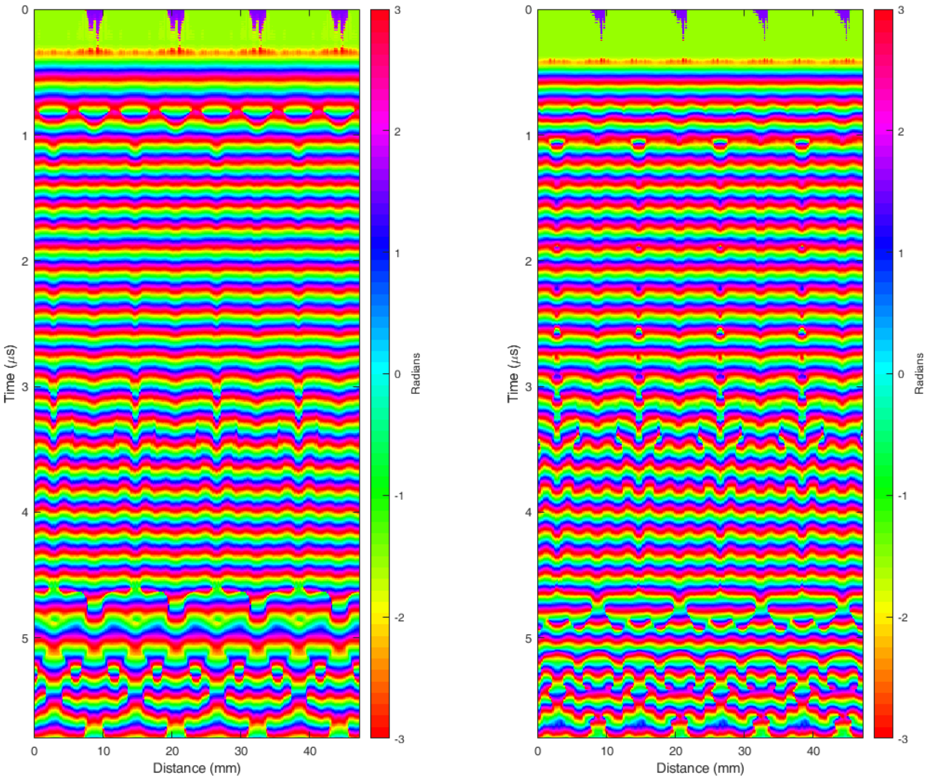

(a) *5 MHz* **(b)** *6.5 MHz*

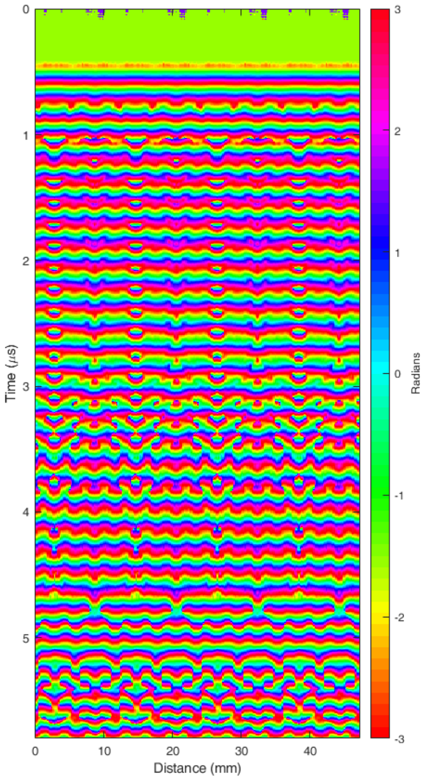

(c) *7.5 MHz*

Figure 5.16: *Instantaneous phase images of 'as designed' FEA geometry for varying transducer frequency*

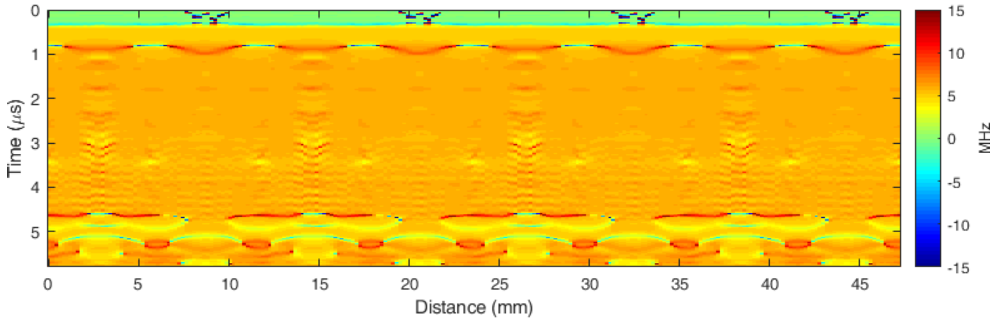

(a) *5 MHz*

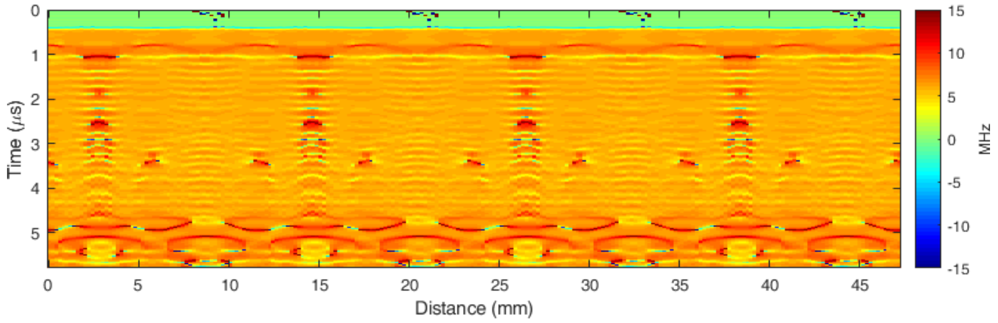

(b) *6.5 MHz*

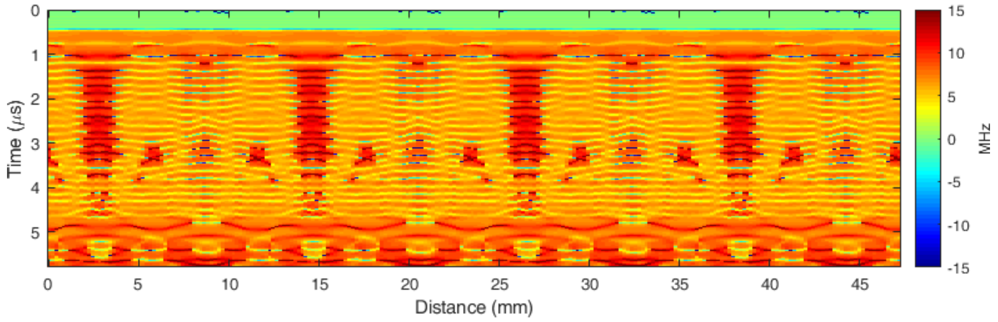

(c) *7.5 MHz*

Figure 5.17: *Instantaneous frequency images of 'as designed' FEA geometry for varying transducer frequency*

It can be seen from the results that the original B-scan images and the instantaneous parameter images each provide different information on the internal structure. The B-scan, Figure 5.14, and instantaneous amplitude, Figure 5.15, are often the first approaches to visualise a test component after performing a B-scan inspection and while this can provide valuable information it is not the optimum approach to fully characterise a composite component. In order to better characterise the complex structure, the phase and frequency instantaneous parameters of the signal can be calculated.

The B-scan and instantaneous amplitude plots can identify the frontwall and backwall of the composite and illustrates these reflections are not from a uniform layer. The higher frequency has the smallest wavelength, and so allows for increased resolution, and can provide an improved image of the top woven layer, however, due to increased reflections through the composite structure, the bottom twill layer becomes more distorted when compared to the lower frequency results. Reflections from the unidirectional layers can also be visualised, however these become lower in amplitude as the depth increases.

If a wave travelling through a composite structure has a frequency spectrum that is centred at the ply-resonance frequency, the instantaneous phase will increase by 2π radians for every ply layer the wave propagates through [137]. The unidirectional ply layers can be identified from each of the frequency inspection's instantaneous phase plots, Figure 5.16. However at the higher frequency of 7.5 MHz there is more distortion as the depth increases. At 5 MHz, there is a distinct indication of the top woven layer, where the groups of two weft fibres can easily be identified with the oval shapes at a time of approximately 0.8 μs. The bottom woven layer can be identified between 4.6 and 5.2 μs in each frequency where there is a pattern of eight curves that represents the eight sections of the bottom twill where the warp tow is above or below the weft tows.

The instantaneous frequency plots, Figure 5.17, can also identify the ply layer interfaces but importantly they have also provided information on the woven layers. The top woven layer can be clearly identified in the 5 MHz inspection. There is a high instantaneous frequency as the warp tow passes over or under the weft tows and when the warp transitions from being above or below the weft tows there is a low instantaneous frequency. This sudden change between high positive and high negative frequency also creates phase singularities in the woven layer. This allows the number of times the warp passes over or under a group of two wefts to be counted, which in this image is 8. There is no clear identification of individual weft tows in any of the images from the different inspection frequencies. However, the approximately constant frequency suggests uniformity of ply spacing. There is also a clear difference in the images for areas where the top warp is above the weft tows and when it is below them as seen in the 7.5 MHz inspection at the distances of 3 mm, 15 mm, 26 mm and 38 mm. In this component section, the warp is below the weft and this creates a column of higher frequency through the sample thickness that indicates a resonance frequency in the top woven layer which creates a long ring down and obscures the structure below. The instantaneous frequency pattern for the bottom woven layer can again be easiest identified in the 5 MHz inspection and is the inverse characteristics of the top woven layer. At a time of 5.2 mm there is a low instantaneous frequency as the warp layer passes above or below the weft layer and a high frequency as the warp layer transitions from being above and below the weft layers.

5.3.2 Varying Transducer F-number

The FEA derived B-scan images and their instantaneous parameters for varying the F-number of a 6.5 MHz transducer can be seen in Figures 5.18 - 5.21. Again, the instantaneous phase plots are presented with a different aspect ratio to better show their capability of identifying the interface between layers.

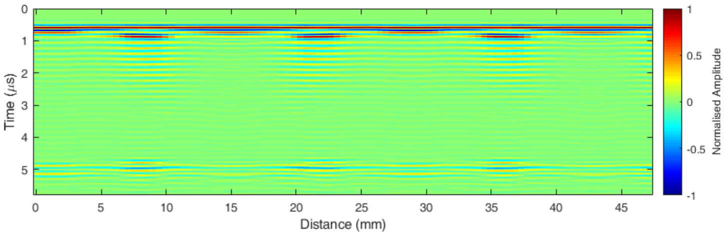

(a) *F-number = 2.5*

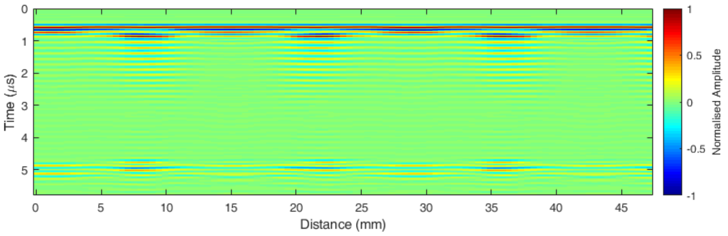

(b) *F-number = 3*

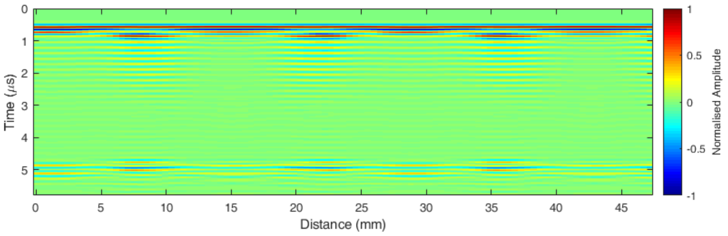

(c) *F-number = 3.5*

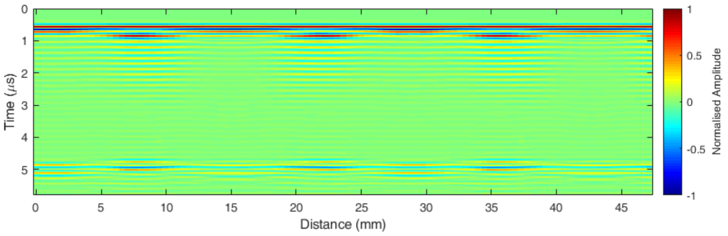

(d) *F-number = 4*

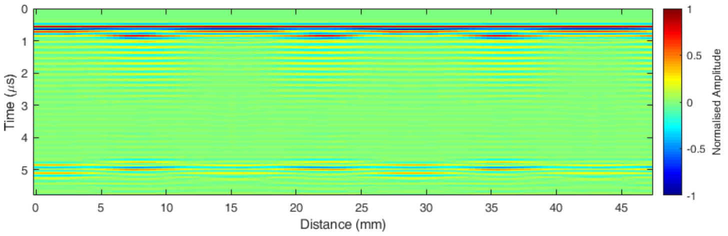

(e) *F-number = 4.5*

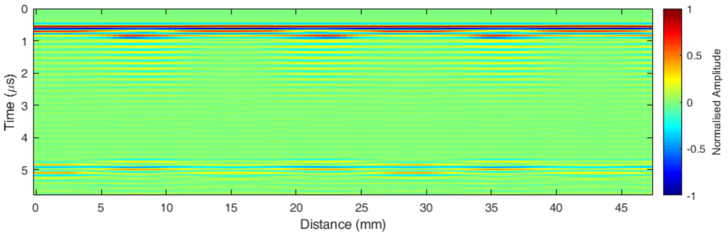

(f) *F-number = 5*

Figure 5.18: *B-scan images of 'as designed' FEA geometry for varying transducer F-number*

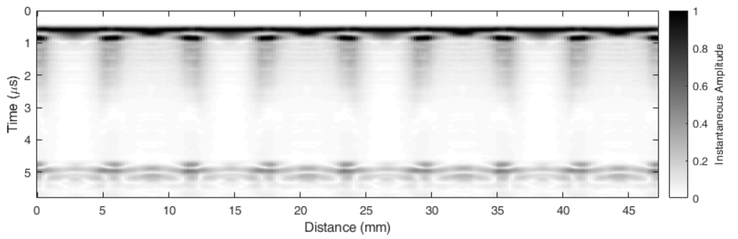

(a) *F-number = 2.5*

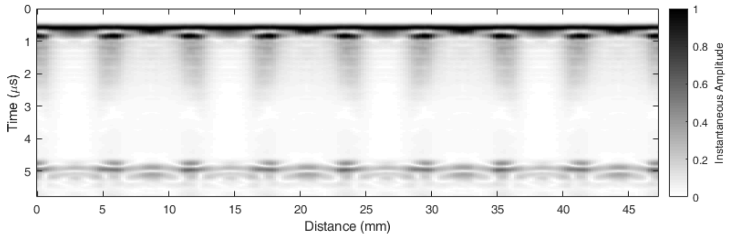

(b) *F-number = 3*

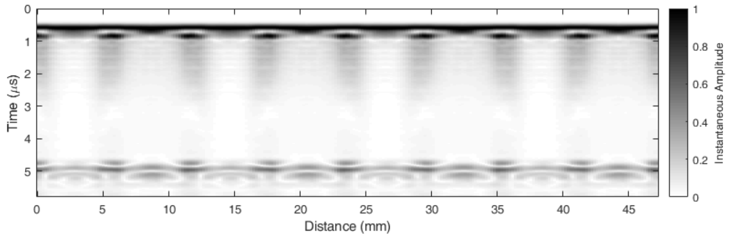

(c) *F-number = 3.5*

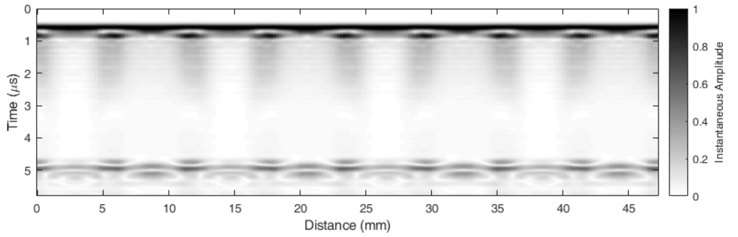

(d) *F-number = 4*

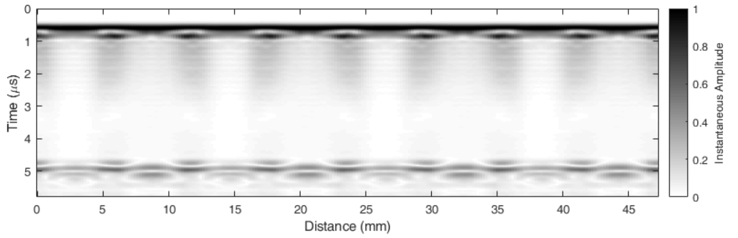

(e) *F-number = 4.5*

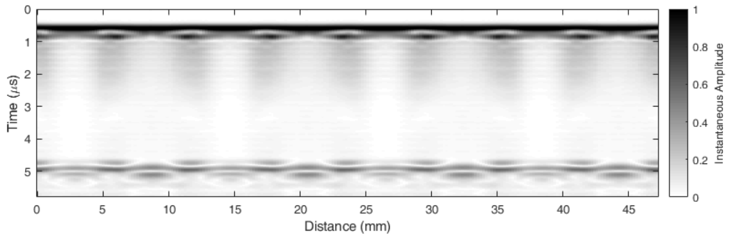

(f) *F-number = 5*

Figure 5.19: *Instantaneous amplitude images of 'as designed' FEA geometry for varying transducer F-number*

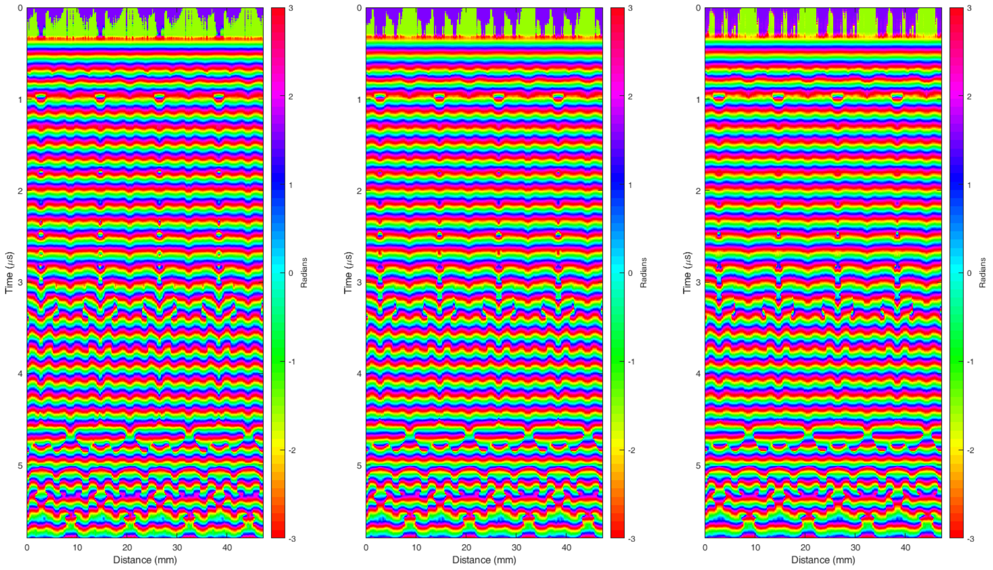

(a) *F-number = 2.5* **(b)** *F-number = 3* **(c)** *F-number = 3.5*

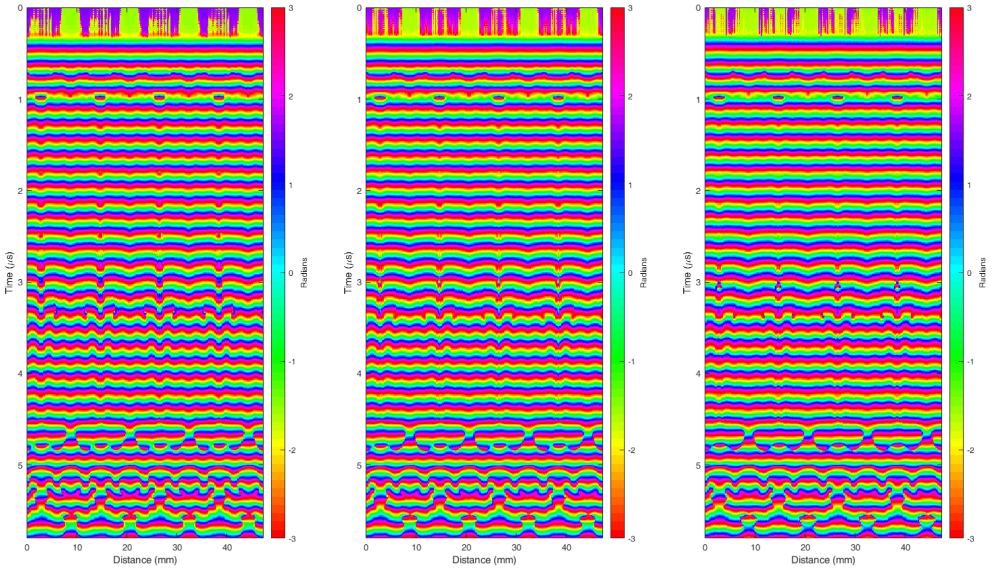

(d) *F-number = 4* **(e)** *F-number = 4.5* **(f)** *F-number = 5*

Figure 5.20: *Instantaneous phase images of 'as designed' FEA geometry for varying transducer F-number*

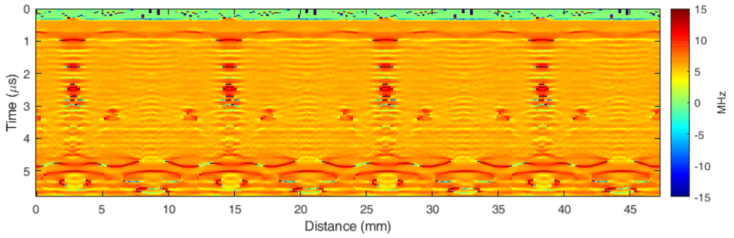

(a) *F-number = 2.5*

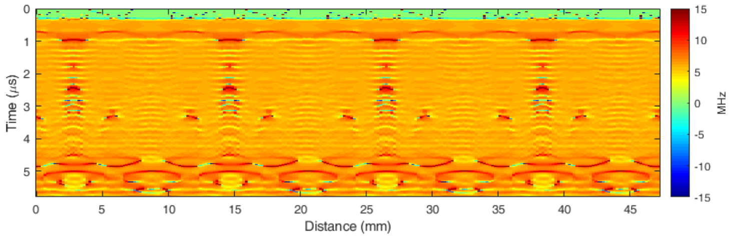

(b) *F-number = 3*

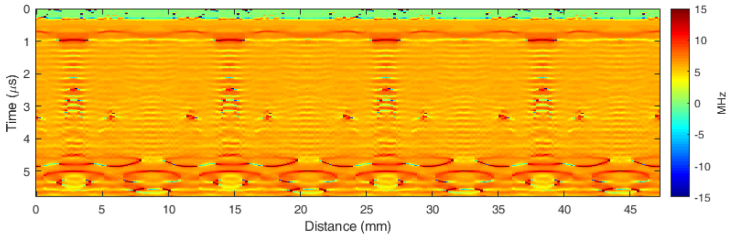

(c) *F-number = 3.5*

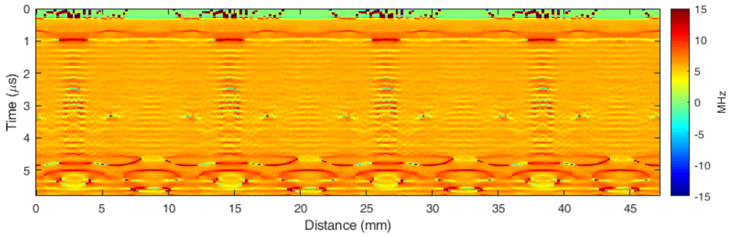

(d) *F-number = 4*

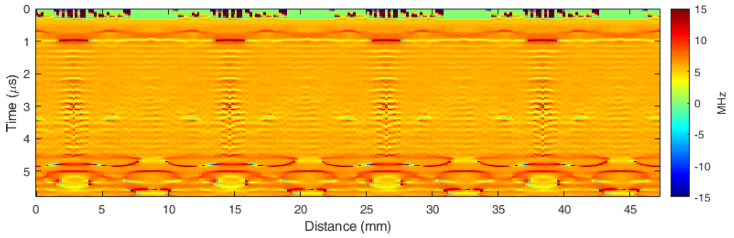

(e) *F-number = 4.5*

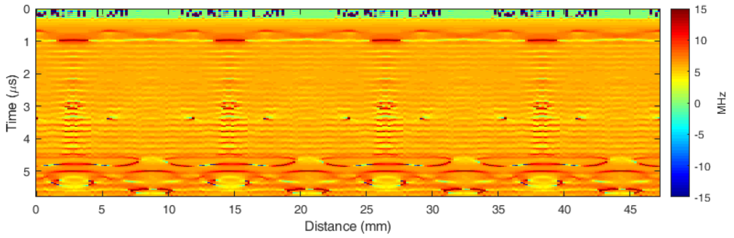

(f) *F-number = 5*

Figure 5.21: *Instantaneous frequency images of 'as designed' FEA geometry for varying transducer F-number*

Comparing the B-scans and instantaneous amplitude plots, there is minimal difference in the unidirectional ply layer responses as the transducer F-number. However, as the F-number increases, the top and bottom woven layers become more focused in the B-scans, Figure 5.18. Comparing the instantaneous phase images, Figure 5.20, as the F-number increases there is an improvement in the definition of the unidirectional ply layers. The largest F-number is also optimum for identifying the top and bottom woven layers and has less distortion in the unidirectional layers at a depth of $3 - 4\ \mu s$ that is caused by the wave becoming distorted after propagating through the top woven layer. The instantaneous frequency plots, Figure 5.21, are very similar across all F-numbers, however similarly to the instantaneous phase, as the F-number increases the distortion in the $3 - 4\ \mu s$ time region caused by the top woven layer reduces.

Overall, the effect of varying the F-number of the transducer is not observed to have a significant impact on the ability of the inspection to characterise the composite sample. The smaller F-number will typically produce the smallest focal spot and have the smallest beam spread. However, these results have shown that this is not beneficial for ply layer identification in the B-scan slice mode, although it would be beneficial for improving in-plane resolution of fibre tows, for in-plane fibre orientation analysis. A small F-number will result in the ultrasonic wave travelling through the composite structure at a larger angle to the normal and due to the anisotropic material properties and layered structure, this will result in greater refraction of the wave. The largest F-number will reduce the angle the wave travels through the composite and this will minimise any refraction effects and provide optimum performance at characterising the composite structure.

5.3.3 3D FEA Model

The FEA derived B-scan images and their instantaneous parameters for the 3D simulations are shown in Figures 5.22 - 5.25. The first 3D simulations, Scan 1, focused the transducer in the centreline of the tow warp, while the second simulations, Scan 2, focused in line with the gap between two adjacent warp tows. The 3D simulations performed used a 5 MHz transducer frequency with a F-number of 3 to match one of the experimental data collections.

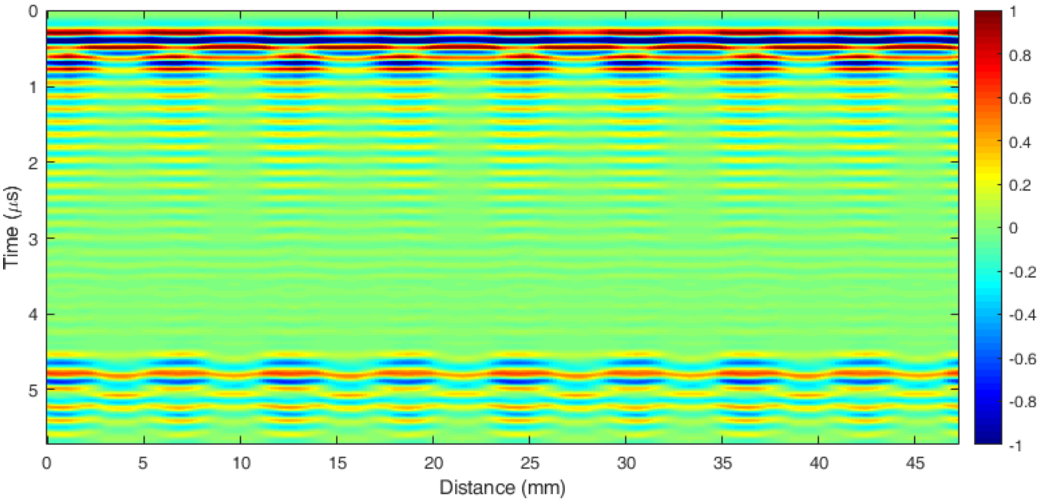

(a) *Scan 1 - focused on tow warp centreline*

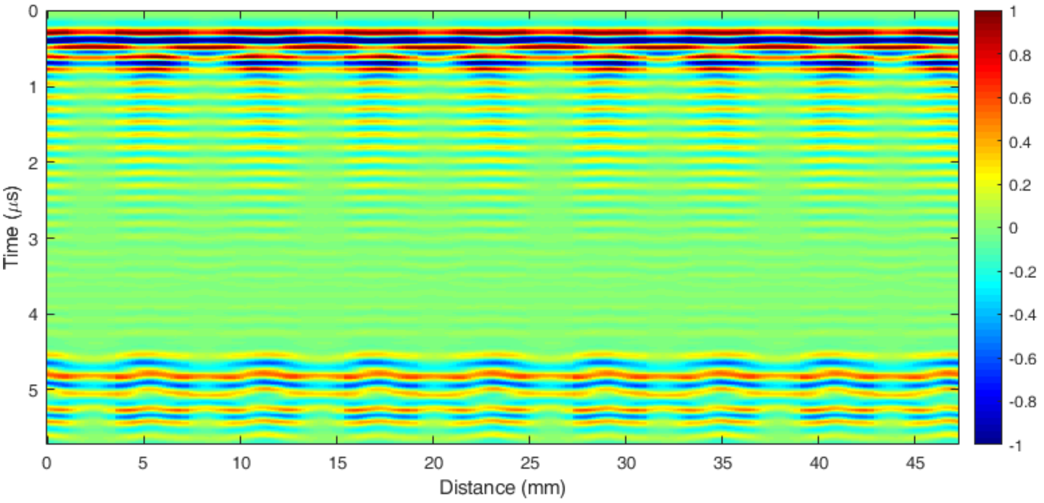

(b) *Scan 2 - focused on gap between two tow warps*

Figure 5.22: *B-scan images of ‘as designed’ geometry for 3D FEA simulations*

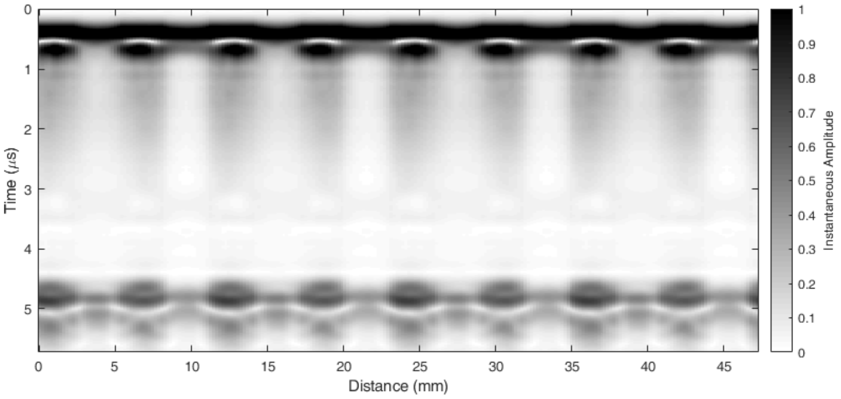

(a) *Scan 1 - focused on tow warp centreline*

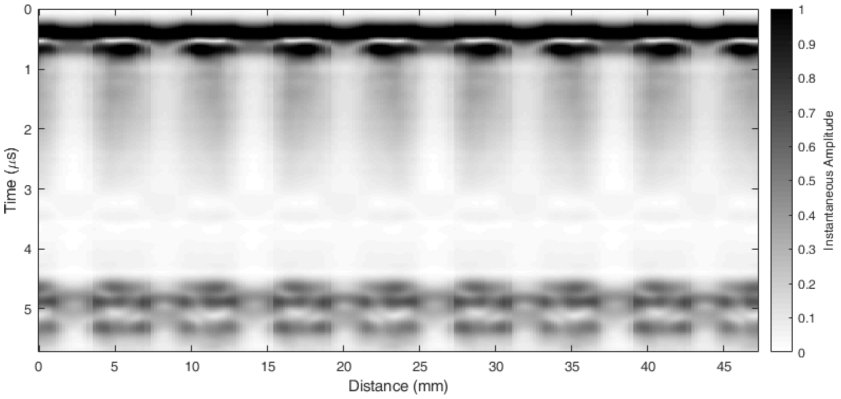

(b) *Scan 2 - focused on gap between two tow warps*

Figure 5.23: *Instantaneous amplitude images of 'as designed' geometry for 3D FEA simulations*

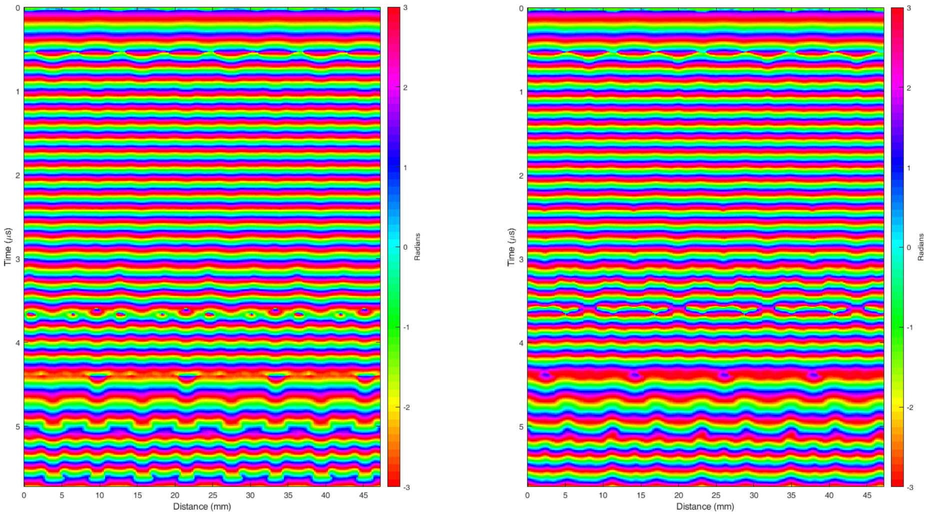

(a) *Scan 1 - focused on tow warp centreline*

(b) *Scan 2 - focused on gap between two tow warps*

Figure 5.24: *Instantaneous phase images of 'as designed' geometry for 3D FEA simulations*

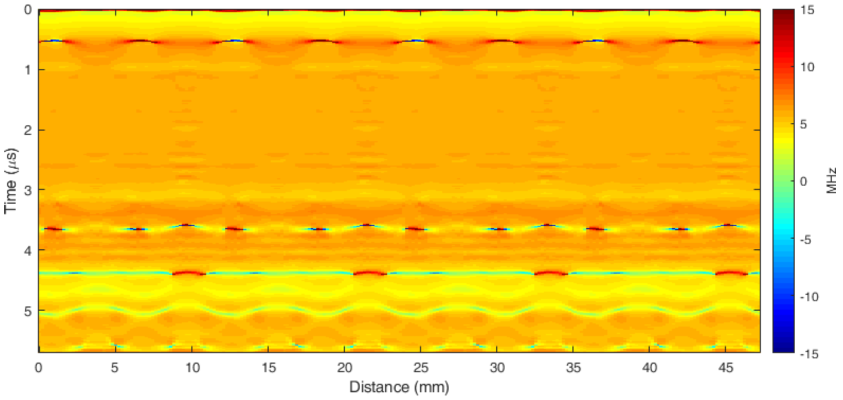

(a) *Scan 1 - focused on tow warp centreline*

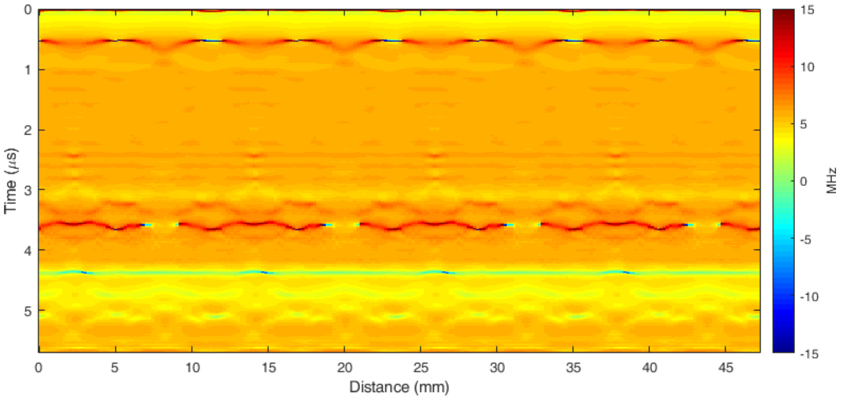

(b) *Scan 2 - focused on gap between two tow warps*

Figure 5.25: *Instantaneous frequency images of 'as designed' geometry for 3D FEA simulations*

The first 3D simulation, Scan 1, focused the transducer on the centreline of the warp tow, which is the same location the 2D simulations were performed, Figures 5.14(a) - 5.17(a). Comparing the 2D and 3D simulations, the B-scans are very similar, which indicates the 2D approximation is suitable to give representative results with a much smaller computation requirement. The biggest difference between the 2D and 3D simulations can be observed in the definition of the woven layers in the B-scan and instantaneous amplitude plots, Figures 5.22 and 5.23(a). In particular, the 3D geometry instantaneous amplitude plot allows the top woven layer definition to be enhanced. This is due to the 2D plane strain simulation assumes the woven layer geometry and the transducer representation as infinite in the non-modelled axis. Whereas, the full 3D model accurately represents the woven layer geometry and the transducer is represented as a square pressure load that will self-focus and provide a closer representation of the practical inspection.

The instantaneous frequency has been shown to be the best parameter to characterise the woven layer features and this parameter does clearly identify differences between the two scan locations. The first scan, Figure 5.25(a), does identify the warp tow travelling over and under the weft tows and creating a wavy shape for the top woven layer. However, in the second scan, , Figure 5.25(b), the transducer is focused on the gap between warp tows and so this waviness is not present in the instantaneous frequency plot.

5.3.4 'As Built' FEA Model Geometry

The FEA derived B-scan images and their instantaneous parameters for the 'as built' geometry, Section 5.2.3.3, are shown in Figures 5.26 - 5.29. Since the unidirectional ply layers have been created using information from the photomicrograph image, the results have not been copied to extend the component width and so the B-scan image area is reduced. The 'as built' FEA geometry was used to recreate the previous 2D simulations performed for varying transducer frequency, Section 5.3.1.

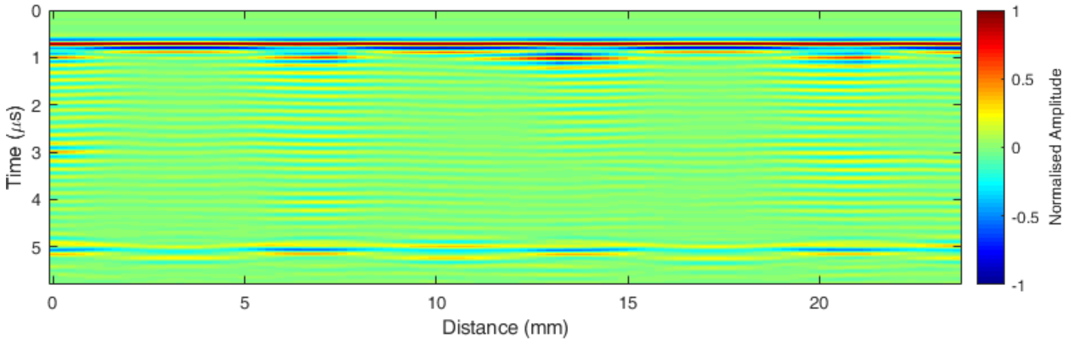

(a) *5 MHz*

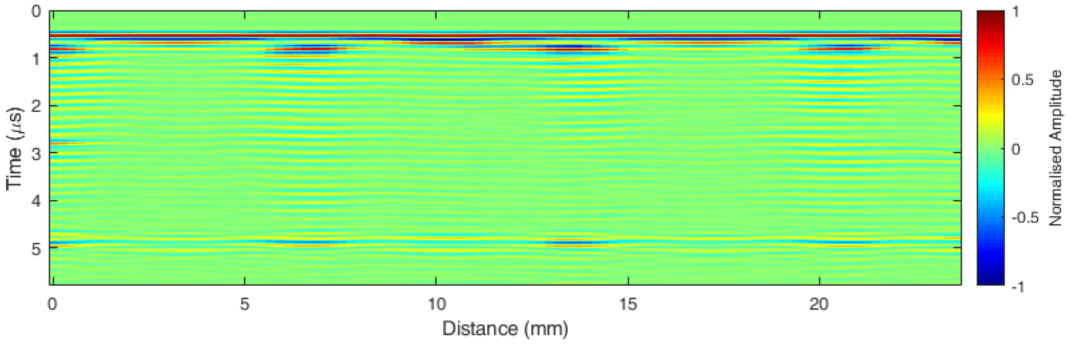

(b) *6.5 MHz*

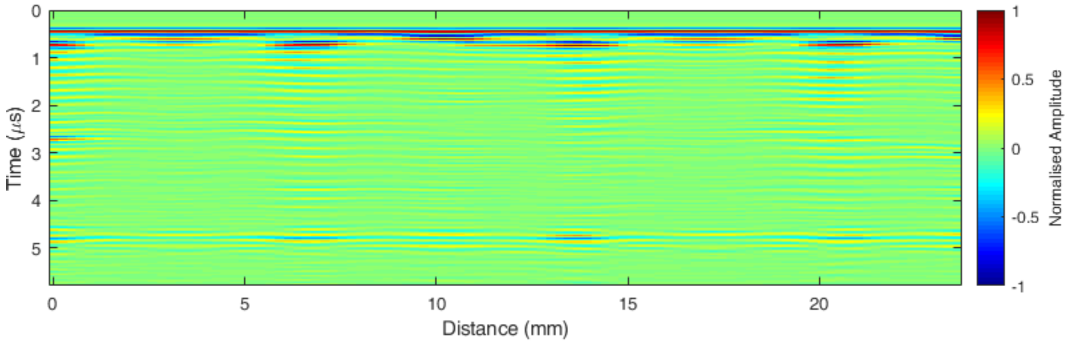

(c) *7.5 MHz*

Figure 5.26: *B-scan images of 'as built' FEA geometry for varying transducer frequency*

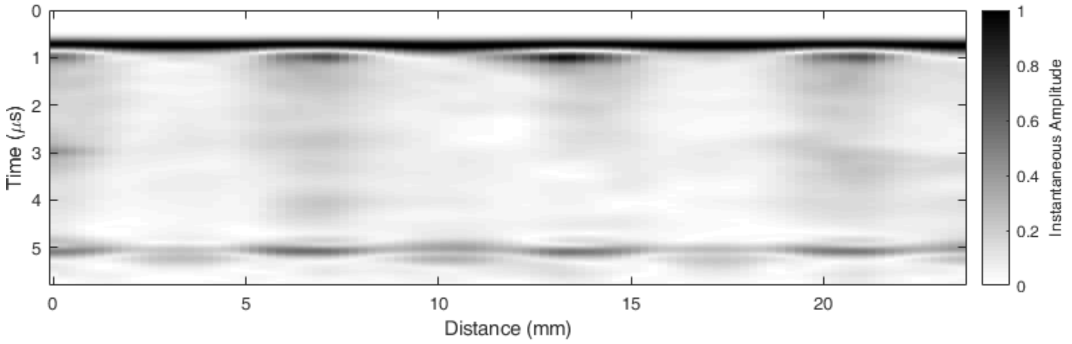

(a) *5 MHz*

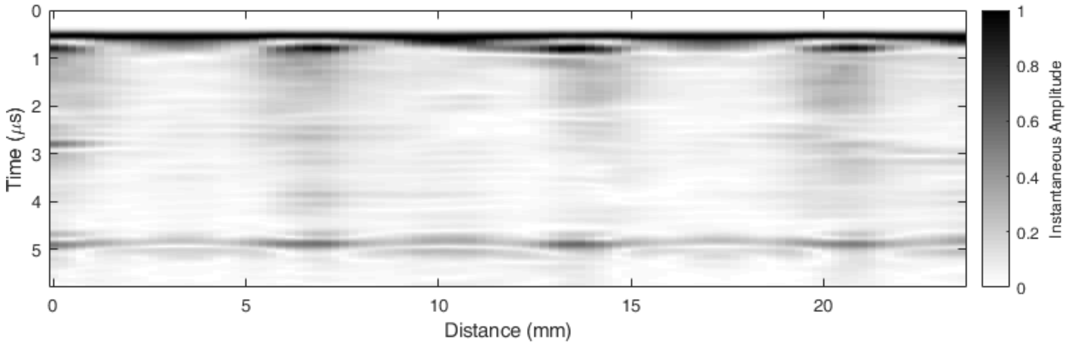

(b) *6.5 MHz*

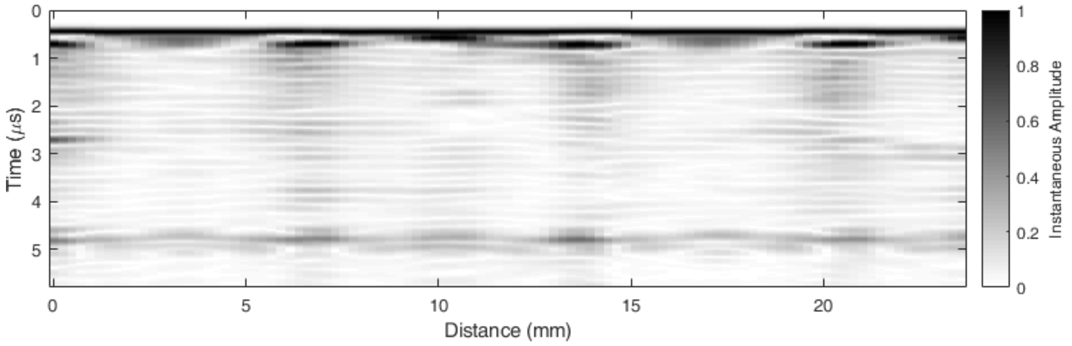

(c) *7.5 MHz*

Figure 5.27: *Instantaneous amplitude images of 'as built' FEA geometry for varying transducer frequency*

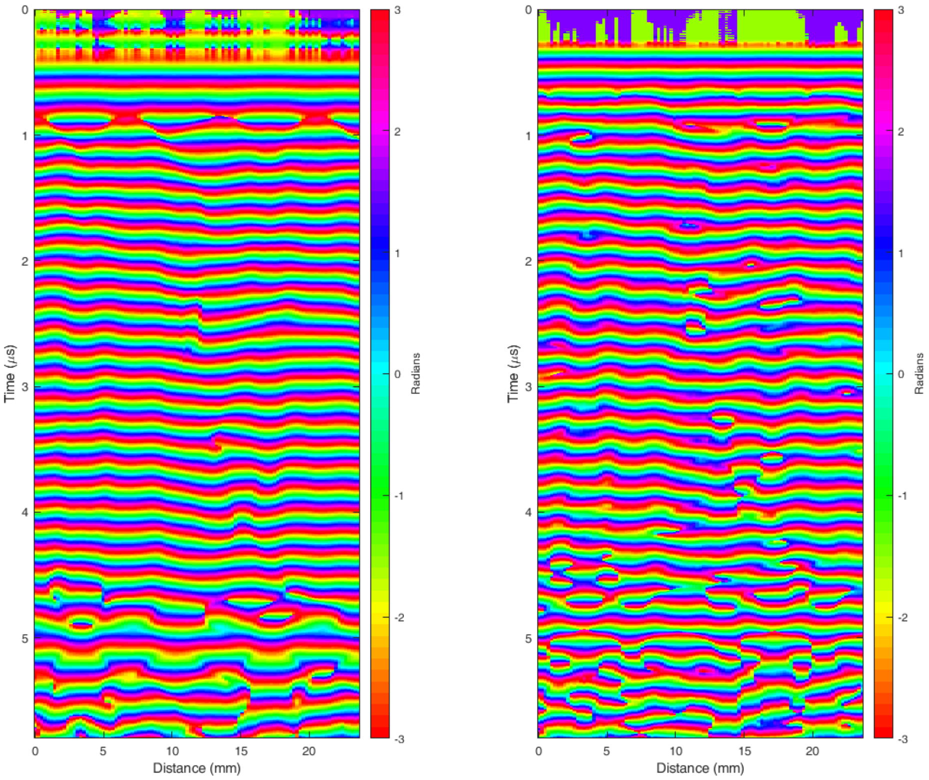

(a) *5 MHz* **(b)** *6.5 MHz*

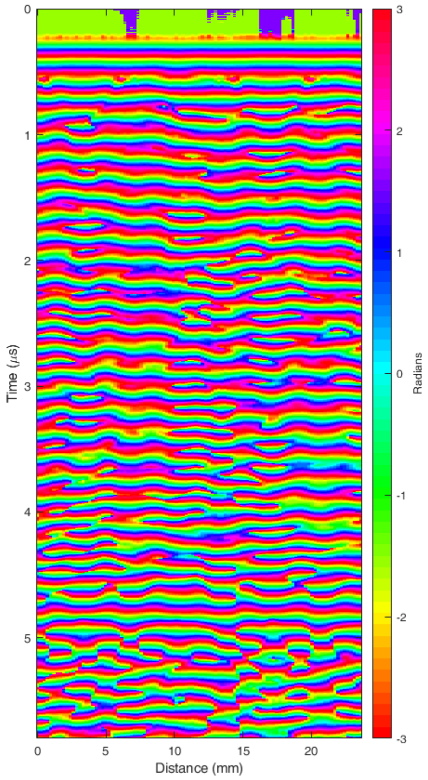

(c) *7.5 MHz*

Figure 5.28: *Instantaneous phase images of 'as built' FEA geometry for varying transducer frequency*

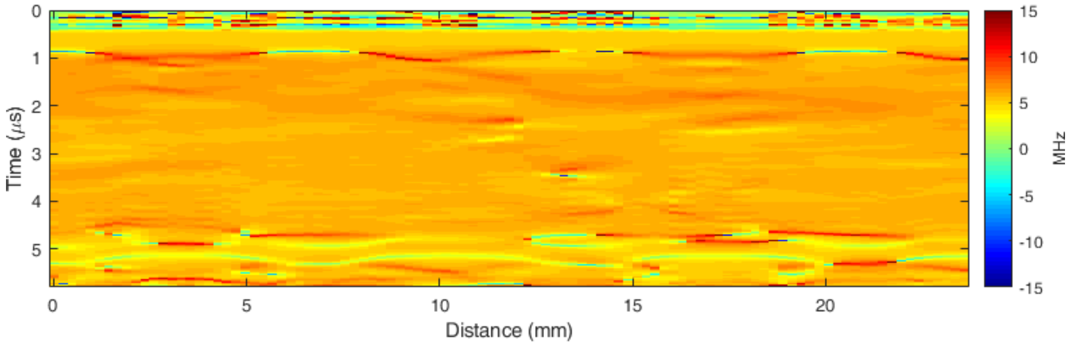

(a) *5 MHz*

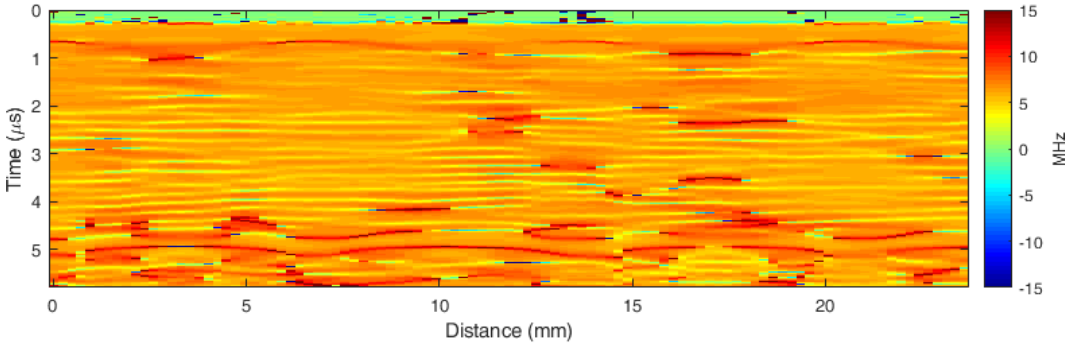

(b) *6.5 MHz*

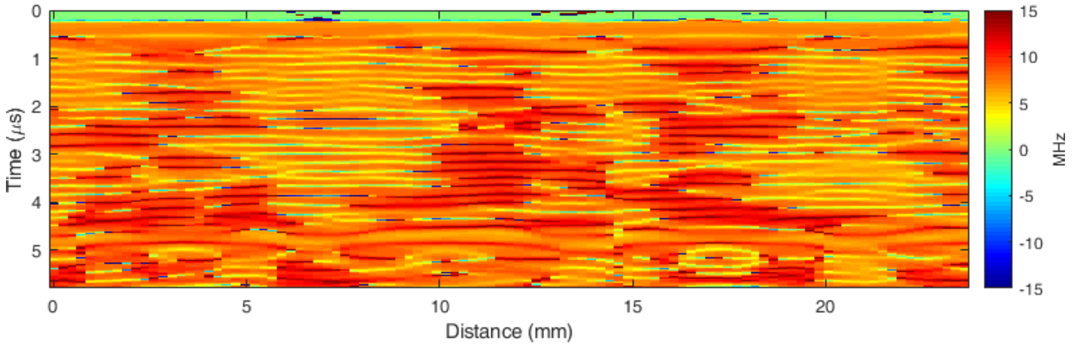

(c) *7.5 MHz*

Figure 5.29: *Instantaneous frequency images of 'as built' FEA geometry for varying transducer frequency*

The B-scan, Figure 5.26, and instantaneous amplitude, Figure 5.27, images for the 'as built' geometry show similarities to the previous, 'as designed' geometry, Figures 5.14 and 5.15, but display differences in the unidirectional ply layer responses. This is due to the 'as built' geometry no longer modelling the ply and resin layers as uniformly flat layers but have spatial out-of-plane variations. The top and bottom twill layers have the same geometry as before and similar responses can are observed in the 2D and 3D FEA simulation images.

The out-of-plane variations of the ply layers can be easily identified in the 5 MHz instantaneous phase plot, Figure 5.28(a), where each unidirectional ply can be identified. At this frequency, there is also a visual correlation between the ‘as built’ and ‘as designed’, Figure 5.16, instantaneous phase profile of both the top and bottom woven layers. For the ‘as built’ 7.5 MHz instantaneous phase image, Figure 5.28(c), there are instances where the second harmonic can be identified due to an increase in ply layer thickness.

The instantaneous frequency images, Figure 5.25, are similar to previous results for the ‘as designed’ geometry, Figure 5.17, with the 5 MHz images capable of identifying characteristic responses of the woven layers. The ‘as built’ bottom woven layer is slightly more distorted due to the inconsistent unidirectional layer structure. In the 7.5 MHz image, areas of higher frequency through the component thickness, due to a resonance frequency in the woven layer, can be seen when the top warp is above the weft toes.

5.3.5 Comparison with Experiment

The experimental B-scan images and their instantaneous parameters for both 5 MHz and 7.5 MHz inspection frequencies are shown in Figures 5.30 - 5.33. These B-scan images have been processed to align the peak response from the frontwall to remove any difference in stand off distance.

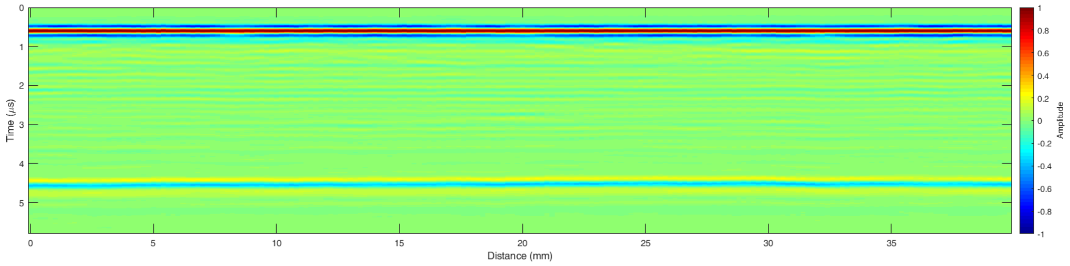

(a) *5 MHz*

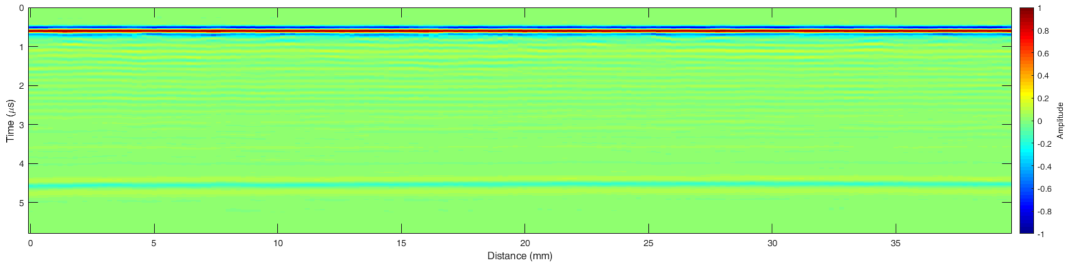

(b) *7.5 MHz*

Figure 5.30: *B-scan images for experimental data collection using two transducer frequencies*

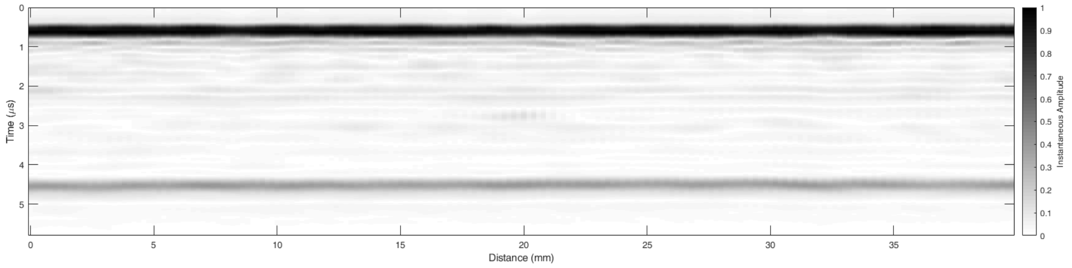

(a) *5 MHz*

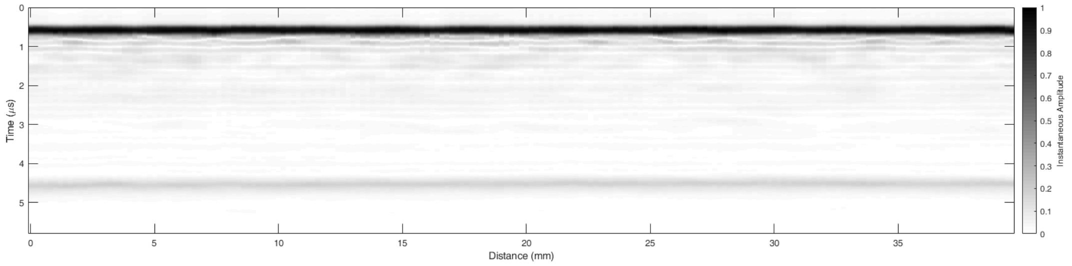

(b) *7.5 MHz*

Figure 5.31: *Instantaneous amplitude images for experimental data collection using two transducer frequencies*

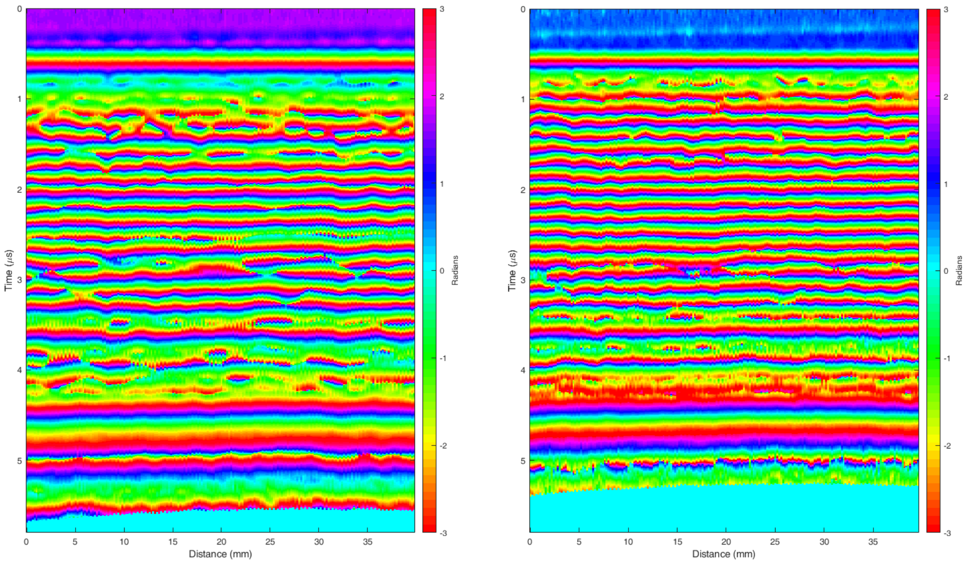

(a) *5 MHz* **(b)** *7.5 MHz*

Figure 5.32: *Instantaneous phase images for experimental data collection using two transducer frequencies*

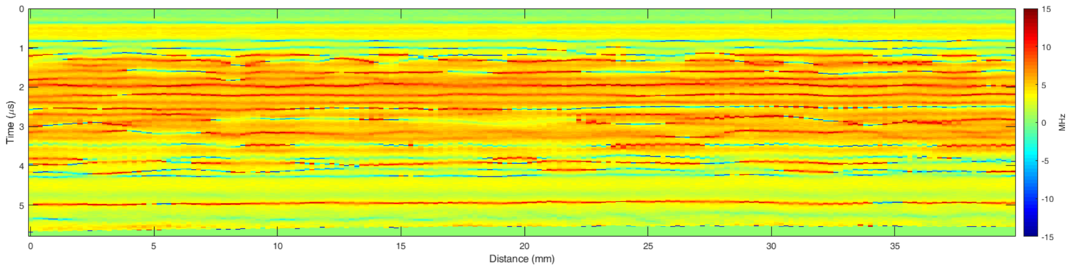

(a) *5 MHz*

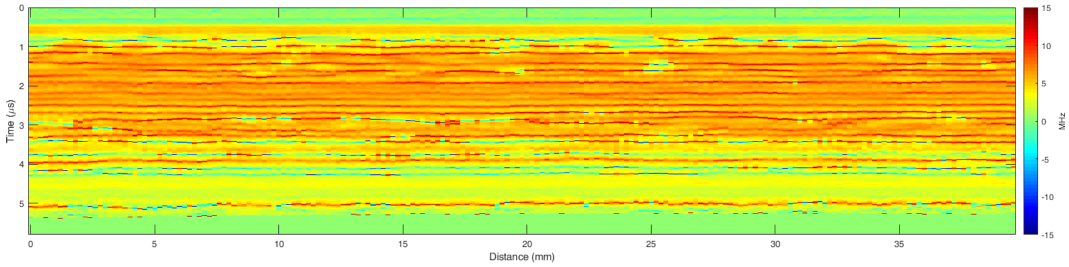

(b) *7.5 MHz*

Figure 5.33: *Instantaneous frequency images for experimental data collection using two transducer frequencies*

The B-scan, Figure 5.30, and instantaneous amplitude, Figure 5.31, plots for these experimental datasets illustrate both the frontwall and back wall as uniform responses. In the instantaneous amplitude plots, there is characteristic responses from the top woven layer visible below the main frontwall response. The unidirectional ply layer responses are almost uniform responses that reduce in amplitude as the depth into the component increases with minor increases in amplitude that indicative of a change in ply or resin layer thickness.

The instantaneous phase, Figure 5.32, allows for the unidirectional ply layers to be visualised, however does not provide a clear representation of the woven ply layers. These woven ply layer characteristics can be seen in the instantaneous frequency, Figure 5.33, plots, which also show regions where the unidirectional ply layers have some waviness and variation in out-of-plane orientation.

Comparison of the experimental results with the 'as built' FEA derived results, Figures 5.26 - 5.29, shows similarities in the B-Scan and Instantaneous amplitude plots. The woven layer structure can be identified more clearly in the 'as built' FEA model as the woven layers are approximated to 2D and have an ideal 'as designed' geometry. The instantaneous frequency images show the least correlation, which can be indicative of differences in transducer input signal. The FEA model has implemented a Ricker wavelet and so will have different characteristics, such as bandwidth, when compared with the experiment signal. This can lead to the 'as built' response being filtered to be the probe frequency rather than the ply resonance.

5.4 Discussion

The first parametric study conducted B-scan inspections on the 'as designed' geometry using different transducer frequencies, Figures 5.14 - 5.17. The F-number of the transducer was kept constant for each frequency and was set to recreate practical 5 MHz and 7.5 MHz transducers that would collect experimental data for comparing with the FEA derived results and validate the models. The other frequency simulated was 6.5 MHz which was the calculated resonance of the unidirectional ply layers in the composite sample. These simulations demonstrated the importance of selecting a suitable frequency for the test component in order to maximise the inspection performance. When possible, the inspection frequency should be selected to be as near as possible to the ply resonance of the component. The inspection frequency below the ply resonance, did provide a good ability to characterise the component, however due to the larger wavelength this frequency will not be able to identify the same level of subtle changes. When the frequency is increased above the ply resonance, the wavelength becomes shorter and can increase the resolution of inspections but for CFRP components this can also make it harder to interpret results to characterise the component.

A second parametric study was conducted with the transducer frequency fixed at 6.5 MHz and the F-number was varied by simulating different transducer focal lengths, Figures 5.18 - 5.21. Overall, changing the transducer F-number over the range of 2.5 - 5 did not have a major impact on the inspection's ability to characterise the inspected CFRP component. Nonetheless, as the F-number became larger a slight overall improvement in the ability to characterise the component was observed in the B-scan images. In the instantaneous amplitude plots, Figure 5.19, the warp and weft fibres in the bottom twill layer could be more clearly identified. Also, it appeared that the distortion created by the wave propagating through the top woven layer was reduced to give a more uniform response for the unidirectional ply layers in the instantaneous amplitude plot, 5.20. Also, the reduction of the impact caused by the top woven layer can be seen in the instantaneous frequency images, Figure 5.21, which also improve as the F-number increases.

The FEA geometry for the ‘as built’ model, was manually constructed from a photomicrograph of the composite sample. This can give a more realistic model geometry, as shown in similarities with experimental instantaneous phase and frequency images, but is limited to approximating to a 2D model. This assumes the geometry in the non-modelled direction as infinite and will over emphasise the response from ply waviness or an increase in resin thickness. This is highlighted in the B-scan and instantaneous amplitude images, which in practice, or in a 3D model, would have a lower response from spatial averaging. The manual generation of the model geometry from the photomicrograph is not ideal and slight inaccuracies have a big impact on the derived results. Refinement of this process will result in a more representative model geometry which offers the potential as a very useful tool for the evaluation and optimisation of CFRP component inspection.

Two experimental scans were performed on the composite and resulting B-scans have been presented to allow for comparisons with the FEA derived results and to provide some validation of the models. There are limitations of both modelling approaches taken, which lead to differences between the FEA derived and experimental B-scans. The ‘as designed’ geometry creates an ideal structure with uniform ply layers, which could easily be identified in the instantaneous phase B-scans. The uniform structure also allowed for the instantaneous frequency to show distinct features of the 2/2 twill woven layers. However, in practice the manufactured component does not have perfectly uniform ply layers as seen in the ‘as built’, Figure 5.29, and experimental results, Figure 5.33.

Ply layers have out-of-plane orientation changes that can impact the ability to visualise all of the unidirectional ply layers and make the woven layer characteristics harder to distinguish. The resin layer thickness will also vary in a practical component which will impact the wave behaviour as is propagates through the structure. In all FEA models, the resin layers were all an equal thickness and so would not account for these subtle variations. There is also uncertainty in the material properties implemented in the FEA models, which as shown in Section 4.2.3, can create discrepancy in derived results, such as changes in time of flight and reflection amplitudes.

5.5 Conclusion

This Chapter has presented the ability of simulation to evaluate and optimise the inspection set-up for CFRP components. The inspection scenario used was a focused single-element immersion inspection of a planar CFRP component containing unidirectional ply layers sandwiched between a top and bottom 2/2 twill layer. The simulations performed investigated the effect of varying input parameters had on the inspections ability to inspect and characterise the test component. Experimental datasets were collected and used to validate the FEA models ability to replicate practical performance.

Presented simulations demonstrate the benefit of modelling to aid the understanding of the ultrasonic response from CFRP components and the ability to optimise the inspection. Optimum inspection set-ups vary depending on the component under inspection and simulation offers a valuable tool to investigate inspection set-up in a reduced time frame. Through the use of parametric studies, input parameters such as transducer frequency and F-number can be investigated to determine their effect on the inspection and which set of parameters are optimum for a given inspection scenario.

Chapter 6

FEA Simulations to Evaluate and Optimise Inspection of Tapered CFRP Components

FEA Simulations to Evaluate and Optimise Inspection of Tapered CFRP Components

In this Chapter the ultrasonic inspection of tapered CFRP components is investigated through FEA simulations. Initial simulations are performed to replicate an experimental inspection of a tapered component to provide validation of the modelling approach. The FEA model geometry is generated using both the plybook method and using a cross sectional image from X-Ray CT data of the component. The plybook method is then utilised to demonstrate its capability to allow for inspections of different component structures to be evaluated and optimised using simulation. Three arbitrary tapered geometries are created with different severity of taper angle. Focused immersion ultrasonic B-scan inspections are simulated for each taper geometry. The resulting B-scans and amplitude maps are used to evaluate the inspection performance. The ability to detect defects, such as porosity and delaminations, is also investigated. Simulations are then used to optimise the inspection set up for the detection of a delamination defect located near the back wall in the tapered region. This work was presented at the 44th Annual Review of Progress in Quantitative Non Destructive Evaluation (QNDE), 2017.

6.1 Introduction

6.1.1 Motivation

Tapered CFRP components offer the ability to modify the component geometry while also reducing the overall weight. The change in component thickness is achieved by terminating individual ply layers at discrete locations known as ply drops. Different severity of taper angles can be designed by varying the location and number of ply drops in the component. The design of these tapered components is critical as the geometrical and material discontinuity at ply drop locations increase interlaminar stress levels, which can lead to delaminations [149].

The ultrasonic NDE inspection of tapered components is challenging due to the geometry of the internal ply layers. The termination of individual ply layers creates variance in the out-of-plane orientation of the plies around the ply drop. The level of out-of-plane orientation variance is related to the severity of taper angle in the component. These changes in orientation also cause different angles of incidence for an ultrasonic wave propagating through the structure. Moreover, the anisotropic material properties of CFRP mean that these changes in orientation and incidence angles can have a substantial impact on how waves propagate through the structure.

Having the ability to simulate ultrasonic inspections of tapered CFRP components offers many advantages. For a given tapered CFRP component, simulations can be undertaken to evaluate the performance of current inspection techniques. Simulations can then be used to optimise inspections or evaluate new inspection approaches to allow for optimal inspections to be performed on the component. Simulations could also be used to aid the design of the tapered components for inspectability. By simulating inspections for different severity of taper angles, the inspection performance can be evaluated to determine at which angle the inspection becomes insufficient at providing an accurate and complete inspection.

6.1.2 Method of Investigation

In this Chapter, initial FEA simulations are performed to validate the modelling approach by replicating an ultrasonic focused immersion inspection of a tapered CFRP component. FEA models of the inspection scenario are constructed and simulations are performed to generate B-Scan data. Similarly to the previous chapter, this initial FEA model geometry would be constructed using two different methods. The first was the plybook method, Section 4.2.6, to create an ‘as designed’ geometry, while the second created an ‘as built’ geometry by utilising an image of the component cross section taked from X-ray CT data. The experimental and FEA derived data from both approaches would be analysed through comparison of the derived B-scan images and images of the signals instantaneous amplitude and instantaneous phase.

To investigate the performance of ultrasonic inspections on tapered CFRP components, three components are designed with different severity of taper angles. The tapered components were generated in the FEA models via the plybook method. Again, simulations were performed to replicate a focused immersion B-scan inspection of each tapered component. As well as investigating the derived B-scan images, the inspections are also evaluated through the use of a B-scan amplitude map which indicates regions of low amplitude in the component. The ability to detect defects is then investigated and further simulations are performed to optimise the inspection of a delamination defect present in a challenging location in one of the taper components.

Defect detectability is investigated by comparing the results from simulations of a defect free taper to a taper containing defects. The signal to coherent noise ratio of the defect is calculated to give an indication of its detectability. Defects are implemented in the model by setting the material stiffness of a set of model elements to zero. These defects replicate porosity or delaminations, which are the most common defects present in manufactured CFRP materials.

The final simulations undertaken in this Chapter are to demonstrate how FEA simulations can be utilised to optimise the ultrasonic inspection of tapered CFRP components. A defect is placed in a taper between adjacent ply layers which have a large out of plane orientation. An initial normal incidence inspection is simulated to give a baseline performance, before the inspection is then optimised by determining the optimum inspection incidence angle to give the best response from the defect.

6.2 FEA Model Development

6.2.1 Real Component

6.2.1.1 Taper Geometry

The initial test component for the FEA model validation is a 16 unidirectional ply CFRP tapered sample that contains 8 ply drops. A cross section image of X-Ray CT data of the component can be seen in Figure 6.1. The sample was manufactured using IMA/M21 ply layers that consist of HexTow IMA fibres impregnated with HexPly M21 epoxy matrix. The ply layers had a thickness of 149 μm with a toughened, 40 μm, resin layer in between and the elastic material properties for the ply layers and resin layers can be seen in Tables 6.1 and 6.2 [150, 151]. The ply orientation lay up of the sample was $[0/45/0/-45]_{2S}$.

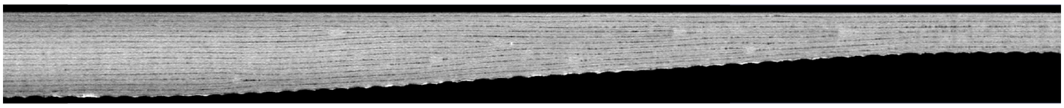

Figure 6.1: *Tapered CFRP Component*

Table 6.1: *Hexel IMA/M21 elastic material properties with E_{11} in the fibre direction*

Property		Value
Density (kg/m^3))		1580
Elastic Modulus (GPa)	E_{11}	162
	E_{22}	10
	E_{33}	10
Shear Modulus (GPa)	G_{12}	5.2
	G_{23}	3.5
	G_{13}	5.2
Poisson's Ratio	ν_{12}	0.35
	ν_{23}	0.5
	ν_{13}	0.3

Table 6.2: *HexPly M21 toughened resin material properties*

Property	**Value**
Density (kg/m^3))	1280
Young's Modulus (GPa)	3.3
Poisson's Ratio	0.42

The experimental data acquisition for this Section was kindly provided from the Ultrasonics and Non-destructive Testing research group at the University of Bristol. The inspection performed was an ultrasonic immersion C-scan using a single element, spherical focused probe. The probe had a nominal centre frequency of 7.5 MHz with a crystal diameter of 0.5″ and a 1.5″ (38 mm) focal length. The probe was positioned above the flat surface of the tapered CFRP component with 35.1 mm stand off from the front surface, putting the focus 1.5 mm into the composite. A normal incidence inspection was performed with a step size of 0.2 mm used for both the longitudinal and lateral axis directions. For the purposes of comparing the experimental data with FEA derived results, a linear scan across the tapered section was taken to produce a single B-scan of data.

The ultrasonic probe was represented as a pressure load in the FEA models using the previously described focused beam approximation, Section 5.2.3.1. To match the experimental transducer focus, a flat transducer was simulated with a width of 1.8 mm and a focal length of 5.4 mm. This approximation allows a more computationally efficient 2D model to be implemented and also the lower propagation distance will reduce numerical dispersion effects.

6.2.1.2 Plybook Generated Geometry

The first FEA model geometry was constructed using the CFRP taper design specifications in the form of a plybook, as described in Section 4.2.6. Using the X-Ray CT data, the location of the ply drops could be determined to allow for the lengths of each ply layer to be added to the plybook. This approach would generate an idealised geometry that represented the design specification of the component.

The plybook was created as a CSV file with the information shown in Table 6.3, containing three columns of information. The first column contained the ply number, the second the ply length and the third the ply layer orientation. The plybook was read into the Matlab script and a TexGen python file was generated. This file was run in TexGen to produce the component and then exported as an Abaqus voxel file. The generated information was finally converted into a table file ready for importing into the FEA model, as illustrated in Figure 6.2.

Table 6.3: *Tapered CFRP component plybook*

Ply Number	**Length (mm)**	**Orientation (°)**
1	35.44	0
2	35.44	45
3	35.44	0
4	35.44	-45
5	10.89	0
6	22.49	45
7	28.01	0
8	16.50	-45
9	35.44	-45
10	35.44	0
11	14.42	45
12	24.91	0
13	18.97	-45
14	7.7	0
15	35.44	45
16	35.44	0

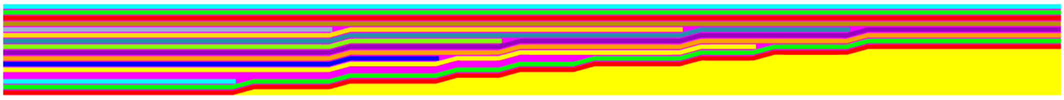

Figure 6.2: *Tapered CFRP component FEA model geometry*

6.2.1.3 Image Processing Generated Geometry

The second approach to generate the FEA model of the tapered CFRP component involved using image processing on an image of the component cross section taken from X-Ray CT data. This would produce a more representative FEA model based on the actual component and is based on the process described in Section 4.2.5. This work was conducted in collaboration with Dr Paul Murray from the Electronic and Electrical Engineering Department at the University of Strathclyde.

The process for generating the FEA model geometry from the X-Ray CT data is outlined below:

- Averaged cross sectional image of sample generated from CT data
- Image processing conducted to generate 2D voxel image, Figure 6.3
- Coordinates of individual ply layers centreline extracted
- Extracted centreline coordinates input into TexGen input file
- TexGen input file executed to generate Abaqus voxel file
- Abaqus voxel file converted into a table file and imported into FEA model, Figure 6.4

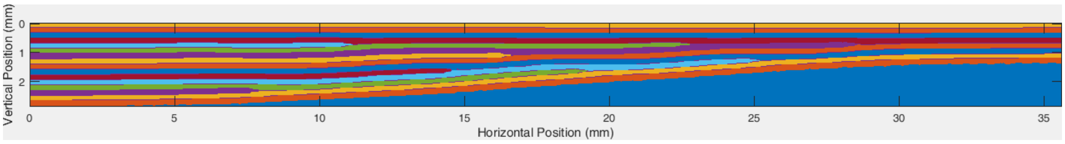

Figure 6.3: *Tapered CFRP somponent image processing result*

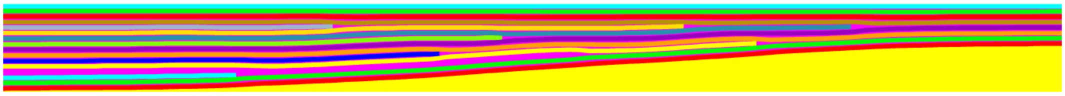

Figure 6.4: *Tapered CFRP component FEA model geometry*

6.2.2 Varying Taper Angle Components

Three tapered CFRP components were designed using the plybook approach (containing an increasing number of ply drops to provide different severity of taper angles). To maintain consistency across the tapers, the ply and resin thickness is kept constant while the ply lay up was also kept as similar as possible. The following design guidelines taken from literature were used to determine the location of the ply drops in each of the tapered components [84, 152, 153]:

- Laminate symmetry in constant thickness sections should be maintained
- Plies should be dropped in decreasing order of stiffness
  - 0° plies should be dropped near the thick section
  - ±45° plies should be dropped in between the thick and thin sections
  - 90° plies should be dropped near the thin section
- Dropping 0° when adjacent to a 90° ply should be avoided
- Inner plies should be dropped first

These three taper designed were constructed using *Hexcel IM7/8552* ply layers and *8552* resin as described in Section 4.2.1, and Tables 4.1 and 4.3. The components were designed with 250 μm ply layers and an inter-ply resin thickness of 10 μm. The components had a total length of 50 mm and the tapered region containing the ply drops was contained in the central 10 mm region. The total number of plies for each taper was kept low to reduce the simulation computation demands, while aiming to achieve taper angles of approximately 20°, 30° and 40°. Full design details of the three tapers are provided in Table 6.4.

Table 6.4: *Taper components details*

Taper Number	Number of plies	Number of ply drops	Taper angle (°)	Thick section lay-up	Thin section lay-up
1	17	9	18	$[[0/\text{-}45/90/45]_s\bar{0}]_s$	$[0/45/90/\text{-}45,\bar{0}]_s$
2	25	16	27	$[[0/\text{-}45/90/45]_3\bar{0}]_s$	$[0/45/90/\text{-}45,\bar{0}]_s$
3	33	24	41	$[[0/\text{-}45/90/45]_{2s}\bar{0}]_s$	$[0/45/\text{-}45/90,\bar{0}]_s$

The designed plybooks were then used as inputs into the Matlab script to generate TexGen python input files, as described in Section 4.2.6. The generated TexGen textiles can be seen in Figure 6.5. Each of the taper geometries were output as Abaqus voxel files before being converted into table files using the Matlab script.

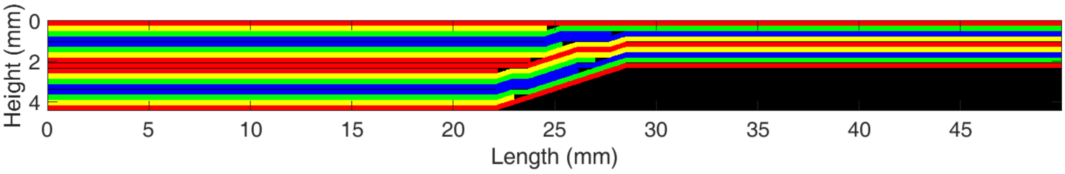

(a) *Taper 1 - 18° taper angle*

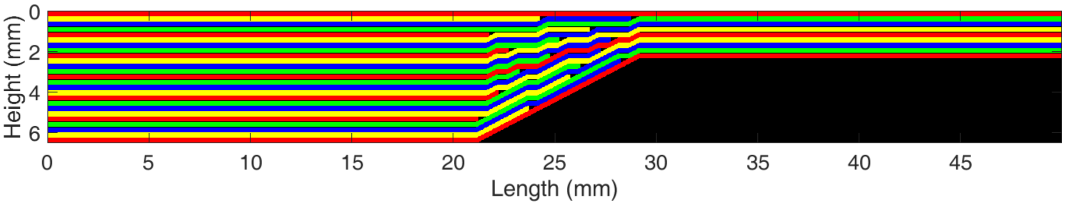

(b) *Taper 2 - 27° taper angle*

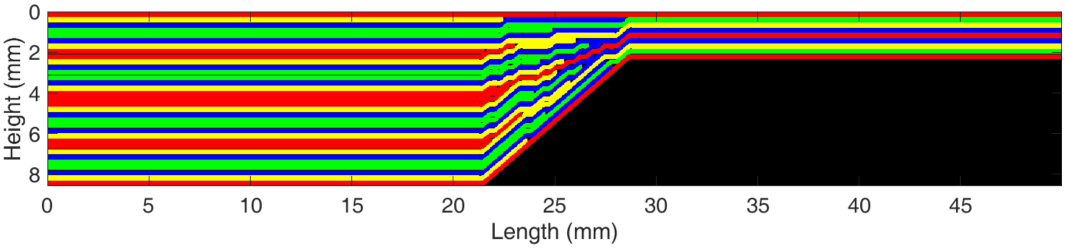

(c) *Taper 3 - 41° taper angle*

Figure 6.5: *Taper geometries where red is 0° plies, green is 45° plies, blue is 90° plies and yellow is −45° plies*

The same transducer focus angles were maintained, however the frequency was dropped to 6MHz to match the ply layer resonance [94, 99]. With the change of frequency, the FEA model transducer width was increased to 2.2 mm with a focal length of 6.6 mm to match the focusing of a 1.5” focal length transducer. For all simulations, the transducer was focused on the mid plane of the component to allow for optimal lateral resolution over the component thickness [154].

6.2.3 B-scan Amplitude Map

A challenge when ultrasonically inspecting a tapered CFRP component is the refraction of the ultrasonic wave propagating through the structure. This is caused by waves arriving at the ply and resin layer interface at oblique incidence angles. Refraction of the ultrasonic wave can lead to areas of the component not being inspected as well as intended. Defects in these areas then become more challenging to identify and locate due to the lower signal amplitude incident on the defect. It is therefore desirable to be able to identify these areas and evaluate inspection performance on tapered components.

The performance of an inspection of a tapered CFRP component can be evaluated through the use of a B-scan amplitude map. This amplitude map can be generated through FEA derived results and provides a visual illustration of the inspection performance by showing regions of low amplitude which are likely to correspond to poor contrast of defect to good material.

When simulating the ultrasonic B-scan, as well as predicting the received time trace, the maximum velocity of each node in the model is calculated and stored. Plotting this maximum particle velocity allows for the beam profile to be illustrated. Once all the simulations are performed, the B-scan amplitude map can be generated by combining the maximum velocity data from each individual simulation. The maximum value at each point in the component is taken to calculate the peak velocity at each point during the entire B-scan. This allows for the B-scan amplitude to be plotted and can be used to identify areas of the component with a lower amplitude. This generation process is illustrated in Figure 6.6.

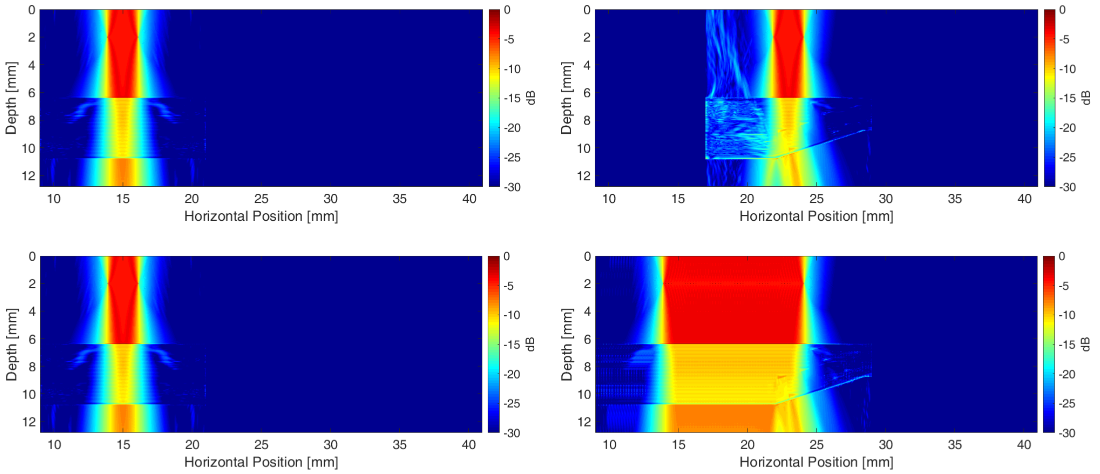

(a) *Transducer at horizontal position 15 mm*

(b) *Transducer at horizontal position 23 mm*

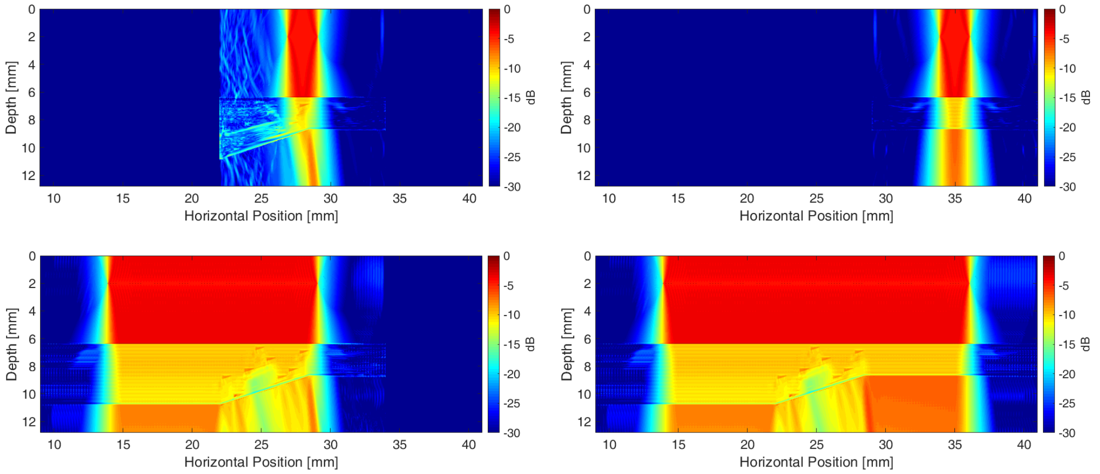

(c) *Transducer at horizontal position 28 mm*

(d) *Transducer at horizontal position 35 mm*

Figure 6.6: *B-scan amplitude map generation. The top image in each sub-figure contains a maximum velocity plot from an individual simulation, while the bottom image contains the generated B-Scan amplitude map*

In Figure 6.6 (b) and (c), the maximum velocity plot for the individual simulation demonstrates the bending of the beam as it travels through the tapered region of the component. This bending is due to the refraction that occurs as the acoustic wave is incident on the material interfaces at oblique incidence angles. As the taper angle increases, the level of beam bending that occurs will increase and result in areas of the component that will be inefficiently inspected due to a reduced signal amplitude penetrating that location. By combining these individual plots into a B-scan amplitude plot, it allows for the complete inspection to be visually evaluated and identify areas in the component that have the potential to be challenging to reliably inspect.

6.2.4 Defect Incorporation

To investigate the ability to detect defects in tapered CFRP components, simulations were performed with structures containing defects. Common defects in CFRP components include porosity, which is the presence of small voids in the resin matrix, and delaminations or disbonds, where adjacent plies become separated. These defects have a detrimental impact on the mechanical strength of the component and so early detection of them is highly important.

Porosity and delamination defects were inserted into the Taper 2 geometry to allow for the ability to detect the defects to be evaluated. The inspections performed replicated the same inspection set up as the B-scans where a normal incidence, 6 MHz focused inspection is performed. The simulation of porosity or delamination defects can be achieved through the addition of void elements in the model geometry. Void elements have zero stiffness and will act as a reflector to ultrasonic waves, similar to how porosity or delamination defects behave.

Porosity defects were inserted into the taper structure at four ply drop locations. This was achieved by creating a circular region of void elements in the resin pocket of a ply drop. The porosity defects had a diameter of 0.2 mm, which is approximately equal to half the wavelength of the input wave. Three delamination defects were also included in the Taper 2 structure by inserting a 0.3 mm wide and 0.04 mm thick void slot on the interface of two adjacent ply layers. Two delamination defects were inserted in flat sections of the component at either side of the taper region and the third delamination defect was inserted in the middle of the taper region. These defects are illustrated in Figure 6.7.

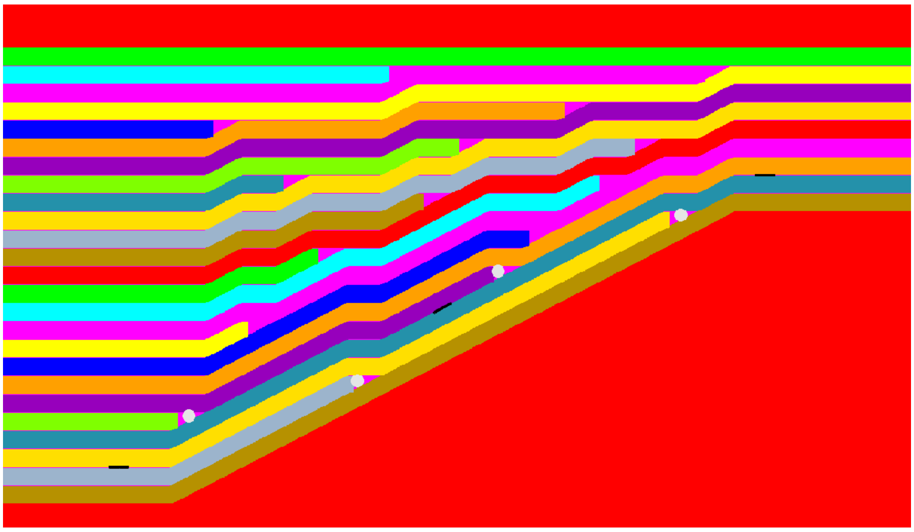

Figure 6.7: *Illustration of defects in Taper 2 components with porosity defects shown as white circles, numbered 1 to 4 from left to right, and delamination defects shown as black slots, numbered 1 to 3 from left to right*

The defect detectability was determined by comparing A-scans performed on the taper structure with and without the defect and then determining the signal to coherent noise ratio (SCNR) of the defect signal. The SCNR values were calculated using Equation 6.1 [155], where the noise relates to coherent noise generated by reflections from the internal structure.

$$SCNR_{dB} = 20\log_{10}\frac{A_{Signal}}{A_{Noise}} \tag{6.1}$$

A_{signal} is calculated as the maximum amplitude of the defect response and A_{noise} is calculated as the root mean square (RMS) value of the interply reflections from the defect free response.

6.3 FEA Derived B-scan Results

6.3.1 Comparison with Experiment

6.3.1.1 B-scan Images

The experimentally collected and FEA derived B-scan datasets were cropped to show the front wall and back wall reflections of the tapered CFRP sample. The full B-scan data and their instantaneous amplitude and instantaneous phase can be seen in Figures 6.8 - 6.10. The aspect ratio of the instantaneous phase images has been adjusted for improved visualisation.

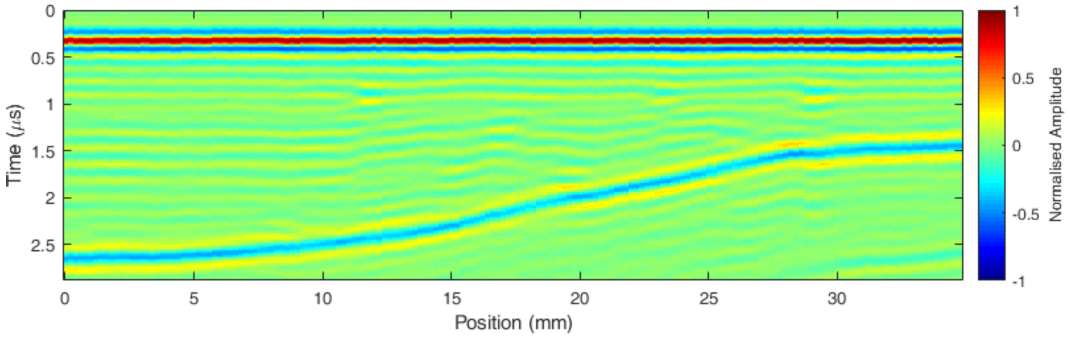

(a) *Experiment*

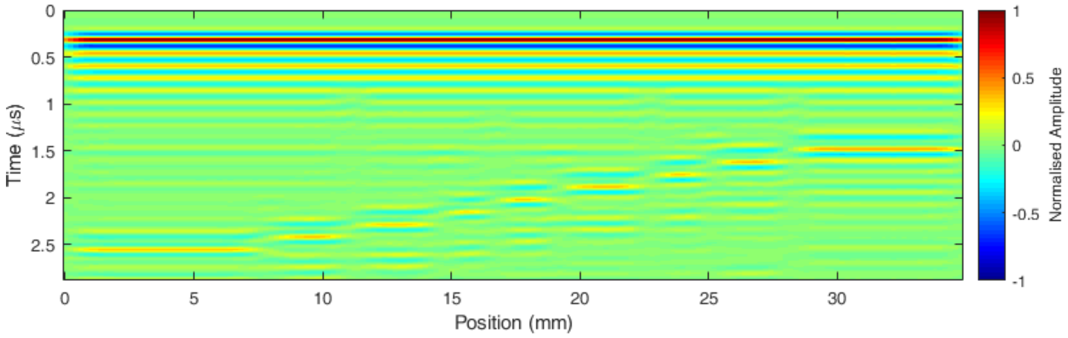

(b) *FEA derived - 'As designed' geometry*

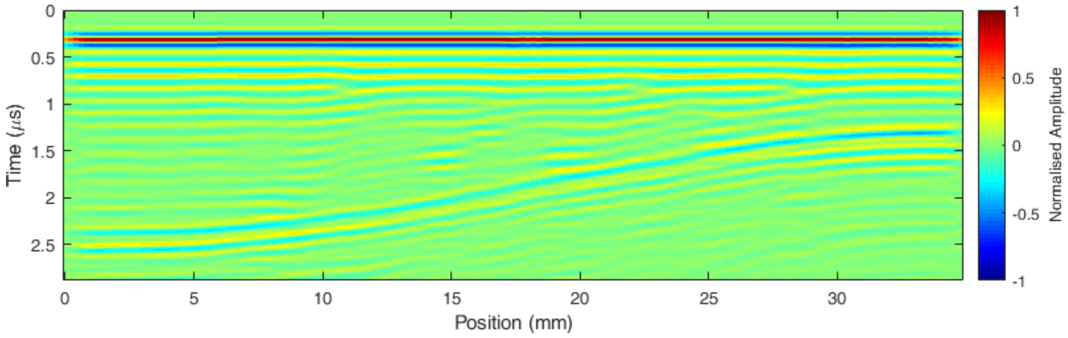

(c) *FEA derived - 'As built' geometry*

Figure 6.8: *B-scan images of tapered CFRP component*

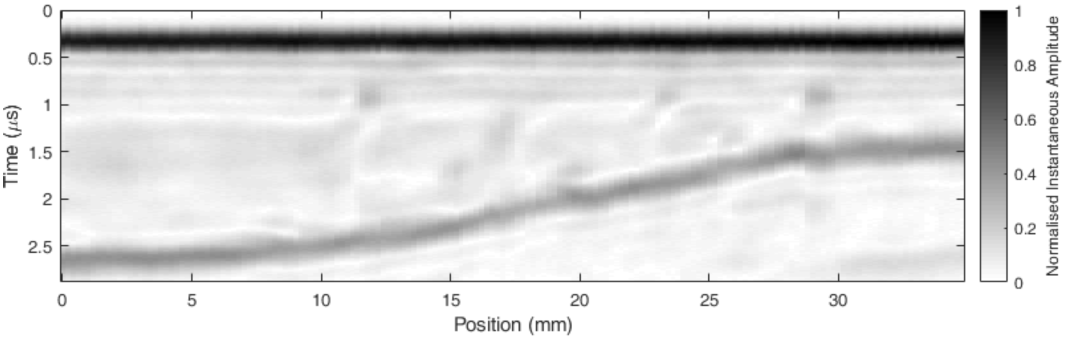

(a) *Experiment*

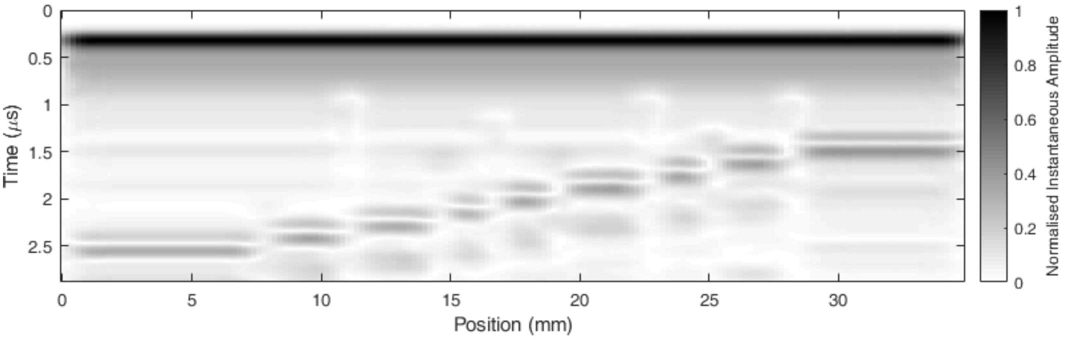

(b) *FEA derived - 'As designed' geometry*

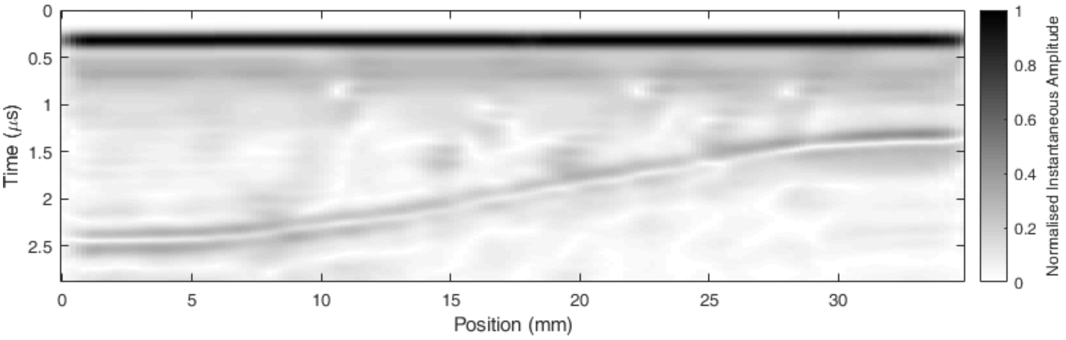

(c) *FEA derived - 'As built' geometry*

Figure 6.9: *Instantaneous amplitude images of tapered CFRP component*

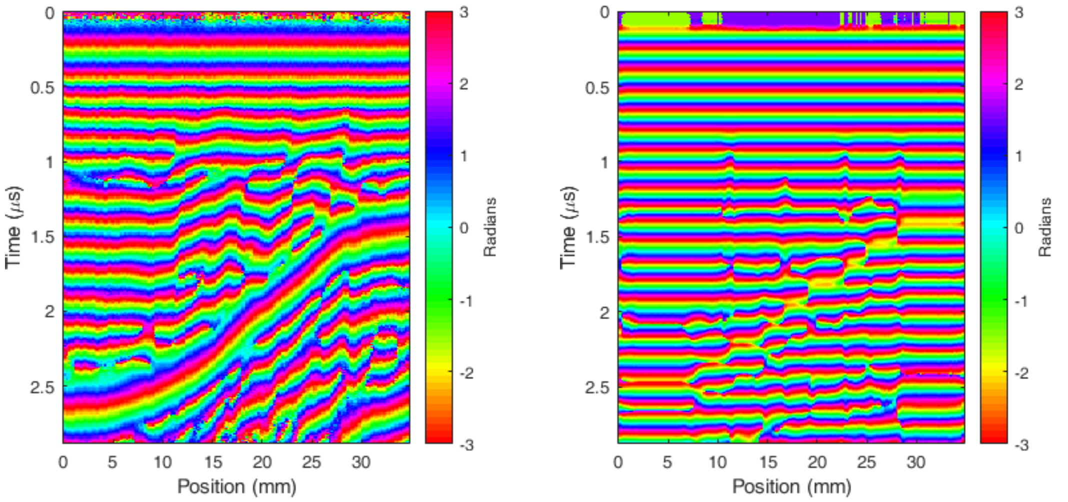

(a) *Experiment* **(b)** *FEA derived - 'As designed' geometry*

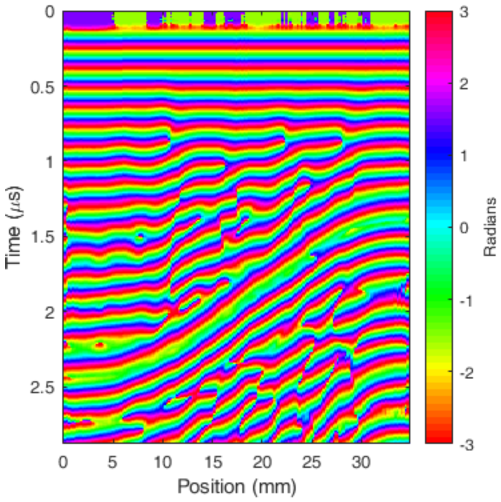

(c) *FEA derived - 'As built' geometry*

Figure 6.10: *Instantaneous phase images of tapered CFRP component*

6.3.1.2 Analysis

Comparison of the B-scans and the instantaneous images shows a reasonable correlation between the experimental and FEA derived results. The main difference is in the back wall outline for the plybook geometry which is due to the taper geometry having an ideal structure which conforms differently around plydrops. This is highlighted in Figure 6.11, which plots the out of plane ply orientation in the FEA model geometries. This shows the very tight conformity of ply with only regions of different orientation around individual plydrops. However, in the image geometry, the ply orientation changes are very gradual which is more representative of the practical component. Improvements could be implemented to improve the plybook generated geometry by altering how ply layers conform around a ply drop.

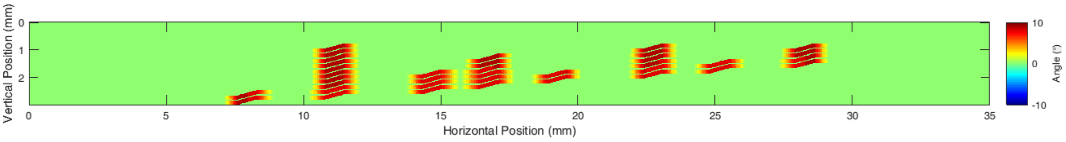

(a) *'As designed' geometry*

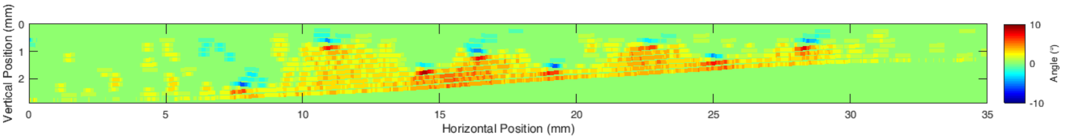

(b) *'As built' geometry*

Figure 6.11: *Out-of-plane ply layer orientation for (a) 'as designed' and (b) 'as built' FEA model geometry*

In the instantaneous phase plots, Figure 6.10, there is a good correlation between experiment and the 'as built' FEA geometry, where the back wall and ply drop locations can be clearly identified. At a ply drop there is an increase of resin thickness which results in a slightly longer propagation time and so a longer phase progression is seen [137]. The 'as designed' FEA geometry does not match experiment as well, which indicates the geometrical representation of the ply drop is not very representative. As previously mentioned, in this ideal geometry the plies conform tightly and so there is a difference in the ply out-of-plane orientation and the shape and size of the resin pocket. This geometrical representation could be improved by modifying how the ply layers conform around a ply drop and the shape of the resin filled pocket, to give a more realistic structure.

The taper sample used in this Section contained toughened resin layers with a thickness of 40 μm. The toughened resin layers have a stronger reflection coefficient than non toughened resin layers, which are much thinner [137]. These toughened laminates also generate phase singularity, where the phase of the signal is unknown due to zero amplitude in the signal [156]. Observing A-scans derived from the FEA models, these phase singularities can be observed, and can be seen at 1.2 - 1.3 μs in Figure 6.12. This demonstrates the FEA model ability to predict experimental behaviour and become a useful tool to help understand and improve ultrasonic inspections.

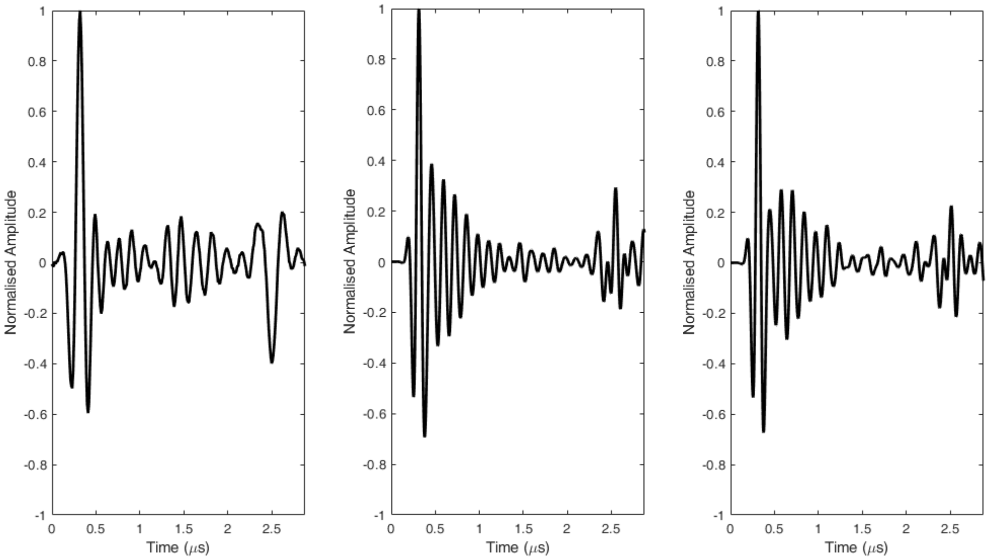

(a) *Experiment* **(b)** *'As designed'* **(c)** *'As built'*

Figure 6.12: *Phase singularity signals seen 1.2 - 1.3 μs in Experimental and both 'as designed' and 'as built' FEA derived A-scan*

6.3.2 Evaluation of Inspection Performance with Increasing Taper Angle

6.3.2.1 B-scan Images

The FEA derived B-scan and amplitude map images for each taper geometry are presented in Figures 6.13 - 6.15.

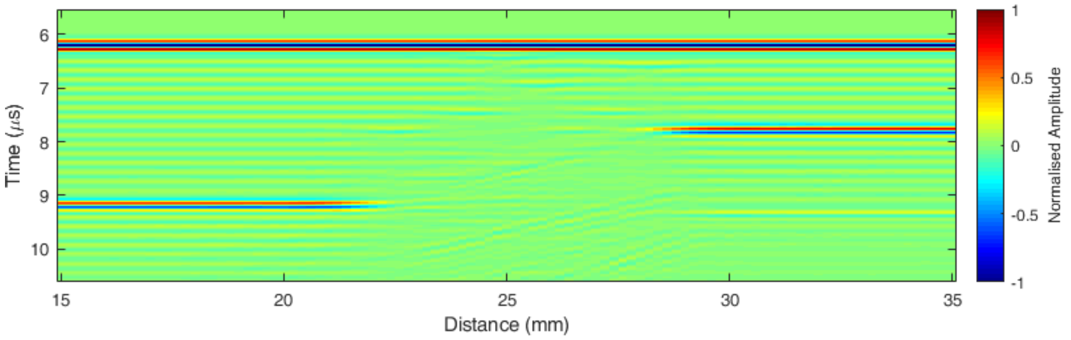

(a) *B-Scan*

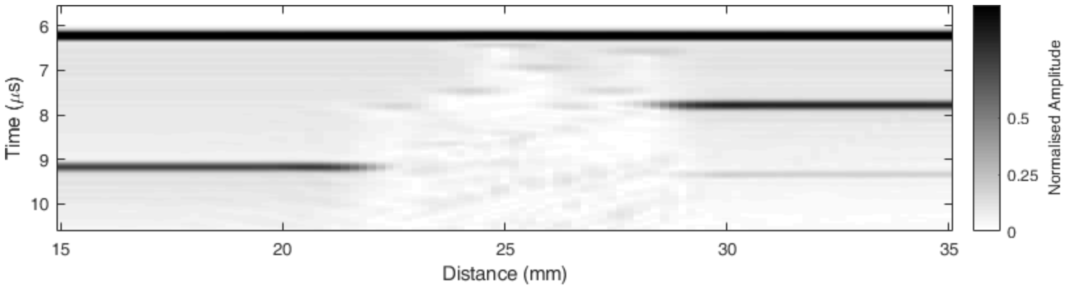

(b) *Instantaneous Amplitude*

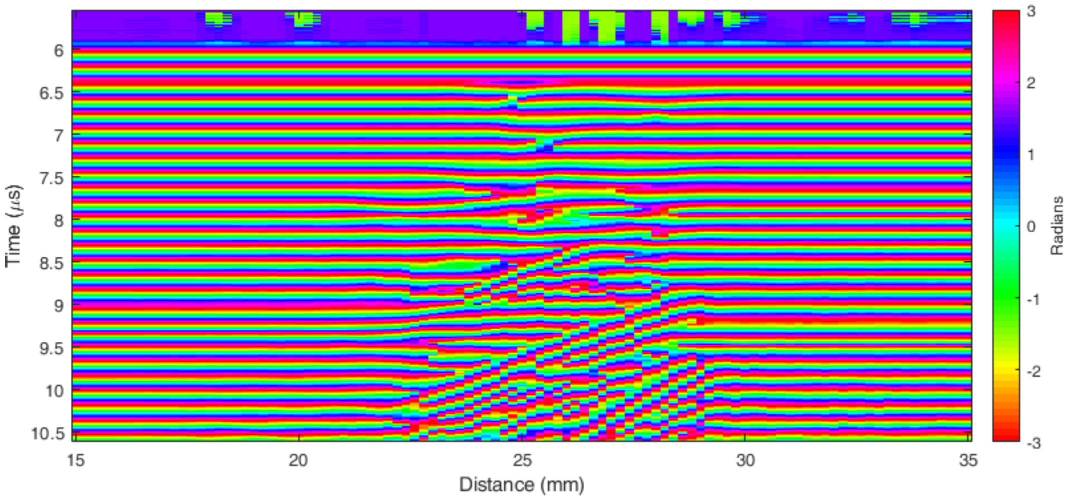

(c) *Instantaneous Phase*

Figure 6.13: *FEA derived B-scan results for taper 1*

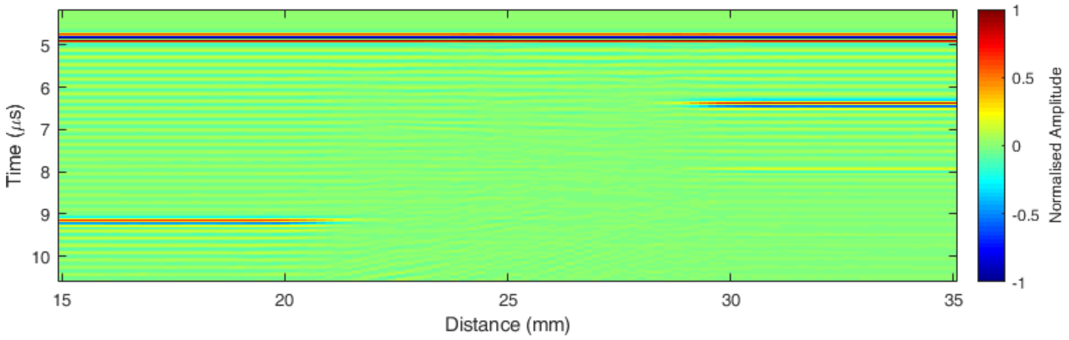

(a) *B-Scan*

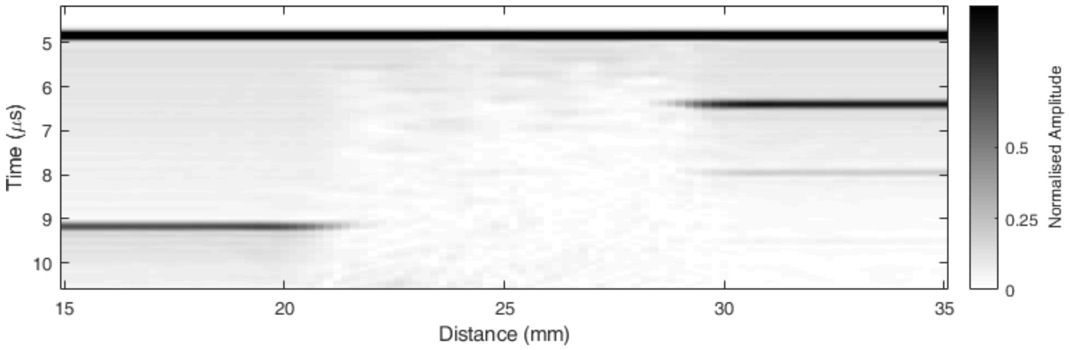

(b) *Instantaneous Amplitude*

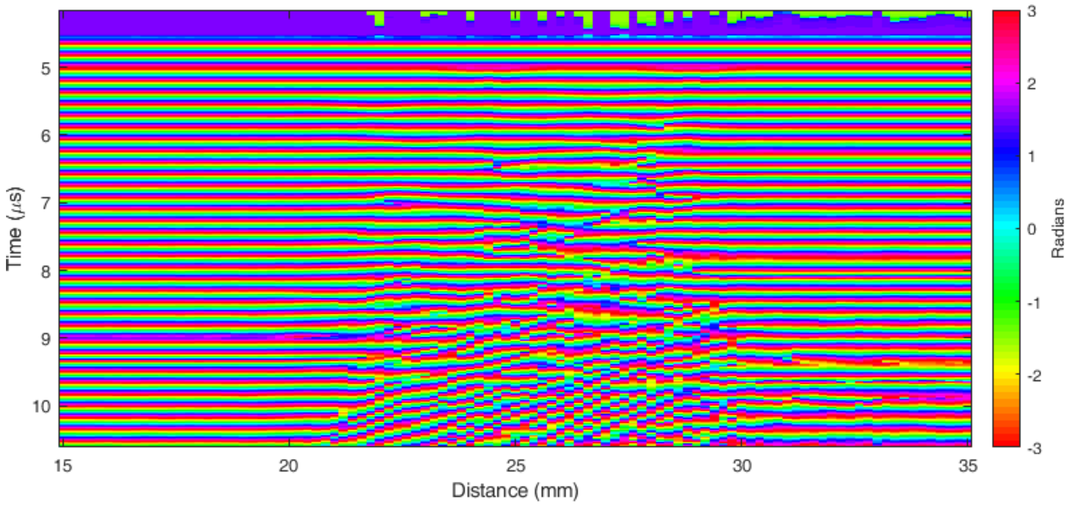

(c) *Instantaneous Phase*

Figure 6.14: *FEA derived B-scan results for taper 2*

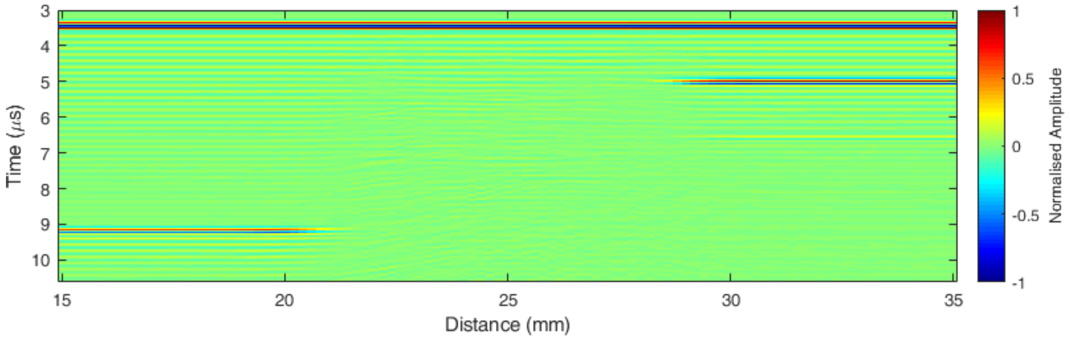

(a) *B-Scan*

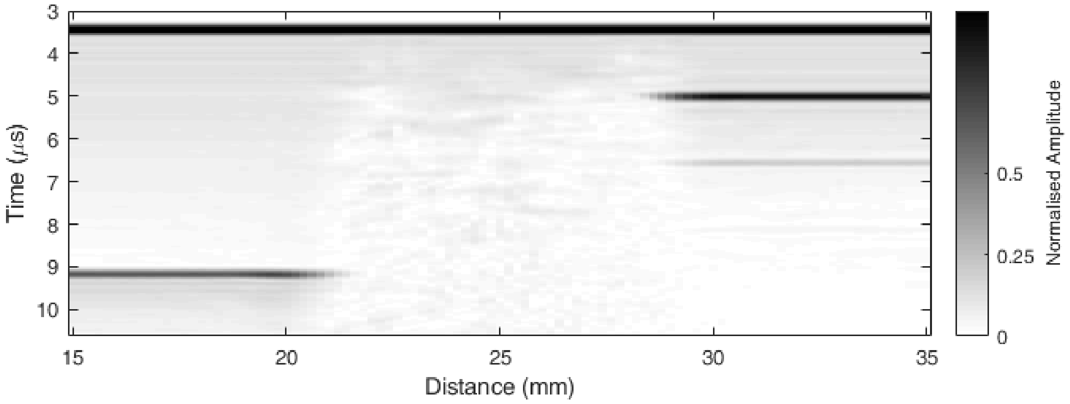

(b) *Instantaneous Amplitude*

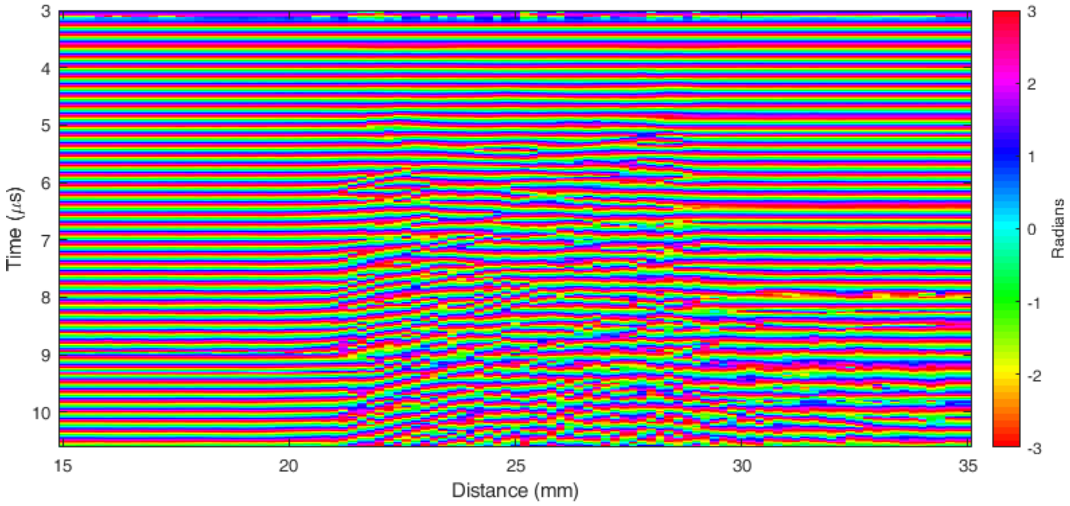

(c) *Instantaneous Phase*

Figure 6.15: *FEA derived B-scan results for taper 3*

6.3.2.2 Amplitude Maps

The FEA derived amplitude map images, in dB scale, for each taper geometry are presented in Figure 6.16.

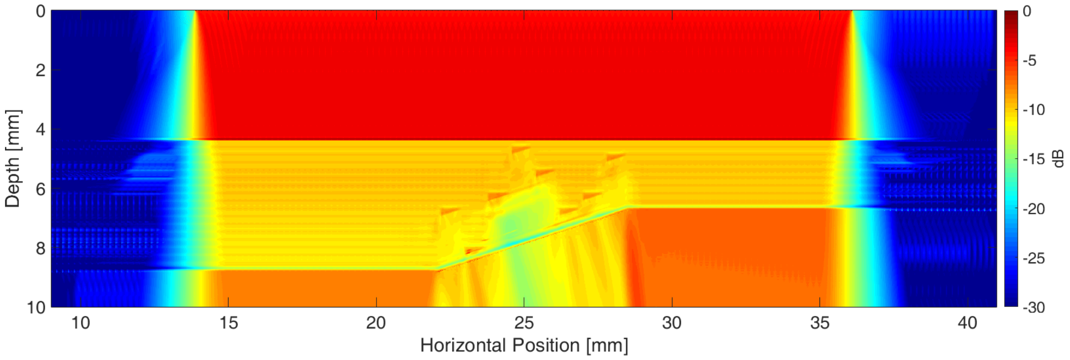

(a) *Taper 1*

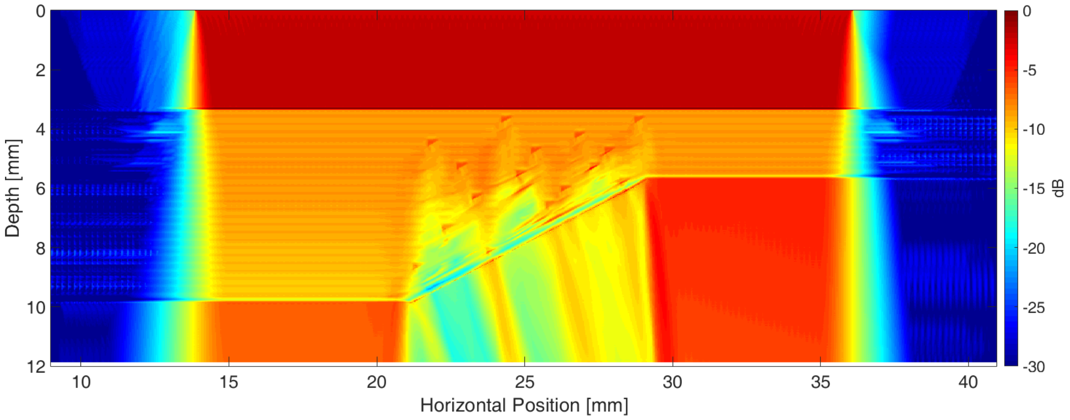

(b) *Taper 2*

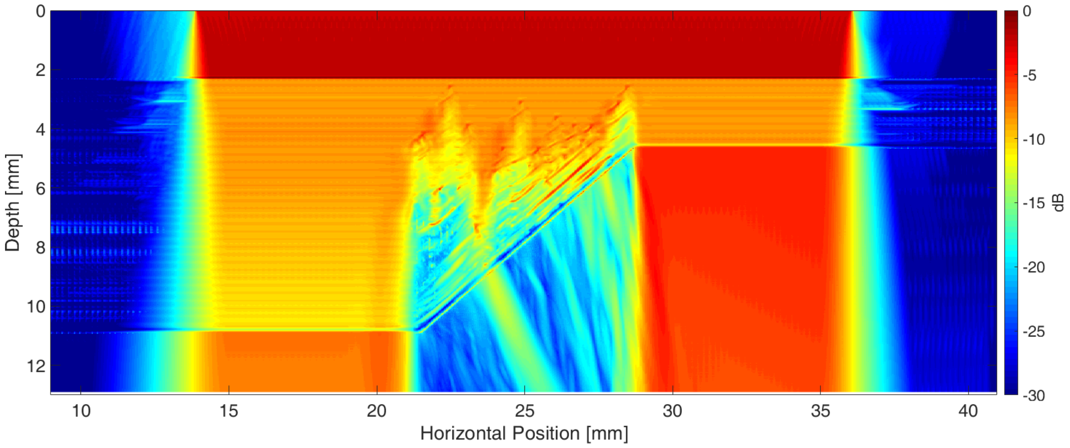

(c) *Taper 3*

Figure 6.16: *FEA derived amplitude map results for increasing taper angle components*

6.3.2.3 Analysis

In each B-scan and instantaneous amplitude image, (a) and (b) in Figures 6.13 - 6.15, the back wall can clearly be identified in the flat sections of the taper. For the tapered region, the back wall signal is not reflected back to the transducer and is only just visible for Taper 1 and completely missing for the higher angled taper geometries in Tapers 2 and 3. Also visible in each B-scan is the reflections from the ply layer interfaces and in the tapered region, stronger reflections from the resin pockets at ply drops near the top surface can also be identified. In the taper region, the ply layer interface and resin pocket reflections become more distorted as the taper angle and depth increases due to the increased scattering and refraction of the wave.

The instantaneous phase images for the tapers, (c) in Figures 6.13 - 6.15, can clearly illustrate the ply layers in the flat sections. The images can also indicate ply drop locations that are close to the surface of the component but as the ply drops become deeper in the taper region of the structures, they become much harder to identify.

To allow for the B-scan inspection to be evaluated, B-scan amplitude maps were generated for each taper geometry, presented in Figure 6.16. It can be seen in the flat sections that the amplitude decreases with depth as expected due to attenuation of the wave from scattering at ply layer interfaces. In the taper region of the CFRP component, it can be seen that the amplitude begins to decrease further due to the internal refraction and reflections that have occurred. As the taper angle increases, regions of low amplitude become more identifyable and for the highest taper angle component, Taper 3, it is very clear to see there are areas with a signal reduction of 10dB from the flat section of the sample at the same depth that indicates the ultrasound has not effectively penetrated this area.

6.3.3 Defect Detection

6.3.3.1 B-scan Images

The FEA derived B-scan and instantaneous amplitude and phase images for Taper 2 with the porosity and delamination defects is presented in Figure 6.17.

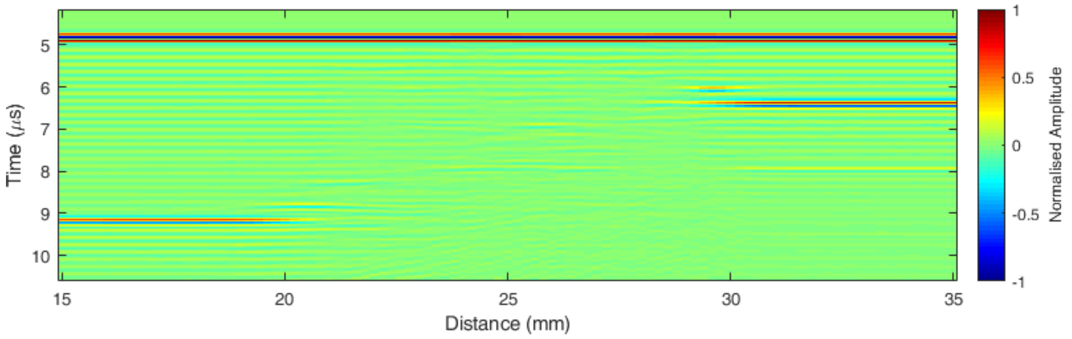

(a) *B-Scan*

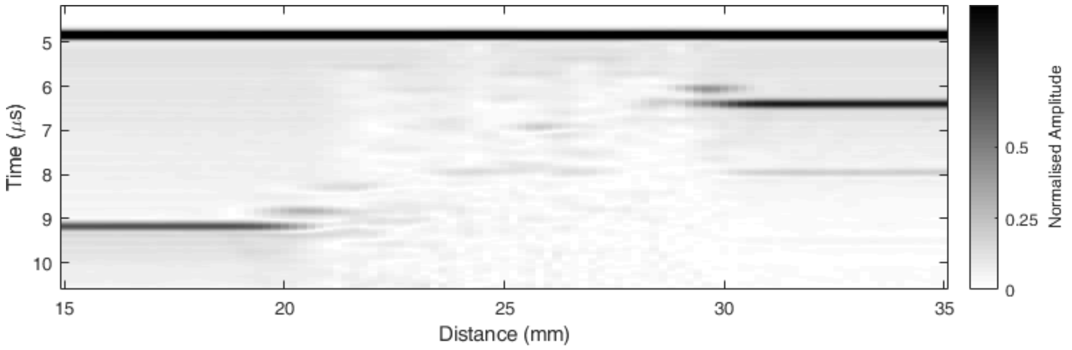

(b) *Instantaneous Amplitude*

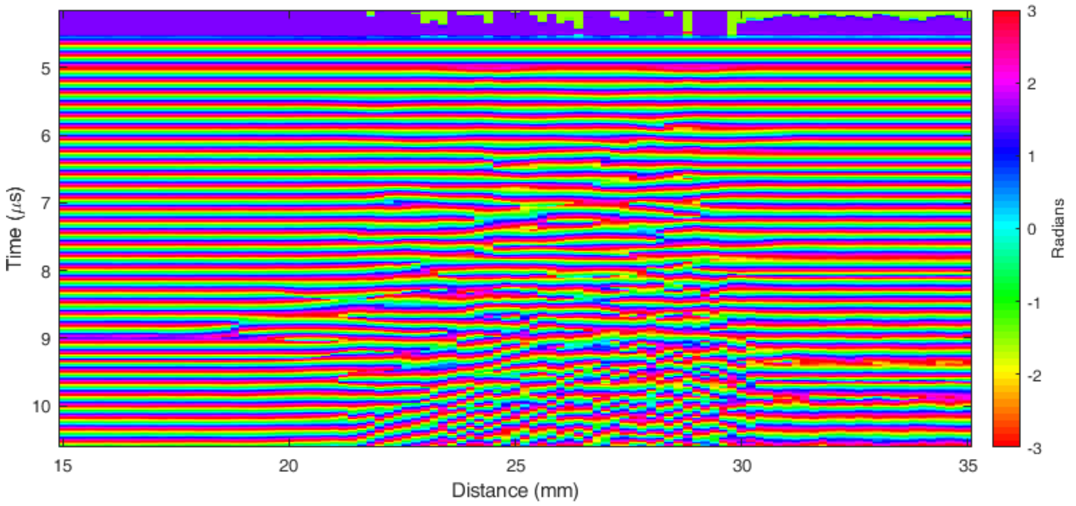

(c) *Instantaneous Phase*

Figure 6.17: *FEA derived B-scan results for taper 2 with defects present*

6.3.3.2 Analysis

Four 0.2 mm diameter porosity defects were inserted into different resin pockets at ply drop locations and three 0.2 mm wide delamination defect was inserted between ply layers. Simulations were performed with and without the defects present to allow for the SCNR associated with the defects to be calculated. The calculated SCNR values can be seen in Table 6.5 and illustrate the ability of the inspection set up to identify these defects.

Table 6.5: *SCNR of defects located in Taper 2*

Defect Reference	**SCNR** (dB)
Porosity defect 1	6.62
Porosity defect 2	7.43
Porosity defect 3	10.62
Porosity defect 4	10.39
Delamination defect 1	12.21
Delamination defect 2	3.36
Delamination defect 3	17.22

The limit of defect detectability is often described as a ratio of 2.5:1 which relates to a SCNR value of 8 dB. Using this definition, the only porosity defects detected are defect numbers 3 and 4. The SCNR of the porosity defects generally increases from porosity defect 1 to porosity defect 4, which relates to the defects becoming closer to the front wall of the component. As the wave travels through the component the amplitude reduces due to attenuation caused by scattering at the ply layer interfaces, which will decrease the SCNR value of defects deeper in the component.

The delamination defects in the flat sections of the component, delamination defects 1 and 3, have the highest SCNR values would also be detected by the inspection. Again, the defect closer to the front wall of the component generates the highest SCNR. Delamination defect 2, which is located in the taper region, has a much smaller SCNR which signifies this defect would be more difficult to reliably detect. The reasoning for this is due to the combination of the delamination defect orientation and location. The delamination is at the same orientation as the ply layers which will reflect the majority of the incident wave away from the transducer. There will be tip refracted waves that propagate back to the transducer, however these will be at a reduced amplitude. The delamination is also located near the backwall within the taper region, which was shown to be an area with low amplitude, Figure 6.14. This indicates the amplitude of the wave that is incident upon the delamination is reduced, which results in a lower received signal amplitude.

6.3.4 Optimisation of Tapered CFRP Component Inspection

6.3.4.1 Overview

It could be seen from Table 6.5 that defects in the section of the taper containing plies orientated away from the horizontal are more challenging to detect. This is due to the orientation of the defect and the reduced signal amplitude at the defect location due to scattering and refraction of the wave propagating through the differently out of plane orientated ply layers. In order to allow for greater sensitivity to defects located in these areas, the inspection set up needs to be improved. Through the use of efficient simulations, it is possible to optimise the inspection set up for greater defect detection.

The inspection set up has three variables: transducer frequency, incidence angle and transducer focal parameters. The transducer frequency can be decreased to increase the wavelength which will reduce the reflections from ply layers and refraction to allow for greater penetration into the sample. However, the larger wavelength will reduce the resolution of the inspection capability. The transducer incidence angle can be altered to counteract refraction that takes place in the component. This allows for the wave to penetrate the intended location in the component and increase the intensity of sound to aid defect detection. The transducer focal parameters control the size and location of the transducer focal spot and the beam angle from the extremities of the transducer surface. The focal parameters can be modified to generate the optimal lateral resolution through the component thickness.

To highlight the capability of utilising simulation to optimise inspections for greater defect detectability, an optimisation study was performed for the delamination defect located in the tapered region. For the optimisation, the transducer focus was set to the defect before a set of simulations was performed with varying incident angles. The simulations were run with and without the defect and the SCNR of the defect was calculated to evaluate the inspection performance. While this optimisation study only considers the focal point location and incident angle, further simulations could be performed to investigate the transducer frequency as well as the transducer dimensions and focal parameters.

6.3.4.2 Results

The SCNR of the delamination defect was calculated for each incident angle as done previously and the results can be seen in Figure 6.18.

At 0° incidence angle, the SCNR value is higher than the previous value, Table 6.5, as the transducer is focused at the defect location and not the midplane of the sample. From the plot it can be seen that 6° is the incidence angle that produces the highest SCNR value for the defect, however between 5° and 8° the SCNR of the defect is almost flat indicating any angle between these values would be efficient.

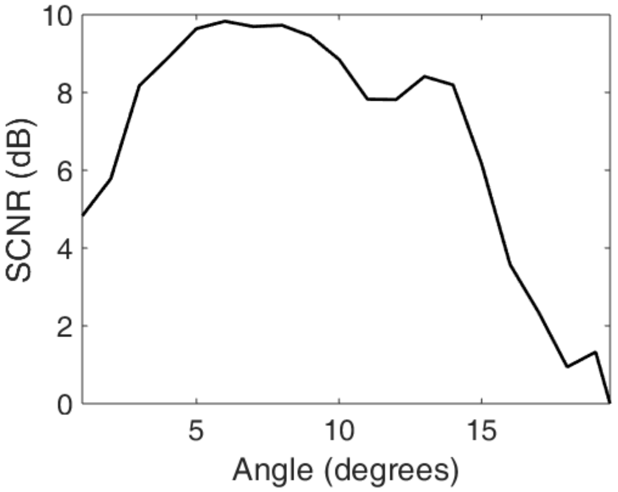

Figure 6.18: *SCNR of delamination defect 2 for varying transducer incident angles*

The derived B-scan and instantaneous amplitude plots for the 6° incident angle inspection of Taper 2 can be seen in Figures 6.19 and 6.20. Plots of results with and without all of the defects present are shown for comparison.

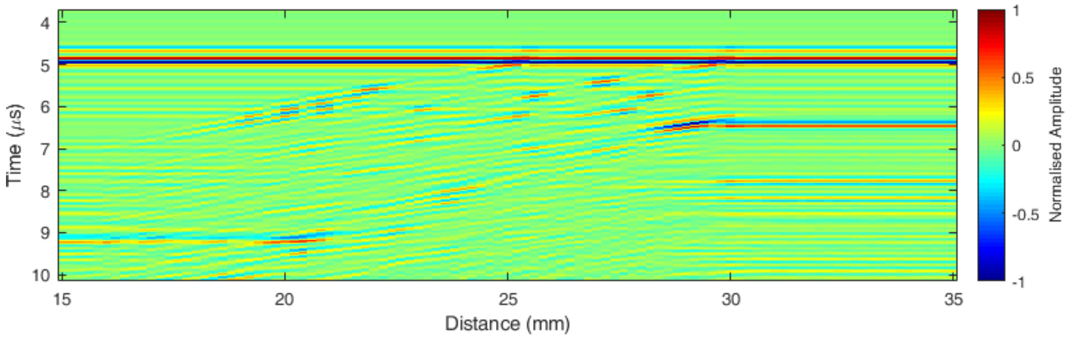

(a) *Without defects present*

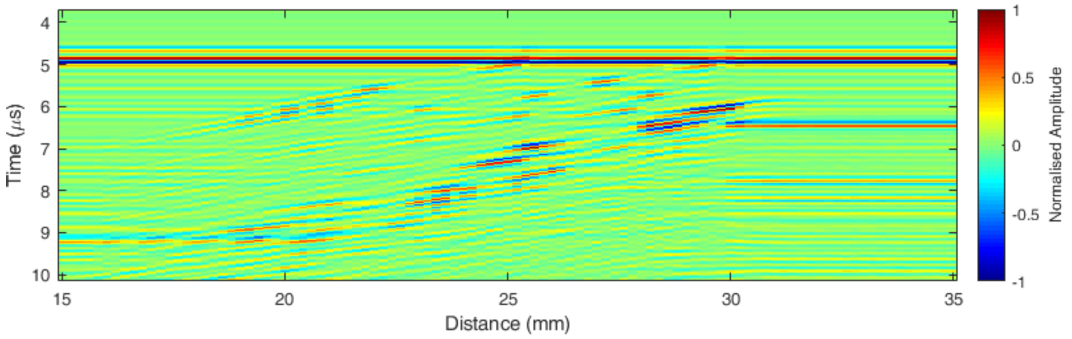

(b) *With defects present*

Figure 6.19: *FEA derived B-scan results for optimised inspection of taper 2 (a) without and (b) with defects present*

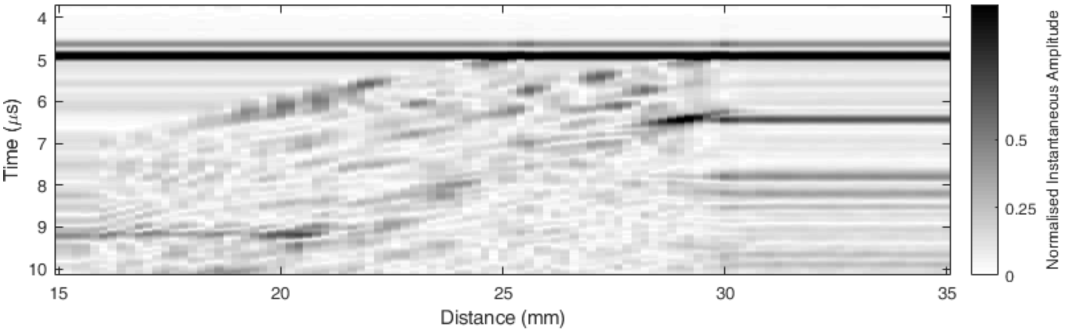

(a) *Without defects present*

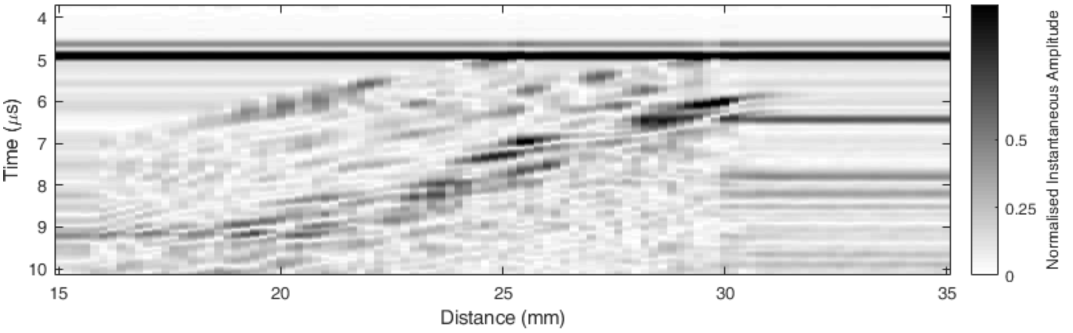

(b) *With defects present*

Figure 6.20: *FEA derived instantaneous amplitude results for optimised inspection of taper 2 (a) without and (b) with defects present*

Comparison of the B-scan and instantaneous amplitude plots, the delamination defect the inspection was optimises for can be identified at a distance of 25 mm and a time of 7 μs. The porosity defect 3, located to the right of delamination 2, can also be clearly identified. This demonstrates the inspection is improved for defect detection in this region of the tapered component. However, this is at the expense of detectability of the other defects. The defects at the thickest region of the taper cannot be easily identified and the defects at the thin region of the taper can be seen but appear similar to the response from the backwall. This new inspection technique also generates stronger reflections from the ply drop regions where there is a pocket of resin material. This can add implications as these responses appear identical to the defect responses and so it is important the structure of the component is known to be confident in identifying if a signal represents a defect or a structural reflection.

Figure 6.21 presents the amplitude map for the optimised inspection set up, which highlights the improvement of the signal amplitude in the tapered region. However, this is at the cost of reduced signal amplitude in the thicker flat region of the composite.

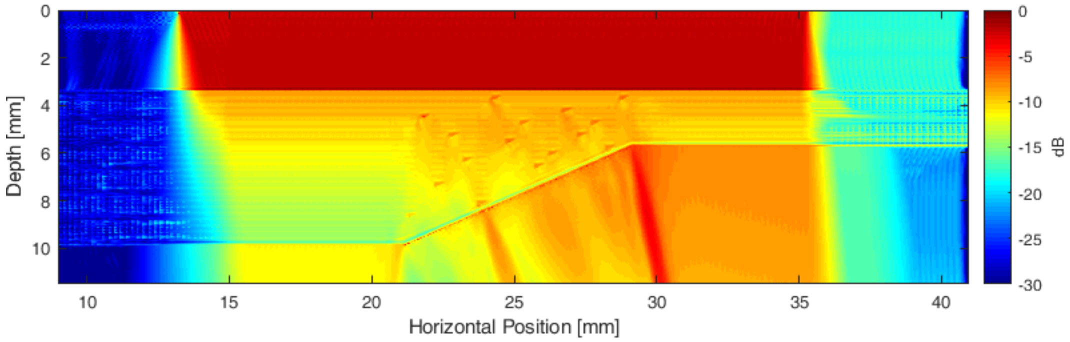

Figure 6.21: *Amplitude map for optimised inspection of Taper 2*

6.3.4.3 Analysis

For this scenario, the incidence angle was selected as the most influential and was the only parameter considered. The incidence angle gave a big change in the received signal amplitude as would be expected with the delamination defect at an oblique angle to the transducer and the refraction of the wave through the component. The optimal incidence angle was shown to be 6°, Figure 6.18.

With the improved inspection incident angle determined, the simulations were performed with the delamination defect present. It is clear to see in the B-scan and instantaneous amplitude plots that there is an improvement in the ability to detect the delamination. The SCNR value of the delamination defect signal was calculated for this improved inspection set up and can be seen in Table 6.6 along with the values calculated for the original 0° incident angle inspection and the difference between the two values.

Table 6.6: *SCNR of defects located in Taper 2 for original 0° and optimised 6° inspection set up*

Defect Reference	**0° Inspection SCNR** (dB)	**6° Inspection SCNR** (dB)	**Difference** (dB)
Porosity defect 1	6.62	5.66	-0.96
Porosity defect 2	7.43	9.81	2.38
Porosity defect 3	10.62	12.86	2.24
Porosity defect 4	10.39	10.38	-0.01
Delamination defect 1	12.21	11.40	-0.81
Delamination defect 2	3.36	14.15	10.79
Delamination defect 3	17.22	19.95	2.73

From Table 6.6, it can be seen that there has been an increase of approximately 11 dB for the optimised 6° incidence angle inspection for delamination defect 2. There has also been an increase in SCNR for porosity defects 2 and 3, and delamination defect 3. The improvement in detection for porosity defects 2 and 3 are due to their location in the tapered region, either side of the delamination defect that the inspection incidence angle was optimised. The delamination 3 defect SCNR is increased as the coherence noise in the flat section received signals is lower for the 6° inspection angle due to the wave not travelling perpendicular to the ply layers. The SCNR of the defects located in the thickest region, porosity defect 1 and delamination defect 1, have a lower SCNR using the 6°, which indicates the signal amplitude from these defects is lower than the previous normal incidence inspection. Using the defect detectability ratio of 2.5:1, the optimised 6° incidence angle inspection would identify all of the defects except porosity defect 1.

The amplitude map for the 6° incident angle inspection, Figure 6.21, has an improved profile in the tapered region, when compared to the previous normal inspection, Figure 6.16(b). The amplitude in the tapered region is more uniform, which indicates the beam is not bending due to refraction at the ply layer interfaces. However, with an increased incidence angle, the amplitude in the thick flat section of the component is degraded, due to a higher amplitude of signal being reflected at the ply layer interfaces.

These results highlights the clear improvement of the inspection set up, that has been achieved through the use of simulation, to improve the detection of defects, in particular delamination defect 2. This process could be repeated to optimise the inspection set up for multiple locations along the tapered region of the component to improve the complete B-scan inspection. The component inspection could then consist of a combination of normal incidence inspection to focus on the flat regions and additional inspections with oblique incidence angles for the tapered region.

Alternatively, the implementation of phased array techniques, such as a sector scan which can focus the beam at multiple locations from a single transducer location, could be investigated. The time delays implemented for the beam steering could be implemented assuming a single isotropic velocity or could be derived through time reversal acoustic simulations [157].

6.4 Discussion

The performance of a normal incidence, focused B-scan inspection of three different taper geometries has been conducted. The inspection performance was assessed through the use of a B-scan amplitude map. These amplitude maps allow for a simple visual illustration of the inspection performance to be evaluated. Comparing the results for the three different severity taper angles, it can be seen the level of amplitude is consistent along all flat sections of the component. However, in the tapered region, the amplitude becomes more inconsistent. This is due to the internal structure of the taper region containing angled ply layers, which cause refraction at their interfaces. The multiple refractions lead to an overall beam steering effect which is stronger for the higher angled taper structure and results in the sound not directly penetrating where intended and can lead to areas of the component with low amplitude. These low amplitude areas can easily be identified in the amplitude maps and are areas where locating defects may be more difficult or impossible.

To further evaluate the inspection performance, simulations were also performed to evaluate the ability to detect defects. The SCNR of the defects, shown in Table 6.5, were calculated to allow for the detectability of the defects to be analysed. It can be seen that the delamination defects 1 and 3 generate the highest SCNR which is due to their location being in the flat sections of the component and so the ultrasonic wave does not suffer from refraction due to varying ply out-of-plane orientations. As the ultrasonic wave travels through the component it becomes attenuated due to scattering at the ply layer interfaces. This attenuation lowers the SCNR for defects deeper in the component as indicated when comparing delamination defects 1 and 3, where defect 3 is deeper in the component and has a lower SCNR value. The porosity defects are also at varying depths and the defect closer to the front wall, porosity defect 4, has the highest SCNR of the porosity defects. The porosity defects and delamination defect 2 are contained within the tapered region of the component, where the ply layers have out-of-plane orientation changes due to ply drops, yet the porosity defects all have a SCNR that is at least, approximately 5dB greater than the delamination defect 2. The reasoning for this is the porosity defects are located within the resin pockets at ply drop locations and the plies between the transducer and the defect are all flat with no out-of-plane orientation changes. However, the delamination defect 2 is contained between angled plies and the ply layers between defect and transducer vary in out of plane orientation. This is illustrated in Figure 6.22, which contains a plot of the out-of-plane orientation of the tapered CFRP ply layers. Also, the amplitude map shown in Figure 6.14, indicates that the level of sound amplitude at the delamination defect is lower than the areas of the porosity defects which will impact the defects SCNR value.

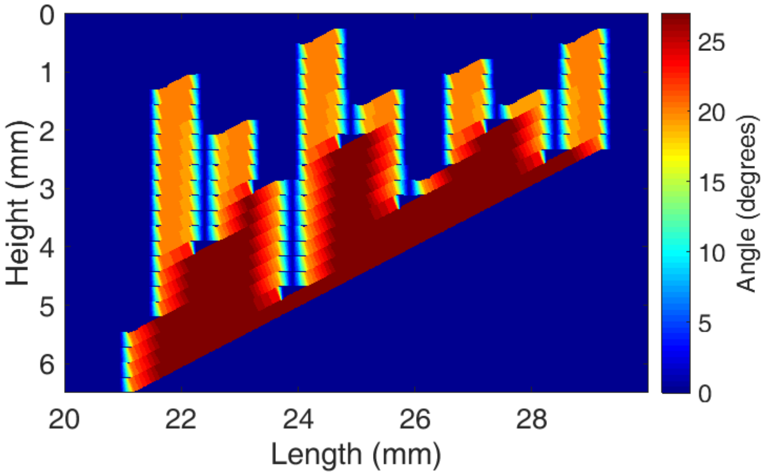

Figure 6.22: *Taper ply layer out-of-plane orientations*

The taper geometry is generated from a plybook and is constructed as an ideal structure with plies conforming around ply drops perfectly. This means the ply layers directly above the resin pockets at a ply drop contain no variation in the out of plane orientation. So when inspecting the porosity defects, the incident wave was not refracted or scattered as much as expected. While, delamination defect 2 is contained in a region where the ply layers have a large out of plane orientation angle. This delamination defect is also at an oblique angle to the transducer and so the signal will be reflected away from the transducer. This is reflected in the fact that this defect had the lowest SCNR, Table 6.5.

As well as evaluating inspection performance and capability, simulation can also be used to optimise inspection set ups. This was done for the delamination defect 2 present in the tapered region of the Taper 2 component. Simulation allows for the various inspection parameters, such as frequency, focal length and location and incidence angle, to be varied to determine the optimal input.

6.5 Conclusion

This Chapter has demonstrated how FEA modelling can be utilised to evaluate and tune the ultrasonic inspection of tapered CFRP components. The ultrasonic inspection of tapered CFRP structures is challenging due to their internal ply layer structure often leading to high levels of refraction of the incident beam. The models are generated using the plybook approach constructed in this research to allow for arbitrary component structures to be simulated. This allows for the models to consider the entire composite geometry, including the thin resin layers and variations of out-of-plane ply orientations. Computationally efficient simulations can then be performed to accommodate for inspection performance to be predicted.

Simulations were performed to replicate a focused immersion B-scan inspection of three different CFRP tapers with different severity of taper angle. As well as generating B-scan images, amplitude maps were also generated to give a visual indication of where sound has penetrated in the component and allow for the inspection performance to be evaluated. Further simulations were then performed to evaluate the ability to identify both porosity and delamination defects within the tapered component. Final simulations demonstrated the ability of simulation to greatly improve the detectability of a delamination defect located within the taper region of the component.

Chapter 7

Conclusions

The work presented in this Thesis details the research conducted to produce FEA models of CFRP structures for the simulation of ultrasonic inspections. The key findings of this research are summarised in this Chapter, along with a list of publications arising from the Thesis. A major aspect of the EngD scheme is to promote technology transfer from research to industry. As a result, this Chapter will discuss the benefits this research has provided to OnScale. Finally, suggestions for future work to be explored are presented.

7.1 Summary of Thesis

This Thesis began with introducing and identifying the industrial motivation for the research conducted. The overall objective of this Thesis was to improve the capability of modelling ultrasonic NDE inspections of CFRP components. In particular, tapered CFRP structures were identified as a current industrial problem.

A literature review was provided to give a background on the research topics covered in the Thesis. This involved an overview of NDE modelling techniques and the methods available. The justification for selecting a FEA approach was provided along with an overview of the OnScale software package used throughout the research. Lastly, an overview of ultrasonic NDE of composite materials was given with a review of current research into their NDE modelling.

The modelling method implemented in the Thesis was initially validated and optimised through the comparison of TFM images generated from FEA derived and experimentally collected FMC data sets. Good correlation between the results demonstrated the modelling method applied was valid and capable at predicting the experimental behaviour.

Generating FEA models of CFRP structures is challenging due to their complex structure and material properties. This Thesis has presented different approaches that have been created to allow for the generation of these challenging components. The techniques created allow for various CFRP components, including flat laminates, woven structures and tapered components, to be constructed in FEA models.

A parametric study was performed to investigate the effect varying transducer frequency and focal angle had on characterising a CFRP sample. Along with B-scan images, the instantaneous parameters of the analytical signal was used to view inspection performance. Results highlighted how simulation can be implemented to provide a method to evaluate and optimise inspection setup.

The benefits of the ability to simulate inspections of CFRP tapers was demonstrated by simulating the inspection of tapers containing various severity of taper angles. Initial simulations validated the FEA model generation through correlation with experimental data. Results highlighted how simulations can be used to evaluate inspection performance of different components through the use of coverage maps and simulating defect detection. Furthermore, simulation can be used to optimise inspections and improve defect detection by improving inspection set up.

7.2 Key Contributions

The use of CFRP components in many industries has become more prominent due to their ability to provide high mechanical strength while also yielding weight savings in structures. These materials pose challenges to ultrasonic NDE techniques as their anisotropic materials and laminate construction cause scattering and refraction of the beam, both of which can detrimentally affect inspection coverage. A suitable approach to help design, evaluate and improve these inspections is through the use of modelling. However, due to the complexity of the required modelling domain, advancements in modelling techniques are required in order to provide accurate and reliable simulations.

Prior to this Thesis, there was a shortage in capability for numerical modelling of ultrasonic NDE inspections of complex composite structures. Many previous studies used approximations to limit the geometry to simple structures and omitted the thin interply resin layers. The generation of FEA models of CFRP structures was a major focus of this research and provided the key outcome of developing an integrated framework to facilitate high quality simulation of CFRP material inspection. Several major considerations are required for FEA modelling of CFRP structures including material properties and complex internal structure.

Validation is essential for every modelling method to ensure derived results are acceptable. The initial research provided a a fundamental evaluation and validation of the OnScale package as a NDE simulation tool. The modelling approach was initially validated for a homogeneous test block, before being extended to CFRP components. Good correlation between FEA derived and experimental data demonstrated the models where valid, while remaining computationally efficient.

CFRP structures can be complex in shape and contain a complex internal ply layer structure. Accurate representation of the geometry is essential for FEA models to ensure derived results are correct. This research derived different approaches to generate FEA models of CFRP structures. These approaches could construct the geometry based on the component design specifications to construct the 'as designed' structure. Alternatively, another approach utiliesd X-Ray CT data or photomicrographs to construct a more representative 'as built' geometry. TexGen was used to generate highly complex structures, including woven or twill layers, to import into the FEA model. As well as this, a method to generate tapered geometries from a plybook was developed. This allows for ultrasonic inspections of desired taper geometries to be simulated.

In all the CFRP models in this research, the resin layers between adjacent ply layers are included to ensure the derived results accurately predict experimental behaviour. These layers were often omitted in previous studies due to the increase in computational costs. However, it has been shown for normal incidence wave propagation, inclusion of these layers is essential to generate the small structural reflections observed in ultrasonic inspections.

The carbon fibre ply layer's material properties are anisotropic and dependant on their orientation. This research developed a method to incorporate material property changes in the model to account for any ply layer out of plane orientation variances. These subtle changes are essential for structures such as tapers or those containing waviness, where the out of plane variances have a profound effect on the wave propagation.

The ability to accurately create these models then allows for ultrasonic inspections of CFRP structures to be evaluated and optimised. It has been shown how simulations can evaluate inspection coverage and defect detectability to evaluate inspection performance. Coverage maps were constructed to offer an effective method to visualise inspection coverage in a complex component, such as a tapered CFRP structure. Finally, inspections can be optimised through simulation sweeps of inspection parameters to improve defect detection.

7.3 Publications Arising from Thesis

Journal Publications:

- H. Reed, C. Leckey, A. Dick, G. Harvey, and **J. Dobson**, "A model based bayesian solution for characterization of complex damage scenarios in aerospace composite structures," *Ultrasonics*, vol. 82, pp. 272-288, 2018

Conference Papers:

- **J. Dobson**, A. Tweedie, G. Harvey, R. O'Leary, A. Mulholland, K. Tant and A. Gachagan, "Finite Element Analysis Simulations for Ultrasonic Array NDE Inspections," in *42nd Review in Quantitative Nondestructive Evaluation*, vol. 1706, pp. 040005-1 040005-14, 2016
- **J. Dobson**, A. Gachagan, R. O'Leary, A. Tweedie, and G. Harvey, "Finite element analysis of ultrasonic CFRP laminate inspection," in *55th Annual British Conference of Non-Destructive Testing (NDT 2016)*, 2016
- H. Zhao, **J. Dobson**, A. Gachagan, T. Lardner, G. Dobie, "Hybrid simulation model of ultrasonic inspection of pressure tubes in nuclear industry," in *55th Annual British Conference of Non-Destructive Testing (NDT 2016)*, 2016
- R. Brown, **J. Dobson**, G. Pierce, B. Dutton, and I. Collison, "Quantifying performance of ultrasonic immersion inspection using phased arrays for curvilinear disc forgings," in *43rd Review in Quantitative Nondestructive Evaluation*, vol. 1806, pp. 040004-1 -040004-7, 2017

7.4 Technology Transfer

The work contained in this Thesis was conducted as part of an EngD program, where the research is aimed at an industrial problem. The project was sponsored by the industrial partner, OnScale, allowed for the company to expand their software capability. During the research program, the author worked closely with both academic and industrial partners to improve the capability of ultrasonic FEA modelling of CFRP components. As well as this, the author also collaborated with researchers based in the NDT of composites group at the University of Bristol. This collaboration allowed for the author to gain knowledge in the NDT inspection of composites and assist with researchers at Bristol's composite simulations.

The key contributions from this Thesis has given OnScale software a platform to perform simulations of ultrasonic inspections of CFRP materials. This expanded capability has generated new customers and has also directly lead to the acquirement of consultancy work with major aerospace industry clients. Several consultancy projects have been undertaken with a total value of over £125,000 and further opportunities in discussion. The consultancy work has been undertaken by the author and has been underpinned by the research contained in this Thesis. Furthermore, the company have recently supported a recent Bristol led EPSRC proposal into advanced 3D non-destructive characterisation of 3D woven composites. This proposal includes an outcome that will aim to allow for TexGen to directly output in a format that can be imported into OnScale.

The combination of the new capabilities of OnScale underpinned by this Thesis, with the ability to access large cloud HPC clusters to run simulations in parallel addresses two major barriers for CFRP simulation.

7.5 Future Work

Suggested future work to continue the research presented in this Thesis can be split into two main categories. The first is from an industrial perspective and would suggest the integration of the modelling capability into the FEA software for greater ease of use. Other suggestions for future work involve the progression of the modelling technique to expand the capabilities.

The method of generating FEA models of complex CFRP components involves several stages and is not straight forward for new users. Future work should look to streamline the process and integrate into the OnScale software. For example, the generation of an arbitrary tapered structure could be integrated into a GUI capable of running the Matlab and TexGen inputs required. This reduces user interaction and becomes a single step process.

The generation of model geometry from real data (X-Ray CT or photomicrographs) generates the most representative model. Future work should look to enhance the image processing of cross section images to improve the model geometry generation. The use of image processing provides a faster and more accurate approach when compared with manually mapping out individual ply layers. The image processing capability leads to the opportunity to generate full 3D FEA models of real CFRP structures. Multiple X-Ray CT images could be processed to generate a 3D table file containing details of the component structure to import into the FEA model. With advances of computing hardware and the capability to access cloud HPC, simulation of large 3D models are feasible. Extending to 3D models will offer a complete insight into full wave propagation behaviour.

The ability to use simulation to optimise the detectability of a single defect has been demonstrated in this research, which could be extended to utilise simulations to create an optimisation process to identify the best option for a complete inspection of a component.

The material properties and geometry generated in the FEA models are the biggest sources of error and further work could be conducted to improve their accuracy. This could be conducted through a material characterisation program to fully asses the relevant acoustic and mechanical properties of constituent materials. This would lead to the implementation of material attenuation into the models that has been omitted from this research. Also, an inverse modelling approach could be utilised, where a 2D array is used to generate the microstructure of a

CFRP component to then implement into a FEA model.

A final suggestion of future work would be to extend the FEA model generation for other types of CFRP structures. In this Thesis, a flat laminate with woven top and bottom layers and tapered structures have been considered. The process of generating the model geometries is very flexible and could easily be extended to other common CFRP structures, such as curved laminates.

References

[1] GlobeNewsWire, "Onscale exits stealth with $3m in seed funding and unveils the industry's first solver-as-a-service platform." https://globenewswire.com/news-release/2018/03/01/1402165/0/en/OnScale-Exits-Stealth-with-3M-in-Seed-Funding-and-Unveils-the-Industry-s-First-Solver-as-a-Service-Platform.html, 2018. Last Accessed: 13-May-2018.

[2] OnScale, "Onscale - the future of engineering." https://onscale.com, 2018. Last Accessed: 13-May-2018.

[3] R. Smith, L. Nelson, N. Xie, C. Fraij, and S. Hallett, "Progress in 3D characterisation and modelling of monolithic carbon-fibre composites," *Insight-Non-Destructive Testing and Condition Monitoring*, vol. 57, no. 3, pp. 131–139, 2015.

[4] L. W. Schmerr, *Fundamentals of Ultrasonic Nondestructive Evaluation.* Springer, 2016.

[5] J. C. Aldrin, "Overview of mathematical modeling in nondestructive evaluation (NDE)," *NASA STI/Recon Technical Report N*, vol. 3, 2002.

[6] E. Ginzel, "NDT modelling: an overview," in *Proceedings of Conference on Modelling in Non-Destructive Testing, Pretoria, South Africa*, 2007.

[7] P. Calmon, A. Lhémery, I. Lecœur-Taıbi, R. Raillon, and L. Paradis, "Models for the computation of ultrasonic fields and their interaction with defects in realistic NDT configurations," *Nuclear Engineering and Design*, vol. 180, no. 3, pp. 271–283, 1998.

[8] C. Huygens, "Traité de la lumiere, 1690," *Project Gutenberg*, 2005.

[9] P. Wilcox, R. Monkhouse, M. Lowe, and P. Cawley, "The use of Huygens' principle to model the acoustic field from interdigital lamb wave transducers," in *Review of Progress in Quantitative Nondestructive Evaluation*, vol. 17, pp. 915–922, 1998.

[10] L. Azar, Y. Shi, and S.-C. Wooh, "Beam focusing behavior of linear phased arrays," *NDT & E International*, vol. 33, no. 3, pp. 189–198, 2000.

[11] E. Jasiūnienė, "Modelling of 3D reflections from triangles using the Huygens approach," *Ultragarsas*, vol. 62, no. 4, pp. 22–27, 2007.

[12] J. Fourier, "On the propagation of heat in solid bodies," *Memoir, read before the Class of the Instut de France*, 1807.

[13] T. Lardner, *New Algorithms for Ultrasonic Non-Destructive Evaluation.* PhD Thesis, University of Strathclyde, 2016.

[14] W. P. Mason, *Electromechanical Transducers and Wave Filters.* D. Van Nostrand Co., 1948.

[15] R. Krimholtz, D. A. Leedom, and G. L. Matthaei, “New equivalent circuits for elementary piezoelectric transducers,” *Electronics Letters*, vol. 6, no. 13, pp. 398–399, 1970.

[16] D. Leedom, R. Krimholtz, and G. Matthaei, “Equivalent circuits for transducers having arbitrary even-or odd-symmetry piezoelectric excitation,” *IEEE Transactions on Sonics and Ultrasonics*, vol. 18, no. 3, pp. 128–141, 1971.

[17] G. Hayward, *Time and Frequency Domain Modelling of the Piezoelectric Transducer.* PhD Thesis, University of Strathclyde, 1981.

[18] G. Hayward, C. MacLeod, and T. Durrani, “A systems model of the thickness mode piezoelectric transducer,” *The Journal of the Acoustical Society of America*, vol. 76, no. 2, pp. 369–382, 1984.

[19] G. Hayward and M. N. Jackson, “Discrete-time modeling of the thickness mode piezoelectric transducer,” *IEEE Transactions on Sonics and Ultrasonics*, vol. 31, no. 3, pp. 137–150, 1984.

[20] G. Hayward and M. N. Jackson, “A lattice model of the thickness-mode piezoelectric transducer,” *IEEE Transactions on Ultrasonics, Ferroelectrics, and Frequency Control*, vol. 33, no. 1, pp. 41–50, 1986.

[21] G. R. Lockwood and F. S. Foster, “Modeling and optimization of high-frequency ultrasound transducers,” *IEEE Transactions on Ultrasonics, Ferroelectrics, and Frequency Control*, vol. 41, no. 2, pp. 225–230, 1994.

[22] J. Johnson, N. Carlson, and D. Tow, “Ray trace calculations of ultrasonic fields,” *Research in Nondestructive Evaluation*, vol. 3, no. 1, pp. 27–39, 1991.

[23] J. Ogilvy, “An iterative ray tracing model for ultrasonic nondestructive testing,” *NDT & E International*, vol. 25, no. 1, pp. 3–10, 1992.

[24] J. Ogilvy, “Computerized ultrasonic ray tracing in austenitic steel,” *NDT International*, vol. 18, no. 2, pp. 67–77, 1985.

[25] J. A. Ogilvy, “Ultrasonic beam profiles and beam propagation in an austenitic weld using a theoretical ray tracing model,” *Ultrasonics*, vol. 24, no. 6, pp. 337–347, 1986.

[26] P. Calmon, S. Mahaut, S. Chatillon, and R. Raillon, “CIVA: an expertise platform for simulation and processing NDT data,” *Ultrasonics*, vol. 44, pp. 975–979, 2006.

[27] M. Darmon, N. Leymarie, S. Chatillon, and S. Mahaut, “Modelling of scattering of ultrasounds by flaws for NDT,” in *Ultrasonic Wave Propagation in Non Homogeneous Media*, vol. 128, pp. 61–71, 2009.

[28] P. C. E. Ginzel, M. Matheson and B. Brown, “Validation of aspects of beamtool,” *NDT.net*, vol. 19, no. 5, 2014.

[29] C. Desilets, G. Wojcik, L. Nikodym, and K. Mesterton, “Analyses and measurements of acoustically matched, air-coupled tonpilz transducers,” in *IEEE International Ultrasonics Symposium*, vol. 2, pp. 1045–1048, 1999.

[30] P. J. Schafbuch, R. B. Thompson, and F. J. Rizzo, “Application of the boundary element method to elastic wave scattering by irregular defects,” *Journal of Nondestructive Evaluation*, vol. 9, no. 2-3, pp. 113–127, 1990.

[31] J. L. Rose *et al.*, “Boundary element modeling for defect characterization potential in a wave guide,” *International Journal of Solids and Structures*, vol. 40, no. 11, pp. 2645–2658, 2003.

[32] R. Courant, K. Friedrichs, and H. Lewy, “On the partial difference equations of mathematical physics,” *IBM Journal of Research and Development*, vol. 11, no. 2, pp. 215–234, 1967.

[33] L. J. Bond, “Finite difference methods applied to ultrasonic non-destructive testing problems,” in *ARPA/AFML Review of Progress in Quantitative NDE*, vol. 1, pp. 310–322, 1980.

[34] L. Bond, M. Punjani, and N. Saffari, “Ultrasonic wave propagation and scattering using explicit finite-difference methods,” in *Mathematical Modeling in NDT*, vol. 1, pp. 81–124, 1988.

[35] R. van Vossen, J. O. Robertsson, and C. H. Chapman, “Finite-difference modeling of wave propagation in a fluid-solid configuration,” *Geophysics*, vol. 67, no. 2, pp. 618–624, 2002.

[36] D. Ostergaard and T. Pawlak, “Three-dimensional finite elements for analyzing piezoelectric structures,” in *IEEE International Ultrasonics Symposium*, vol. 1, pp. 639–644, 1986.

[37] R. Lerch, “Finite element analysis of piezoelectric transducers,” in *IEEE International Ultrasonics Symposium*, vol. 2, pp. 643–654, 1988.

[38] R. Lerch, “Simulation of piezoelectric devices by two-and three-dimensional finite elements,” *IEEE Transactions on Ultrasonics, Ferroelectrics, and Frequency Control*, vol. 37, no. 3, pp. 233–247, 1990.

[39] G. Hayward and J. A. Hossack, “Unidimensional modeling of 1-3 composite transducers,” *The Journal of the Acoustical Society of America*, vol. 88, no. 2, pp. 599–608, 1990.

[40] J. Hossack and G. Hayward, “Assessment of different pillar geometries for 1-3 composite transducers using finite element analysis,” in *IEEE International Ultrasonics Symposium*, vol. 1, pp. 389–392, 1990.

[41] J. A. Hossack and G. Hayward, "Finite-element analysis of 1-3 composite transducers," *IEEE Transactions on Ultrasonics, Ferroelectrics, and Frequency Control*, vol. 38, no. 6, pp. 618–629, 1991.

[42] J. Dziewierz, A. Gachagan, R. O'Leary, and S. N. Ramadas, "Numerical optimisation of piezocomposite material properties using 3D finite-element modeling," in *16th International Congress on Sound and Vibration (CSV16)*, vol. 5, 2009.

[43] P. Reynolds and V. Pereyra, "Application of optimisation techniques to finite element analysis of piezocomposite devices," in *IEEE International Ultrasonics Symposium*, vol. 1, pp. 634–637, 2004.

[44] L. L. Ries and S. W. Smith, "Finite element analysis of a deformable array transducer," *IEEE Transactions on Ultrasonics, Ferroelectrics, and Frequency Control*, vol. 46, no. 6, pp. 1352–1363, 1999.

[45] S. Zhou, P. Reynolds, and J. A. Hossack, "Improving the performance of capacitive micromachined ultrasound transducers using modified membrane and support structures," in *IEEE International Ultrasonics Symposium*, vol. 4, pp. 1925–1928, 2005.

[46] M. J. Lowe, "Matrix techniques for modeling ultrasonic waves in multilayered media," *IEEE Transactions on Ultrasonics, Ferroelectrics, and Frequency Control*, vol. 42, no. 4, pp. 525–542, 1995.

[47] F. Moser, L. J. Jacobs, and J. Qu, "Modeling elastic wave propagation in waveguides with the finite element method," *NDT & E International*, vol. 32, no. 4, pp. 225–234, 1999.

[48] A. Gachagan, A. McNab, and P. Reynolds, "Analysis of ultrasonic wave propagation in metallic pipe structures using finite element modelling techniques," in *IEEE International Ultrasonics Symposium*, vol. 2, pp. 938–941, 2004.

[49] S. Ham and K.-J. Bathe, "A finite element method enriched for wave propagation problems," *Computers & Structures*, vol. 94, pp. 1–12, 2012.

[50] A.-C. Hladky-Hennion, "Finite element analysis of the propagation of acoustic waves in waveguides," *Journal of Sound and Vibration*, vol. 194, no. 2, pp. 119–136, 1996.

[51] A.-C. Hladky-Hennion, P. Langlet, and M. De Billy, "Finite element analysis of the propagation of acoustic waves along waveguides immersed in water," *Journal of Sound and Vibration*, vol. 200, no. 4, pp. 519–530, 1997.

[52] M. Castaings and M. Lowe, "Finite element model for waves guided along solid systems of arbitrary section coupled to infinite solid media," *The Journal of the Acoustical Society of America*, vol. 123, no. 2, pp. 696–708, 2008.

[53] W. Hassan and W. Veronesi, “Finite element analysis of Rayleigh wave interaction with finite-size, surface-breaking cracks,” *Ultrasonics*, vol. 41, no. 1, pp. 41–52, 2003.

[54] T. Weiland, “A discretization model for the solution of Maxwell's equations for six-component fields,” *Archiv Elektronik und Uebertragungstechnik*, vol. 31, pp. 116–120, 1977.

[55] P. Fellinger, R. Marklein, K. Langenberg, and S. Klaholz, “Numerical modeling of elastic wave propagation and scattering with EFIT - elastodynamic finite integration technique,” *Wave Motion*, vol. 21, no. 1, pp. 47–66, 1995.

[56] R. Marklein, “The finite integration technique as a general tool to compute acoustic, electromagnetic, elastodynamic, and coupled wave fields,” *Review of Radio Science*, vol. 2002, pp. 201–244, 1999.

[57] R. Marklein, “Ultrasonic wave and transducer modeling with the finite integration technique (FIT),” in *IEEE International Ultrasonics Symposium*, vol. 1, pp. 563–566, 2002.

[58] F. Schubert, “Numerical time-domain modeling of linear and nonlinear ultrasonic wave propagation using finite integration techniques - theory and applications,” *Ultrasonics*, vol. 42, no. 1, pp. 221–229, 2004.

[59] J. Prikšaitis, L. Mažeika, R. Barauskas, E. Žukauskas, and A. Kriščiūnas, “Influence of the numerical dispersion effects in the modelling of ultrasonic measurements,” *Physics Procedia*, vol. 70, pp. 532–536, 2015.

[60] P. Calmon, “Recent developments in NDT simulation,” in *5th World Congres on Ultrasonics*, vol. 1, pp. 443–446, 2003.

[61] J. Zhang, B. W. Drinkwater, P. D. Wilcox, and A. J. Hunter, “Defect detection using ultrasonic arrays: The multi-mode total focusing method,” *NDT & E International*, vol. 43, no. 2, pp. 123–133, 2010.

[62] P. Rajagopal, E. A. Skelton, W. Choi, M. J. Lowe, and R. V. Craster, “A generic hybrid model for bulk elastodynamics, with application to ultrasonic nondestructive evaluation,” *IEEE Transactions on Ultrasonics, Ferroelectrics, and Frequency Control*, vol. 59, no. 6, pp. 1239–1252, 2012.

[63] H. Zhao, J. Dobson, A. Gachagan, T. Lardner, and G. Dobie, “Hybrid simulation model of ultrasonic inspection of pressure tubes in nuclear industry,” in *55th Annual Conference of the British Institute of Non-Destructive Testing (NDT 2016)*, pp. 1–10, 2016.

[64] J. Zhang, B. W. Drinkwater, and P. D. Wilcox, “Comparison of ultrasonic array imaging algorithms for nondestructive evaluation,” *IEEE Transactions on Ultrasonics, Ferroelectrics, and Frequency Control*, vol. 60, no. 8, pp. 1732–1745, 2013.

[65] W. Choi, E. Skelton, M. Lowe, R. Craster, and P. Rajagopal, "Generic hybrid models for three-dimensional ultrasonic NDE," in *American Institute of Physics Conference Proceedings*, vol. 1430, pp. 126–133, 2012.

[66] J. R. Pettit, *Modelling the Ultrasonic Response from Rough Defects using Efficient Finite Element Modelling Techniques.* EngD Thesis, Imperial College London, 2014.

[67] S. Kolkoori, *Quantitative Evaluation of Ultrasonic Wave Propagation in Inhomogeneous Anisotropic Austenitic Welds using 3D Ray Tracing Method: Numerical and Experimental Validation.* PhD Thesis, Technische Universität Berlin, 2013.

[68] K. Kirk and N. Schmarje, "Experimental and simulated performance of lithium niobate 1-3 piezocomposites for 2MHz non-destructive testing applications," *Ultrasonics*, vol. 53, no. 1, pp. 185–190, 2013.

[69] D. Robertson, G. Hayward, A. Gachagan, J. Hyslop, and V. Murray, "A new low frequency piezoelectric composite transducer," in *IEEE International Ultrasonics Symposium*, vol. 3, pp. 1670–1673, 2004.

[70] A. C. Parr, R. L. O'Leary, and G. Hayward, "Improving the thermal stability of 1-3 piezoelectric composite transducers," *IEEE Transactions on Ultrasonics, Ferroelectrics, and Frequency Control*, vol. 52, no. 4, pp. 550–563, 2005.

[71] G. Wojcik, J. Mould, N. Abboud, M. Ostromogilsky, and D. Vaughan, "Nonlinear modeling of therapeutic ultrasound," in *IEEE International Ultrasonics Symposium*, vol. 2, pp. 1617–1622, 1995.

[72] G. Harvey and A. Gachagan, "Simulation and measurement of nonlinear behavior in a high-power test cell," *IEEE Transactions on Ultrasonics, Ferroelectrics, and Frequency Control*, vol. 58, no. 4, 2011.

[73] T. Hellen and A. Becker, *Finite Element Analysis for Engineers - A Primer.* NAFEMS, 2013.

[74] G. L. Wojcik, D. Vaughan, N. Abboud, and J. Mould, "Electromechanical modeling using explicit time-domain finite elements," in *IEEE International Ultrasonics Symposium*, vol. 2, pp. 1107–1107, 1993.

[75] D. Powell, P. Reynolds, D. Vaughan, J. Mould, and C. Desilets, "The impact of element taper and inhomogeneous material properties on ultrasonic array performance," in *IEEE International Ultrasonics Symposium*, vol. 2, pp. 1161–1166, 2002.

[76] M. B. Drozdz, *Efficient finite element modelling of ultrasound waves in elastic media.* PhD Thesis, Imperial College London, 2008.

[77] P. Huthwaite, "Accelerated finite element elastodynamic simulations using the GPU," *Journal of Computational Physics*, vol. 257, pp. 687–707, 2014.

[78] G. Marsh, “Boeing’s 787: trials, tribulations, and restoring the dream,” *Reinforced Plastics*, vol. 53, no. 8, pp. 16–21, 2009.

[79] J. Kollgaard, S. LaRiviere, D. O. Thompson, and D. E. Chimenti, “NDE challenges with future commercial aircraft – A Boeing perspective,” in *American Institute of Physics Conference Proceedings*, vol. 975, pp. 23–28, 2008.

[80] G. Marsh, “Airbus takes on Boeing with reinforced plastic A350 XWB,” *Reinforced Plastics*, vol. 51, no. 11, pp. 26–29, 2007.

[81] G. Marsh, “Airbus A350 XWB update,” *Reinforced Plastics*, vol. 54, no. 6, pp. 20–24, 2010.

[82] F. C. Campbell, *Structural Composite Materials.* ASM international, 2010.

[83] xComposites, “Woven fabrics.” http://www.xcomposites.com/woven.html. Last Accessed: 24-June-2018.

[84] A. Mukherjee and B. Varughese, “Design guidelines for ply drop-off in laminated composite structures,” *Composites Part B: Engineering*, vol. 32, no. 2, pp. 153–164, 2001.

[85] D. Cairns, J. Mandell, M. Scott, and J. Maccagnano, “Design and manufacturing considerations for ply drops in composite structures,” *Composites Part B: Engineering*, vol. 30, no. 5, pp. 523–534, 1999.

[86] F.-X. Irisarri, A. Lasseigne, F.-H. Leroy, and R. Le Riche, “Optimal design of laminated composite structures with ply drops using stacking sequence tables,” *Composite Structures*, vol. 107, pp. 559–569, 2014.

[87] R. Smith, “Composite defects and their detection,” *Materials Science and Engineering*, vol. 3, pp. 103–143, 2009.

[88] W. Hou and W. Zhang, “Advanced composite materials defects/damages and health monitoring,” in *Proceedings of the IEEE 2012 Prognostics and System Health Management Conference*, vol. 1, pp. 1–5, 2012.

[89] P. Olivier, J. Cottu, and B. Ferret, “Effects of cure cycle pressure and voids on some mechanical properties of carbon/epoxy laminates,” *Composites*, vol. 26, no. 7, pp. 509–515, 1995.

[90] M. Wisnom, “The role of delamination in failure of fibre-reinforced composites,” *Philosophical Transactions: Mathematical, Physical and Engineering Sciences*, vol. 370, no. 1965, pp. 1850–1870, 2012.

[91] S. Gholizadeh, “A review of non-destructive testing methods of composite materials,” *Procedia Structural Integrity*, vol. 1, pp. 50–57, 2016.

[92] R. A. Smith, L. J. Nelson, M. J. Mienczakowski, and R. E. Challis, "Automated analysis and advanced defect characterisation from ultrasonic scans of composites," *Insight - Non-Destructive Testing and Condition Monitoring*, vol. 51, no. 2, pp. 82–87, 2009.

[93] L. Nelson, R. Smith, and M. Mienczakowski, "Ply-orientation measurements in composites using structure-tensor analysis of volumetric ultrasonic data," *Composites Part A: Applied Science and Manufacturing*, vol. 104, pp. 108–119, 2018.

[94] R. A. Smith, L. J. Nelson, M. J. Mienczakowski, and P. D. Wilcox, "Ultrasonic tracking of ply drops in composite laminates," in *American Institute of Physics Conference Proceedings*, vol. 1706, pp. 1–10, 2016.

[95] M. Ibrahim, R. Smith, and C. Wang, "Ultrasonic detection and sizing of compressed cracks in glass-and carbon-fibre reinforced plastic composites," *NDT & E International*, vol. 92, pp. 111–121, 2017.

[96] M. Mienczakowski, *Advanced ultrasonic NDE of composite airframe components: physics, modelling and technology.* PhD Thesis, University of Nottingham, 2010.

[97] R. J. Freemantle, *Ultrasonic compression wave evaluation of adhered metal sheets and thin sheet materials.* PhD Thesis, University of Keele, 1995.

[98] M. Mienczakowski, A. Holmes, R. Challis, D. O. Thompson, and D. E. Chimenti, "Modeling of ultrasonic wave propagation in composite airframe components," in *American Institute of Physics Conference Proceedings*, vol. 975, pp. 995–1001, 2008.

[99] R. A. Smith, *Use of 3D ultrasound data sets to map the localised properties of fibre-reinforced composites.* PhD Thesis, University of Nottingham, 2010.

[100] L. Wang and S. Rokhlin, "Stable reformulation of transfer matrix method for wave propagation in layered anisotropic media," *Ultrasonics*, vol. 39, no. 6, pp. 413–424, 2001.

[101] S. Rokhlin and L. Wang, "Ultrasonic waves in layered anisotropic media: characterization of multidirectional composites," *International Journal of Solids and Structures*, vol. 39, no. 16, pp. 4133–4149, 2002.

[102] S. Rokhlin and L. Wang, "Stable recursive algorithm for elastic wave propagation in layered anisotropic media: Stiffness matrix method," *The Journal of the Acoustical Society of America*, vol. 112, no. 3, pp. 822–834, 2002.

[103] Y. Humeida, V. J. Pinfield, R. E. Challis, P. D. Wilcox, and C. Li, "Simulation of ultrasonic array imaging of composite materials with defects," *IEEE Transactions on Ultrasonics, Ferroelectrics, and Frequency Control*, vol. 60, no. 9, pp. 1935–1948, 2013.

[104] N. Gengembre, P. Calmon, O. Pétillon, S. Chatillon, D. O. Thompson, D. E. Chimenti, C. Nessa, S. Kallsen, and L. Poore, “Prediction of ultrasonic fields into composite multi-layered structures: Homogenization approach for the direct field and statistical approach for the inner reflections,” in *American Institute of Physics Conference Proceedings*, vol. 657, pp. 957–964, 2003.

[105] S. Deydier, N. Leymarie, P. Calmon, V. Mengeling, D. O. Thompson, and D. E. Chimenti, “Modeling of the ultrasonic propagation into carbon-fiber-reinforced epoxy composites, using a ray theory based homogenization method,” in *American Institute of Physics Conference Proceedings*, vol. 820, pp. 972–978, 2006.

[106] K. Jezzine, D. Ségur, R. Ecault, N. Dominguez, and P. Calmon, “Hybrid ray-FDTD model for the simulation of the ultrasonic inspection of CFRP parts,” in *American Institute of Physics Conference Proceedings*, vol. 1806, p. 090016, 2017.

[107] C. A. Leckey, M. D. Rogge, C. A. Miller, and M. K. Hinders, “Multiple-mode lamb wave scattering simulations using 3D elastodynamic finite integration technique,” *Ultrasonics*, vol. 52, no. 2, pp. 193–207, 2012.

[108] C. A. Leckey, M. D. Rogge, and F. R. Parker, “Guided waves in anisotropic and quasi-isotropic aerospace composites: Three-dimensional simulation and experiment,” *Ultrasonics*, vol. 54, no. 1, pp. 385–394, 2014.

[109] D. Singh, R. El Guerjouma, and M. Bentahar, “Interaction of fundamental lamb modes with a point impact damaged zone in composite plates,” in *Acoustics 2012*, pp. 2423–2428, 2012.

[110] C.-T. Ng and M. Veidt, “Scattering of the fundamental anti-symmetric Lamb wave at delaminations in composite laminates,” *The Journal of the Acoustical Society of America*, vol. 129, no. 3, pp. 1288–1296, 2011.

[111] D. Pain, *Detection and quantification of fibre waviness in composite laminates using ultrasonic arrays.* PhD Thesis, University of Bristol, 2014.

[112] C. A. Leckey, K. R. Wheeler, V. N. Hafiychuk, H. Hafiychuk, and D. A. Timuçin, “Simulation of guided-wave ultrasound propagation in composite laminates: Benchmark comparisons of numerical codes and experiment,” *Ultrasonics*, vol. 84, pp. 187–200, 2018.

[113] I. A. Veres, R. A. Smith, and V. J. Pinfield, “Comparison of numerical and effective-medium modeling of porosity in layered media,” *IEEE Transactions on Ultrasonics, Ferroelectrics, and Frequency Control*, vol. 62, no. 6, pp. 1086–1094, 2015.

[114] R. B. Tayong, M. J. Mienczakowski, and R. A. Smith, “3D ultrasound characterization of woven composites,” in *American Institute of Physics Conference Proceedings*, vol. 1949, pp. 1–11, 2018.

[115] J. Dobson, A. Tweedie, G. Harvey, R. O'Leary, A. Mulholland, K. Tant, and A. Gachagan, "Finite element analysis simulations for ultrasonic array nde inspections," in *42nd Annual Review of Progress in Quantitative Nondestructive Evaluation*, vol. 1706, pp. 1–14, 2016.

[116] C. Holmes, B. W. Drinkwater, and P. D. Wilcox, "Post-processing of the full matrix of ultrasonic transmit–receive array data for non-destructive evaluation," *NDT & E International*, vol. 38, no. 8, pp. 701–711, 2005.

[117] Harfang Microtechniques Inc., "Characterisation block product specifications," 2006.

[118] J.-F. Lee, R. Lee, and A. Cangellaris, "Time-domain finite-element methods," *IEEE Transactions on Antennas and Propagation*, vol. 45, no. 3, pp. 430–442, 1997.

[119] W. Gropp, E. Lusk, N. Doss, and A. Skjellum, "A high-performance, portable implementation of the {MPI} message passing interface standard," *Parallel Computing*, vol. 22, no. 6, pp. 789 – 828, 1996.

[120] J. Dziewierz, *2D ultrasonic phased arrays for quantitative characterisation of complex defects.* PhD Thesis, University of Strathclyde, 2015.

[121] A. McGilp, *Adaptation of TFM for inspection of complex components.* EngD Thesis, University of Strathclyde, 2016.

[122] J. Dziewierz and A. Gachagan, "Computationally efficient solution of Snell's law of refraction," *IEEE Transactions on Ultrasonics, Ferroelectrics, and Frequency Control*, vol. 60, no. 6, pp. 1256–1259, 2013.

[123] J. Dziewierz, A. Gachagan, N. Lord, and A. Mulholland, "An application-specific design approach for 2D ultrasonic arrays," in *51st Annual Conference of the British Institute of Non-Destructive Testing 2012 (NDT 2012)*, 2012.

[124] A. McGilp, J. Dziewierz, T. Lardner, A. Gachagan, J. MacKersie, and C. Bird, "Inspection of complex components using 2D arrays and TFM," in *53rd Annual Conference of the British Institute of Non-Destructive Testing (NDT 2014)*, 2015.

[125] R. Chandra, *Parallel programming in OpenMP.* Morgan Kaufmann, 2001.

[126] R. L. O'Leary, G. Brown, and G. Harvey, "Droplets, vapours and clouds-a new approach to capacitive transducer manufacture," in *IEEE International Ultrasonics Symposium*, pp. 1113–1116, 2013.

[127] B. Zhang, G. Allegri, M. Yasaee, and S. Hallett, "Micro-mechanical finite element analysis of z-pins under mixed-mode loading," *Composites Part A: Applied Science and Manufacturing*, vol. 78, pp. 424–435, 2015.

[128] H. Lin, L. P. Brown, and A. C. Long, "Modelling and simulating textile structures using texgen," in *Advanced Materials Research*, vol. 331, pp. 44–47, 2011.

[129] Hexcel, "Hexcel hextow im7 eu data sheet." http://www.hexcel.com/user_area/content_media/raw/IM7_HexTow_DataSheet.pdf. Last Accessed: 12-November-2017.

[130] Hexcel, "Hexcel hexply 8552 eu data sheet." http://www.hexcel.com/user_area/content_media/raw/HexPly_8552_eu_DataSheet.pdf. Last Accessed: 12-November-2017.

[131] P. P. Camanho, P. Maimí, and C. Dávila, "Prediction of size effects in notched laminates using continuum damage mechanics," *Composites Science and Technology*, vol. 67, no. 13, pp. 2715–2727, 2007.

[132] J. Lee and C. Soutis, "A study on the compressive strength of thick carbon fibre-epoxy laminates," *Composites Science and Technology*, vol. 67, no. 10, pp. 2015–2026, 2007.

[133] M. A. Jimenez and A. Miravete, "Application of the finite-element method to predict the onset of delamination growth," *Journal of Composite Materials*, vol. 38, no. 15, pp. 1309–1335, 2004.

[134] H. Reed, C. A. Leckey, A. Dick, G. Harvey, and J. Dobson, "A model based bayesian solution for characterization of complex damage scenarios in aerospace composite structures," *Ultrasonics*, vol. 82, pp. 272–288, 2018.

[135] A. P. Boresi, R. J. Schmidt, and O. M. Sidebottom, *Advanced mechanics of materials*, vol. 6. Wiley New York, 1993.

[136] P. P. Parlevliet, H. E. Bersee, and A. Beukers, "Residual stresses in thermoplastic composites–a study of the literature. part iii: Effects of thermal residual stresses," *Composites Part A: Applied Science and Manufacturing*, vol. 38, no. 6, pp. 1581–1596, 2007.

[137] R. A. Smith, L. J. Nelson, M. J. Mienczakowski, and P. D. Wilcox, "Ultrasonic analytic-signal responses from polymer-matrix composite laminates," *IEEE transactions on ultrasonics, ferroelectrics, and frequency control*, vol. 65, no. 2, pp. 231–243, 2018.

[138] A. Ataş, A. Hodzic, and C. Soutis, "Strength prediction of bolted joints in cross-ply laminates based on subcritical damage modelling," in *ECCM15 - 15th European Conference on Composite Materials*, pp. 24–28, 2012.

[139] Y. Shi, T. Swait, and C. Soutis, "Modelling damage evolution in composite laminates subjected to low velocity impact," *Composite Structures*, vol. 94, no. 9, pp. 2902–2913, 2012.

[140] A. Jumahat, C. Soutis, F. Jones, and A. Hodzic, “Fracture mechanisms and failure analysis of carbon fibre/toughened epoxy composites subjected to compressive loading,” *Composite Structures*, vol. 92, no. 2, pp. 295–305, 2010.

[141] M. C. Waterbury and L. T. Drzal, “Determination of fiber volume fractions by optical numeric volume fraction analysis,” *Journal of Reinforced Plastics and Composites*, vol. 8, no. 6, pp. 627–636, 1989.

[142] S. He, Y. Wen, W. Yu, H. Liu, C. Yue, and J. Bao, “Study on voids of epoxy matrix composites sandwich structure parts,” in *IOP Conference Series: Materials Science and Engineering*, vol. 182, pp. 1–8, 2017.

[143] G. Nikishkov, Y. Nikishkov, and A. Makeev, “Finite element mesh generation for composites with ply waviness based on x-ray computed tomography,” *Advances in Engineering Software*, vol. 58, pp. 35–44, 2013.

[144] A. A. Case, *Permeability of hybrid composites subjected to extreme thermal cycling and low-velocity impacts.* PhD Thesis, Georgia Institute of Technology, 2004.

[145] S. Heimbs, S. Heller, P. Middendorf, F. Hähnel, and J. Weiße, “Low velocity impact on CFRP plates with compressive preload: Test and modelling,” *International Journal of Impact Engineering*, vol. 36, no. 10, pp. 1182–1193, 2009.

[146] F. A. Duck, *Physical properties of tissues: a comprehensive reference book.* Academic press, 2013.

[147] E. Ginzel, “Beam width analysis,” *NDT.net*, vol. 6, no. 9, 2001.

[148] A. Dixit, H. S. Mali, and R. Misra, “Unit cell model of woven fabric textile composite for multiscale analysis,” *Procedia Engineering*, vol. 68, pp. 352–358, 2013.

[149] K. He, S. Hoa, and R. Ganesan, “The study of tapered laminated composite structures: a review,” *Composites Science and Technology*, vol. 60, no. 14, pp. 2643–2657, 2000.

[150] T. A. Fletcher, T. Kim, T. J. Dodwell, R. Butler, R. Scheichl, and R. Newley, “Resin treatment of free edges to aid certification of through thickness laminate strength,” *Composite Structures*, vol. 146, pp. 26–33, 2016.

[151] M. Mulle, R. Zitoune, F. Collombet, L. Robert, and Y.-H. Grunevald, “Embedded fbgs and 3-d dic for the stress analysis of a structural specimen subjected to bending,” *Composite Structures*, vol. 91, no. 1, pp. 48–55, 2009.

[152] P. C. Paul, C. Saff, K. B. Sanger, M. Mahler, H. P. Kan, and E. F. Kautz, “Out of plane analysis for composite structures,” 1990.

[153] G. Allegri, L. Kawashita, R. Backhouse, M. Wisnom, and S. Hallett, “On the optimization of tapered composite laminates in preliminary structural design,” in *Proceedings of the ICCM17 conference. EICC, Edinburgh, UK; 27th–31st July*, pp. 27–31, 2009.

[154] R. Ambu, F. Aymerich, F. Ginesu, and P. Priolo, “Assessment of ndt interferometric techniques for impact damage detection in composite laminates,” *Composites Science and Technology*, vol. 66, no. 2, pp. 199–205, 2006.

[155] K. M. Tant, *Time-frequency domain modelling for ultrasonic nondestructive testing.* PhD Thesis, University of Strathclyde, 2014.

[156] R. Smith, L. Nelson, and M. Mienczakowski, “Phononic band gaps and phase singularities in the ultrasonic response from toughened composites,” in *Review of Progress in Quantitative Nondestructive Evaluation*, vol. 1949, pp. 1–10, 2018.

[157] G. Harvey, A. Tweedie, C. Carpentier, and P. Reynolds, “Finite element analysis of ultrasonic phased array inspections on anisotropic welds,” in *AIP Conference Proceedings*, vol. 1335, pp. 827–834, AIP, 2011.

Appendix A

OnScale Table File

OnScale table files are native files that, when imported into an input file, assigns material properties to the grid elements based on elements coordinates. The table file contains its own grid coordinates and details the material contained in each element. The input file searches the table file and assigns the model element material properties by relating the model grid element coordinates with the coordinates contained in the table file. Input file grid and table file grids do not need to be consistent as the input file will interpolate the table file to the model grid.

It is common for table files to be utilised when the variation of materials throughout the model is complex and not easily represented by the standard subcommands used to assign materials to contiguous regions of the grid. Table files can be in ASCII or binary formay, and can be generated based on experimental data or on some statistical algorithm used to represent the spatial variation of material properties.

Contained in a OnScale table file is details of the x, y and z grid coordinates, material names and details of the material contained in each grid element. A simple table file example is shown on the following page.

```
hedr 0
info 1
xcrd 6
0 1 2 3 4 5
ycrd 6
0 1 2 3 4 5
zcrd 2
0 0
name 3
Mat1 Mat2 Mat3
matr 25
1 1 1 1 1 1 1 1 1 1 2 2 2
2 2 3 3 3 3 3 3 3 3 3 3
```

In the above table file example:

‘hedr 0’	represents the table header
‘info 1’	represents the table info
‘xcrd 6’	indicates there are 6 x grid coorinates
‘0 1 2 3 4 5’	represents the x coordinate values
‘ycrd 6’	indicates there are 6 y grid coorinates
‘0 1 2 3 4 5’	represents the y coordinate values
‘zcrd 2’	indicates there are 2 z grid coorinates
‘0 0’	represents the z coordinate values
‘name 3’	indicates there are 3 material names
‘Mat1 Mat2 Mat3	represents the material names
‘matr 25’	indicates the number of grid elements
‘1 1 ... 2 2’ *‘2 2 ... 3 3’*	incidates the material contained in each grid element

Key points to note:

- Grid coordinates are in meters and a scaling factor can be applied to the table file when imported into an input file
- x, y and z grid coordinate values can be entered over multiple lines
- The material names must correspond to materials used in the input file that the table file is imported into
- Material names can be input over multiple lines
- The final input vector that indicates the material contained in each grid element, indicates the material by its location in the input material names. For example, 1 gives the element the material properties of the first material named
- The final input vector steps through the grid elements by first stepping along the x direction, followed by y and lastly z

An illustration of the geometry generated by the example table file is shown in Figure A.1

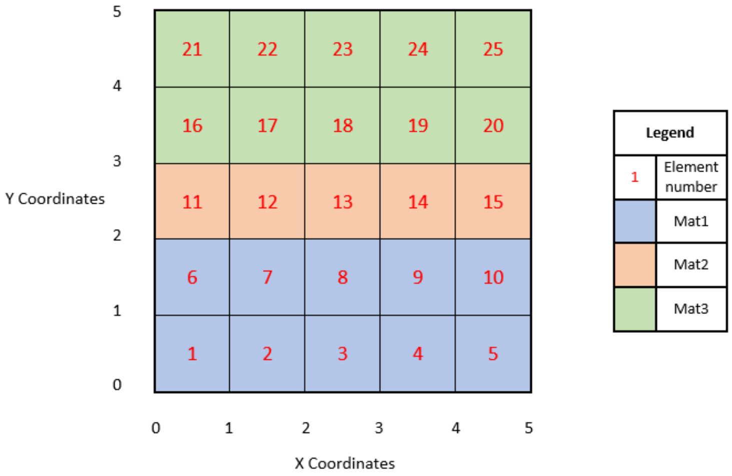

Figure A.1: *Illustration of example table file created geometry*